UCL Chemical Engineering: Doctoral Thesis

The application of bulk acoustic wave (BAW) resonators for the *in-situ* investigation of polymer electrolytes and high-temperature media

2017

Vidal J Bharath

Supervisors: Prof. D Brett
Dr. G Manos

A thesis submitted for the partial fulfilment of the requirements for the degree of Doctor of Philosophy at University College London

Declaration

I, Vidal J Bharath, confirm that the work presented in this thesis is my own. Where information has been derived from other sources, I confirm that this has been indicated in the thesis.

.....
Signature

.....
Date

Acknowledgements

Firstly, I'd like to thank Professor Dan Brett. Thank you for persuading me to do a PhD. The time I've spent in the Electrochemical Innovation Lab (EIL) have been truly outstanding. Thank you for the most memorable of experiences and providing me with the introduction and opportunity to work in such an interesting field. Long may our journey continue.

A massive thank you must also go to my other supervisors (officially and otherwise) Dr. George Manos, Dr. Paul Shearing and Professor Eva Sorenson; the life skills, support and personal development you've each given me has meant more than you know.

A special thanks must also go to the 'Senior team' of Jay, Toby and Tom. You three have been the technical sounding board for which most of this work has been built. Your willingness to help, your keen eyes for detail and problem solving assistance have added to the EIL immeasurably and make it the place it is. How you guys get any time to do your own work is still a mystery to me.

The EIL is a truly special place to do a PhD, the technical work is regularly quantified and measured, however the social side of this group is unparalleled. And so I must add thanks to my fellow socialites; thanks for the early morning emergency theory meeting coffees and the less academic late night drinks. It would not be possible to thank you all here, but I must give a special mention to Erik, Rhod, James, Leon, Ishanka, Dina, Dami, Shade, Amal, Chun and all the others who have made working in a cooped up basement all the more bearable – desirable even. To the 'commercialisation-geek squad'; 'How about that ride in?' I look forward to our future business endeavours and the ever present back up movie-script style heists we have in store. Never change.

Finally, I'd like to thank Amisha and my family. Your love and support is what keeps me going. Thank You.

Abstract

With the realities of the energy and environmental crises drawing ever closer, the need to fast-track the development of promising future renewable energy technologies such as fuel cells is of paramount importance. However, with significant technical barriers to overcome before transition to a fully renewable energy based low carbon economy, the world must, in the short term, continue to rely on existing electricity generation methods such as crude oil refining. It is therefore critical that there remains a focus on advancing and maximising both future and existing technologies' power conversion efficiencies.

Electricity generation technologies represent complex systems; advanced non-intrusive *in-situ* investigations can significantly aid with technological advancements through fundamental understanding of the processes occurring at the interfacial level. Intimate knowledge of the morphological and structural phenomena occurring at the interface can be gathered using techniques such as bulk acoustic wave (BAW) resonators and provide new insight into factors such as operating conditions to guide future technological developments of complex systems.

This thesis outlines the establishment of surface developed, BAW resonators for non-intrusive, *in-situ* application within bespoke, calibrated experimental set ups to elucidate the interfacial phenomena in the viscoelastic phase, and specifically within both the fuel cell industry and the refinement of heavy crude oil as indicated below.

Low-temperature fuel cells (specifically proton exchange membranes (PEMs)) represent a promising constituent in the low carbon economy for portable and automotive power. Yet, issues pertaining to durability and cost hinder the technology's commercialisation. Recent reaction kinetics development in the less well established alkaline anion-exchange membrane (AAEM) fuel cell however, has shown avenues for significant cost reductions. However, the AAEM is not without challenges; linked primarily to hydration states, many reports have shown the technology's susceptibility to chemical degradation when operated at temperatures $\geq$ 65 ^{O}C; carbon

dioxide poisoning when operating in air; and general system integration issues due to a lack of understanding of the AAEM's swelling and water loading mechanisms.

A commercially available thin-film AAEM is investigated here using a novel composite (ionomer-cast) quartz crystal microbalance (QCM) and crystal admittance spectroscopy (CAS) for interfacial characterisation. The study focuses on operation in the presence of hydration and how this affects the ionomer's water uptake, loading and swelling mechanisms as well as the susceptibility of the cationic groups to resist cleavage in the presence of hydroxide ions, leading to E2-(Hofmann) elimination. Operation in conditions that can induce carbonate formation and interaction within the membrane are also investigated.

The world's ever-increasing energy demand has however not just progressed the development of future renewables such as fuel cells, but also required the innovative use of traditional and non-traditional resources such as 'heavy' crude oil. However, with significantly more variable compositions of saturates, aromatics, resins and asphaltenes (SARAs) between wells compared to traditional crude oil supplies, refining and transportation of heavy crude oil using existing infrastructure has become subject to spurious effects of fouling.

Fouling from heavy crude oil in pipelines and refinery equipment is unpredictable, causes major flow assurance issues and occurs primarily as a result of asphaltene destabilisation. Current monitoring and mitigation techniques require time-intensive, large-volume analysis that is not able to react quickly enough to changing oil grades.

As such, this study outlines the development of a novel high temperature, high pressure, rapid, low-volume on-site feedback system for fouling detection and characterisation using an iron-electrodeposited gallium orthophosphate microbalance (iGCM). The iGCM coupled with X-ray computer tomography is used here to offer new insight into the phenomena occurring at the iron–oil interface and thus providing the necessary flow assurance information required to implement fouling rejection or conversion techniques.

Publications

Primary Publications

- V.J. Bharath, J. Millichamp, T.P. Neville, T.J. Mason, P.R. Shearing, R.J.C. Brown, G. Manos, D.J.L. Brett, "**Measurement of water uptake in thin-film Nafion and anion alkaline exchange membranes using the quartz crystal microbalance**," Journal of Membrane Science, vol. 497, pp. 229-238, Jan 1 2016.

- V.J. Bharath, R. Jervis, J. Millichamp, T.P. Neville, T.J. Mason, B. Tjaden, P.R. Shearing, R.J.C. Brown, G. Manos, D.J.L. Brett, "**Alkaline anion-exchange membrane degradation as a function of humidity measured using the quartz crystal microbalance**," International Journal of Hydrogen Energy, vol. 42, no. 9, pp. 6243-6249, Mar 2 2017.

- V.J. Bharath, R. Jervis, J.J. Bailey, E. Engebretsen, J. Millichamp, T.P. Neville, T.J. Mason, P.R. Shearing, R.J.C. Brown, G. Manos, D.J.L. Brett, "**Effect of humidity on the interaction of CO_2 with alkaline anion-exchange membranes probed using the quartz crystal microbalance**," *International Journal of Hydrogen Energy,* vol. 42, no. 38, pp. 24301-24307, Aug 18 2017.

Secondary Publications

- L.D. Brown, R. Abdulaziz, R. Jervis, V. Bharath, T.J. Mason, R.C. Atwood, C. Reinhard, L.D. Connor, D. Inman, D.J.L. Brett, P.R. Shearing, "**A novel molten-salt electrochemical cell for investigating the reduction of uranium dioxide to uranium metal by lithium using in situ synchrotron radiation**," *Journal of Synchrotron Radiation*, vol.24 (2), pp. 439-444, 2017.

- L.D. Brown, R. Abdulaziz, R. Jervis, V.J. Bharath, R.C. Atwood, C. Reinhard, L.D. Connor, S.J.R. Simons, D. Inman, D.J.L. Brett, P.R. Shearing, "**Following the electroreduction of uranium dioxide to uranium in LiCl–KCl eutectic in situ using synchrotron radiation**," *Journal of Nuclear Materials*, vol. 464, pp. 256-262, 2016.

Author's Conference Presentations

- **Characterisation of Thin Film Alkaline Anion-exchange Membranes for Fuel Cells Using a Quartz Crystal Microbalance and Crystal Admittance Spectroscopy**, *Nov. 2015, Zing Hydrogen and Fuel Cells Conference, Cancun Mexico*

- **Characterisation of Thin Film Nafion and Alkaline Anion-exchange Membrane Fuel Cells Using a Quartz Crystal Microbalance (QCM)**, *May 2015, STFC Batteries, Early Career Researcher Conference, Abingdon, UK*

- **The Application of a Bulk Acoustic Wave (BAW) resonator as an *in-situ* sensor for visco-elastic operation using admittance**, *Apr. 2014, University College London, PhD Seminar Series, London, UK*

List of Abbreviations

AAEM	Alkaline anion-exchange membrane
A-FC	Alkaline fuel cell
API	American Petroleum Institute
BAW	Bulk acoustic wave
BVD	Butterworth Van-Dyke
CAS	Crystal admittance spectroscopy
CV	Cyclic voltammetry
DLD	Drive level dependence
EIS	Electrochemical impedance spectroscopy
FC	Fuel cell
FRA	Frequency response analyser
GCM	Gallium orthophosphate microbalance
GDL	Gas diffusion layer
HOR	Hydrogen oxidation reaction
IEC	Ion exchange capacity
IPA	Isopropanol
LGS	Langasite
MEA	Membrane electrode assembly
ORR	Oxygen reduction reaction
PEM	Proton exchange membrane
PG	Pressure gauge
ppm	Parts per million
PRV	Pressure relief valve
QCM	Quartz crystal microbalance
QNRF	Qatar National Research Fund
RH	Relative humidity
SANS	Small-angle neutron scattering
SARA	Saturates, aromatics, resins, asphaltenes
SAXS	Small-angle X-rays scattering
SPE	Solid polymer electrolyte
TAW	Transverse acoustic wave
TCF	Temperature coefficient of frequency
TPR	Triple phase boundary
UFO	Unidentified floating object

Nomenclature

f	Frequency
τ	Time
ρ	Density
λ	Water uptake
δ	Depth of decay
η	Viscosity
θ	Phase angle
μ	Shear modulus
m	Mass
A	Area
C_f	Integral of sensitivity coefficient
c_f	Sensitivity coefficient
T	Temperature
Z	Impedance
Y	Admittance
G	Conductance
B	Susceptance
C	Capacitor
L	Inductor
R	Resistor
M	Molecular weight
Q	Charge
i	Current
F	Faraday's Constant
t	Thickness
ξ_{22}	Quartz permittivity
h	Crystal thickness
K_Q^2	Electrochemical coupling constant for quartz
ω	Angular excitation frequency
N	Overtone number
c_{66}	Quartz elastic constant

Subscripts

r	Resonant
s	Series
p	Parallel
Fe	Iron
q	Quartz
L	Liquid
f	Film
w	Wet
d	Dry
i	Ionomer
0	Fundamental
pi	Piezoelectric material

Contents

Declaration ii
Acknowledgements iii
Abstract iv
Publications vi
List of Abbreviations viii
Nomenclature ix
Contents x
List of Figures xiii
1 Introduction 1
1.1 The Fuel Cell Application 3
1.2 Heavy Crude Oil Fouling Detection 4
2 Literature Review 6
2.1 Bulk Acoustic Wave Resonators 6
2.2 The Piezoelectric Effect 7
2.3 BAW Resonator Background 9
2.3.1 Mass Monitoring 10
2.3.2 Energy Trapping and Radial Sensitivity 12
2.4 Viscoelastic film / Liquid operation 13
2.4.1 Background 13
Kanazawa and Gordon 15
Bruckenstein and Shay 15
2.4.2 Viscous Phase Oscillation Fundamentals 17
2.4.3 Non-ideal Resonator Response 18
2.5 Crystal Impedance / Admittance Spectroscopy 20
2.6 Equivalent Circuit Representation 24
2.6.1 Unperturbed Microbalance Equivalent Circuit 24
2.6.2 Perturbed Crystal Equivalent Circuit 26
2.6.3 The Effect of Changing Parameters 31
2.7 Electrochemical Quartz Crystal Microbalance (eQCM) 36
3 Fuel Cell Application 37

3.1 Introduction 37
3.2 Literature Review 40
3.2.1 What is a Fuel Cell? 40
3.2.2 Proton Electrolyte Membrane (PEM) Fuel Cells 40
3.2.3 Alkaline Membrane Fuel Cells 42
3.2.4 AAEM Operational Issues 45
3.2.5 The Application of a BAW Resonator 55
3.3 Methodology 58
3.3.1 Quartz Crystal Microbalance 58
3.3.2 Rig Development 60
3.3.3 Electrolyte Casting 67
3.3.4 Investigation of Specific Operation and Alterations 72
3.4 Results and Discussion 80
3.4.1 Feasibility Studies 80
3.4.2 Investigations 97
3.5 Conclusions 131
3.5.1 Future work 132
4 Fouling detection in high temperature media 134
4.1 Introduction 134
4.2 Literature Review 136
4.2.1 Crude Oil 136
4.2.2 Transportation and Refining 139
4.2.3 Fouling 140
4.2.4 Microbalance Application 147
4.3 Methodology 152
4.3.1 Rig Design 152
4.3.2 Microbalance 156
4.3.3 Iron Electrodeposition 161
4.3.4 Crude Sample 164
4.4 Results and Discussion 165
4.4.1 Suitability and Calibration Studies 165
4.4.2 Iron Electrodeposition 182
4.4.3 iGCM Operation 189

4.4.4 *In-situ* Application 194
4.5 Conclusion 199
4.5.1 Future work 200
5 Overall Conclusions 202
5.1 Technique 202
5.2 Application 202
6 References 205

List of Figures

Figure 1: BAW resonator schematic 6
Figure 2: The converse piezoelectric effect 7
Figure 3: Resulting atomic displacement and change in electrical charge with an applied stress 8
Figure 4: Standing Wave Schematic 9
Figure 5: TAW propagation through a resonator and a contacting thin-film, indicating the fulfilment of the standing wave condition 11
Figure 6: TAW propagation dampening through a contacting liquid media 16
Figure 7: The non-slip condition between the BAW resonator top electrode and the monolayer of the contacting species 19
Figure 8: Nyquist plot for a) an ideally oscillating resonator b) a real oscillating resonator with an introduced static capacitance (Section 2.6) from a holder for example 21
Figure 9: Example of typical admittance Cartesian plots – admittance magnitude is shown in black and the phase plot in blue (these typical plots were generated using simulation data within the ZView modelling software) 23
Figure 10: Lumped parameter dashpot schematic 24
Figure 11: The Butterworth Van Dyke (BVD) equivalent circuit 25
Figure 12: Modified BVD equivalent circuit 27
Figure 13: Microbalance admittance a) loci b) magnitude and c) phase responses to rigid mass loading (the unperturbed system is shown in black and the perturbed system in red) d) tabulated key metrics 33
Figure 14: Microbalance admittance a) loci, b) magnitude and c) phase responses for a viscous loading (the unperturbed system is shown in black and the perturbed system in red) d) tabulated key metrics 35
Figure 15: PEM-FC operation schematic 41
Figure 16: A-FC operating schematic 43
Figure 17: AAEM-FC operating schematic 44
Figure 18: Nafion structure 47
Figure 19 : The Cluster Model theory for hydrated Nafion microstructure adapted from Gierke *et al.* 48
Figure 20: Hoffman (E2) elimination reaction mechanism. 50
Figure 21: Direct nucleophilic degradation, Pathway 1 51

Figure 22: Direct nucleophilic degradation, Pathway 2 51
Figure 23: Quartz crystal microbalance double anchor electrode schematic 59
Figure 24: 'Base-rig' set up. 61
Figure 25: The fuel cell humidification chamber / cell. The QCM is housed within the holder in the translucent section to the right of the image. 63
Figure 26: Schematic of the final iteration of the QCM holder: a) shows the top section of the holder, b) the bottom section with the QCM and c) the complete holder. 65
Figure 27: The holder shown in its assembled form including the base plate for mounting into the cell. 66
Figure 28: Initial *ex-situ* casting process by micropipette directly onto the microbalance surface. 68
Figure 29: *In-situ* casting chamber – retrofitted into the translucent section of the cell as shown in Figure 25 69
Figure 30: Casting success for a a) non-diluted ionomer dispersion which resulted in a poorly distributed ionomer layer and b) diluted ionomer dispersion showing a significantly more uniform, well-confined ionomer layer 71
Figure 31: Degradation investigation rig set up. The red box shows the additional mass spectrometer added to the system to provide off-gas analysis. 75
Figure 32: *In-situ* carbonation rig. The red box indicates the additional air inlet added to provide atmospheric CO_2 to the ionomer. 77
Figure 33: *Ex-situ* carbonate interaction rig set up 79
Figure 34: The effect of temperature on a 6 MHz crystal microbalance's resonant frequency during heating and cooling 81
Figure 35: Graphical representation of the magnitude of noise experienced for an unperturbed microbalance operating at 55 ^{O}C and 80 ^{O}C for 5 minutes at resonant frequency 83
Figure 36: QCM frequency stability when held at a range of relative humidities at 80 ^{O}C and under a flow of 100 ml min^{-1} of N_2 84
Figure 37: Cast frequency profile for a a) 12.9 nm Nafion ionomer and b) 12 nm Tokuyama AS-4 ionomer. Numbers on the Figure relate to 1) electrolyte application to the microbalance 2) initial rapid dying phase 3) slow drying phase and 4) subsequent new resonant frequency 88

Figure 38: SEM ionomer homogeneity scans for a) an unperturbed QCM gold electrode b) a 33 nm AS-4 cast composite resonator 90
Figure 39: Ionomer cast boundaries on the QCM gold electrode 91
Figure 40: Unperturbed and cast 37 nm Nafion composite resonator admittance response. Key metrics tabulated for reference. 93
Figure 41: Unperturbed and 68 nm cast AS-4 composite resonator admittance response. Key metrics tabulated for reference. 94
Figure 42: Graphical representation of the magnitude of noise experienced for an unperturbed, Nafion and Tokuyama AAEM cast microbalance operating at 80, 80 and 55 ^{O}C and 30% RH respectively 96
Figure 43: Nafion ionomer water uptake for 33 nm (black line) and 60 nm (red line) thick ionomers operating through a range of RHs. The frequency response for the 33nm composite resonator operating through the humidity range is shown in the inset 97
Figure 44: A snapshot of the CAS response for a 33 nm Nafion composite resonator operating through a range of RHs and hydration states: (a) admittance locus and (b) magnitude of admittance Bode plot. 100
Figure 45: (a) Series resonant frequency and (b) percentage decrease in the amplitude of admittance as a function of RH for a 33 nm Nafion composite resonator (linear sections added as a guide to the eye). 101
Figure 46: Change in composite resonator's resistance (R_2) in the modified BVD equivalent circuit as a function of RH (linear sections added as a guide to the eye)..... 103
Figure 47: AS-4 ionomer water uptake for a 23 nm (black), 39 nm (red) and 100 nm (blue) thick ionomers operating through a range of RHs. The frequency response for a 39 nm composite resonator operating through the humidity range is shown in the inset 104
Figure 48: Segment of CAS results for a 39 nm AAEM composite resonator operating through a range of RHs and hydration states: (a) Admittance locus and (b) magnitude of admittance plot 107
Figure 49: (a) Change in series resonant frequency and (b) percentage decrease in amplitude of admittance for a 39 nm AAEM composite resonator versus RH and hydration (linear sections added as a guide to the eye). 108
Figure 50: Change in the AS-4's composite resonator's resistance *(R_2)* in the modified BVD equivalent circuit as a function of RH (linear sections added as a guide to the eye)..... 110

Figure 51: The measured frequency response for a 100 nm composite resonator when operating at temperatures between 55 ^{O}C and 65 ^{O}C. The inset image shows a zoomed in analysis of the frequency response for the composite resonator when operating at 65 ^{O}C. 113
Figure 52: The measured frequency response profile for a 100 nm AS-4 composite resonator operating at 55 ^{O}C, 65 ^{O}C and again at 55 ^{O}C at 66% RH 114
Figure 53: The measured frequency response profile for a 100 nm AS-4 composite resonator operating at 55 ^{O}C, 65 ^{O}C and again at 55 ^{O}C at 11% RH 115
Figure 54: CAS response for a 100 nm AS-4 composite resonator operating at 55 ^{O}C before (black line) and after (red line) operation at 65 ^{O}C and 11% RH for 50 mins. Figure b inset shows an enlarged version of the $|Y|_{max}$ peaks for each response 117
Figure 55: The composite resonator's percentage shift in R_2 (representing the viscoelastic change in the film) when operating before and after exposure to elevated temperatures as a function of relative humidity. 118
Figure 56: In-line mass spectrometry data for the composite resonator operating at: a) 55°C (inset shows the full relative intensity scale) and b) 65°C. (the results presented here are taken at 0% RH) 120
Figure 57: Unperturbed microbalance operation under a nitrogen and subsequently air environments at 55 ^{O}C and 40% relative humidity 123
Figure 58: Resonant frequency and resistance response for a 33 nm cast Nafion microbalance operating under a nitrogen and subsequently air environment at 55 ^{O}C and 40% relative humidity. 124
Figure 59: The % ohmic resistance change for the A201 membranes when operating in nitrogen (blue section) and subsequently in air containing atmospheric carbon dioxide at 0, 50 and 100% RH at 55 °C (represented as 50 s averaged intervals). 125
Figure 60: (a) Transient frequency responses for AS-4 composite resonators operating in nitrogen and subsequently in air at a range of RHs. (b) Change in the composite resonators' steady state frequency response when operating in nitrogen and subsequently in air at a range of RHs. 127
Figure 61: API gravity classification 137
Figure 62: SARA separation analysis schematic 138
Figure 63: In-line pig schematic 141

Figure 64: Typical 3-electrode electrodeposition experimental set-up..... 150
Figure 65: Accelerated fouling detection rig Set-up 153
Figure 66: Pressurised chamber housing the microbalance holder and elevation stage 154
Figure 67: Electrical T-piece connection schematic detailing internal wiring channels developed from fish bone beads 156
Figure 68: The corresponding temperature and coupling coefficients for a $GaPO_4$ crystal's angle of cut, reproduced from [241]..... 158
Figure 69: Temperature coefficients of $GaPO_4$ at Y-11.1° cut compared to AT-cut quartz, reproduced from [248]. 159
Figure 70: Microbalance holder schematic. Manufactured in-house using one piece of unfired pyrophyllite and rapid prototyping equipment..... 161
Figure 71: Gamry instruments BAW holder modified for use as an eGCM holder with an electrodeposition bath shown here a) closed and b) open, indicating its operation. 162
Figure 72: eGCM electrodeposition bath set up for iron electrodeposition 163
Figure 73: QCM frequency response for operation between 25 °C and 600 °C, showing failure at 435 °C [255]..... 166
Figure 74: GCM frequency response for operation up to 900 °C, showing a reduced temperature coefficient between 400 – 600 °C [255]..... 167
Figure 75: Measured and calculated GCM temperature profiles for operation between 50 °C and 600 °C..... 167
Figure 76: GCM temperature stability shown at temperatures between 300 °C and 600 °C. 169
Figure 77: The crude-GCM composite resonator shown here before heating to disperse the heavy crude..... 170
Figure 78: The frequency response for a GCM-crude sample heated between 150 – 530 °C in order to determine the composite resonator's critical temperature. 171
Figure 79: CAS responses for the GCM-crude resonator operating at temperature between 176 – 245 °C in order to determine the 'true' critical temperature. 173
Figure 80: The heating and cooling frequency responses for a GCM-crude resonator operating between 215 – 530 °C 174
Figure 81: The frequency shift for a QCM (black plot) and a GCM (red plot) for operation under pressure between 1 and 8 bar (gauge). 176

Figure 82: QCM frequency stability when operating at pressures between 1-8 bar 177
Figure 83: GCM frequency stability when operating at pressures between 1-8 bar 178
Figure 84: The admittance response for a QCM operating in pressurised environments of $1 - 8$ bar. 179
Figure 85: The admittance response for a GCM operating in pressurised environments of $1 - 8$ bar. 180
Figure 86: eGCM response for iron electrodeposition when the system is held at -15 mA for 4 s (literature plating values). 183
Figure 87: Literature coated iron electrodeposited iGCM SEM and EDX analysis 184
Figure 88: Relevant plating negative potential section of a cyclic voltammogram employing the electrodeposition setup described in Figure 72, with a GCM working electrode 185
Figure 89: eGCM frequency response for the iron electrodeposition process when the system is held at -0.9 mA for 80s. 186
Figure 90: Calculated value plating procedure iGCM, where the dark grey central area shows the addition of the iron layer to the platinum double anchor electrode. 187
Figure 91: Calculated coat iron electrodeposited iGCM SEM and EDX analysis 188
Figure 92: iGCM CAS responses for the a) literature and b) calculated platings, indicating minimal change to the system's Q-factor as a result of iron electrodeposition of 10.9 and 17.4 ng respectively 190
Figure 93: iGCM frequency stability when operating in an environment of flowing argon (100 ml min^{-1}) at a range of temperatures between $250 - 600$ ^{o}C 191
Figure 94: iGCM frequency stability when operated in argon at pressures between $1 - 8$ bar. 192
Figure 95: iGCM frequency response when held under two test conditions of 250 ^{o}C at 5 bar (black line) and 350 ^{o}C at 3 bar (red line). 193
Figure 96: The active iGCM response when in contact with ~ 0.01 mg of heavy vacuum residue. The response is initially taken after composite resonator stabilisation and the inset image shows the active response between achieving T_C and reporting a stable frequency response. 194

Figure 97: The admittance response for the iGCM in contact with 0.01 mg of heavy vacuum residue before and after being held at 300 ^{O}C and 3.5 bar. Key metrics are also presented 196
Figure 98: X-ray tomography reconstructions of a) the iron – crude interface on the GCM and b) a zoomed in image of the same. 198

List of Tables

Table 1: Base case ZView2 fitting data 31
Table 2: All known properties for the Nafion and Tokuyama dispersions 67
Table 3: Frequency data for cast a) Nafion and b) AS-4 ionomers and their corresponding mass changes and subsequent thickness' 86
Table 4: Mass number peaks registered in Figure 56b when the composite resonator is operating at 65°C and suggested corresponding elements and hydrocarbon fractures. 121
Table 5: Traditional crude oil composition [158]. 136
Table 6: Asphaltene heteroatom's common functional groups 142
Table 7: Piezocryst's GCM frequency and temperature relationship nomenclature..... 168
Table 8: Temperature vs. θ_{min} 172

1 Introduction

The effects of global warming and the price volatility associated with fossil fuels and traditional electricity generation methods has resulted in a clear demand for renewable energy technologies. Electricity currently generated from renewable sources such as solar and wind is intermittent resulting in an unreliable supply and subsequently unpredictable strains on the grid. These technologies therefore require advancements in grid storage solutions coupled with balancing and demand shaping to be truly widespread. Recent advancements in alkaline anion-exchange membrane (AAEM) fuel cells have however provided an avenue for a scalable, constant and stable electricity generation mechanism when supplied with hydrogen. Fuel cells are not yet without challenges, and require extensive research to elucidate issues pertaining to early on-set degradation, durability issues and importantly cost ($/kW) parity compared to existing electricity generators.

The renewable energy forecast is very promising and will undoubtedly play a large role in meeting our future energy demands and improving our environmental outlook. However, until achieving the above outlined improvements the world will continue to rely on the more consistent current electricity generation mechanisms such as fossil fuels to meet its ever increasing demand. It is therefore imperative that we continue to improve the efficiencies of, and advance these existing technologies during the transition to a renewable energy reliant low carbon economy.

Crude oil has long provided the world with its most plentiful fuel resource, however dwindling traditional reserves have recently forced refineries to draw on the more abundant heavy crude oil supply. Advancements in heavy crude refining has meant it can now produce similar products to traditional crude during the refining process. Heavy crude oil supplies contain more variable compositions of 'harsh ingredients' such as saturates, aromatics, resins and asphaltenes (SARAs) between wells. The presence of SARAs and particularly destabilised asphaltenes in heavy crude oil systems can lead to unpredictable fouling throughout the production chain causing severe flow assurance, safety and economic issues. Without a better fundamental understanding of the factors that affect the fouling properties of a particular

oil blend, there will continue to be uncertainty over the transport and refinement of heavy crude oil within the industry. This will hinder the efficient, cost-effective production of consumer ready fuels, resulting in continued price volatilities.

In order to both improve existing and help develop promising future energy technologies, a better fundamental understanding of what happens at the interfacial level in complex processes is vital. Advanced non-intrusive *in-situ* interfacial investigations can provide real-time structural and morphological characterisation as processes occur, providing new insight into the effect of operating conditions and guiding future technological developments.

There are many *in-situ* analytical methods to study interfaces, one of which is the application of a bulk acoustic wave resonator (BAW) such as a piezoelectric crystal microbalance.

BAW resonators comprise a thin piezoelectric material (for example quartz) sandwiched between two metal electrodes. When an alternating electrical field is introduced across the BAW resonator, it results in a vibrational motion at the piezoelectric material's resonant frequency. The resonant frequency varies for each resonator and is dependent on the electrode mass; it is this unique feature that gives rise to the piezoelectric microbalance's ability to measure interfacial mass changes with nanogram resolution.

BAW resonators represent a mature mass measurement method, especially in their application of mass deposition and depletion in the gas phase. BAW resonator operation in both viscoelastic media and harsh environments (temperatures and pressures) is less well established and is discussed in further detail throughout this work.

This thesis outlines the development of BAW resonators for use as *in-situ* monitoring devices to characterize complex processes in the viscoelastic phase. The study is divided into two distinct sections; the first concentrating on the interfacial properties of a novel alkaline anion-exchange membrane fuel cell ionomer, whilst the second part focuses on the fouling detection and characterisation occurring in heavy crude oil in transition pipelines and refinery equipment.

1.1 The Fuel Cell Application

Fuel cells are seen as one of the big contributors in the development of the low carbon economy; with a wide range available, they are a diverse power producer. With no point-of-use emissions or particulates and no moving parts in the stack, fuel cells can potentially provide a large part of the answer to our growing energy demand. However, fuel cells and particularly low-temperature proton exchange membrane fuel cells (PEM-FCs) are not without challenges and have struggled for commercialization, mainly due to electro-catalyst cost and durability issues.

Alkaline anion-exchange membrane (AAEM) fuel cells are a novel solid polymer electrolyte (SPE) version of the alkaline fuel cell (A-FC). Operating in an alkaline medium has the benefit of more facile oxygen reduction kinetics at the cathode, compared to traditional acid-based PEM-FCs, and AAEM fuel cells are therefore able to utilize more cost-effective non-precious metal catalysts. The AAEM is expected to negate many of the issues experienced with the aqueous A-FC, such as carbonate salt precipitation when operated in the presence of CO_2 from the air and also issues pertaining to transport and the use of a caustic electrolyte.

AAEMs are at a relatively early stage of development and face specific (often hydration-related) technological challenges compared to PEMs as outlined below.

- As with all SPEs, the AAEM's water management, uptake, sorption mechanisms, swelling characteristics and stability govern its operation and performance efficiency. However with additional cationic groups (often quaternary ammonium groups, R_4N^+) added to the AAEM to improve conductivity, there have been reported incidents of reduced mechanical strength and chemical stability of the membrane during hydration. With inconsistent literature results as discussed in Section 3.2.4.1, understanding of these mechanisms for system integration is ambiguous and cannot be relied upon.

- Chemical instability and degradation mechanisms that arise as a result of increased operating temperature and specifically E2 (Hofmann) elimination have been demonstrated for several AAEMs when operating at temperatures ≥ 65 ^{O}C, consequently reducing kinetic advantage. At elevated temperatures, the OH^- conducting ions have been shown to irreversibly cleave the tethered cationic head groups from the polymer backbone reducing its ionic conductivity.

- Finally, with immobilised cations (in contrast to the A-FC), carbonate ion interaction and subsequent precipitation of salts are unlikely when operating in air; however, varying degrees of performance effects have been seen within the literature as discussed in Section 3.2.4.3.

This work employs a composite (AAEM ionomer-cast, surface developed) quartz crystal microbalance (QCM) along with crystal admittance spectroscopy (CAS) to explore each of the above phenomena for interfacial characterisation of a commercially available AAEM as a function of its hydration state and under various operating conditions.

1.2 Heavy Crude Oil Fouling Detection

The world's ever-increasing energy consumption, coupled with its dwindling conventional fuel supplies and the associated price volatility, has led a push towards new technologies such as fuel cells and other future renewables. However, with technological bariers to overcome before wide-spread implementation, the world will continue to rely on traditional electricity generation mechanisms such as crude oil. It is therefore crucial that there is a continued focus on improving the power conversion efficiencies of traditional and non-traditional resources such as 'heavy' crude oil.

Crude oil has for a long time served the world as its largest energy vector; however, with depleting supplies, refineries are beginning to draw on the

more abundant heavy crude oil reserves. Whilst these heavy crudes can produce similar products to their lighter counterparts during the refining process, they also contain a larger, more variable composition of SARA components, which in their raw forms can cause severe fouling of transmission pipelines and refinery equipment.

Fouling is one of the oil industry's biggest issues; resulting in either downtime to clean or replace sections of pipe, as well as leading to increased pressure drops which may result in burst pipelines and well heads, loss of product and environmental disaster. Fouling occurs primarily as a result of asphaltene destabilisation and is currently treated through rejection or conversion of the precipitating products. However, current monitoring and mitigation feedback systems are time intensive, high volume studies which do not allow the refinery and drilling experts to react quickly enough to changing oil grades.

This study in collaboration with the Qatar National Research Fund (QNRF) outlines the development of a rapid, low volume on site feedback system for fouling characterisation in pseudo- pipelines and refinery equipment using a high-temperature BAW resonator.

The investigation uses an iron electrodeposited gallium orthophosphate microbalance (iGCM) in contact with a heavy crude oil sample with the ability to operate under a range of conditions to provide an end-user device with the necessary flow assurance information required to implement fouling rejection or conversion techniques.

The chapter also outlines the efficiency, development and characterisation of the electrodeposited-iron GCM (iGCM) through the innovative application of the electrochemical GCM (eGCM). It shows the stable operation of the iGCM under the investigative range of conditions and shows an early example of the system's combined functionality, implementing both active and passive oscillation coupled with X-ray tomography reconstructions to provide new insight into the phenomena occurring at the iron – oil interface.

2 Literature Review

2.1 Bulk Acoustic Wave Resonators

Bulk acoustic wave (BAW) resonators is a name given to a unique range of devices that work using the piezoelectric effect. BAW devices have been researched for many decades for applications such as sonar, frequency control and in particular military communications [1]. In recent years, however, both the cost and size of these devices have reduced significantly, leading to a growing interest in the field. BAW resonators have become very popular as a means for nonintrusive *in-situ* mass measurement for their nanogram resolution and small size; these are sometimes referred to as crystal microbalances. Figure 1 shows a schematic of a typical BAW resonator in which a piezoelectric material is sandwiched by 2 metal electrodes, as discussed in Section 2.3.

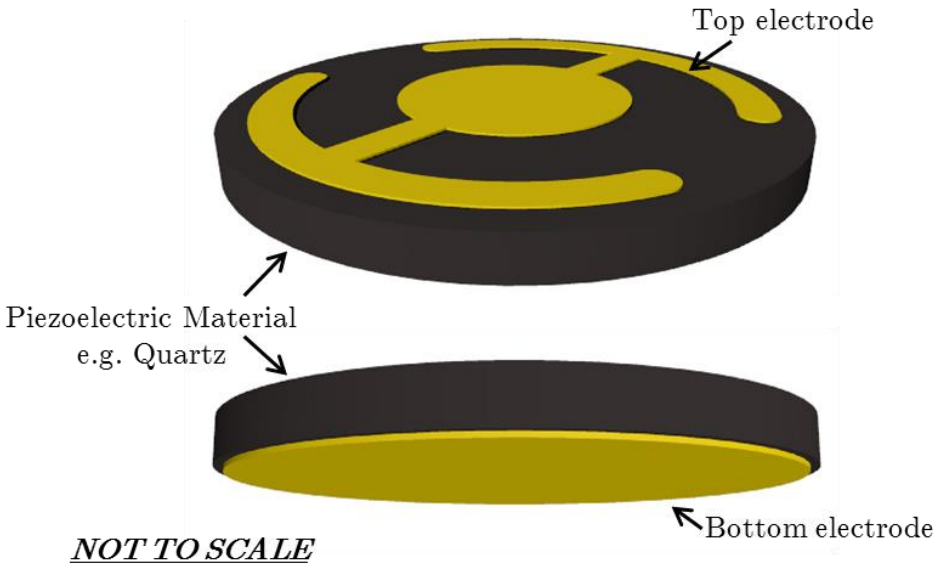

Figure 1: BAW resonator schematic

There is much literature on the applications of these versatile resonators; however, only the most relevant are discussed in this chapter. For further examples and applications, the reader is directed to review articles [2-4].

2.2 The Piezoelectric Effect

Piezoelectricity or 'pressure electricity' was first coined by the Curie brothers Pierre and Jacques in 1880. They demonstrated that the application of a mechanical stress to certain crystal materials (Rochelle salt, tourmaline and quartz for example) resulted in an electrical polarization across the crystal of a magnitude proportional to the applied stress. In 1881, the Curie brothers experimentally validated the converse piezoelectric effect proposed mathematically by Lippmann; the application of a voltage across the crystal afforded a corresponding mechanical strain, as shown in Figure 2 [2, 4].

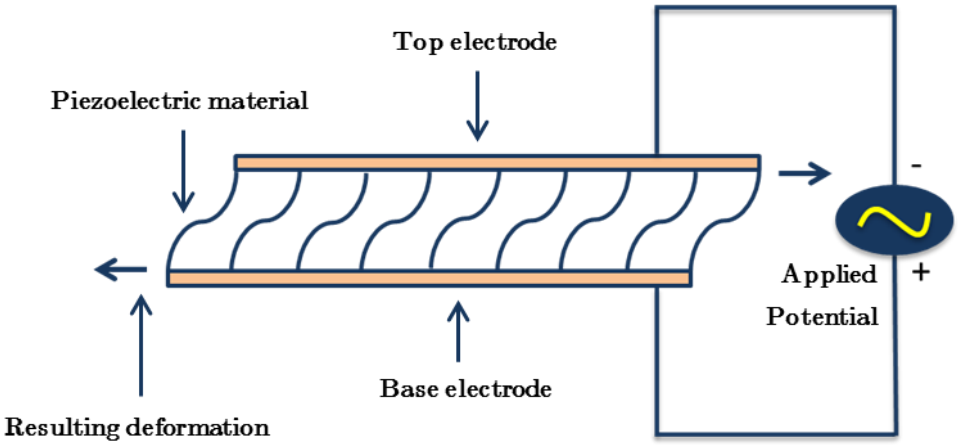

Figure 2: The converse piezoelectric effect

Piezoelectricity is a phenomenon exclusive to acentric materials, i.e. materials that crystalize in non-centrosymmetric space groups. The crystals of an acentric material have dipoles associated with the orientation of atoms in the crystalline lattice and therefore have a polar axis. When the crystal is under stress, charges are generated as the dipoles shift as a result of the displacement of atoms in the acentric crystalline material. When a stress is applied in a specific direction, the atomic displacement produces a corresponding change in the net dipole moment, producing a net change in electrical charge on the crystal face, as shown in Figure 3 [2].

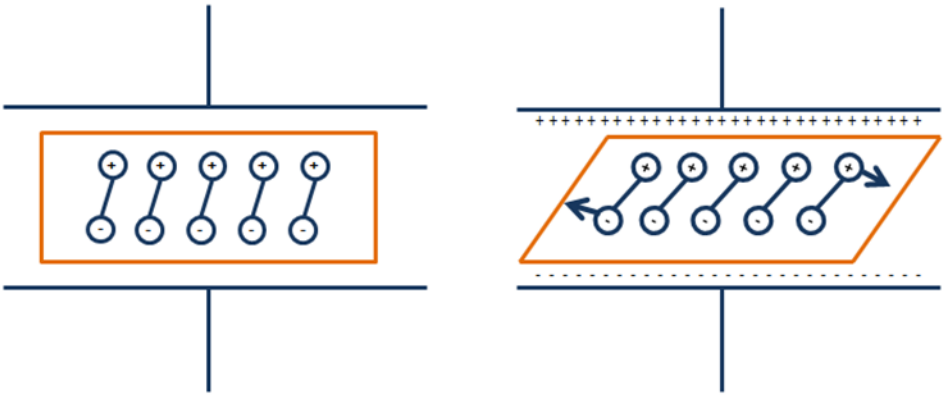

Figure 3: Resulting atomic displacement and change in electrical charge with an applied stress

The converse piezoelectric effect, shown in Figure 2, forms the basis for the crystal microbalance's operation. To apply a potential across a piezoelectric material, electrical connections must be made to and from the material's surface; this is often done through the use of two electrodes. Figure 1 shows the crystal microbalance assembly which contains the piezoelectric material sandwiched by two conductive metal electrodes. The application of an external potential across the electrodes results in an internal mechanical stress and consequently a shear deformation of the piezoelectric material (often referred to as a crystal). If an alternating current is applied across the crystal, it will result in a physical vibration equal to the frequency of the applied field. When the frequency of the applied field is of a similar magnitude to the crystal's fundamental frequency, the crystal mechanically oscillates at its resonant frequency. These oscillations produce a stable shear wave through the material in a realignment of the lattice structure that propagates its thickness perpendicular to the electrode. The reflection of the shear wave into the crystal of thickness t_{pi} at the surfaces is referred to as a transverse acoustic wave (TAW). A standing wave condition can be established when the reflection and the acoustic wavelength are exactly equal to $2t_{pi}$, as shown in Figure 4.

The standing wave condition provides the basis for BAW resonator operation, and without perfectly timed interference of the two propagating waves within the resonator due to mass or viscous overloading, for example, the

resonator's harmonics become prone to spurious and incomplete interference, yielding unreliable and ambiguous frequency responses.

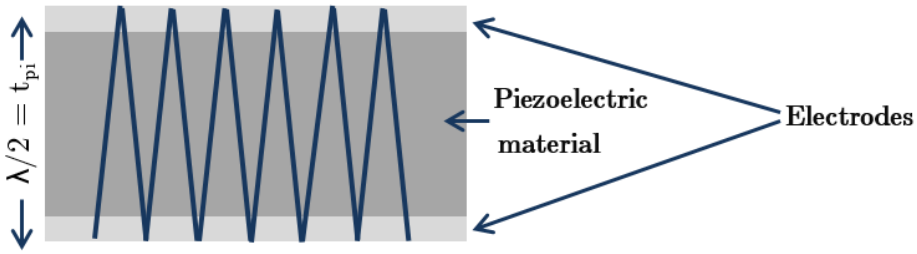

Figure 4: Standing Wave Schematic

The fundamental frequency (f_0) of the acoustic wave in the resonant condition is given by Equation (1), where μ_{pi} refers to the piezoelectric material's shear modulus and ρ_{pi} is the material's density.

$$f_0 = \frac{\sqrt{\mu_{pi}}}{2t_{pi}\sqrt{\rho_{pi}}} \tag{1}$$

2.3 BAW Resonator Background

The cut and preparation of the piezoelectric material are vital to ensure the stability of the narrowly packed oscillations; the angle of cut allows the BAW resonator to be tailored to emphasise stability of operation, mass measurement resolution and temperature coefficients. A low temperature coefficient is desirable as it allows the BAW resonator to operate at different temperatures with little effect on its frequency from temperature. AT cut quartz crystals are the most commonly used piezoelectric material because of its high availability, low-cost production and low temperature coefficients. However, other cuts also exist including BT and SC, each providing a range of different properties. BAW resonators are commonly found as 5 MHz or 10 MHz and the frequency of oscillation is inversely proportional to the crystal thickness. Whilst higher frequency crystals provide more sensitive

data analysis, they are also more difficult to handle as the material is thinner, more brittle and difficult to use, as explained by Equation (1).

BAW resonators can be thought of as an energy storage device by removing the external input; in the absence of any loss mechanism a BAW resonator should theoretically oscillate at its natural frequency indefinitely, however, this is not the case as energy dissipates to the surroundings. A BAW resonator's ability to store (or lose) energy gives rise to a crystal classification system known as its quality or Q-factor. The Q-factor is defined as the ratio of the energy stored per cycle to the energy dissipated per cycle [3] and is typically greater than 10^5 in air, [4] but is reduced in contact with liquid / viscoelastic media [2]. The Q-factors of a resonator operated in different environments can be represented through phase angle plots developed when passively operating the resonator, as discussed in Section 2.5.

2.3.1 Mass Monitoring

2.3.1.1. Sauerbrey's Equation

In 1958, Sauerbrey [5] published a relationship that allowed the change in resonant frequency (Δf) of a BAW resonator to be related directly to a change in mass on its surface (Δm), as shown in Equation (2). It is this relationship, and the work published by Sauerbrey, that has led to the widespread use of BAW resonators as microbalances for many *in-situ* mass monitoring applications.

$$\Delta f = \frac{-2 f_o^2 \Delta m}{A\sqrt{\mu_q \rho_q}} \tag{2}$$

The Sauerbrey equation relates frequency changes on a BAW resonator to area-specific mass changes on the electrode surface (where A is the resonators electrode area). This appropriately gives rise to the term crystal microbalance. The Sauerbrey equation makes several assumptions which can lead to limitations in its applicability, these include: any mass deposited on the crystal is assumed rigid under oscillation and also evenly spread across the electrode surface at a mass ≤ 2% of the quartz mass [5, 6]. Sauerbrey also stated that the deposited mass is assumed to have the same density and

transverse velocity as the quartz. The relationship states that the frequency shift resulting from a mass deposited at some radial distance from the centre of the crystal will be the same regardless of the radial distance [2]. Finally, when a mass or layer is added to the microbalance, it is assumed that the acoustic wave travels across the interface and propagates through the additional film thickness (t_f) and the resonator is still able to fulfil the standing wave condition, as shown in Figure 5.

Resonators operate using the standing wave phenomenon and without perfectly timed interference of the two waves propagating the resonator, the resonant frequency registered is likely to be unpredictable as the wave reflects at the electrode surfaces producing incomplete harmonics. If the resonator is overloaded, its harmonics are prone to spurious constructive and destructive interference of the standing wave propagating the microbalance. The standing wave condition is further discussed in Sections 2.4.3 and 4.4.3.1.

This assumed ideal propagation indicates continuous shear stress and particle displacement across the whole interface; this is known as the no-slip condition and is further discussed in Section 2.4.3.

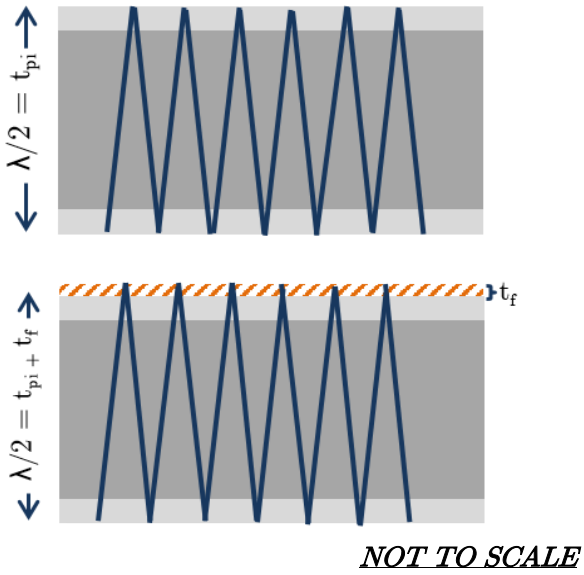

Figure 5: TAW propagation through a resonator and a contacting thin-film, indicating the fulfilment of the standing wave condition

2.3.2 Energy Trapping and Radial Sensitivity

One of the Sauerbrey equation assumptions states that the resulting frequency shift from a mass deposition will remain the same regardless of the deposition's radial distance from the crystal centre. However, in fact, the actual frequency change based on the location of the mass is given by the differential sensitivity coefficient c_f in Equation (3a). C_f represents the integration of c_f across the entire microbalance surface area and is given in Equation (3b).

$$c_f = \frac{df}{dm} = S \tag{3a}$$

$$C_f = \int_0^{2\pi} \int_0^r S(r, \Phi) r \, dr \, d\Phi \tag{3b}$$

As c_f is not constant across the microbalance, Sauerbrey introduced another assumption: any deposited film is thought to be uniform across the active region of the microbalance. Studies by both Sauerbrey [5] and Ullevig [7] show the greatest radial sensitivity coefficient of a microbalance is at its centre, and gradually decreases in a Gaussian-like manner towards the electrode boundary. These findings have been confirmed using admittance and charge polarization to show that the shear amplitude of the crystal follows the same distribution [8, 9]. In both cases, the authors showed a decrease in surface shear velocity and oscillation amplitude as a function of the distance from the microbalance centre. Sekimoto further confirmed these findings through the solution of the wave equation of motion under a boundary condition of zero velocity at the electrode edge [10]. This phenomenon can be explained by energy trapping. Energy trapping is a result of the confinement of crystal oscillation to its regions covered by electrodes and hence it has a higher density compared to the regions not covered with electrodes, resulting in larger vibrational amplitude at the centre of crystals that reduces towards the edge. The convex shape of the resonator, combined with its small size, means that oscillation or acoustic energy is trapped at the resonator's centre (this can be detected by X-ray topography) so that very little dispersion can

occur at the edge. In most resonators this area is approached by the shape of the electrodes, this is the phenomenon known as energy trapping.

The energy trapping studies discussed above indicate the crystal is most sensitive at its centre. Thus in any work conducted, it is vital to ensure that coatings or loadings occur exclusively to a finite yet evenly spread / consistent area at the crystal electrode surface. Specific microbalance holder designs should ensure that any effects that may be felt from energy trapping will be limited or mitigated.

BAW resonators have been used extensively in the gas phase for *in-situ* mass monitoring and these applications are well documented elsewhere [3, 4]. This project however concentrates on the application of the BAW resonator in contact with viscoelastic media and so forms the main focus of the following sections.

2.4 Viscoelastic film / Liquid operation

2.4.1 Background

Whilst crystal microbalances have been commonly employed for nanogram mass detection in the gas phase, early adopters found operation in liquid media to be a much more difficult feat. It was widely accepted that the viscous hydrodynamic effects would cause excessive damping of the oscillation that would lead to inaccurate mass measurements [11].

However, in 1979, Nomura and Hattori [12] investigated the effect that cyanide solution had on a silver surface using a quartz crystal microbalance with a silver coated electrode, suspended in a cyanide solution. They were unable to record *in-situ* changes in frequency and instead took dry frequency readings before and after submersion into the cyanide solution. Whilst there are of course many potential inaccuracies with this pseudo-*in-situ* method, it is the earliest record of crystal microbalance operation in the liquid phase.

The *in-situ* operation of a piezoelectric microbalance in the liquid phase was first achieved in 1980 by Konash and Bastiaans [13]. This work used a resonator with only one face exposed to the liquid phase and the other exposed

to air. The crystal's behaviour was studied in a flow cell set up to simulate liquid chromatography. They found that the crystal's resonant frequency differed with each liquid tested and attributed these changes to density or surface adsorption. In 1982, Nomura and Okuhara [14] confirmed this single electrode exposure operation. Their work continued to show that the crystal was able to oscillate in a variety of solutions and organic solvents and subsequently suggested the relationship shown in Equation (4) that related the expected frequency shift to the liquid phase density (ρ) and viscosity (η). The disadvantage of this relationship, however, is that it was not established using a physical model and consequently is specific only for the crystal used in its development.

$$\Delta f = \left(4.76\,\eta^{1/2} + 8.66\,\rho^{1/2} - 6.22\right) \times 10^3\ Hz \qquad (4)$$

Following the work of Nomura and Okuhara, in 1983 Bruckenstein and Shay [15] monitored the crystal frequency shifts resulting from metal deposition and oxide formation on the microbalance in both gaseous and liquid media. Their results showed that the crystal sensitivity to thin films was the same in each phase; this fundamental work has been of extreme importance and shows that crystal microbalances can indeed be an accurate *in-situ* mass measurement tool in the liquid phase.

Since the empirical model proposed by Nomura and Okuhara, there have been many other models developed to predict the frequency change of a microbalance in liquid phase operation based on physical characteristics such as viscosity and density [16]. However, it is the physical models proposed by Kanazawa and Gordon [17, 18] and Bruckenstein and Shay [19] in 1985 that have been adopted most widely in the literature; these are further described below.

Kanazawa and Gordon

$$\Delta f = f_o^{\frac{3}{2}} \sqrt{\left(\frac{\rho_L \eta_L}{\pi \rho_q \mu_q}\right)} \tag{5}$$

Bruckenstein and Shay

$$\Delta f = f_o^{\frac{3}{2}} \sqrt{\left(\frac{\rho_L \eta_L}{4\rho_q \mu_q}\right)} \tag{6}$$

Where,

Δf = Frequency shift due to liquid contact (Hz)

f_o = Fundamental frequency (Hz)

η_L = Contacting liquid viscosity (mPa)

ρ_L = Contacting liquid density ($kg\ m^{-3}$)

ρ_q = density of piezoelectric material ($kg\ m^{-3}$)

μ_q = shear modulus of piezoelectric material (mPa)

Kanazawa and Gordon modelled the crystal microbalance as a perfectly elastic solid in contact with a viscous fluid. The frequency shift is a result of coupling the oscillation of the crystal; a standing shear wave within the crystal, with a damped propagating shear wave in the liquid as shown in Figure 6. The relationship derived in Equation (5) expresses the expected change in the resonant frequency of a crystal due to the contact of one electrode with a non-gaseous phase. It is stated in terms of characteristics specific to both the crystal and the contacting media. The relationship developed in Equation (5) assumes that the transverse velocity of the crystal surface is identical to that of the adjacent fluid layer – the no-slip condition. Kanazawa and Gordon, continue to explain that in the proposed model, the crystal does not drive the contacting liquid bulk, but instead the transverse displacement decays exponentially in the liquid, as described in Section

2.4.2. Physically, the model predicts that only a thin layer of film will undergo displacement at the resonator surface, and the response will be a function of the mass of this layer.

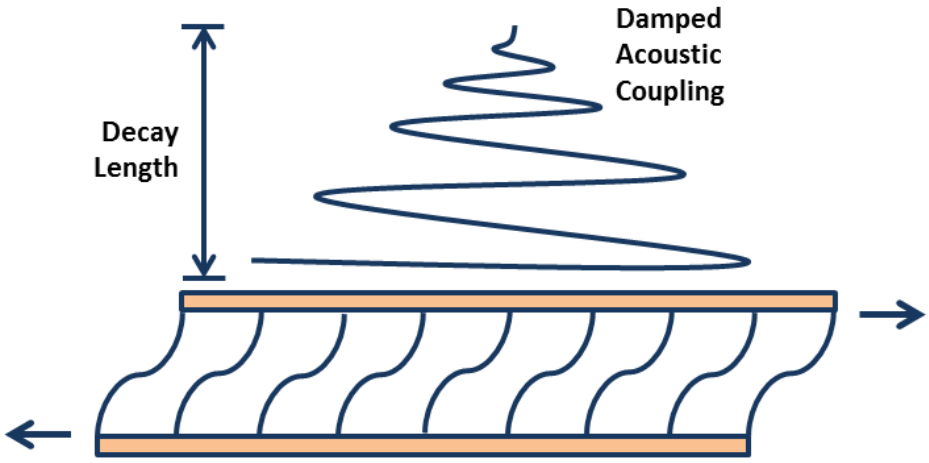

Figure 6: TAW propagation dampening through a contacting liquid media

Bruckenstein and Shay derived a similar relationship to that of Equation (5) using dimensional analysis, as shown in Equation (6).

Though slightly different, both relationships show that the resonant frequency shift is highly dependent on the density and viscosity of the contacting liquid media. The predicted frequency shifts are normally not achieved in practice due to surface roughness and other factors that cause non-ideal responses, as discussed in Section 2.4.3.

Further fundamental work to understand BAW resonator behaviour in the liquid phase was conducted by Yao and Zhou [20]. This study presents resonator operation in various liquid types, including organic liquids and mixtures, as well as aqueous solutions of various electrolytes. They go further to explore how the physical properties of the liquid and media temperature affect the resonator's oscillation / ability to operate.

The paper presented by Yao and Zhou found that all liquids have a critical temperature (T_C) below which the microbalance would not operate. They were able to show that this critical temperature increased with increasing

concentration of electrolyte in an aqueous solution. Similarly, they proved that in an organic liquid, the critical temperature also increases with longer carbon chains. The work also shows that grounding their detection cell reduced the critical operating temperature, allowing the crystal to operate at colder temperatures. However, when grounding the cell for operation in long chain organic solvents (of particular interest in Chapter 4) this decrease in temperature was hardly experienced, suggesting it works only with liquids with greater dielectric constants or electrical conductance.

2.4.2 Viscous Phase Oscillation Fundamentals

When a crystal is operating with one electrode in solution and one electrode open to air, a negative frequency shift is experienced from operation in air alone. The oscillation dampening experienced is a result of the electromechanical coupling of the shear transverse wave and the mechanical properties of the contacting medium that are reflected in the resonator's electrical response, as discussed above. The damped transverse wave propagates perpendicular to the plane of the shear deformation with its amplitude diminishing exponentially until it reaches zero at its decay depth (δ); described in Figure 6 and Equation (7).

The oscillation energy from the resonator is converted to thermal energy within the solution as the TAW diminishes. The rate of energy conversion from oscillation to thermal is dependent on the coupling of the electrode to the liquid phase and the ability of the TAW to penetrate the liquid. The decay depth is given by Equation (7) where η_L, ρ_L and ω are the contacting liquid's viscosity, density and resonator's angular excitation frequency respectively.

$$\delta = \sqrt{\left(\frac{2\eta_L}{\omega\rho_L}\right)} \tag{7}$$

2.4.3 Non-ideal Resonator Response

Whilst it has been well established that a microbalance's frequency changes while operating in the liquid phase, it must be noted that these shifts cannot be solely attributed to changes in mass on the electrode, as given by the Sauerbrey equation [5].

Equations (5) and (6) developed by Kanazawa and Gordon [18] and Bruckenstein and Shay [19] have shown that a microbalance operating in solution is sensitive to changes in both the solution's density and viscosity. Viscous coupling of the contacting liquid medium to the crystal surface results in both a decrease in its resonant frequency and resonance dampening. The effect of an increasing viscoelasticity of the contacting film / media on the crystal electrode has been described by Martin *et al.* [21] and also Topart and Noel [22]. In both cases they showed increases in the media's viscosity, resulting in a reduction of the resonant frequency, but showed no sign of mass deposition.

Factors other than viscoelasticity that contribute to non-ideal Sauerbrey Equation resonator responses include the following (for a more extensive review, the reader is referred to [2]):

Surface Roughness
The electrode surface stress and roughness have been found to affect the resonant frequency as described by Schumacher *et al.* [23, 24]. The surface roughness refers specifically to the microscopic roughness seen on the BAW resonator's electrodes. The electrode roughness traps liquid within its cavities and crevices; the unexpected trapped liquid causes an additional mass on the resonator and hence a reduced resonant frequency, whilst not purposefully loading the microbalance.

Radial Mass Sensitivity
As discussed in Section 2.3.2, though the vibration within a BAW resonator is concentrated in the electrode-covered regions, the BAW resonator does suffer from radial mass sensitivity. This can cause skewed frequency responses; however, the introduction of plano-convex resonators coupled with uniform mass distribution significantly reduces this issue [7].

Interfacial Slippage

It is important to consider interfacial slippage when operating a BAW resonator in the liquid phase. During oscillation, it is assumed that there is no slippage between the BAW resonator's electrode and the first monolayer (thin film deposition or liquid), as shown in Figure 7. This phenomenon is known as the non-slip condition and is difficult to model or predict; however different contacting media have different affinities for and thus adhesion to the electrode surface. The non-slip condition assumption predicts a perfect adhesion to the electrode and hence a greater frequency drop.

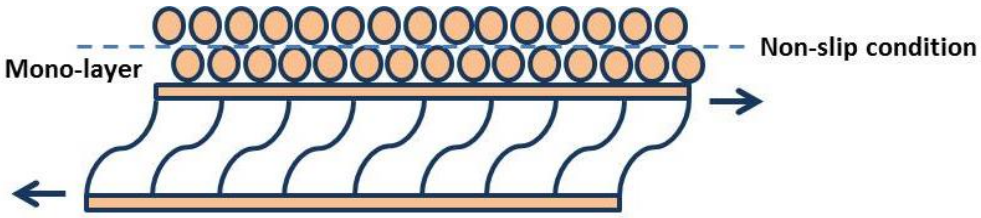

Figure 7: The non-slip condition between the BAW resonator top electrode and the monolayer of the contacting species

Liquid Ordering

Liquid ordering is a phenomenon in which molecules become 'packed' near an electrode; water, for example, forms an ice-like lattice structure. This formation causes a variation in the dielectric properties of the medium, which is also found to affect the resonant frequency [25, 26]. The formation of a lattice also potentially leads to a change in local viscosity of the contacting medium, resulting in unexpectedly large frequency shifts. Liquid ordering has the potential to result in large shifts in the resonant frequency; however, a study by Rajakovic *et al.* [11] has reported this phenomenon to be small in magnitude.

In each case, the above-listed factors affect the resonant frequency if not accounted for / kept constant. For the investigations presented in the following chapters, it was important to appreciate and account for the fact that the resonant frequency would not be affected only by mass loading, but also by changes in the contacting media's properties. Consequently, it is not possible to make *in-situ* mass measurements in the viscous phase as mass

loading rather than changes to the liquid media through active frequency measurements alone.

However, techniques such as crystal impedance (or admittance) spectroscopy [2, 27] can measure the electrical characteristics of a BAW resonator over a range of frequencies near resonance; simplifying frequency contributions and thus providing a more accurate representation of the phenomena occurring at the interface.

The interaction between the mechanical displacement and electrical potential in a BAW resonator causes mechanical interactions between the BAW resonator and the contacting media to influence its electrical characteristics, particularly near the resonant frequency, i.e. maximum amplitude [2, 28]. The BAW resonator's electrical characteristics can be evaluated using crystal impedance or admittance (the reciprocal of impedance) spectroscopy; defined as the ratio of the measured current output for an applied voltage. The admittance provides significant information about the system such as energy stored and power dissipation in both the BAW resonator and perturbing media.

2.5 Crystal Impedance / Admittance Spectroscopy

BAW resonators can be operated in one of two ways; (i) *active* operation in which the microbalance operates at its resonant frequency allowing active measurements of frequency changes; (ii) *passive* operation requires the microbalance to be connected to an external instrument which applies a sinusoidal voltage at a range of frequencies near the crystal's resonant frequency - crystal admittance spectroscopy (CAS). The resulting voltages are then measured and the electrical characteristics of the resonator can be determined [16]. CAS allows the deviation from rigidity of a surface film on a microbalance to be determined.

The CAS data can be analysed using equivalent circuits in which the resonator's electrical responses can be interpreted as mechanical properties of the surface film perturbation. This technique can provide useful insight into the physical properties of surface rigid mass and viscoelastic layers, as well as contacting liquid media, this is further discussed in Section 0.

Impedance is the measure of current that passes through a sample or system at an applied voltage over a range of frequencies. The measured impedance varies with the applied voltage frequency in a way that's specifically related to the properties of the material under test. The measured response may be a result of the physical structure of the material, chemical processes occurring in it or a combination of both.

To measure either impedance or admittance, an impedance analyser needs to be employed. Instruments like this measure the impedance (Z), phase angle (θ), admittance (Y), conductance (G), and susceptance (B) along with other parameters. The admittance (Y) of the microbalance is more commonly measured in the literature than the impedance of the system (Z).

The system's admittance response can be calculated using Equation (8) and can be represented as a Nyquist plot as shown in Figure 8.

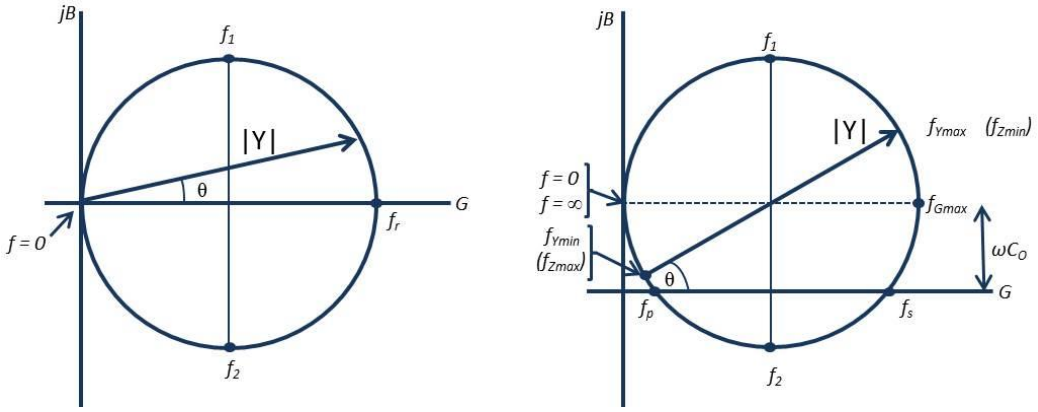

Figure 8: Nyquist plot for a) an ideally oscillating resonator b) a real oscillating resonator with an introduced static capacitance (Section 2.6) from a holder for example

Figure 8a shows the admittance locus or Nyquist plot for an ideal unperturbed microbalance, which can be modelled using a series LCR network as discussed in Section 2.6.1. The x-axis represents the real part of the admittance, and the y-axis its imaginary component.

The magnitude of admittance can be calculated from Equation (9), which is a resultant of the real and imaginary vectors defined by the admittance loci at a given frequency.

$$Y = G + jB \tag{8}$$

$$|Y| = (G^2 + B^2)^{\frac{1}{2}} \tag{9}$$

In Figure 8a, as the frequency increases from $f = 0$ the admittances imaginary component jB reaches its maximum value at f_1 where Y" is at its maximum. As the frequency continues to increase, the admittance locus crosses the x-axis, where the admittance's real component is at its maximum – the resonant frequency (f_r). At the resonant frequency, the system's admittance is at its maximum value, and the phase angle $\theta = 0$, fulfilling the standing wave condition. Finally, f_2 is the frequency at which Y" is at its minimum value.

The admittance response for a real system in which an additional static capacitance is introduced (for the microbalance holder for example – Section 2.6.1) is shown in Figure 8b.

The introduction of a holder (static capacitance) causes the locus to shift up the imaginary axis and results in several new useful frequencies. The maximum and minimum susceptance still occur at the same place, the location of the maximum admittance magnitude shifts to a lower frequency than that of maximum capacitance. The resonant frequency can now be defined at two points where the locus crosses the real axis at the series (f_s) and parallel (f_p) resonant frequencies. At each resonant frequency the phase angle is zero and at f_s the real part of the admittance is a little less than the real maximum and similarly, at f_p it is a little greater. The minimum admittance frequency occurs at just greater than f_p.

As well as the Nyquist plots shown in Figure 8, admittance data is also represented as Cartesian plots of $|Y|$ (magnitude) and θ (theta) vs frequency, as shown in Figure 9. The $|Y|$ and theta plots are extremely useful in the

explanation of a BAW resonator's behaviour, contacting masses and operating environment.

The $|Y|$ plot furnishes data about f_{Ymin} and f_{Ymax}, and is fundamental to the equivalent circuit fitting discussed in Section 0. At frequencies away from resonance, the capacitive reactance dominates (i.e. the voltage is leading the current); however, as the frequency approaches the resonant region, the inductive reactance increases, thus cancelling the capacitive reactance until the point f_{Ymin} is reached and the admittance is at its lowest value. At f_s the reactance cancels and thus the network reactance is zero. As frequency continues to increase, the inductive reactance continues to dominate and the admittance reaches f_p where the parallel reactances cancel and reaches a maximum at f_{Ymax}.

The phase plot must cross the x-axis at two distinct points (in a real-physical system) defining the series and parallel resonant frequencies; thus satisfying the standing wave condition.

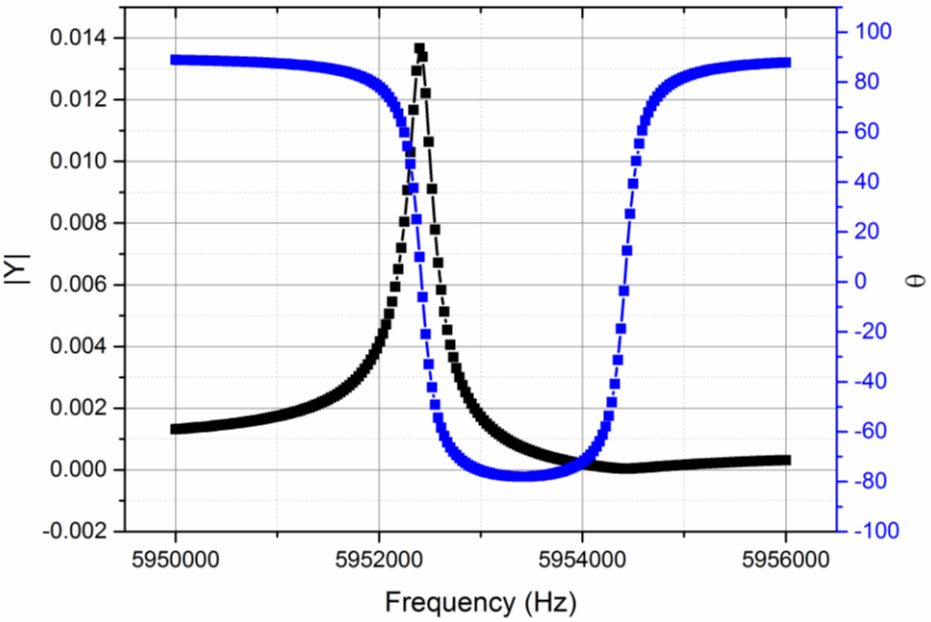

Figure 9: Example of typical admittance Cartesian plots – admittance magnitude is shown in black and the phase plot in blue (these typical plots were generated using simulation data within the ZView modelling software)

2.6 Equivalent Circuit Representation

Equivalent circuits are commonly applied to understanding the physical properties of a system analysed using electrochemical impedance spectroscopy (EIS) [29, 30]. This approach can also be used to better understand the phenomena occurring on the BAW resonator interface. With only a few lumped elements, an equivalent circuit simulates the electrical-mechanical characteristics of the BAW resonator over a range of frequencies near resonance. The model relates the circuit elements to physical microbalance properties, as well as any deposited layers or surrounding media. Fitting and understanding how circuit components relate to electrical measurements greatly facilitates the system characterisation and allows mass loading and viscoelastic properties to be better deciphered.

2.6.1 Unperturbed Microbalance Equivalent Circuit

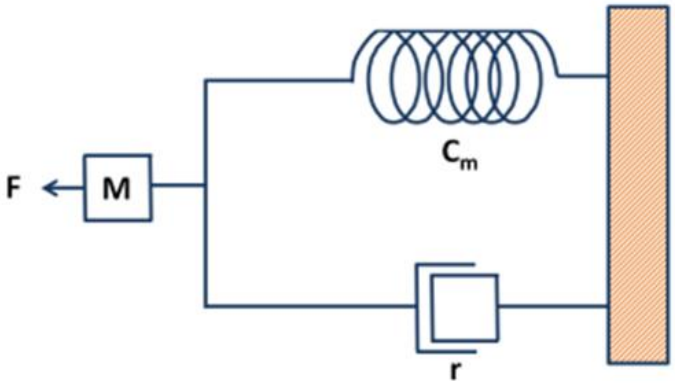

Figure 10: Lumped parameter dashpot schematic

The electrochemical properties of a piezoelectric resonator can be modelled on a system consisting of lumped parameter elements of mass, compliance (an object's ability to yield elastically when a force is applied) and resistance based on a 'dashpot' mechanical model of a mass M attached to a spring of compliance C_m and a piston with friction r, as shown in Figure 10. Cady [31] and subsequently Bottom represented this model by a series of lumped pa-

rameters; an electrical network of inductive, capacitive and resistive components in series. The resulting circuit is known as the Butterworth Van-Dyke (BVD) and represents an unperturbed crystal operating in the gaseous phase and is shown in Figure 11.

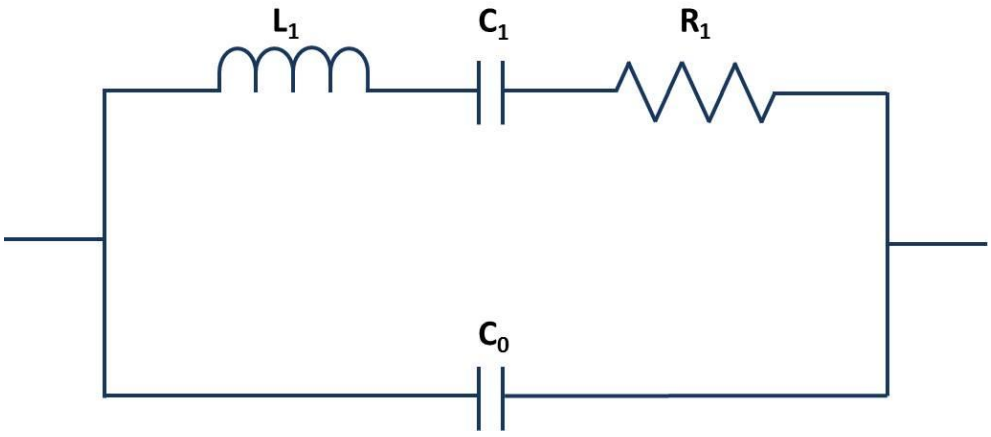

Figure 11: The Butterworth Van Dyke (BVD) equivalent circuit

The BVD circuit can be thought of in two parts, the static arm and the motional arm. The motional arm is the main point of focus as it is responsible for the system's electromechanical properties. The static capacitance term in the BVD (C_O) dominates the admittance away from resonance, whilst the motional arm's contribution is greatest near resonance [32, 33]. Fitting of the circuit model to electrical measurements allows properties of both the electrode surface and liquid contacting media to be analysed.

The Butterworth Van-Dyke motional arm components are related to the mechanical model as follows:

The mass term represents the inertial properties of the crystal and is substituted for inductance L_1 in the BVD circuit. The circuit inductance is affected by the mass being displaced during oscillation; consequently the inductance changes with microbalance mass loading.

The spring corresponds to the system's compliance, it is related to the energy storage and is dependent upon the operating media's elasticity; this is represented by the capacitor (C_1) on the motional arm of the BVD. A fully

charged capacitor represents the maximum crystal displacement, whilst a fully discharged capacitor represents the maximum velocity of the piezoelectric material.

The piston shown in the mechanical microbalance representation is equivalent to the resistive element in the motional arm. It represents the energy loss from the system during oscillation to internal friction - heat generation from the quartz lattice movements and acoustic losses.

The BVD circuit is an excellent representation for the unperturbed crystals in the gas phase; however, though attempts have been made to use it, it is of little use for mass loaded crystals operating with or in a viscous phase [34-36]. When a crystal is immersed in a liquid or has a viscoelastic contacting medium, energy passes from the crystal to the medium in the form of an acoustic wave dependant on the properties of the sensor-media interface, which are not included in this model [16]. Thus a circuit which takes into account both mass loading and the effect of a contacting liquid on a microbalance's performance must be employed for accurate data to be gathered.

2.6.2 Perturbed Crystal Equivalent Circuit

The studies presented within this thesis are multi-faceted with microbalance operation in contact with both rigid and viscoelastic media as well as operation in humidified, pressurised and heated environments. It is therefore essential to provide a means to distinguish between frequency changes due to mass loading and those changes that arise as a result of the contacting media properties.

Martin *et al.* [37] proposed the modified equivalent circuit shown in Figure 12 for a BAW resonator with a contacting rigid mass and / or viscous (liquid / viscoelastic thin film) loading.

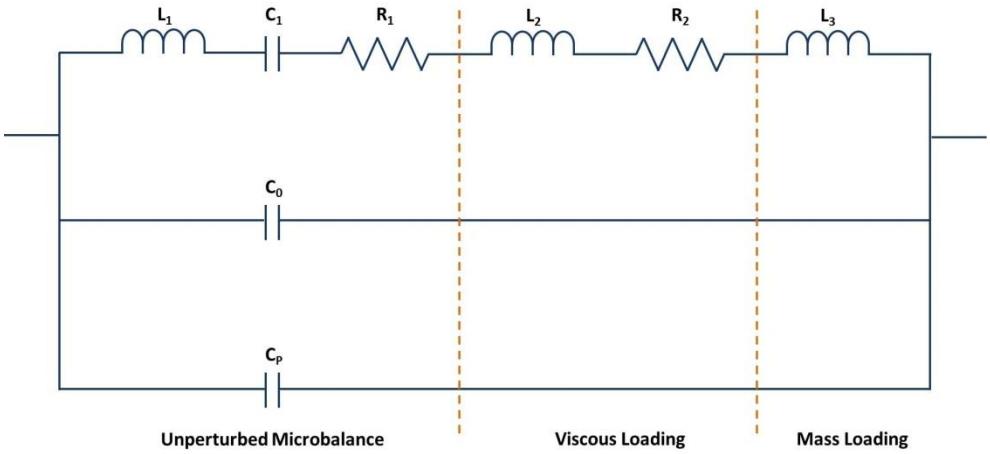

Figure 12: Modified BVD equivalent circuit

The model proposed by Martin *et al.* assumes the following key principles:

1) The electrodes surrounding the microbalance are or infinitesimal thickness and are located at the top and bottom of the microbalance.

2) The loaded mass is very thin compared to the acoustic wavelength and is rigidly attached to the microbalance electrode – as with the Sauerbrey Equation.

3) When the microbalance is oscillating in contact with a viscous loading, a damped shear wave is radiated into the liquid.

4) Finally, the contacting viscous thickness can be assumed to be either larger than the radiated shear wave – i.e. semi-infinite for contacting liquid systems or finite for a thin film layer. Both assumptions change the modelling parameters as identified by Bandey *et al.* [28]; however, have little effect in operation fitting parameters apart from multi-layered systems, as described below.

Figure 12 introduces four new terms to the original BVD equivalent circuit:

- For a microbalance in contact with a viscoelastic contacting mass, there is an additional inductance (L_2) and a resistance (R_2). For a finite thin-film layer, the acoustic wave generated at the resonator-film interface propagates into the media and is reflected at the film-air interface. This phenomenon allows surface admittance to detect the phase shift and attenuation of the wave propagating the contacting film, i.e. the difference between the initial propagating and reflecting wave through the media

- For an additional rigid mass loading to the microbalance surface, a third inductance (L_3) is introduced. A rigid mass loading (alternatively called an ideal mass layer) refers to a film which is both thin and sufficiently rigid that there is negligible acoustic phase shift of the propagating wave through the layer. In this case, the thin layer is assumed infinitesimally thin, but still imposes a finite mass that moves synchronously with the BAW resonator.

- In the case of a multi-layered system, for example, a thin film composite resonator submerged within a semi-infinite liquid, an additional viscous loading modification must be introduced with further inductance (L_X) and resistance (R_X) terms used to represent the additional media [2, 28, 38].

Equations (10) a-g derived by Martin *et al.* describes the corresponding parameters in the 'perturbed equivalent circuit' shown in Figure 12. For further explanation of these equations, including their derivations, the reader is directed to [37].

$$C_O = \frac{\xi_{22} A}{h}$$

$$C_1 = \frac{8C_O K_O^2}{(N\pi^2)}$$

$$L_1 = \frac{1}{\omega_f^2 C_1}$$

$$R_1 = \frac{\eta_q}{c_{66} C_1}\left(\frac{\omega}{\omega_f}\right)^2$$

$$L_2 = \frac{\omega_f L_1}{N\pi}\left(\frac{2\rho\eta}{\omega\, c_{66}\rho_q}\right)^{\frac{1}{2}}$$

$$R_2 = \frac{\omega_f L_1}{N\pi}\left(\frac{2\omega\rho\eta}{c_{66}\rho_q}\right)^{\frac{1}{2}}$$

$$L_3 = \frac{2\omega_f L_1 \rho_f}{N\pi\sqrt{c_{66}\rho_q}}$$

(10) a-g

Where:

ξ_{22}	Quartz permittivity
h	Crystal thickness
K_O^2	Electrochemical coupling constant for quartz
f_s	Series resonant frequency
η	Liquid shear viscosity
η_q	Effective quartz viscosity
ω	Angular excitation frequency
ω_f	Surface film angular excitation frequency
ρ	Liquid density

ρ_f	Density of surface film
ρ_q	Quartz density
N	Overtone number
c_{66}	Quartz elastic constant

For an unperturbed microbalance, $\rho_f = \rho\eta = 0$, thus $L_2 = R_2 = L_3 = 0$, and Figure 12 reduces to the original BVD circuit [39]. As discussed by Beck *et al.* [35] viscous loading causes an increase in both the motional inductance L_2 and the resistance R_2. Martin *et al.* continues to show mass loading affects only L_3; together these findings allow frequency responses and perceived loadings to be distinguished from one another.

Martin *et al.* continued to show that the results that arise from both the perturbed and unperturbed microbalances are related. It is shown therefore that characterization of the unperturbed microbalance is important in determining the response of a given mass or liquid perturbation. Similarly, for systems employing multiple layers / phases, the unperturbed composite resonator must first be characterised using equivalent circuits before the exposure to surface modifying media in order to accurately determine the effect of said media on the system.

Finally, the new term C_p represents the parasitic capacitance; this term was added by Martin *et al.* to account for a capacitance arising from the holder, and depends on the geometry of the holder and the electrode pattern on the microbalance surface. C_0 and C_p are shown in Figure 12 in parallel and may be thought of as indistinguishable from one another; however, C_0 arises as a result of fields across the quartz and enters into the motional circuit elements; C_p comes from the field's external to the microbalance and therefore doesn't affect the motional arm.

The following section explores how crystal admittance spectroscopy can be used to analyse the properties of the electrical characteristics of the microbalance. It also shows how fitting of parameters can give rise to equivalent circuit values. The ability to express mechanical properties of the QCM as electrical equivalents greatly improves its characterisation. The components of the equivalent circuit can be calculated using network analysis, and thus

the use of electrochemical admittance allows determination of the BAW resonator's properties and its contacting medium.

2.6.3 The Effect of Changing Parameters

Similar to the work of Yang and Thompson [40], this section illustrates the effect that key equivalent circuit parameters have on the admittance profiles of a microbalance. This process is useful as it allows the user to understand the real-time admittance responses and subsequently what's happening in the system, often without the need to fit the data.

The major focus of the work presented in the following chapters deals with changes in the composite resonator's system viscoelastic and rigid loading components of the modified BVD. Therefore, a short study is presented below indicating how a resonator's admittance response is affected by rigid and viscoelastic mass loading. For a more exhaustive discussion on other aspects of resonator fitting, the reader is directed to more extensive modelling investigations [33, 38, 40].

In each data set, the base case refers to an ideal oscillating microbalance operating at 55 ^{O}C in 100 ml min^{-1} of air at 0% RH; each set represents the effect a particular parameter has on the admittance profile and discusses the associated factors that may affect this parameter in line with the equivalent circuit diagrams presented above. The 'base case' data set used in each of these examples was taken for a fitted experimentally unperturbed microbalance operating at 55 ^{O}C in 100 ml min^{-1} of air at 0% RH as indicated in Table 1. These simulations were generated using ZView2 modelling software and are adapted from an experiment using a 6 MHz Quartz Crystal Microbalance (QCM). The subsequent perturbations were then over-laid to the experimental data as indicated by Martin *et al.* as a means to elucidate the effect specific perturbations have on the fit data as indicated in the following figures by the black plots.

Table 1: Base case ZView2 fitting data

C_0 (F)	L_1 (H)	C_1 (F)	R_1 (Ω)
9.077×10^{-12}	0.055	1.297×10^{-14}	73.5

2.6.3.1. The Effect of Rigid Mass Loading (L_3)

Figure 13 a-c shows the admittance response for an 6 MHz BAW resonator before and after rigid mass loading. Figure 13a depicts the admittance loci for both systems, Figure 13b shows the magnitude of admittance plots and finally, Figure 13c shows the phase angle plots for both the unperturbed and perturbed systems.

The admittance loci responses are shown in Figure 13a for an unperturbed microbalance in black and for the same microbalance with an additional rigid mass on its electrode surface (composite resonator) in red. Both plots follow the same trend and indicate that the admittance locus is unaffected by the addition of a mass on the crystal surface. No change in the admittance locus radii indicates that both the unperturbed and composite resonator experiences the same resistance to oscillation (R_2). The admittance locus radius is directly proportional to the microbalances resistance, as given in the BVD and other equivalent circuits – the smaller the radius, the greater the resistance value.

Figure 13b shows the magnitude of admittance response for both the unperturbed and composite resonators. For the loaded resonator, there is a distinct shift in the plot to a lower frequency range. The magnitude plot is made up of two peaks – the first high peak indicates the series resonant frequency, and the lower peak represents the parallel resonant frequency. The series resonant frequency and its magnitude are vital in diagnosing mass deposition types. In the case of a rigid mass deposition, the series resonant frequency shifts to a lower value; however, its amplitude remains unaffected.

The phase angle plot is represented in Figure 13c shows a distinct shift to a lower frequency range when an additional rigid mass is present on the BAW resonators electrode. The shift to the 'left' indicates that the microbalance has a new lower resonant frequency, confirming the general trend observed using the Sauerbrey equation. Importantly, however, neither the value of θ_{min} nor the phase bandwidth changes with an additional mass on the crystal surface. The phase bandwidth is defined as the frequency range (Δf) when the phase angle is negative. A phase angle response such as the one discussed above is indicative of a purely rigid mass loading.

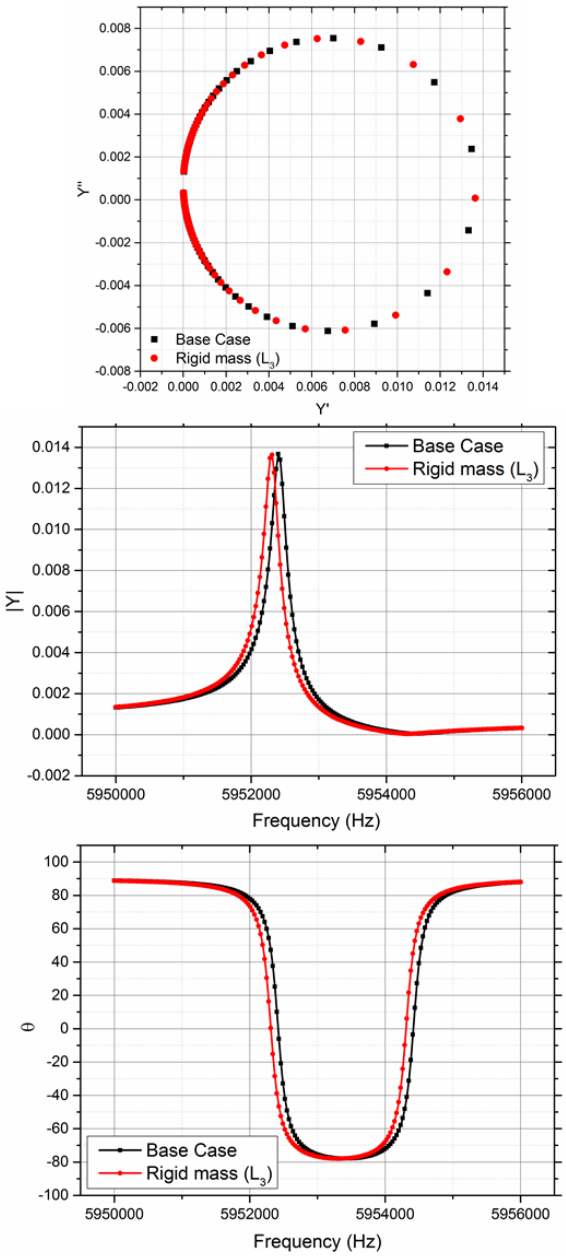

Parameter	Unperturbed	Perturbed
Loci Diameter	0.0136	0.0136
$\lvert Y_{max} \rvert$ frequency (Hz)	5.9524×10^6	5.9523×10^6
$\lvert Y_{max} \rvert$	0.0137	0.0137

Figure 13: Microbalance admittance a) loci b) magnitude and c) phase responses to rigid mass loading (the unperturbed system is shown in black and the perturbed system in red) d) tabulated key metrics

2.6.3.2. The Effect of Viscous Loading ($L_2 + R_2$)

As above, Figure 14a-c shows the admittance response to an unperturbed (black line) microbalance and for the same microbalance with an additional viscous contacting media (red line).

Figure 14a shows the admittance locus responses for an unperturbed and viscous contacting (composite) microbalance. It is clear that when there is a contacting viscous medium on the resonator surface, its resistance to operation increases significantly – i.e. a smaller radius locus. The increased resistance to operation comes as a result of TAW dampening in the viscous phase, as discussed in Section 2.4.2.

The magnitude of admittance plot for both the unperturbed and composite resonator is shown in Figure 14b. The introduction of a viscous loading leads once more to a shift to a lower frequency, as well as damping of the series resonant frequency peak to a lower amplitude.

Finally, the phase angle responses for an unperturbed and composite resonator are given in Figure 14c. Similarly, for a rigid deposition, the introduction of a viscous contacting medium results in a shift in the plot to a lower frequency range. Unlike the rigid mass loading shown in Figure 14b, the composite resonator bandwidth increases and the value of θ_{min} increases in the presence of a viscous loading. These responses are seen only as the resonator couples with a more viscous medium.

Martin *et al.* [37] have described that an increase in the contacting media's viscosity leads to increased damping of both the phase angle and admittance magnitude plots and the simulation shown in Figure 14a-c is typical of that with viscous / viscoelastic loading.

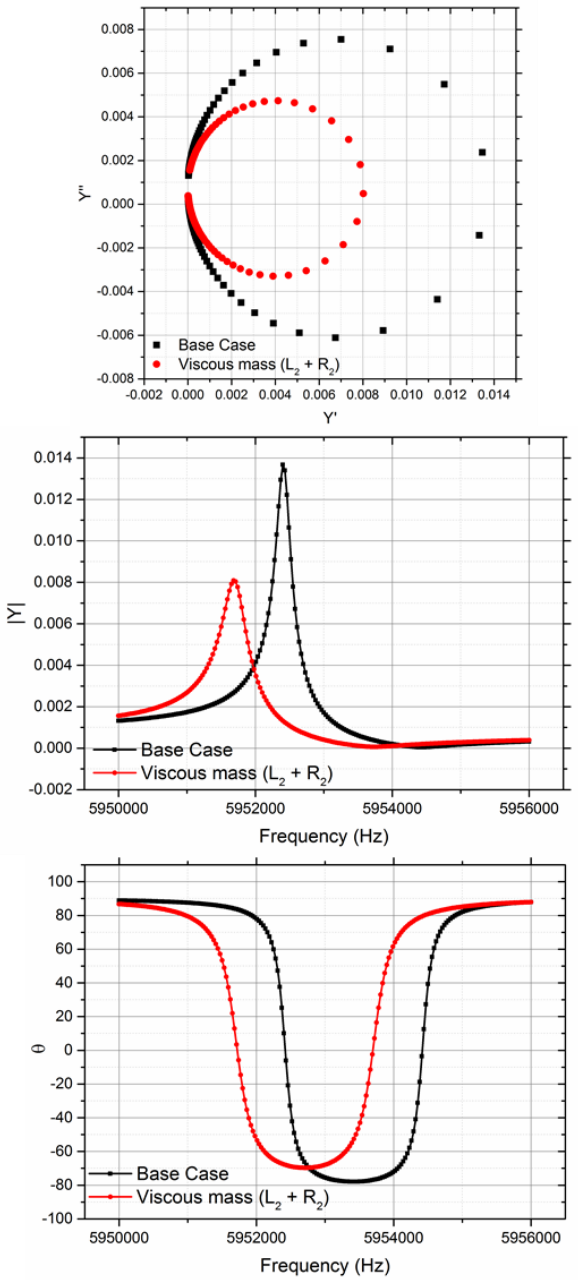

Parameter	Unperturbed	Perturbed
Loci Diameter	0.0135	0.0080
$\|Y_{max}\|$ frequency (Hz)	5.9524×10^6	5.9517×10^6
$\|Y_{max}\|$	0.0137	0.0081

Figure 14: Microbalance admittance a) loci, b) magnitude and c) phase responses for a viscous loading (the unperturbed system is shown in black and the perturbed system in red) d) tabulated key metrics

2.7 Electrochemical Quartz Crystal Microbalance (eQCM)

Between 1982-86, Nomura *et al.* [41-43] and Bruckenstein and Shay [19] conducted work on microbalances to better understand the oscillation behaviour when used in an electrolytic solution. They were able to use the QCM's ability to oscillate in solution to perform *in-situ* electrogravimetry in controlled electrochemical conditions to successfully study the formation of an electrodeposited layer or film on the QCM's working electrode.

The use of a BAW resonator (often a QCM) in a conducting medium as the working electrode in a conventional three-electrode setup for *in-situ* analysis is referred to as an electrochemical quartz crystal microbalance (eQCM) [44, 45].

The first application of the eQCM involved electrodeposition of metals onto electrode surfaces [19]. Bruckenstein and Shay reported an electrodeposition of 10 layers of silver on the metal working electrode at an accuracy of 3 % when compared to the predicted Sauerbrey equation. The electrochemical BAW resonator theory is briefly implemented in this work and is further discussed in Sections 4.2.4.3 and 4.3.3.

3 Fuel Cell Application

This Chapter begins by reproducing and investigating published literature on the water uptake of the Nafion ionomer commonly used in Proton Electrolyte Membrane (PEM) fuel cells using humidified nitrogen. Whilst Nafion has been at the forefront of fuel cell research for decades, there are still conflicting theories about its hydrated microstructure and water loading mechanisms. Models for its loading characteristics have been presented for over 40 years [46-48]; however these are yet to be conclusively validated. The preliminary work presented here is an analysis of the Nafion ionomer's water loading characteristics using an in-situ composite BAW resonator and electrochemical crystal admittance spectroscopy.

The chapter evolves to focus on a novel solid polymer AS-4 alkaline anion exchange membrane (AAEM) developed by Tokuyama Co. (Japan). AAEM fuel cells are a solid polymer electrolyte iteration of the original aqueous alkaline fuel cell. Again, understanding its water uptake, loading and sorption characteristics are critical to understanding the technologies operation and performance limitations and so these factors are assessed here. It is also well documented that AAEMs can suffer from deleterious performance effects as a result of thermal and subsequent chemical degradation as well as carbon dioxide poisoning. The effect of these factors on the AAEM's performance are poorly understood and so are further explored in this investigation using surface developed in-situ BAW resonators.

3.1 Introduction

There is greater demand than ever for a greener energy economy. Fuel cells are considered a potentially integral technology in achieving this goal. A fuel cell operates by converting chemical energy directly into electricity, without the production of any particulates or greenhouse gas emissions at

point-of-use. With no moving parts in the stack itself, fuel cells can offer higher efficiencies than the equivalent combustion engine whilst also providing improved energy storage and reduced 'charge' times when compared to batteries.

However, fuel cells are not without challenges. The major hindrance to the technology's commercialisation is its cost per kilowatt compared to existing electricity generation technologies. A fuel cell is made up of the components described in Section 3.2.1 and elsewhere [49, 50], where the main working part, the membrane electrode assembly (MEA) comprises an electrocatalyst, often containing a precious metal such as platinum, and an ionic polymer membrane. The membrane and the catalyst provide a significant contribution to the fuel cell's overall cost.

Alkaline anion-exchange membrane fuel cells (AAEMs) have the potential to replace the traditional acidic proton exchange membrane (PEM) fuel cells for low-temperature applications [51-56]. With more facile oxygen reduction reaction (ORR) kinetics than traditional PEM fuel cells, the alkaline medium allows implementation of lower cost, non-precious metal electrocatalysts at the cathode [57, 58], compared to the more resilient precious metals (e.g. Pt) required in acidic media [57-64]. In addition, the AAEM is a solid polymer electrolyte and so can be incorporated into compact designs, as seen with acid based proton exchange membrane fuel cells [53, 65].

This study is broken down into three investigations, as outlined below:

The first investigation explores the water uptake, sorption mechanics and swelling characteristics of thin-film Nafion and the commercially available AS-4 Tokuyama alkaline anion-exchange membrane ionomer from the vapour phase using surface developed *in-situ* BAW resonators. The water uptake measures the number of water molecules adsorbed by the ionomer per functional group and is determined *in-situ* using the BAW resonators frequency responses allowing for comparison with nanogram precision. Crystal admittance spectroscopy, along with equivalent circuit fitting, is applied to both thin films for the first time and is used to investigate the ionomer's viscoelastic changes during hydration; to elucidate the mechanisms at play during low, medium and high relative humidities.

Many AAEMs are reported to suffer from increased instability within alkaline media (degradation) via a number of routes, including nucleophilic elimination when operated at temperatures above 60°C, somewhat eliminating the kinetic advantage of operating at higher temperatures. Nonetheless, modelling studies have indicated that the membrane hydration could show improved resistance to alkaline instability and subsequent degradation when operated at elevated temperatures. This second investigation uses the AS-4 composite BAW resonator to examine the thermal stability of the ionomer as a function of humidity. The results show that hydration improves ionomer resistance to degradation, as the ions within the system (namely the OH^- nucleophile and cationic headgroups) become less reactive. In-line mass spectrometry data confirms that the ionomer degrades during the elevated temperature excursions used in this study.

Finally, the third investigation explores the issues relating to degradation and specifically the ionomer's interaction with CO_2 (often referred to as CO_2 poisoning). With hydration playing a key role in solid polymer electrolyte fuel cell operation, this study examines how membrane hydration affects the AAEM interaction with CO_2. The change of membrane conductivity upon exposure to atmospheric CO_2 has been compared with the change in viscoelastic properties of a cast thin-film ionomer, both as a function of humidity. The effect of CO_2 on the membrane as a function of hydration suggests a link to its solvation and swelling regimes and thus the access of CO_2 to the ionic channels within the membrane. The thin-film BAW composite resonator study has shown that during the solvation (pore opening) regime, there is a linear increase in CO_2 uptake as water can further permeate the pore system and the cationic headgroups become increasingly accessible. During the transition to the pore swelling regime, there is a step increase in CO_2 uptake as the network is thought to be fully open; as such, subsequent increases in RH do not indicate any significant increase in CO_2 uptake.

3.2 Literature Review

3.2.1 What is a Fuel Cell?

Fundamental fuel cell operation is not dissimilar to that of a battery; there is direct conversion of chemical energy to electrical energy, albeit with a constant supply of fuel and oxidant. A fuel cell is comprised of an anode, where a fuel is oxidised, and a cathode where an oxidant is reduced; these are sandwiched around a conductive electrolyte. Fuel cells were originally developed in 1839 by Sir William Grove; however, the discovery of 'cheap' oil and gas meant that further advancements from this concept were slow, and it wasn't until the 1960s when NASA revisited the fuel cell that further development began. The earliest fuel cells contained an aqueous caustic electrolyte which had many disadvantages namely portability, leading the current trend toward solid polymer electrolytes (SPEs), and in particular towards low-temperature acidic proton exchange membrane (PEM) fuel cells.

3.2.2 Proton Electrolyte Membrane (PEM) Fuel Cells

Fuel cells operate through a direct electrochemical redox-reaction that produces an electrical current. The redox-reaction in a hydrogen/oxygen fuel cell comprises two electrochemical half reactions; the hydrogen oxidation reaction (HOR) at the anode [50]:

$$2H_2 \rightleftharpoons 4H^+ + 4e^- \tag{11}$$

And the oxygen reduction reaction (ORR) at the cathode:

$$O_2 + 4H^+ + 4e^- \rightleftharpoons 2H_2O \tag{12}$$

Giving the overall redox reaction:

$$H_2 + \frac{1}{2}O_2 \rightleftharpoons H_2O \tag{13}$$

Hydrogen is supplied to the anode and air/oxygen to the cathode. The gases diffuse through to the catalyst layer where it meets the electrolyte at the

triple phase boundary (TPB). At the TPB, the HOR and ORR occur on the anode and cathode respectively, separated by the acidic proton exchange membrane. The protons released in Equation (11) at the anode diffuse through the membrane to the cathode to recombine with the generated electrons, which travel through the external circuit creating a current due to the membrane's impermeability as shown in Figure 15.

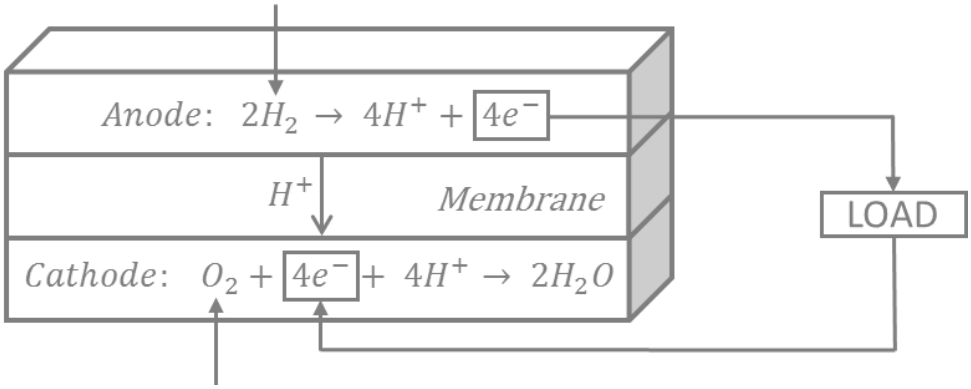

Figure 15: PEM-FC operation schematic

In recent years, much of the low-temperature fuel cell research has concentrated on acidic proton electrolyte membrane fuel cells (PEM-FCs) [66], for their high efficiencies and high peak power densities. These properties coupled with low operating temperatures make PEM-FCs extremely attractive for applications from portable automotive power to large stationary power. However, issues pertaining to reliability, durability and particularly cost have plagued the technology's otherwise imminent commercialisation. The main cost contributor to the PEM-FC is its expensive precious metal catalyst. Efforts to find alternative inexpensive electrocatalysts to replace the existing Pt group metals whilst maintaining stable and efficient operation within the acidic operating environment have so far proven unsuccessful. Whilst there are many groups working on these alternatives [57, 58, 67] several researchers have begun to revisit the alkaline fuel cell.

3.2.3 Alkaline Membrane Fuel Cells

Alkaline membrane fuel cells are seen as a potentially viable option for low-temperature applications. The PEMs greatest barrier to low-temperature fuel cell commercialization is its cost per kW; the majority of which stems from the membrane and the electrocatalysts required to speed up the otherwise slow ORR kinetics; however, alkaline fuel cell ORR kinetics are much more facile [68]. Faster ORR kinetics allows the implementation of cheaper non-precious metal cathode electrocatalysts such as gold, silver, nickel, or potentially a lower loading of Pt group metals [69-71]. The catalyst cost reduction felt as a result of faster ORR kinetics has the potential to push fuel cell commercialization one step closer.

3.2.3.1. Aqueous Electrolyte Alkaline Fuel Cells

Knowledge of the alkaline fuel cell's (A-FC) faster ORR kinetics has been around since the 1960s [72] and led to its early domination of fuel cell development and subsequent use on the NASA Apollo space missions. The A-FC shown in Figure 16 is similar to a PEM but instead of a solid polymer electrolyte, it uses an aqueous KOH electrolyte contained in a matrix.

The half-reactions shown below don't differ significantly to that of an acidic fuel cell except here OH^- ions mediate the half reactions [50].

The hydrogen oxidation reaction (HOR) at the anode:

$$2H_2 + 4OH^- \rightleftharpoons 4H_2O + 4e^- \tag{14}$$

The oxygen reduction reaction (ORR) at the cathode:

$$O_2 + 2H_2O + 4e^- \rightleftharpoons 4OH^- \tag{15}$$

The overall redox reaction: [60]

$$H_2 + \frac{1}{2}O_2 \rightleftharpoons H_2O \tag{16}$$

Within the half reactions two of the issues seen with the A-FC can be seen. Equation (13) in the acidic media fuel cells shows the generation of one mole of water at the anode during the HOR and the consumption of one mole of water at the cathode during the ORR. However, in an A-FC, the HOR at the anode produces four moles of water, as shown in Equation (14); however, Equation (15) shows that the ORR consumes only two moles of water at the cathode. This expedited rate of water production during the HOR in an A-FC has the potential to flood the anode and cause huge water management issues.

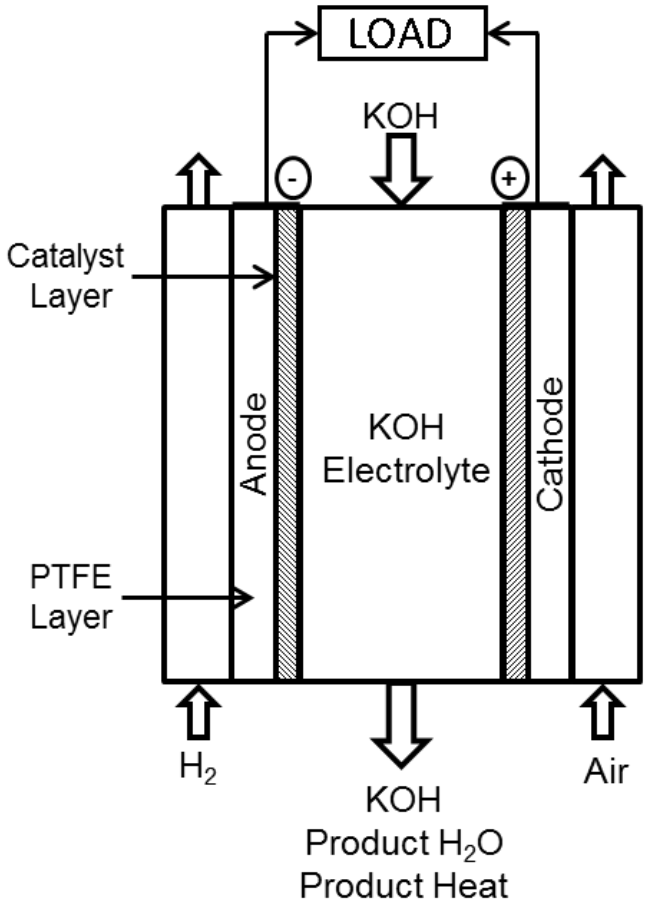

Figure 16: A-FC operating schematic

However, in A-FCs metal carbonates form from the interaction of dissolved carbon dioxide from the air and metal cations (M) such as K^+ and Na^+, within the aqueous electrolyte as described in Equation (17) [53].

$$CO_{2(g)} + 2MOH_{(aq)} \leftrightarrow M_2CO_{3(aq)} + H_2O_{(l)} \quad (17)$$

These metal carbonates precipitate and not only decrease the concentration of solvated OH^- ions but also form layers on the electrode surfaces, blocking active sites, gas diffusion layers (GDLs) and significantly reducing system performance [50, 73].

These issues were in some cases resolved by the implementation of gas scrubbers and other pre-treatment processes of the reactants, significantly increasing the cost per kW [51, 74]. These factors coupled with portability and weeping of caustic electrolyte led fuel cell research towards the more popular PEM technology. However, recent developments in SPE alkaline anion-exchange membrane fuel cells (AAEM-FCs) have begun to shift the focus once more.

3.2.3.2. Alkaline Anion Exchange Membrane Fuel Cells

The AAEM-FC operates with very similar principles to the PEM fuel cell i.e. electrochemical conversion of hydrogen to electricity using a solid polymer electrolyte as shown in Figure 17. However, the AAEM-FC maintains the A-FC's half equations and hence its ORR kinetics, thus allowing the benefit of catalyst cost reductions whilst nullifying many of its caustic aqueous electrolyte issues [53].

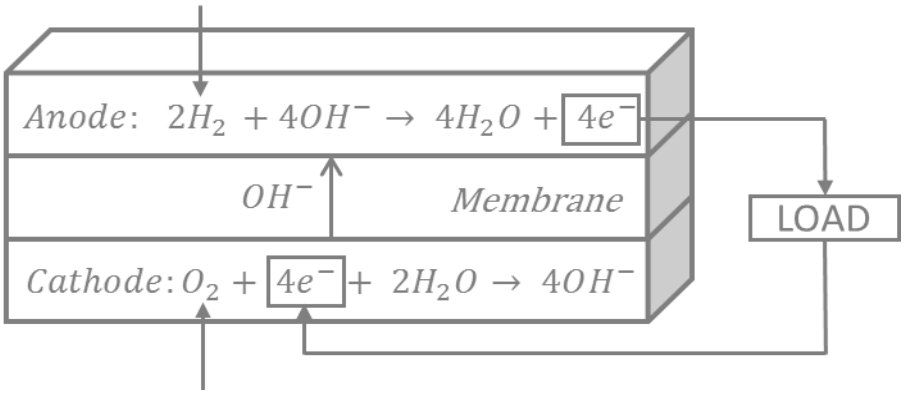

Figure 17: AAEM-FC operating schematic

Coupled with improved portability, the implementation of an SPE allows the AAEM to potentially address the issue of carbonate precipitation. In an A-FC, the carbonate salt precipitates as a result of the lower solubility of M_2CO_3 and the excess availability of M^+ ions. However, in an OH^- conducting solid polymer electrolyte, the cations are spatially separated and covalently bonded to a polymer backbone. Therefore, even though CO_3^{2-} ions interact with the cation, the precipitation of the salt is thought to be significantly less likely [60, 74-76].

With some of the A-FC issues seemingly addressed, the AAEM-FC has the potential to replace the traditional acidic PEM-FC for low-temperature applications. With more facile ORR kinetics than traditional PEM fuel cells, the alkaline medium allows implementation of lower cost, non-precious metal electrocatalysts [57, 58], compared to the more resilient precious metals (e.g. Pt) required in acidic media [59-61]. The AAEM, therefore, offers the potential of bringing the cost of electricity ($/kW) closer in line with that of traditional electricity generators and so advancing fuel cell commercialisation. However, with AAEM development in its infancy, the technology has not been extensively examined, nor does it operate without issues, as discussed in Section 3.2.4.

3.2.4 AAEM Operational Issues

With no industry standard AAEM (such as Nafion for PEMs), many different operational observations populate the literature. The major operational issues in the literature are summarised below and discussed in further detail in the outlined sections:

- The AAEMs water management and specifically uptake, sorption mechanisms, swelling characteristics and stability govern its operation and performance efficiency [77]. However, the available literature provides contradictory analyses of these characteristics and this is further discussed in Section 3.2.4.1.

- Section 3.2.4.2 describes the chemical instability and degradation mechanisms that arise as a result of increased operating temperature and specifically E2 (Hofmann) elimination that has

been demonstrated for several AAEMs when operating at temperatures $\geq 65^{o}$C. At elevated temperatures, the OH^- conducting ions have been shown to irreversibly cleave the tethered cationic head groups from the polymer backbone reducing its ionic conductivity [53, 78].

- Finally, with immobilised cations, carbonate ion interaction and subsequent precipitation of salts are unlikely when operating in air; however, performance effects have been seen to varying degrees and this is further discussed in Section 3.2.4.3.

3.2.4.1. Water Uptake and Hydration Mechanisms

In a fuel cell, the SPE membrane serves to conduct ions (often H^+ or OH^-) between electrodes (anode to cathode in acidic fuel cells and cathode to anode in alkaline fuel cells); the membrane should also be a good electrical insulator and be impermeable to reactant species. The most common SPE membrane is Nafion (DuPont) and is often used in PEM fuel cells and electrolysers, whilst advancements in alkaline SPEs has led to the first commercially available AAEM – the AS-4 produced by Tokuyama Co. (Japan).

Water management in SPE fuel cells is essential to achieving optimal operation; SPEs must be hydrated to allow sufficient protonic and hydroxide ion conduction in PEM and AAEM fuel cells respectively, whilst excessive liquid water will cause deleterious performance effects [79]. Water transport across SPEs is driven by several mechanisms, including diffusion by activity gradients, convection through hydraulic pressure differences and electro-osmotic drag.

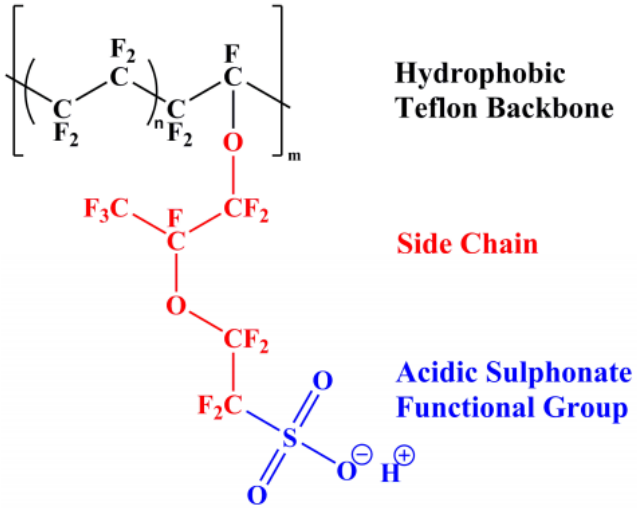

Figure 18: Nafion structure

Water uptake and transport through PEMs, and specifically Nafion (Figure 18), has been extensively studied; however, the microstructure of hydrated Nafion is currently a subject of intense study and speculation [80]; the most established theory is the Cluster–Network model presented in the 1980s [46, 47, 81]. The Cluster-Network model considers the ionomer as a network of ionic clusters formed by the sulphonic groups arranged as inverted micelles (roughly 4 nm diameter) and interconnected by narrow water channels (1 nm in diameter). Through techniques such as small angle X-ray scattering (SAXS), authors such as Gierke *et al.* [46] have shown that as the Nafion ionomer adsorbs water, the cluster diameter, exchange sites per cluster and number of water molecules per exchange site, all increase as shown in Figure 19. Other publications, such as the work presented by Schmidt-Rohr and Chen [82], have shown through modelling techniques that the hydrated ionomer structure corresponds more closely to inverted-micelle cylinders with average channel diameters of 2.4 nm.

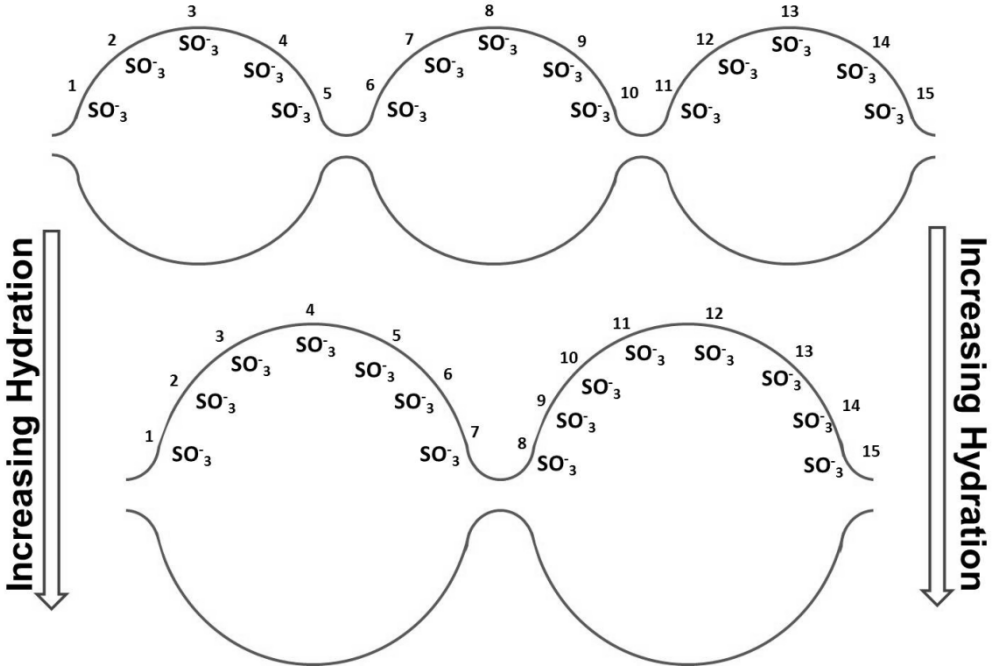

Figure 19 : The Cluster Model theory for hydrated Nafion microstructure adapted from Gierke *et al.*

Experimental work by Zawodzinski *et al.* [83, 84] has somewhat extended and explained the Cluster–Network model and has shown that Nafion hydrates through two distinct regimes. At low relative humidities (RHs), it is suggested that only a small quantity of water is adsorbed and the uptake corresponds to the solvation of the protons and sulphonate ions. The water in the polymer during this regime strongly interacts with the ionic components within the ionomer and these interactions help overcome the strong tendency of the polymer to exclude water due to its hydrophobic nature and swelling resistance. The second regime, which occurs at higher RHs, is thought to correspond to a large water uptake, in which the adsorbed water molecules fill the ionomer's micro-channels and result in membrane swelling.

The study of thin film (≤ 1 μm) Nafion ionomers has been explored in a limited capacity and remains somewhat ambiguous [80, 85, 86]. Characterisation work presented by Wood *et al.* [87] Karan and co-workers [88, 89] as well as Dishari and Hickner [90] have shown the presence of an ultra-thin ≤ 55 nm hydrophilic layer developed on self-assembled thin film Nafion ionomers. The work continues to show that the water uptake values recorded

at the ultra-thin film thicknesses are significantly higher and is thought to be dominated by this hydrophilicity; however, as the self-assembled layer is developed, the results show that the ionomer then exhibits more traditional hydrophobic tendencies, similar to that of bulk Nafion.

There is a growing body of literature on water management properties of AAEMs [91-93]; however, studies to date have neglected to consider the transport phenomenon at the interfacial level. The AS-4 ionomer is a commercially available, proprietary AAEM made by Tokuyama Co. (Japan). Whilst the exact chemical composition of the Tokuyama membrane is not certain, it is known to be made up of a hydrocarbon backbone with terminated quaternary ammonium functional groups. Many experiments have been conducted to characterise AAEM performance, durability and electro-osmotic drag [94-96] and it is proposed that as with Nafion, the ionomer hydrates and hydrophilic regions will swell, though little is understood about AAEM water sorption or how swelling affects ion conductivity.

It has been well documented that AAEMs have a significantly lower ionic conductivity than the PEM equivalent [95, 97]. To compensate for this, it is common for manufacturers to introduce additional functional groups on the polymer backbone to increase the ionomer's ion exchange capacity (IEC) [98]. Excessive water loading is reported to cause mechanical instability in AAEMs [95] and consequently, the study of ionomer morphology during hydration (specifically when the ionomer is in a 'fully hydrated' state) is imperative. Similarly, improved understanding of interfacial water uptake, loading mechanisms and consequent hydroxide ion conductivity is required for AAEM ionomers.

3.2.4.2. AAEM Instability at Elevated Temperatures

AAEMs contain positively charged (cationic) headgroups that have been suggested to dissociate more weakly than the sulphonic acid groups found in Nafion; coupled with the inherently lower electrochemical mobility of OH^- ions compared to protons, means that AAEMs typically have ionic conductivities approximately a quarter of those for PEMs [98]. Many AAEMs include more cationic groups along the polymer backbone to improve their IEC and thus the ionic conductivity; however, the increased fixed charge concentration is thought to lead to deterioration of the AAEMs' mechanical properties [97, 99, 100].

The most common cationic group in AAEMs is quaternary ammonium, $[R_4N^+]$ [62], which is often used as it has higher stability within alkaline media compared to phosphonium or sulphonium groups [101]. However, it has been well documented that AAEMs can also suffer from chemical instability in alkaline environments [51, 96, 101], with chemical degradation stemming largely from nucleophilic attack by hydroxide ions on the cationic fixed charged sites; a process accelerated by operation at elevated temperatures.

For example, the quaternary ammonium group is susceptible to cleavage in the presence of hydroxide ions, leading to the E2 elimination reaction (the Hofmann elimination) shown in Figure 20.

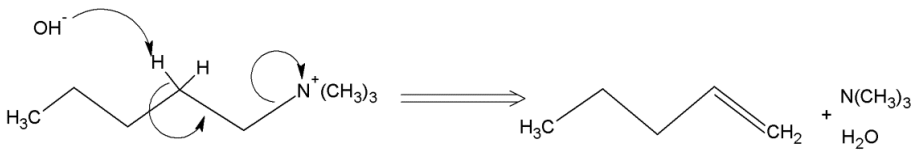

Figure 20: Hoffman (E2) elimination reaction mechanism.

During E2 elimination, hydroxyl ions attack β-hydrogens, leading to the formation of an alkene, an amine and a water molecule. Most work to date has suggested that Hofmann elimination is negligible below 60 ^oC, but much

faster at higher temperatures, resulting in significant membrane degradation [102-104]. This is an obvious limitation for current alkaline membranes as the kinetic benefit of operating at higher temperatures is unobtainable.

The other key mode of ionomer degradation is direct nucleophilic displacement at the cation site; this can occur through two possible reaction pathways for quaternary ammonium charge sites, as shown below in Figure 21 and Figure 22. In these cases, the hydroxide ions attack at either the methyl group, forming methanol, or at the C-C bond between the alpha and beta carbons to cleave the cation site (S_N2 reaction) [51]. These mechanisms are further discussed elsewhere [105, 106]. Other degradation routes presented within the literature include deprotonation of the [R_4N^+] headgroups to produce nitrogen ylide intermediaries [107, 108] and specific studies on the degradation of the polymer backbone put forward by Arges *et al.* [109, 110], Chen and Hickner [111] and Mohanty *et al.* [112]. The consequence of these degradation mechanisms is a loss in the number of ion-exchange groups and a subsequent decrease in OH^- conductivity, with consequences for fuel cell performance.

Figure 21: Direct nucleophilic degradation, Pathway 1

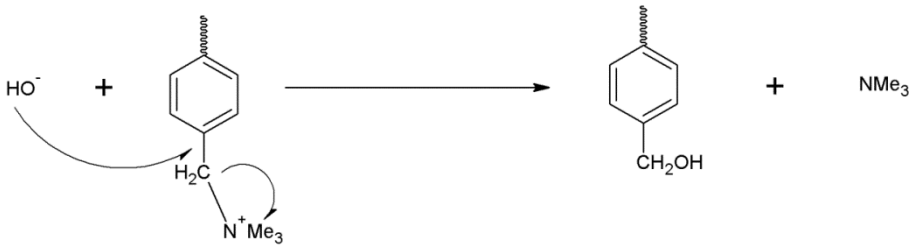

Figure 22: Direct nucleophilic degradation, Pathway 2

As with most SPEs, AAEM hydroxyl conduction improves with hydration as the ionomer channels solvate and subsequently swell [113, 114]. There is a balance between improved membrane conductivity through hydration and the deleterious effects on the performance seen in fuel cells caused by the formation of liquid water blocking reactant channels and gas diffusion layer pores. Recently published work [105, 108, 115] on formulated head groups have added a new dynamic to this balance, indicating a correlation between ion solvation (and hence ionomer hydration) and ionomer degradation by nucleophilic attack.

A model presented by Chempath *et al.* [105] implements an untethered cationic head group, $[N(CH_3)_4]^+$, and shows that the degradation mechanisms appear more aggressive in a system with low water content. Work by Macomber *et al.* [108] reports a similar conclusion, where the thermal degradation of tetramethyl ammonium hydroxide is retarded by hydration. In both cases, the investigations explain that a dehydrated membrane exhibits more aggressive degradation, as both the hydroxyl ions and cations remain unsolvated and thus more reactive [105, 108].

3.2.4.3. Carbonate Ion Interaction and Conductivity

Compared to the A-FC, the AAEM-FC is much more portable and does not suffer from weeping of caustic electrolyte and leaking issues [53]; however, recent reports suggest it is still susceptible to carbonate formation [60, 74-76]. In A-FCs, metal carbonates form from the interaction of dissolved carbon dioxide from the air and metal cations (M) within the aqueous electrolyte, such as K^+ and Na^+, as described in Equation (17) [53]. These metal carbonates precipitate and not only decrease the concentration of solvated OH^- ions but also precipitate, forming layers on the electrode surfaces, blocking active sites, gas diffusion layers (GDLs) and significantly reducing system performance.

Recall,

$$CO_{2(g)} + 2MOH_{(aq)} \leftrightarrow M_2CO_{3(aq)} + H_2O_{(l)} \quad (17)$$

The AAEM has immobilised cationic functional groups tethered to its polymer backbone and thus the effect of carbonate formation on the system's ionic performance has been a topic of much debate. The membrane is still expected to form immobilised metal carbonates; however, these are thought to have minimal deleterious performance effects on fuel cell operation as they cannot dissociate from the ionomer backbone and cause the aforementioned blocking issues seen in the A-FC [116, 117]. Some studies have shown that the presence of carbonate ions can, in fact, enhance fuel cell performance through improved membrane chemical stability and thus long-term operation [76, 116]; whilst others have presented opposing results, through a reduction in both ionic conductivity and its impact on the hydrogen oxidation reaction (HOR) [118-122].

Investigations have proven that the ionomer can operate in the carbonate (CO_3^{2-} / HCO^{3-}) form [121]; however, the reported conductivities have been significantly lower when compared to operation in the OH^- form [123]. Varcoe *et al.* [76] have presented a potential solution, known as the self-purging mechanism, in which a humidified system can return to OH^- operation having been in the carbonate form. This mechanism requires the system to run at high current densities and in CO_2 free conditions; allowing the carbonate ions to be replaced by OH^- ions generated at the anode [118].

Even with promising commercialisation prospects, the effect of CO_2 interaction, membrane degradation and poor understanding of the system's hydration mechanisms have resulted in very few commercially available AAEMs and thus no industry-leading standard (such as Nafion). Many examples in the literature are conducted on in-house fabricated membranes; generally at the lab scale development stages and hence have huge discrepancies in findings, such as conductivity and thermal and chemical stability [53].

As discussed, Tokuyama Co's AS-4 AAEM provides an ionic conductivity more comparable to that of Nafion; however little is known of the membrane's properties or how it functions in different operating conditions. Published work by Tokuyama and specifically Yanagi and Fukuta [121], has shown that the membrane is hindered by operation in air, resulting in reduced conductivity in the A201 membrane from 42 mS cm^{-1} in the OH^- form to 10 mS cm^{-1} in the carbonate form.

The investigation presented by Yanagi and Fakuta monitored the concentration of the anion species after exposure to ambient air from N_2 using Cl^- ion exchange and titration based on the Warder method [121]. The results indicate that the absorption of CO_2 by the (wet) system was very fast and all OH^- anions were converted to a combination of the carbonate (CO_3^{2-} / HCO^{3-}) form within 30 mins [121].

The findings presented by Yanagi and Fakuta can be further analysed and potentially explained as the introduction of CO_2 can cause it to dissolve into a humidified AAEM system and form a chemical equilibrium with carbonic acid, as shown in Equation (18); the CO_2 can also react directly with and consume the inherent OH^- ions in the system, as shown in Equation (19).

$$CO_{2(g)} + H_2O_{(l)} \leftrightarrow H_2CO_{3(aq)} \tag{18}$$

$$CO_{2(aq)} + OH^- \leftrightarrow HCO_3^- \tag{19}$$

Carbonic acid can be considered a diprotic acid and can, therefore, form hydrogen carbonates in the presence of H_2O (Equation (20)) and carbonates containing CO_3^{2-} (Equations (21) and (22)) [124].

$$H_2CO_3 + H_2O \leftrightarrow H_3O^+ + HCO_3^- \tag{20}$$

$$HCO_3^- + H_2O \leftrightarrow H_3O^+ + {CO_3}^{2-} \tag{21}$$

$$HCO_3^- + OH^- \leftrightarrow H_2O + {CO_3}^{2-} \tag{22}$$

Equations (18) - (22) indicate that the introduction of CO_2 into an AAEM system will not only form carbonate anions that may attach to the polymer's tethered cationic active sites, but also lowers the pH as the system becomes

more acidic, as well as consuming OH^- ions reducing membrane conductivity and hence performance [125].

Water management and ionomer hydration play a key role in effective fuel cell operation, including ionic conductivity [126] and ionomer degradation [127]. Equations (18) - (22) show that water may also play a key role in the mechanisms involved in reducing fuel cell performance through interaction with CO_2. It is therefore crucial that we understand if and how the system's operational humidity affects the processes discussed above.

3.2.5 The Application of a BAW Resonator

Section 3.2.4 has outlined some of the major operational concerns of the AAEM-FC. In order to commercialise the AAEM-FC, the issues of water sorption and swelling characteristics, thermal and chemical instability and carbonate ion interaction must be understood and addressed. In each case, the membrane's characteristics and morphological changes must be investigated as a function of its operating conditions in order to optimize the AAEMs operation, performance and cost.

This study will examine each of the aforementioned operational issues on an interfacial level using the nanogram resolution mass monitoring capability of composite BAW resonators coupled with crystal admittance spectroscopy.

Electrolyte mass changes during this study are likely to be in the nanogram region; making a BAW resonator and specifically a quartz crystal microbalance (QCM) an ideal *in-situ* mass measurement device. As discussed in Chapter 2, a BAW resonator is able to operate under a range of conditions and in an array of media. One of the more difficult challenges with an *in-situ* sensor of this type is the ability to distinguish between different types of loading i.e. whether a change in frequency response can be attributed to additional mass loading or simply changes in the operating environment or changing membrane characteristics. However, the application of crystal admittance spectroscopy (CAS) and its equivalent circuits as discussed in Sections 2.5 and 0 respectively allows specific frequency shifts to be categorized.

CAS will provide unique insight into how the ionomers are affected by water, degradation and carbonate interaction; providing a clearer picture of whether responses are related to rigid or viscoelastic properties for instance.

A 2013 publication by Abuin *et al.* [80] showed the use of a QCM for *in-situ* mass monitoring in a PEM-FC to understand how Nafion's swelling and water sorption properties were affected by the presence of a substrate. This work was of particular interest, as it encompassed a similar technique to that used here; employing the QCM as a means to measure the mass change on the crystal surface and hence to determine the water uptake by the Nafion ionomer. However, whilst showing how the water uptake of the Nafion varies with its thickness, Abuin *et al.* had issues with electrolyte casting, conducting this as an *ex-situ* process. Consequently, the reported masses and Nafion thicknesses published are inaccurate under dry conditions, thus making it impossible to calculate and compare accurate water uptake results for the ionomer when operating under humidified conditions. A similar issue was found with work published by Kongkanand [86], who showed that the Nafion water uptake was affected by temperature and very slightly by membrane thickness.

Studies on Nafion have described water uptake trends and some have commented on the so-called Schroeder's Paradox - a phenomenon used to describe the difference in solvent uptake by a polymer when exposed to saturated vapour and pure liquid [80, 85, 86]. However, to date, most QCM studies have limited the analysis to a simple consideration of the frequency of operation as the key metric of water uptake and overlooked viscoelastic effects, loading mechanisms and subsequent swelling of the interfacial layer upon hydration. Using the QCM to investigate viscoelastic changes of the ionomer during hydration provides potential insight into hydrated microstructure and the links between hydration states and ionic conductivity.

A similar technique of *in-situ* monitoring will be conducted throughout this work with the *in-situ* casting of a thin layer of electrolyte on the BAW resonator surface to give a 'true' *in-situ* indication of what is happening at the electrolyte – electrode interface. The QCM allows thin film deposition of ionomers to be cast and allows *in-situ* non-intrusive operation. The use

of thin ionomer films ensures there is no contribution of internal water diffusion within the film and simplifies the analysis.

The following section outlines the three thin-film ionomer investigations encompassed within this study:

- The first part of this study investigates the water uptake and loading mechanisms of both thin-film Nafion and a commercially available AS-4 AAEM ionomer whilst operating in a range of humidified environments using the QCM and CAS. Whilst the Nafion ionomer's water uptake and loading mechanisms are reasonably well understood, the knowledge of the same within the AAEM is significantly lower. The Nafion investigation presented during this study is novel in its own right through the application of CAS, but also serves as a means by which to validate the experimental set-up and feasibility for thin film ionomer studies for the unknown AS-4 ionomer.

- With the AAEM hydration mechanisms better understood, the second investigation experimentally explores how specific ionomer hydration affects the thermal and chemical degradation mechanisms of the AS-4 ionomer using a QCM. In-line mass spectrometry is used alongside the QCM in this study to further elucidate the importance (and limitations) of cation and hydroxide ion solvation for the stability of an AAEM ionomer.

- The final investigation within this study examines how reactant humidity (and hence membrane hydration) affects the AAEM interaction with atmospheric levels of CO_2. The change of membrane resistance with exposure to air (as a source of CO_2) is compared with the change in viscoelastic properties of a thin-film ionomer, both at steady state and as a function of humidity.

3.3 Methodology

This study has been divided into the investigations outlined in Section 3.2.5; however, many of the key operating principles remain the same between investigations and thus employs the same 'base-rig' set up. Rig modifications and changes in the methodology have been made for specific investigations and these are clearly highlighted where relevant.

This section outlines and justifies the equipment selection, development and material choices used through this study.

3.3.1 Quartz Crystal Microbalance

The *in-situ* interfacial electrolyte investigations proposed in Section 3.2.5 required nanogram resolution mass monitoring to detect the smallest changes within the system in order to provide useful insight into processes occurring at the interfacial level. The required level of accuracy made the BAW resonator the ideal mass monitoring device for these applications.

The investigations within this study have application conditions between $50 - 80\ ^{o}C$ at a range of relative humidities and involve polymer surface modification of the BAW resonator for *in-situ* application. It was, therefore, necessary to find a BAW resonator able to operate with an attached thin film layer within the defined conditions.

There are a range of BAW resonators suitable for this operation, each with varying levels of frequency stability and mass sensitivity as described by [128]. However, the quartz crystal microbalance (QCM) represents a mature, reliable, stable, consistent and cost-effective mass monitoring device. The QCM has proven applications across many polymer studies including previous work with Nafion [80, 86, 129], where it has shown excellent stability and accuracy of mass measurement. The QCM was therefore chosen for these investigations and a further feasibility study is presented in Section 3.4.1 [130, 131].

The QCM is a very popular BAW resonator for the aforementioned reasons and it is therefore available in a range of resonant frequencies, each with

unique advantages and disadvantages. High frequency (10 MHz) BAW resonators use very thin piezoelectric material which provides excellent mass deposition resolution; however, the thinner resonators are more brittle and difficult to operate with surface modifications which can lead to breakage. Similarly, with lower frequency (≥ 5 MHz) BAW resonators the opposite is true; i.e. whilst less prone to breakage, they have lower mass monitoring resolution.

QCM resonators are also available with a wide variety of electrode materials and designs. The electrode material provides an electrically conductive attachment to the piezoelectric material (often using a thin chromium (or similar) adhesion layer) and the electrode designs allow applicability over a large range of investigations.

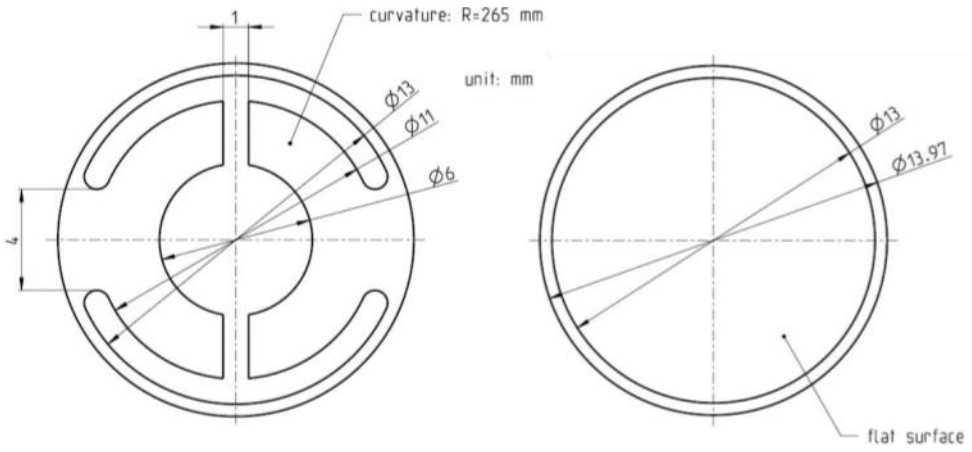

Figure 23: Quartz crystal microbalance double anchor electrode schematic

This study employed 6 MHz QCM resonators with gold 'double anchor' electrode designs (Inficon, USA) as shown in Figure 23. The double anchor electrode design was chosen as it provides a defined 6 mm centre electrode to be cast as discussed in Section 3.4.1.3. The gold electrode was employed (rather than sputtered silver or a high-stress alloy) as it does not oxidise, has an indefinite shelf life and has a proven stability and accuracy in applications across many industries. Finally, 6 MHz QCMs were chosen as a trade-off between mass monitoring resolution (6 MHz QCMs provide 0.4 ng resolution) and ease of use within bespoke rig designs.

3.3.2 Rig Development

The experimental rig is initially set up as shown in Figure 24 (hereunder referred to as the 'base-rig') and is developed to provide both a dry (0 % RH) and humidified (0.5% - 100% RH) supply of nitrogen to the QCM under test which is housed in the fuel cell humidification chamber (hereunder known as the cell). The literature presented in Section 3.2.4.3 suggests that the AAEM is expected to interact and form carbonate ions in the presence of CO_2 (even at atmospheric concentration levels) [120, 132] and so all investigations were conducted within the sealed cell in CO_2 - free conditions as discussed in Section 3.3.4.3. The base rig was the initial test station developed for the water uptake and hydration mechanism investigation; alterations for further investigations are discussed in Section 3.3.4.

Nitrogen (BOC, UK) is supplied compressed at 300 bar in a compressed gas cylinder; it is piped to a 5 bar 2-stage regulator, valve tap and filter through (1/4") nylon piping (FTI, Sussex UK) to a mass flow controller (Bronkhorst, Suffolk UK). The mass flow controller allows a desired flow of nitrogen into a dry stream through a desiccant or via the dew point humidifier (Arbin Instruments, USA). The dew point humidifier was connected to cooling and deionised water supplies and allowed a precise gas dew point supply temperature to be set. The dew point specific or dry gas is fed to the cell, where it fills the QCM housing chamber (which is constantly replenished at a rate of 100 ml min^{-1}). The gas then continues through the chamber and is subsequently vented.

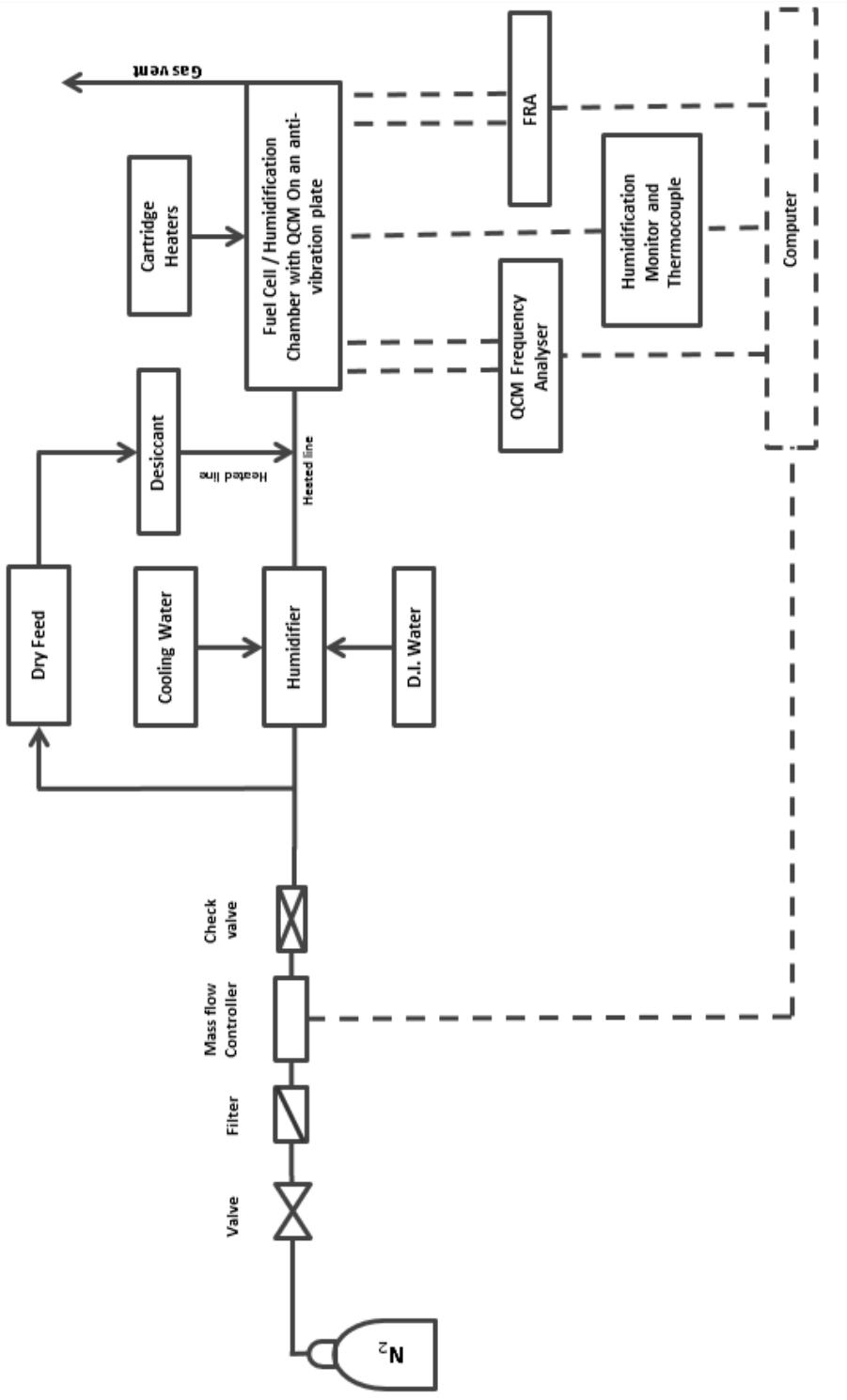

Figure 24: 'Base-rig' set up.

It was found that microbalances are not only very sensitive to the smallest change in just their operating environment, but also from noise in the room (such as electrical interference or something as simple as a slamming door), thus any movement or vibration of the rig could render the experimental results useless. Therefore, the cell was grounded and situated on an anti-vibration plate to nullify the effect of any external interference.

The QCM response is recorded in one of two ways depending on the investigation under consideration:

- Active oscillation – The QCM is connected to a Quartz Crystal Microbalance Analogue Controller – QCM200 (Stanford Research Systems, USA). The QCM200 records the resonant frequency changes (0.1 Hz resolution) to a LabView program via an RS-232 port to the lab computer.

- Passive Oscillation or crystal admittance spectroscopy (CAS) – the QCM is connected to a Solartron 1260A impedance / phase gain analyser. The impedance analyser works as described in Section 2.5 and records the subsequent impedance / admittance using ZPlot and ZView software through the GPIB ports to the lab computer. In generating the admittance profiles, ZPlot linearly scans a frequency range defined by the resonator's resonant frequency (determined through active oscillation), collecting 400 points with a 1 s integration time.

In each case, 0.25 mm diameter, 99.99+% purity platinum wire (Goodfellows, UK) was used for the electrical connections in order to induce a potential over the QCM. Platinum weave mesh (open area 65%, wires / cm: 32 × 32, 0.06 mm diameter, 99.9 % purity) was also used to make electrical connections to the QCM bottom electrode.

3.3.2.1. The Cell (humidification chamber)

Figure 25 shows the cell in more detail. It was designed in-house and has been developed to simulate an adaptable pseudo fuel cell capable of a range of operating environment and comprises a gas inlet and outlet, cartridge heaters, a thermocouple and humidification probes. The cell design allows for very versatile operating conditions to be employed, such as temperature, humidity and gaseous environment.

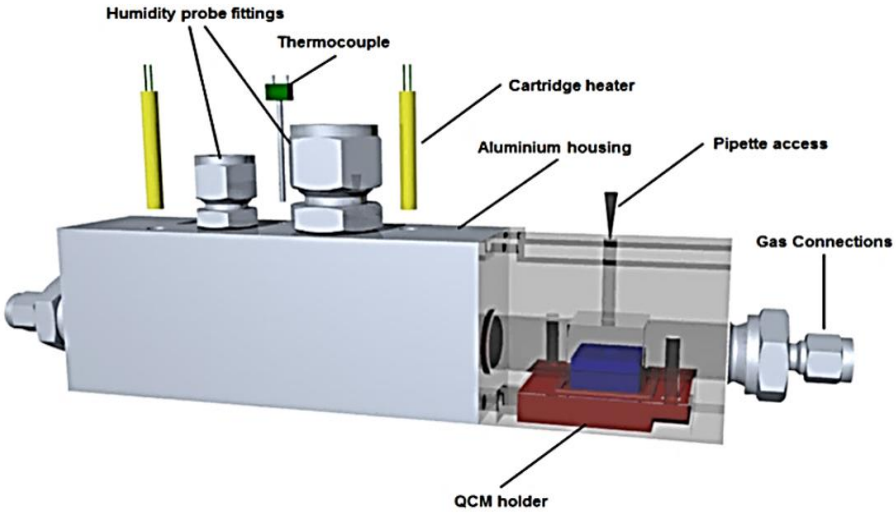

Figure 25: The fuel cell humidification chamber / cell. The QCM is housed within the holder in the translucent section to the right of the image.

The temperature within the cell is maintained using two cartridge heaters and a thermocouple connected to an accurately tuned PID controller (Eurotherm, UK). The cell is made of aluminium to ensure that the heat provided from the cartridge heaters is efficiently distributed to the microbalance – this was confirmed using sticky thermocouples placed on the microbalance surface and temperature profile developed using a thermal imaging camera.

The gas inlet and outlet to the cell are discussed earlier in Section 3.3.2 and allow nitrogen (and / or air – Section 3.3.4.3) to be supplied to the cell at a range of relative humidities from the mass flow controllers. Figure 25 also shows the fittings for the humidity probe (Vaisala, Finland) used to monitor the system's relative humidity.

Finally, the microbalance holder can be seen in the translucent section of the cell in Figure 25 and this is further discussed in Section 3.3.2.2. The translucent section of the cell doubles as the casting bay and contains an access point for *in-situ* electrolyte casting via micro-pipette as described in Section 3.3.3.

3.3.2.2. Microbalance Holder

Many commercial microbalance holders and experimental prefabricated set-ups exist on the market. These well-tested pieces of equipment offer stable frequency analysis and allow mass monitoring for a range of general applications. However, to understand the *in-situ* analysis and the fundamental processes occurring in a novel system such as this, a new rig and non-intrusive microbalance holder had to be developed to assimilate the conditions under which these interfacial phenomena occur. Figure 26 shows the QCM holder developed for this investigation which is housed in the cell as shown in Figure 25 and Figure 27. The holder was designed and manufactured in-house using drawing software (Rhino, UK) and rapid prototyping CNC machines to execute. The holder was originally cut from PTFE; however, this design was rapidly changed and the holder was instead manufactured from one piece of unfired pyrophyllite as shown. The PTFE holder whilst excellent in holding the crystal in place and providing good electrical connections through a combination of platinum wire and mesh had one massive drawback; its excellent insulation properties. As the chamber and feed gas heated up, the holder maintained a much lower temperature and hence promoted water condensation from the humidified gas stream. The condensation of water onto the holder led to a combination of water on the QCM surface as well as an increased level of moisture near the QCM and hence produced a local relative humidity higher than the rest of the chamber leading to increased water loading on the crystal surface at seemingly low relative humidities.

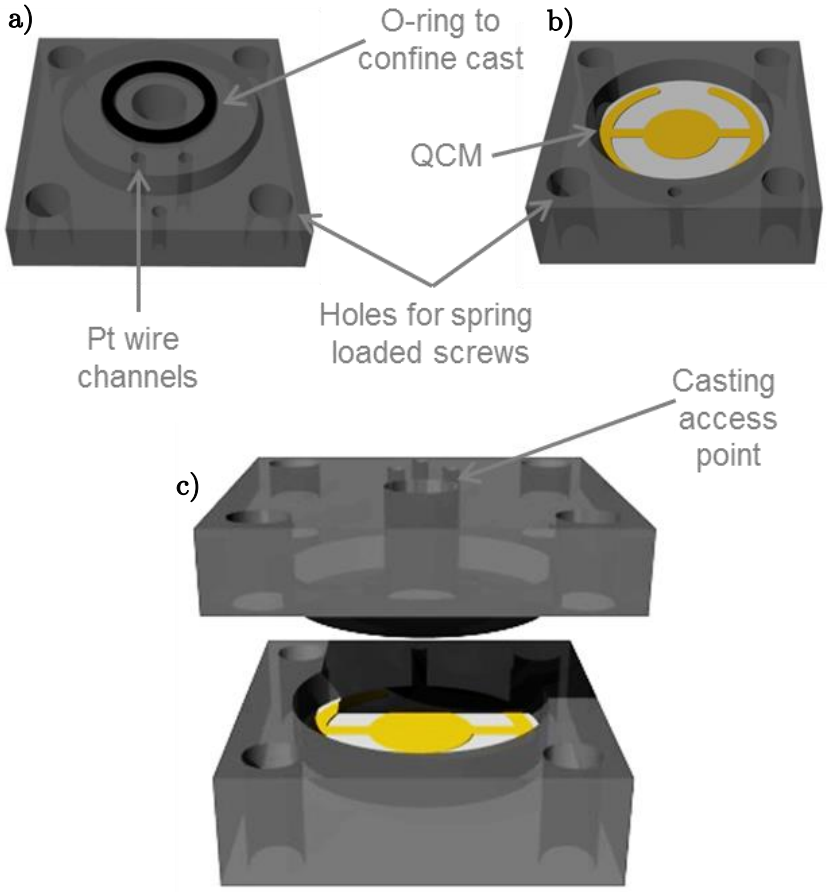

Figure 26: Schematic of the final iteration of the QCM holder: a) shows the top section of the holder, b) the bottom section with the QCM and c) the complete holder.

Pyrophyllite has more similar heating properties to the aluminium cell than the PTFE and therefore does not cause unexpected water condensation, giving more accurate and stable results of the electrolyte's water uptake. Figure 26a, b and c show the top, bottom and full schematic of the pyrophyllite QCM holder respectively.

The holder shown in Figure 26 was developed after several iterations. This was a direct result of understanding the energy trapping phenomenon [2, 133] practically and developing a holder that would have minimal effect on the microbalance's operation. The holder was extensively tested and modified to its final design as shown in Figure 26 in order to minimise the effect

of static capacitance; a factor present in all systems from the resonator holder.

In the final design shown in Figure 26, the top and bottom pyrophyllite sections of the holder are drilled in each corner to allow four spring loaded fasteners to attach the top and bottom of the holder securely to the base for operation within the cell as shown in Figure 27. This ensured the QCM was held firmly and with equal pressure from each side reducing static capacitance, improving electrical contact and maintaining clamping pressure throughout the study. The Pt wire channels shown in the design allow Pt wire connections between the analysis machinery and the top and bottom electrodes of the QCM. The electrical connections were also developed over somewhat of an iterative process, beginning with coiled platinum wire in a spring formation loosely connecting to the electrodes to spot welding and finally using a combination of platinum wire and spot welded Pt mesh.

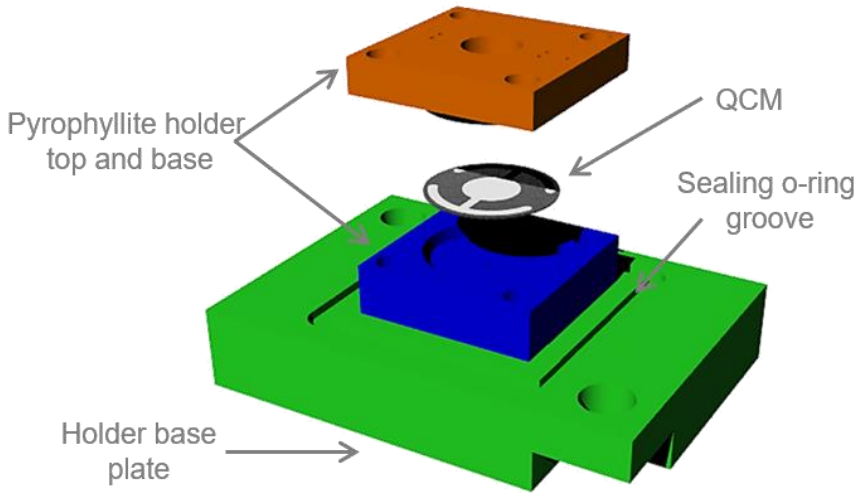

Figure 27: The holder shown in its assembled form including the base plate for mounting into the cell.

The central hole coupled with the O-ring in the top section of the holder allows only the 6 mm central electrode region of the QCM to be in contact with the operating atmosphere. This hole also provides access for the films to be cast on the microbalance *in-situ* as described in Section 3.3.3. The

implementation of the O-ring also allows continuity across all experiments as the cast ionomer is confined to a specific area and reduces the risk of spurious radial mass loading which produces non-ideal frequency responses and also allows accurate determination of the film thickness.

3.3.3 Electrolyte Casting

This project uses two electrolytes to simulate the interfacial interactions of the acidic and alkaline electrolytes; Nafion D1021 dispersion (DuPont, USA) and the AS-4 AAEM (Tokuyama, Japan) respectively. The known properties of each electrolyte are shown in Table 2.

Table 2: All known properties for the Nafion and Tokuyama dispersions

	Nafion D 1021	Tokuyama AS4
Dispersion Components (Wt.%)	Polymer: 10 – 12% Water: 87 – 90% Dimethylsulfoxide (< 1%) Mixed Ethers and other (< 1%)	4.29% Solid mass
Density (g cm^{-3})	1.8	0.94
Equivalent weight (g mol^{-1})	1100	-
IEC	0.00091	0.00180
Viscosity at 25 ^{o}C (mPa s)	2 - 10	-

To develop *in-situ* resonators with properties similar to those of the electrolyte under investigation, each electrolyte dispersion was cast onto the QCM's double-anchor electrode surface. The cast was confined to the centre of the double-anchor electrode using the holder discussed in Section 3.3.2.2. This allowed continuity across all experiments as the cast is confined to a specific area; hence reducing the chance of spurious radial mass loading that produces non-ideal responses.

Initially, electrolyte casting was carried out *ex-situ* in an open-air environment using a micro-pipette as shown in Figure 28 and allowed to passively dry before being placed in the cell.

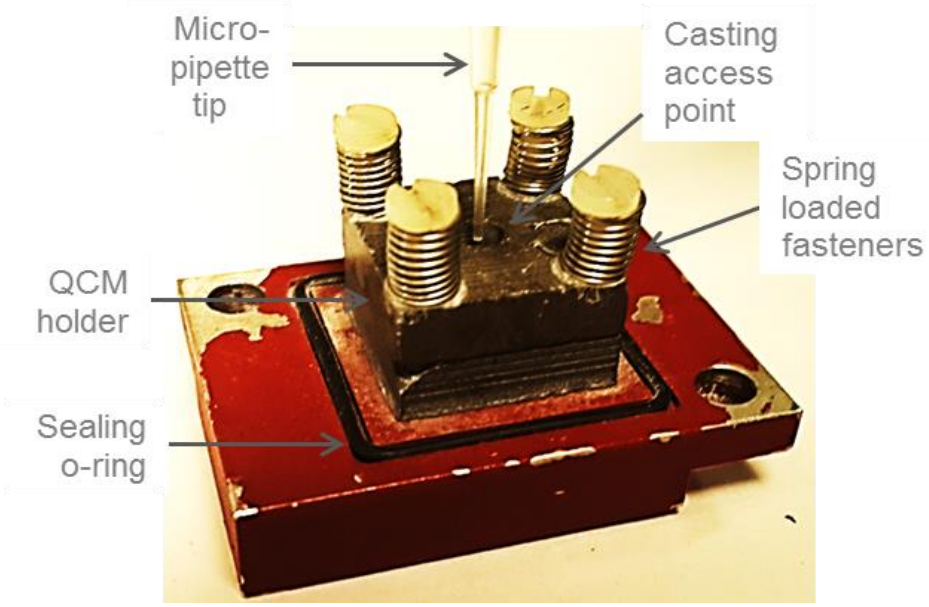

Figure 28: Initial *ex-situ* casting process by micropipette directly onto the microbalance surface.

However, the literature presented in Section 3.2.4.3 indicated that the AS-4 ionomer with [R_4N^+] cationic headgroups would be affected by the interaction of atmospheric CO_2 within minutes [53, 121, 134]. With the drying process taking up to 20 minutes, an alternative method of applying the cast ionomer in a CO_2-free atmosphere was developed. Figure 29 shows the *in-situ* ionomer casting attachment designed and retrofitted to the original cell design as shown in Figure 25. The adapted *in-situ* casting chamber provided access to a dry 0 % RH nitrogen environment under which the ionomer casting could be conducted under a controlled environment; this method provided repeatable ionomer casting and ensured the micro-pipette was always held at the same height and angle above the microbalance.

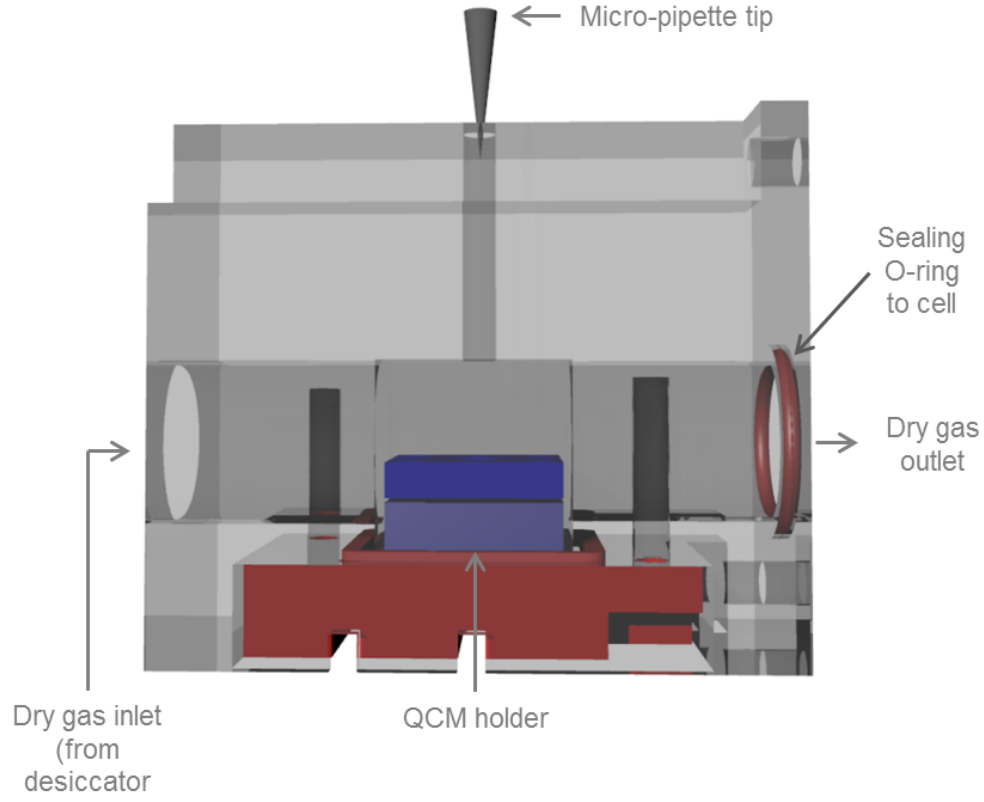

Figure 29: *In-situ* casting chamber – retrofitted into the translucent section of the cell as shown in Figure 25

The dilutions of both Nafion D1021 and the AS-4 AAEM are provided as thick viscous dispersions (datasheet available in Table 2). The initial electrolyte casting attempts in which 1 μL of (either) dispersion was added directly to the microbalance electrode's surface resulted in large frequency fluctuations away from the (expected) resonant frequency; ultimately culminating in microbalance failure, due to overloading. Coupled with the crystal's inability to oscillate near its resonant region, it was also noted that the electrolyte did not disperse across the exposed microbalance area upon drying as shown in Figure 30a. The cast area in this case was confined to the electrolyte drop – this is likely due to high surface tension of the dispersion. This phenomenon made it impossible to accurately determine the ionomer

thickness and resulted in an interaction with the operating environment that could not solely be attributed to the ionomer's properties.

The microbalance failure was likely due to operation in a highly viscous medium below its critical temperature (Section 2.4.2 and 4.4.1.2); the electrolyte dispersion therefore required dilution. Diluting the electrolyte provided a two-fold benefit - ensuring the microbalance operation under (wet) electrolyte loading as well as reducing the dispersion surface tension and thus allowing it to spread evenly across the entire O-ring confined area on the microbalance's double-anchor electrode.

The Nafion electrolyte dispersion which is supplied suspended in deionised water was further dispersed in methanol whilst the Tokuyama dispersion was further diluted with isopropanol (IPA). The suspension media were chosen to help distribute the ionomer evenly over the crystal surface and promote quick evaporation whilst not affecting the ionomer structure or stability. The dilution methods produced better cast results that provided visual uniformity covering the centre electrode as shown in Figure 30b and have also been inspected in Section 3.4.1.3 using SEM to ensure the thin film is evenly distributed preventing misreported thicknesses and spurious radial mass loading on the microbalance.

During the casting process, diluted dispersions of each ionomer were cast *in-situ* to the microbalance double anchor electrode surface via a micro-pipette under a stream of 100 ml min^{-1} 0% RH N_2. All ionomers were cast at 0 % RH to eliminate the water content contribution to the ionomer thickness calculations. The Nafion ionomers were cast and operated at 80 ^{O}C, whilst the AAEM ionomers were cast at 55 ^{O}C to limit the effect of nucleophilic displacement and subsequent membrane degradation as discussed in Section 3.2.4.3 [51, 53, 78]. The composite resonators (which refer to the ionomer coated microbalances) were subsequently held at either 80 or 55 °C for 1 hour after the cast was applied to allow the ionomer to anneal.

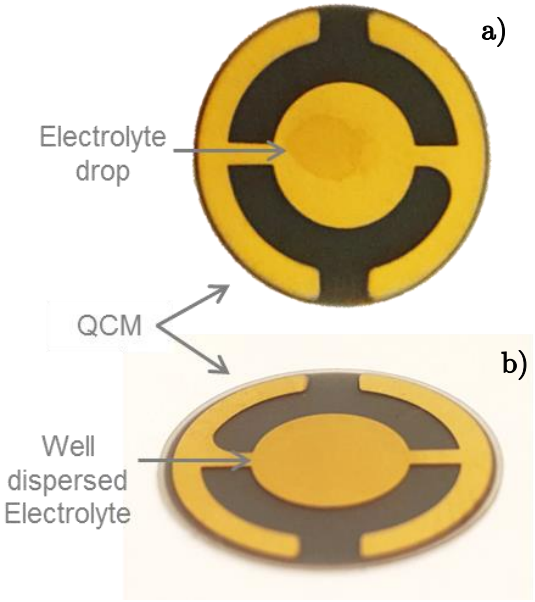

Figure 30: Casting success for a a) non-diluted ionomer dispersion which resulted in a poorly distributed ionomer layer and b) diluted ionomer dispersion showing a significantly more uniform, well-confined ionomer layer

The dry membrane thickness can be determined using the Sauerbrey Equation (2) and Equation (23):

$$t_i = \frac{m_i}{A\,\rho_i} \tag{23}$$

Where t_i is the ionomer thickness; m_i is the ionomer mass (determined from the Sauerbrey Equation); A is the cast area; and ρ_i the density of the recast ionomer.

As with other thin film ionomer studies [80, 85, 86, 135], this study uses thin-film ionomers with thicknesses ranging from 20 nm to 100 nm. Ionomers within this range were chosen in order to minimise contribution from internal water diffusion, but also to ensure they were well within the operating range of the resonator. This was an important factor as this study involved subjecting the composite resonator to conditions which would cause ionomer loading (water and carbonate ions for example), and maintaining a suitable

Q-factor and ensuring the composite resonator was able to fulfil the standing wave condition was therefore of critical importance.

CAS was implemented throughout this study to elucidate the phenomenon occurring on the composite resonators' interface. However, it was also used to ensure the composite resonator was always able to fulfil the standing wave condition and maintain a high Q-factor as discussed in Section 2.2 [136].

3.3.4 Investigation of Specific Operation and Alterations

This section discusses the nuances of the rig operations and alterations for each investigation within this study. All alterations from the original base rig setup shown in Figure 24 have been discussed in the relevant sections below and have been further highlighted using red boxes for ease of differentiation.

3.3.4.1. Water Uptake and Hydration Mechanisms

The rig shown in Figure 24 was specifically developed to study the water uptake, loading mechanisms and swelling properties of both thin-film Nafion and a commercially available AAEM ionomer through a range of humidities using the QCM and CAS.

An ionomer's water uptake (λ) is defined as the number of moles of water adsorbed per mole of functional group present (mol/mol) – it is electrolyte specific. It provides a useful way to directly compare the water sorption properties of different membrane types and thicknesses; it is calculated using Equation (24) or (25) depending on the available ionomer information.

$$\lambda = \frac{m_w M_o}{m_d M_w} \tag{24}$$

Where M_w and M_o are the molecular weight of water and the ionomer's exchange sites respectively and m_d and m_w are the dry and wet mass of the electrolyte at a given humidity.

However, in the case of the AS-4 ionomer the chemical makeup and thus the number of moles of functional group present per mass of membrane material is not available. However, another method to determine the water uptake exists through the membrane's ion exchange capacity (IEC), as shown in Equation (25). This method has been verified by calculating Nafion's water uptake using both methods [114].

$$\lambda = \frac{\varphi}{IEC \times 100 \times M_w} \tag{25}$$

Where φ is defined by:

$$\varphi = \frac{m_w - m_d}{m_d} \times 100 \tag{26}$$

The IEC represents the conducting ion content per gram of polymer (mmol g^{-1}) [53], m_w the molecular weight of water m_d and m_w represent the dry membrane mass and water mass in the membrane at a given humidity, respectively [114].

Thin film ionomers of both Nafion and AS-4 were cast with a thickness ranging from $20 - 100$ nm, supported on a QCM electrode. The Nafion and AS-4 composite resonators were exposed to nitrogen under a range of humidities and the consequent water uptake values and swelling characteristics determined through a combination of passive and active oscillation methods. Active oscillation measurements, in which the composite resonator's frequency response is measured when a specific voltage is applied, were carried out using a QCM analogue controller (QCM200, Stanford Research Systems, USA). The admittance response is achieved using a Solartron 1260A impedance / phase-gain analyser.

3.3.4.2. Degradation

This investigation experimentally explored how specific hydration levels affect the degradation mechanisms of the AS-4 ionomer using QCM composite resonators. In-line mass spectrometry was also used in this investigation for off-gas analysis to complement the QCM results and to further elucidate the importance (and limitations) of cation and hydroxide ion solvation for the stability of an AAEM ionomer.

During this investigation, the resonator is initially actively oscillated during the casting process to determine the ionomer thickness, as described; it was subsequently passively oscillated to determine the effect of operation at elevated temperatures through a range of relative humidities.

After annealing, the composite resonator is passively operated at 55°C until it attains a stable frequency. The operating temperature is then ramped and held at 65°C for 45 mins, it is then cooled back to 55°C. This investigation is repeated through a range of relative humidities with a freshly cast 100 nm composite resonator for each run. CAS data is recorded before and after the microbalance temperature ramp and the corresponding response in the system's frequency and viscoelasticity is measured.

The apparatus and rig design used throughout this investigation are shown in Figure 31. The alteration to the original rig is minimal for this investigation and includes the addition of a mass spectrometer (Hiden, UK) that was used to analyse the components of the exhaust gas exiting the humidification chamber, to evaluate the extent of thermal degradation occurring.

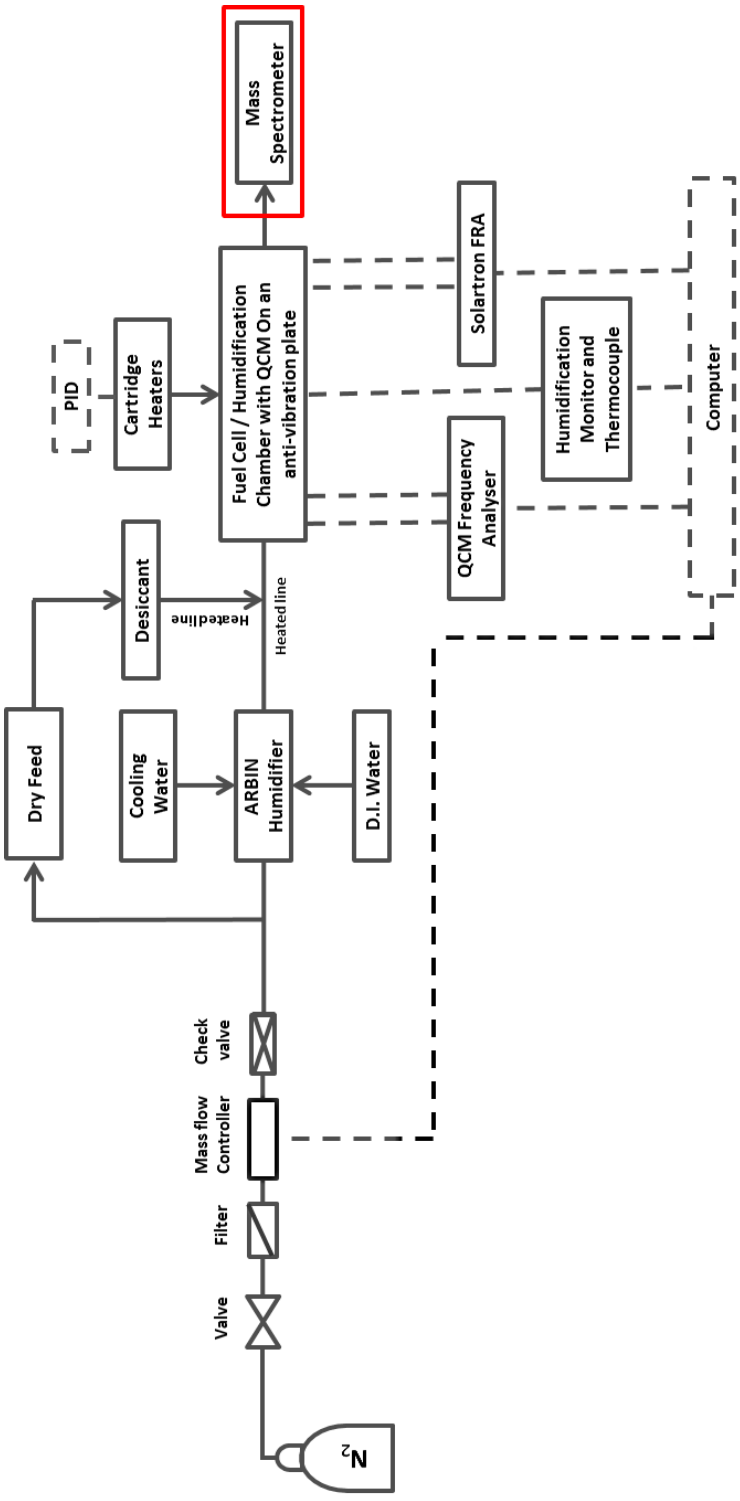

Figure 31: Degradation investigation rig set up. The red box shows the additional mass spectrometer added to the system to provide off-gas analysis.

3.3.4.3. Carbonate Ion Interaction

The carbonate interaction investigation examined how reactant humidity (and hence membrane hydration) affects how CO_2 interacts with the AS-4 ionomer. This investigation also employed an *ex-situ* analysis of how Tokuyama's A-201 sheet membrane's change in resistance with exposure to air (as a source of CO_2). It is then compared with the change in viscoelastic properties of a thin-film ionomer, both at steady state and as a function of humidity. The effect of CO_2 on the membrane material as a function of hydration was also analysed.

The base-rig was altered for the *in-situ* carbonate interaction analysis by the introduction of an air input (containing CO_2) as shown in Figure 32. The air cylinder (BOC, UK) was attached to a valve, filter, mass flow controller and check valve and added to the system using a T-piece. After annealing, the 65 ± 4 nm composite resonators continue to operate under a nitrogen stream at 100 ml min^{-1} and 55°C; the same dew point humidifier was used to attain the system's relative humidity and is specific for each sub-investigation. The frequency was measured actively, and once the composite resonator achieved a stable frequency, the nitrogen was switched to a stream of air (BOC, UK) at the same flow rate and RH with ~ 400 ppm CO_2 concentration.

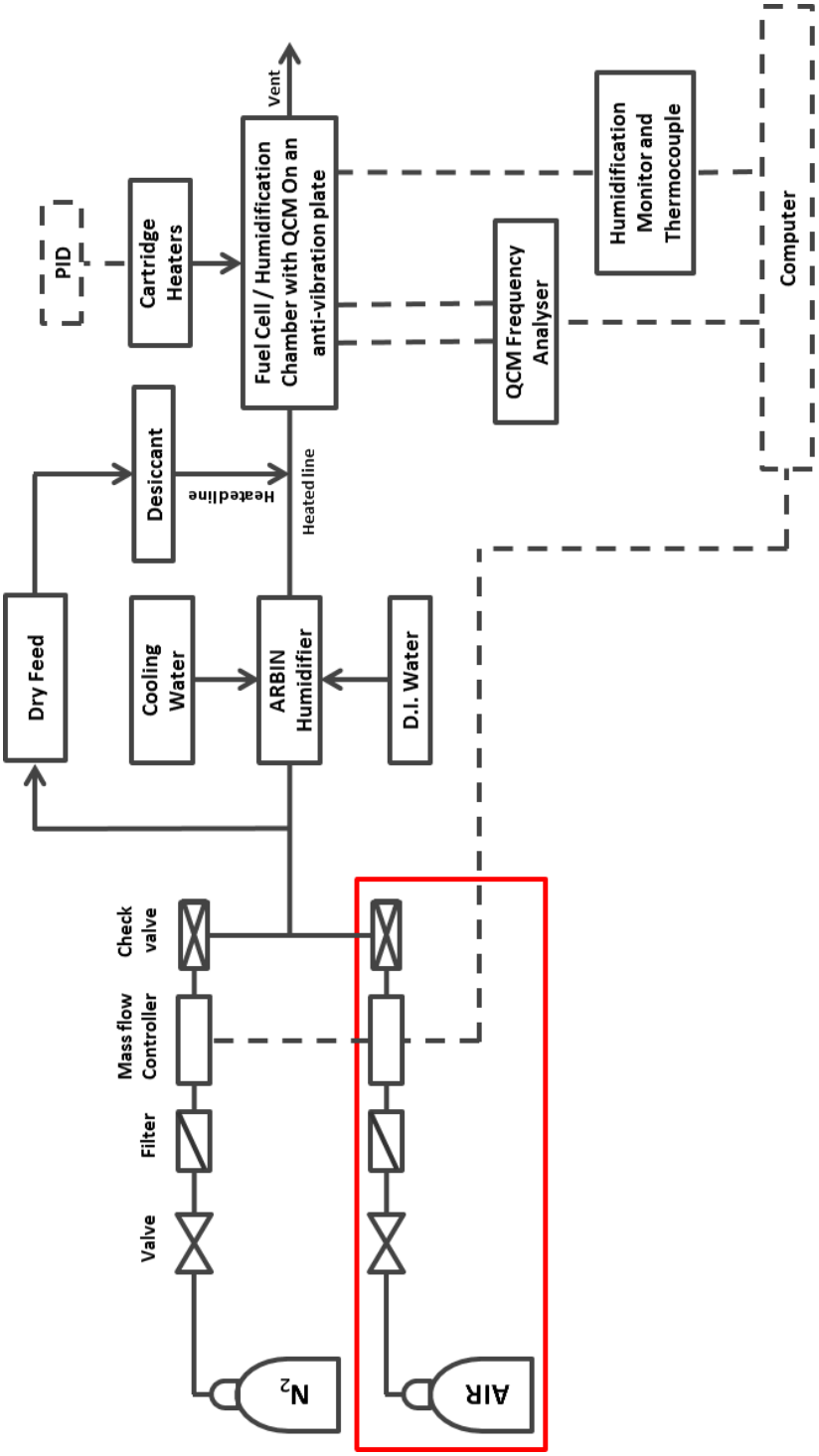

Figure 32: *In-situ* carbonation rig. The red box indicates the additional air inlet added to provide atmospheric CO_2 to the ionomer.

A new rig was developed for the *ex-situ* carbonate ion interaction analysis and is shown in Figure 33. For this part of the investigation a commercially available, proprietary alkaline anion-exchange sheet membrane (A201, Tokuyama, Japan) was operated in an in-house fabricated closed-cathode fuel cell (5 cm^2 active area), with nitrogen running over both sides at a range of humidities. The A201 membrane was soaked in 1 M KOH for 5 hours to convert it from the Cl^- form to the OH^- form; it was then rinsed in deionised water, pat-dried and inserted into the cell where it was held under stable conditions at 55 °C with 100 ml min^{-1} of N_2 passing over each side. Using electrochemical impedance spectroscopy (EIS), the high-frequency intercept with the real axis of the Nyquist plot was used to determine the resistance of the system. Once the EIS high-frequency intercept was constant, the supply of nitrogen was switched to air (at the same relative humidity), and the corresponding high-frequency measurement recorded until stable. This process was repeated at a range of RHs delivered the dew point humidifier (Arbin, USA).

The membrane's transient high-frequency intercept was measured using an IviumStat (Alkatek, UK). Impedance spectroscopy was measured potentiostatically at open circuit voltage, 0 V, with AC amplitude of 10 mV; the amplitude was the smallest system perturbation which initiated a clear current response. The high-frequency impedance was measured at 35 kHz every second; determined by performing impedance sweeps between 100 kHz and 100 Hz to find the high-frequency intercept before the introduction of air to the system. The impedance sweep was also performed at the end of each experiment to confirm a negligible shift in the high-frequency intercept.

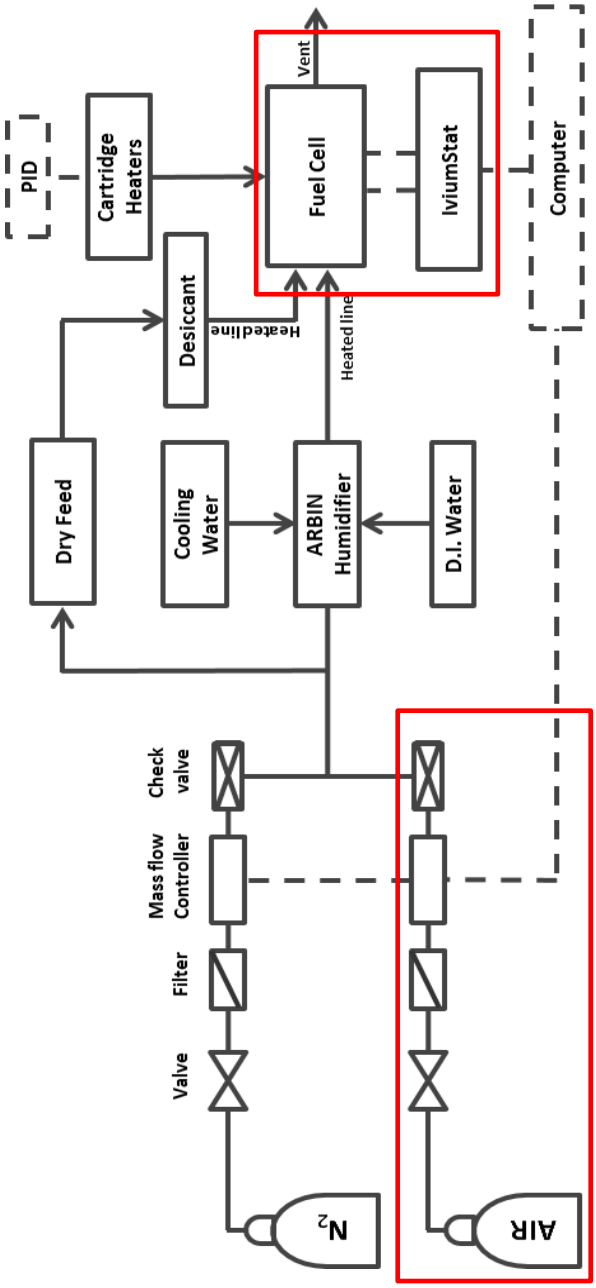

Figure 33: *Ex-situ* carbonate interaction rig set up

3.4 Results and Discussion

This Section initially presents a QCM (and by extension, rig and equipment) feasibility study for application in this study followed by the results from the investigations proposed in Section 3.2.5.

3.4.1 Feasibility Studies

Before commencing with any investigations, it was first important to assess the developed rig and determine its suitability for microbalance measurements. A microbalance measures frequency changes within a system that can relate directly to precise changes on its electrode surface; however to do this accurately (Section 2.4.3 – non-ideal responses) they must oscillate without interference from any source other than that being investigated. To this end, the rig setup and stability, as well as the choice of resonator, was of paramount importance in this investigation.

Whilst there are several commercially available BAW resonators that could be applicable to this study, the QCM was chosen for the reasons discussed in Section 3.3.1. However, to ensure the QCM's feasibility, it was first tested under the investigative range of temperatures and humidities employed during this study.

Whilst extremely accurate and generally stable in oscillation, the use of a piezoelectric microbalance raises issues in terms of comparability and repeatability. As each microbalance contains slight variations, no two microbalance resonant frequencies are ever the same. Though microbalances often produce very similar responses to conditions and thus provide a visual comparison between resonators, the physical numbers often do not match. Thus, frequency shifts experienced during experimentation are often reported by the change in a frequency from a specific point. This work will present resonant frequency shifts using the following relationship: $\Delta f / f_{t0}$ where Δf represents the change in frequency at any given time from the frequency at time '0' (f_{t0}); the resultant frequency shift is reported in parts per million (ppm). Presentation of results in this manner still produces the same shape distribution as the measured frequency data but on a smaller, more comparable scale and is common for work of this nature [137, 138].

3.4.1.1. The Effect of Temperature

The QCM is used in this study as a composite resonator to monitor a range of effects on both the Nafion D1021 and the AS-4 AAEM ionomers. It is well reported in the literature that ideal operating temperatures for these electrolytes are 80 ^{O}C and 55 ^{O}C respectively [51, 139]. The QCM has proven stable operation at temperatures up to 300 ^{O}C above which it presents a significantly deteriorated temperature coefficient up to its Curie temperature (573 ^{O}C) where it loses its piezoelectric properties [137, 140]. Figure 34 shows the frequency response for an unperturbed (no ionomer layer) QCM operating between temperatures of 35 ^{O}C and 80 ^{O}C. It shows the QCM's frequency response during both the heating and cooling process at 0% relative humidity under a 100 ml min^{-1} flow of nitrogen.

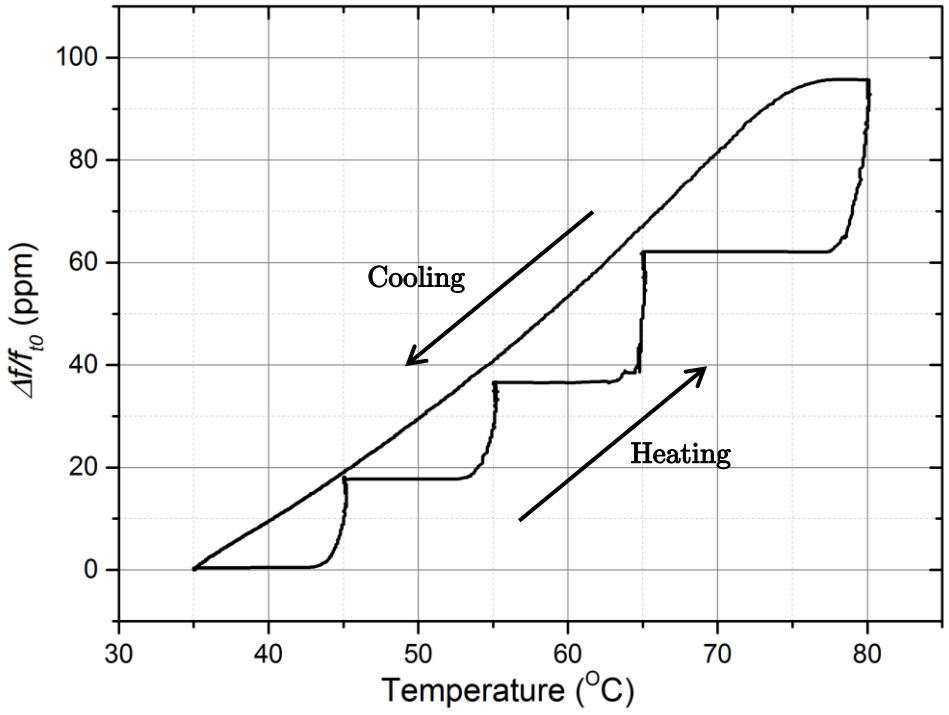

Figure 34: The effect of temperature on a 6 MHz crystal microbalance's resonant frequency during heating and cooling

The QCM is heated from 35 ^{O}C to 80 ^{O}C in 10 ^{O}C ramp steps as shown; the operating temperature is held until the resonator's oscillation is stable. The

heating profile shows a linear correlation between the microbalance's resonant frequency and operating temperature. Figure 34 also indicates that at elevated temperatures, the shift in resonant frequency increases with increasing temperature; when the temperature is ramped from 35 ^{O}C to 45 ^{O}C, the resonant frequency shift is 17 ppm compared to 32 ppm when the temperature is ramped from 65 ^{O}C to 80 ^{O}C. This is likely a result of lattice excitation and the consequent temperature coefficient variations associated with this QCM's angle of cut. The following investigations are carried out at distinct temperatures and importantly it can be seen that when operating at each of the above temperatures, the microbalance oscillation is stable – this is further explored in Figure 35.

In Figure 34 as the microbalance cools from 80 ^{O}C to 35 ^{O}C, its resonant frequency begins to decrease linearly until it is held at 35 ^{O}C. It returns from a 96 ppm shift to its original operating frequency (0 ppm) at 35 ^{O}C; indicating that during this operating range, the QCM does not exhibit signs of hysteresis.

Hysteresis is often a result of a mass deposition (or degradation) or structural damage of the piezoelectric material; however, the results obtained here (and confirmed by [2]) shows that quartz can operate within these operating conditions without structural damage.

Figure 35 further explores the microbalance's operation at the investigative temperatures of both 55 ^{O}C and 80 ^{O}C to assess the frequency stability or 'noise' experienced by the microbalance during operation.

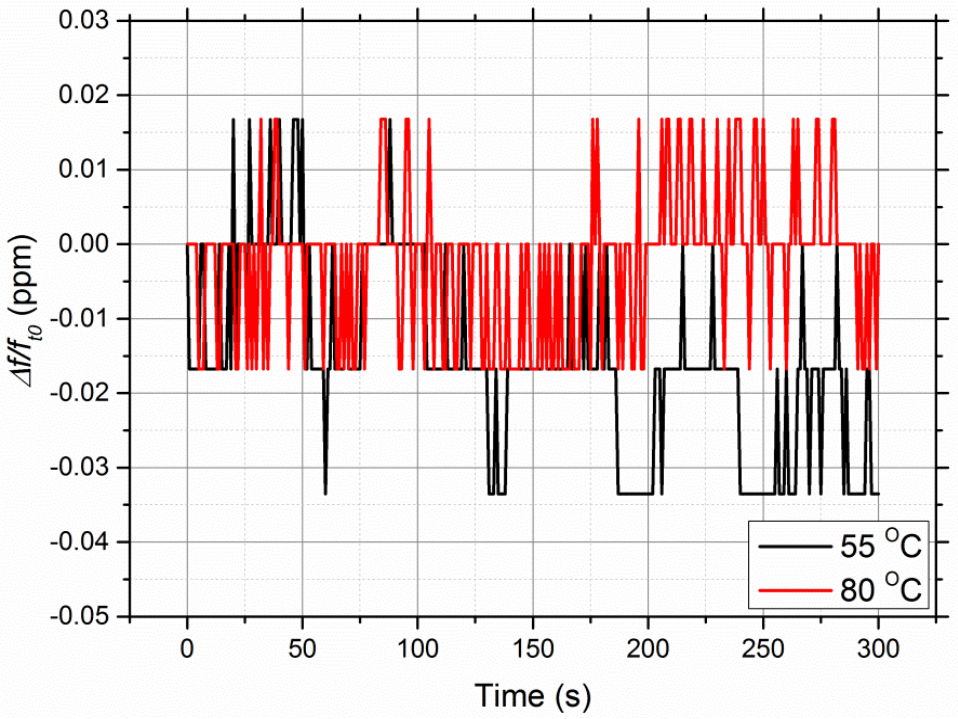

Figure 35: Graphical representation of the magnitude of noise experienced for an unperturbed microbalance operating at 55 °C and 80 °C for 5 minutes at resonant frequency

The stability / noise response was monitored for an unperturbed microbalance when operating at both 55 and 80 °C as shown in Figure 35. The microbalance was inserted into the cell in the base rig configurations shown in Figure 24 where it operated for 5 minutes at a specific temperature with a 100 ml min^{-1}, 0% RH nitrogen stream flowing through the cell.

The maximum frequency deviation exhibited in either study was ± 0.03 ppm (0.2 Hz) relating to a 7×10^{-10} g mass change on the electrode surface. This negligible frequency / mass shift can, therefore, be considered the limitation in resolution of the system.

3.4.1.2. The Effect of Humidity

Many elements of this study required operation of the composite resonator under humidified conditions. As with temperature, it was important to understand how the microbalance itself was affected, if at all by humidity and whether the experimental responses obtained were as a result of the electrolyte behaviour or because of the microbalance operation.

The QCM has a proven application in many *in-situ* monitoring environments including use as a humidity sensor [141-143]. However basic published literature on the effect operational humidity has on the QCM's resonant frequency stability is not available, and thus is explored here.

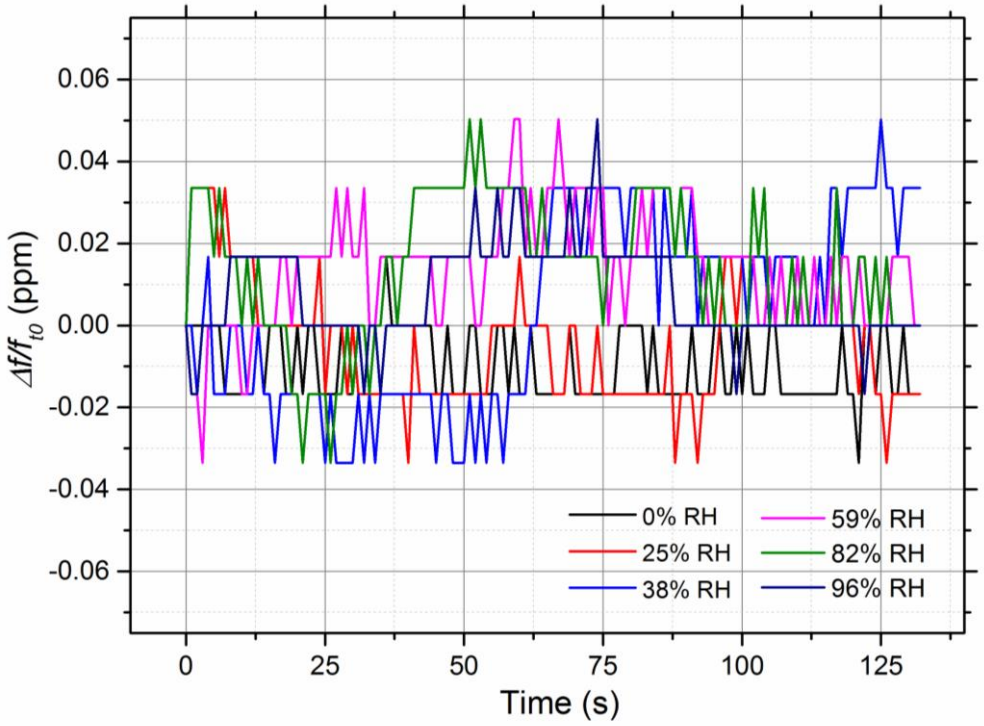

Figure 36: QCM frequency stability when held at a range of relative humidities at 80 ^{O}C and under a flow of 100 ml min^{-1} of N_2

Figure 36 shows the frequency response in ppm of a microbalance operating in a 100 ml min^{-1} flow of nitrogen at a range of relative humidities (0 – 100 %) at 80 ^{O}C within the base rig setup shown in Figure 24.

This investigation was conducted by maintaining the QCM's operating temperature at 80 ^{O}C (to assimilate the harshest available conditions that will be faced during this study) within the cell whilst varying the dew point humidifier settings to achieve the investigative range of relative humidities.

As with temperature, the QCM exhibits very stable frequency responses when operating through the range of relative humidities. When operated at the RHs shown in Figure 36, the frequency has a maximum deviation of $\pm$ 0.04 ppm (0.3 Hz); this small fluctuation can once more be considered as the limitation in resolution of the system.

After the final investigation at 96% RH, the humidified nitrogen stream was replaced by a 0% RH flow (100 ml min^{-1}) and the microbalance was left to re-equilibrate overnight. As the humidification cell's relative humidity returned to 0%, the microbalance's resonant frequency too returned to that of the original value (0 ppm shift). Again, the resonator indicated no sign of hysteresis; and thus confirms the microbalance's ability to operate within a humidified environment.

The above two subsections have shown that the QCM is able to function with a high degree of stability when operating in the base experimental rig setup and under the investigative range of temperatures and humidities for this study. The resonator's ability to operate efficiently with the ionomer surface development (creating the composite resonator) is explored in Section 3.4.1.3.

3.4.1.3. Electrolyte Casting

In developing an *in-situ* electrolyte sensor, the composite resonator must exhibit identical properties to that of the electrolyte under test as discussed in Section 3.3.3.

This Section describes the development of an *in-situ* electrolyte – composite resonator, in which ionomer dispersions of electrolyte were applied to the crystal microbalance electrode surface via micro-pipette as discussed in Section 3.3.3. Once applied, both Nafion and AS-4 electrolyte dispersions dry and anneal in a stream of 0% RH nitrogen to reveal a cast electrolyte on the QCM electrode – the composite resonator.

The dispersed electrolytes were added to the microbalance in different volumes to achieve a variety of electrolyte thicknesses on the QCM. In each case, a specific volume of diluted dispersion was added to the microbalance and allowed to dry and anneal for 1 hour. The resulting mass deposition could then be calculated using the Sauerbrey equation and the subsequent ionomer thickness calculated from the confined cast area. This method has proved extremely reproducible and provided several composite resonators with similar thickness electrolytes. Table 3a and b show examples of the Nafion and AS-4 ionomer thicknesses used in parts of this investigation respectively.

Table 3: Frequency data for cast a) Nafion and b) AS-4 ionomers and their corresponding mass changes and subsequent thickness'

N.o.	Frequency change (Hz)	Nafion mass (µg)	Nafion Thickness (nm)
1	484	1.69	33
2	868	3.04	60

N.o.	Frequency change (Hz)	Tokuyama mass (µg)	Tokuyama Thickness (nm)
1	181	0.63	23
2	294	1.03	39
3	763	2.67	100

To confirm the casting procedure's accuracy, a rough calculation using crude estimates for the dilution ratio of Nafion (1 part Nafion dispersion (10% wt polymer – Table 2) to 100 part Methanol) is conducted below to validate the measured contacting mass.

For this example, consider the 33 nm Nafion ionomer layer; it is cast from 0.1 μL of (1:100) Nafion dispersion yielding a mass content of 1.80 μg. This calculation is based on a Nafion density 1.80 g cm^{-3} and an assumed 10 wt% Nafion polymer content within the supplied dispersion. Compare this theoretical calculation to the measured contacting mass on the QCM in Table 3a in which the 33nm ionomer layer relates to a deposited mass of 1.69 μg determined using the Sauerbrey equation. The crude calculation has made several assumptions (such as exactly 10% wt Nafion polymer in the supplied dispersion); however the theoretical and measured masses are accurate to ~ 6% and therefore suggest that the casting mechanism is providing mass depositions within the expected mass ranges.

Unfortunately, without a better understanding of the AS-4 electrolyte dispersion, the same calculation is impossible for the AAEM ionomer; however, the Nafion calculation suggests the validity of the method as a casting process.

It should be noted here, that the measured frequency changes are taken after the annealing process and thus provides the dry film mass and hence validates the use and improves the accuracy of the Sauerbrey equation.

The following study describes the ionomer casting frequency profiles and assesses the composite resonator's operation using crystal admittance spectroscopy.

3.4.1.4. Frequency Response

During the casting process, it was important to record the QCM's initial and final resonant frequencies to determine the cast ionomer thicknesses. However, the highly sensitive frequency cast profiles are also indicative of

the processes occurring on the resonator's electrodes and so further understanding of these profiles provides a means by which to ensure that there were no unexpected processes occurring during the casting procedure.
Figure 37a and b show the cast frequency profile for a Nafion and AS-4 cast ionomer respectively. For this study, the annealing process is not shown and ionomers of roughly 15 nm were attempted to be cast for the purpose of figure resolution.

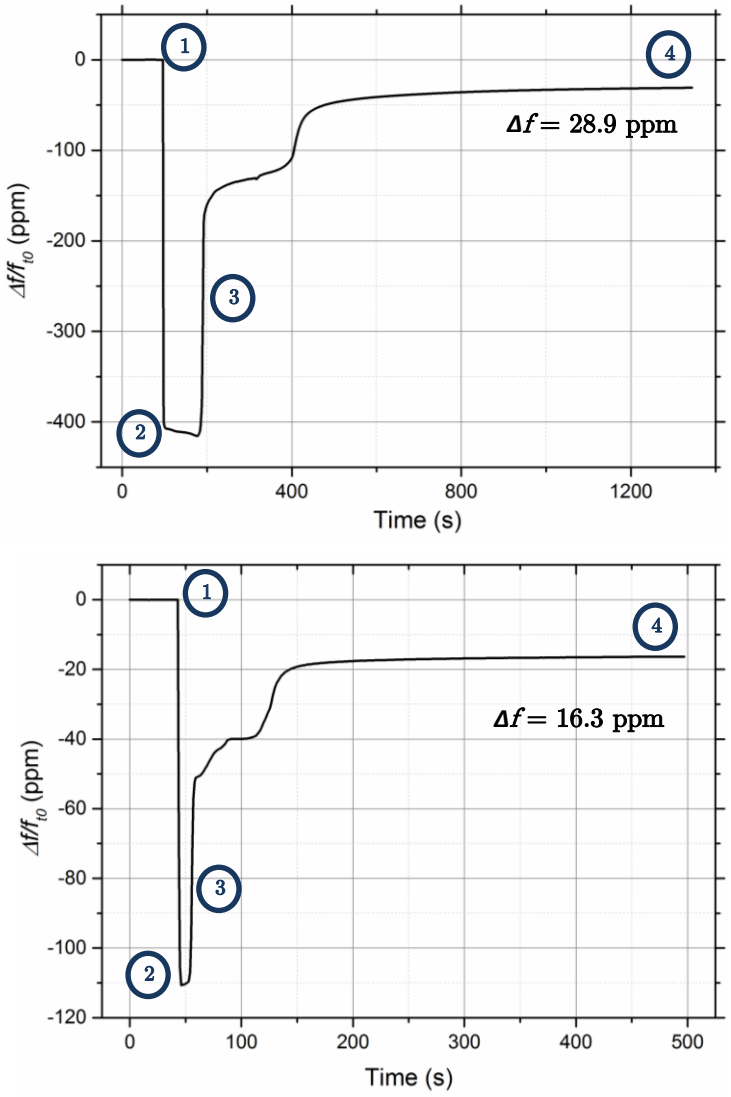

Figure 37: Cast frequency profile for a a) 12.9 nm Nafion ionomer and b) 12 nm Tokuyama AS-4 ionomer. Numbers on the Figure relate to 1) electrolyte application to the microbalance 2) initial rapid dying phase 3) slow drying phase and 4) subsequent new resonant frequency

Both ionomers show very similar cast profiles and the trends observed suggest the following processes (numbers correspond to labels on Figure 37a and b):

1. Stable frequency response under 0% RH N_2 at 100 ml min^{-1}, followed by the application of the electrolyte dispersion via micropipette at point 1.
2. The additional mass of the dispersion to the microbalance surface results in a significant decrease in the frequency of the resonator shown at point 2.
3. However, as the methanol and IPA begin to evaporate from the QCM surfaces, the frequency begins to increase once more, as shown at point 3. The drying phase in both profiles has proven to be multi-step with a quick initial frequency increase as the suspending solutions dry, followed by a slower phase which is thought to be as the trapped solution within the ionomer channels dry.
4. The resulting stabilised frequency is defined as a new resonant frequency as shown at point 4 (albeit normally after annealing).

The frequency difference between the original resonant frequency and the cast resonant frequency (points 1 and 4), can be processed using the Sauerbrey equation to determine the contacting electrolyte mass. The electrolyte thickness can then be determined using Equation (23).

The cast profiles shown in Figure 37 occur at different rates, and this is likely due to the differences in the suspending solution evaporation time and ionomer densities. In order to cast ionomers of ~15 nm thickness, different amounts of Nafion and AS-4 dispersion were added to the QCM. As the Nafion density is roughly twice that of the AS-4 ionomer, twice the dispersion was added to the microbalance surface to produce layers of similar thicknesses as shown in Figure 37. Consequently, with twice the dispersion added to the microbalance not only does the drying profile take longer, but also, the initial contacting mass was larger as illustrated by the Δppm recorded at point 2 in Figure 37.

3.4.1.5. Cast Ionomer Homogeneity

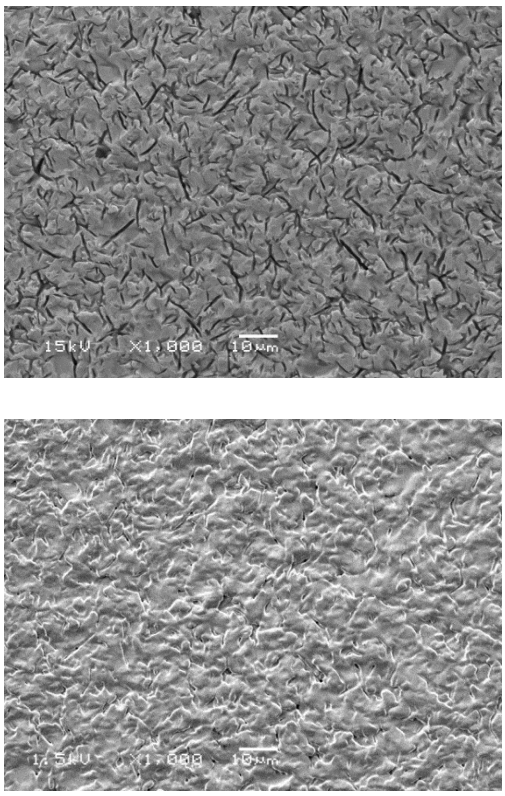

Figure 38: SEM ionomer homogeneity scans for a) an unperturbed QCM gold electrode b) a 33 nm AS-4 cast composite resonator

Figure 38 shows the AS-4 ionomer cast homogeneity and indicates that the ionomer dilution disperses evenly over the QCM surface providing consistent layers of homogenous thicknesses. The composite resonator does not show the presence of large ionomer deposits or areas of uncast electrode within the confined electrode area. The even distribution of ionomer not only provides accurate thickness calculations, but also ensures an accurate frequency response from the composite resonator; negating the effect of radial mass loadings.

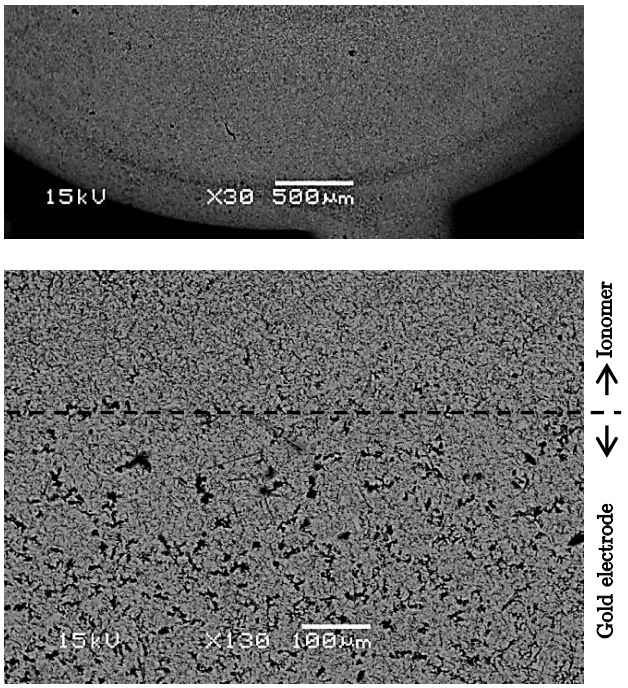

Figure 39: Ionomer cast boundaries on the QCM gold electrode

Figure 39a shows the SEM image for the cast AS-4 ionomer onto the micro-balance double-anchor electrode. At ×30 magnification, a 'ring divide' can be seen between the ionomer cast area and the bare electrode where the O-ring is used to confine the dispersion. Figure 39b shows a ×130 magnification of this boundary edge and shows the difference between the cast and uncast areas on the electrode. It can be seen that the uncast area shows more holes / defects in comparison to the cast area, but most importantly, there is evidence of a clear divide between the cast and uncast area thus suggesting ionomer homogeneity up till the boundary edge.

3.4.1.6. Crystal Admittance Response

Frequency data for the casting processes as shown in Figure 37 are used for indicating an additional contacting mass on the microbalance surface. However, it is only through crystal admittance spectroscopy (CAS) that it is possible to determine not only the type of mass deposited on the crystal surface, but more importantly whether the composite resonator is able to fulfil the standing wave condition (Section 2.2). The CAS process is used throughout this study and is simply demonstrated here.

Figure 40 and Figure 41 a-c show the admittance responses for an unperturbed and subsequently loaded 37 nm Nafion and a 68 nm AS-4 cast composite resonator respectively. These ionomer thicknesses relate to very similar contacting masses (544 Hz and 516 Hz = 1.88 μg and 1.81 μg respectively) and were chosen to highlight the differences in the composite resonator's operation when in contact with almost identical ionomer masses of different viscoelasticities.

In each figure, the black plot represents the uncast QCM's admittance responses and the red plot, the composite resonators admittance response. Both investigations were carried out at 50 ^{O}C under a 100 ml min^{-1} flow of 0% RH N_2.

Figure 40 and Figure 41 show the admittance responses for a 1.88 μg (37 nm) and 1.81 μg (68 nm) deposition of Nafion and AS-4 ionomer respectively. Using Section 2.6.3 as a guide, both admittance responses suggest the addition of a viscoelastic rather than a rigid contacting layer. Upon comparison of the two responses, however, it can be seen that the AS-4 ionomer (of similar mass to Nafion) produces a significantly more viscoelastic contacting layer response. As described in Section 2.6.3, the introduction of a viscoelastic layer CAS response is differentiated from a rigid response by a decreasing loci radius and value of $|Y|_{max}$ and an increasing θ_{min} value.

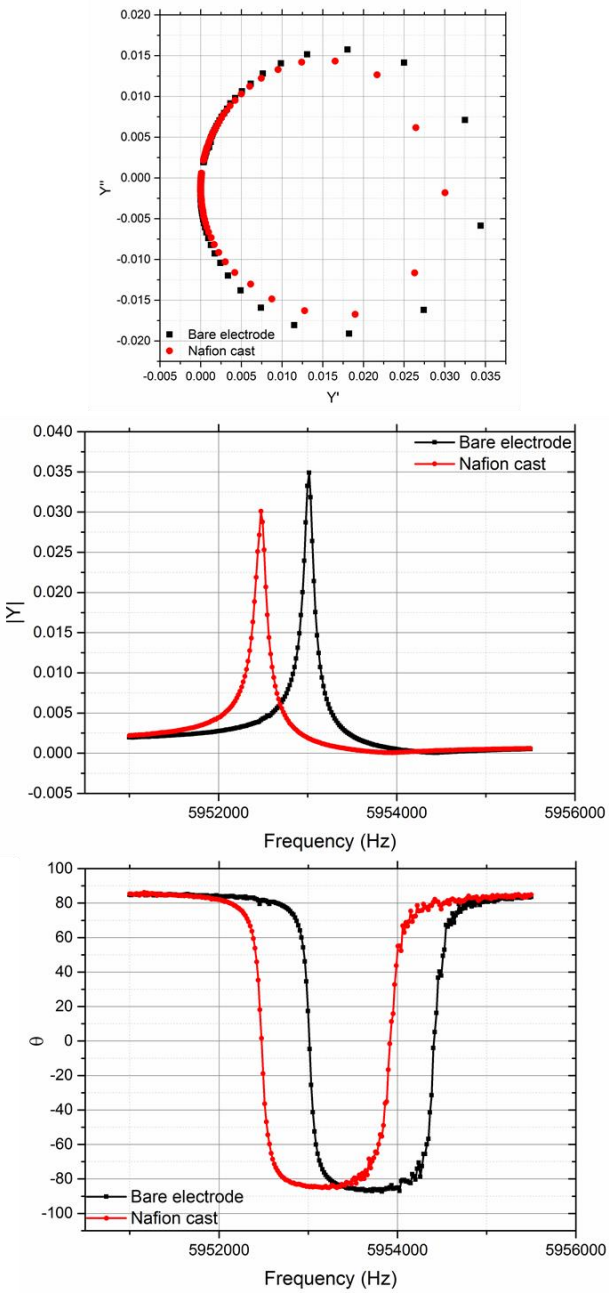

Parameter	Unperturbed	Perturbed
Loci Diameter	0.0344	0.0300
$\|Y_{max}\|$ frequency (Hz)	5.95302×10^6	5.95248×10^6
$\|Y_{max}\|$	0.0349	0.0301

Figure 40: Unperturbed and cast 37 nm Nafion composite resonator admittance response. Key metrics tabulated for reference.

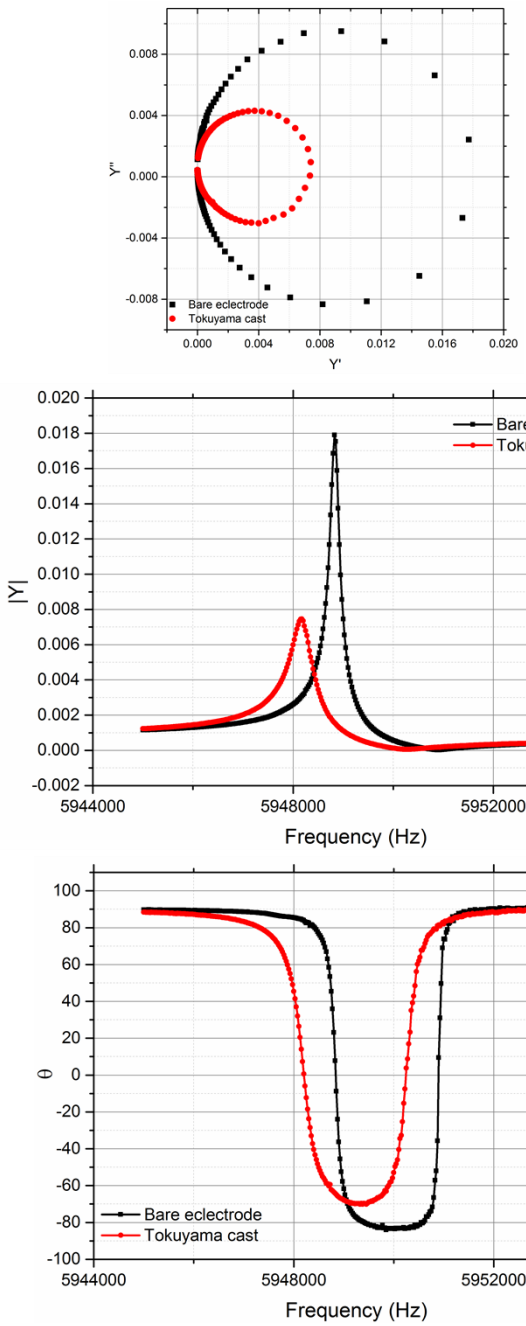

Parameter	Unperturbed	Perturbed
Loci Diameter	0.0177	0.0074
$\lvert Y_{max} \rvert$ frequency (Hz)	5.94833×10^6	5.94818×10^6
$\lvert Y_{max} \rvert$	0.0179	0.0075

Figure 41: Unperturbed and 68 nm cast AS-4 composite resonator admittance response. Key metrics tabulated for reference.

The responses shown in Figure 40 and Figure 41 also provide confirmation that the composite resonators are able to fulfil the standing wave condition as each plot is able to register both an f_s and an f_p indicting the usability of the resonator as an *in-situ* mass monitoring device [144]. The Figures also show that the composite resonators provide a decrease in the Q-factor compared to the unperturbed system; indicated by the widening of the bandwidth. The increased bandwidth and subsequent Q-factor reduction relate directly to increased energy losses in the QCM as a result of being in contact with a more viscous medium. The Figures show signs of a significantly more reduced Q-factor for the more viscoelastic AS-4 ionomer; this is likely to continue to decrease when under application in this study as the ionomer becomes hydrated for example. Ensuring a high Q-factor provides more accurate and stable results as discussed in Section 2.4; therefore, as with other thin film investigations, [136] it is important to ensure that thin ionomer films were deposited, so that during operation, a high Q-factor can still be attained even in the harshest investigative conditions, thus allowing the ability to fulfil the standing wave condition and provide accurate mass monitoring throughout [135].

This Section has introduced and defined the effect of electrolyte loading. It has shown the methods in which to determine the mass and thickness of the contacting ionomer as well as the method by which to characterise the type of loading on the composite resonator. The final rig feasibility study involves the stability of operation of the composite resonators under the investigative conditions.

3.4.1.7. Stability of the Cast Resonators

With the addition of thin film layers to the resonator surface, the mass deposition and consequently the shift in the microbalance's resonant frequency is small as shown in Section 3.4.1.4. As a result, the effect of the additional layer on the crystal's stability is expected to be negligible and is further analysed in this section.

To determine the cast microbalance stability, the composite resonator is operated within the cell at 80 ^{o}C and 55 ^{o}C for the Nafion and AS-4 composite resonators respectively in a 100 ml min^{-1} flow of nitrogen at 30% RH.

The frequency responses for each composite resonator is shown in Figure 42 along with an unperturbed QCM (at 80 ^{o}C and 30% RH) used as a 'control'.

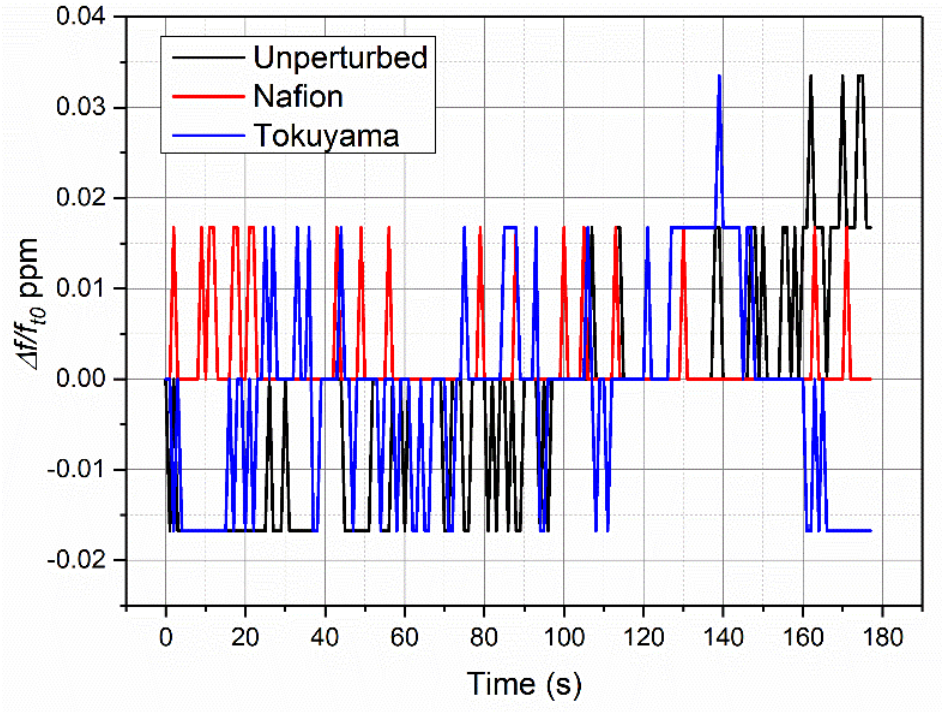

Figure 42: Graphical representation of the magnitude of noise experienced for an unperturbed, Nafion and Tokuyama AAEM cast microbalance operating at 80, 80 and 55 ^{o}C and 30% RH respectively

Figure 42 shows the stability of an unperturbed QCM (black line), 33 nm Nafion (red line) and 42 nm AS-4 (blue line) composite resonator, operating under the aforementioned conditions. Both composite resonators show noise levels of ±0.02 ppm under these conditions, which is very similar to the system's resolution determined throughout Section 3.4.1.

The above sections have shown not only the resonators, but also the composite resonators ability to operate stably under the investigative conditions in the proposed rig set up. It has also discussed the limitations of what can be practically examined in terms of ionomer thickness for example and shown examples of passive and active microbalance operation. It can, therefore, be concluded that the cast ionomer composite resonators would perform suitably as an *in-situ* fuel cell ionomer sensor.

3.4.2 Investigations

This study is made up of the individual investigations outlined in Section 3.2.5; the results for each are detailed in the following sub-sections.

3.4.2.1. Water Uptake and Hydration Mechanisms

Nafion

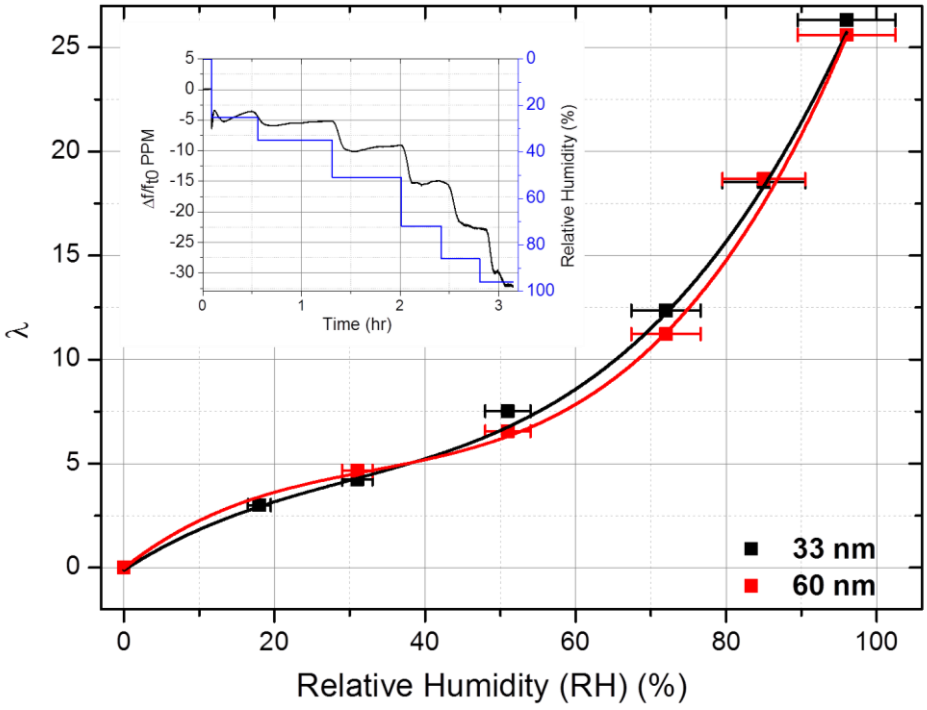

Figure 43: Nafion ionomer water uptake for 33 nm (black line) and 60 nm (red line) thick ionomers operating through a range of RHs. The frequency response for the 33nm composite resonator operating through the humidity range is shown in the inset

Figure 43 inset shows the microbalance frequency response for a 33 nm cast Nafion membrane operating over a range of RHs. The decreasing resonant frequency response with increased humidity is consistent with an increase of mass (electrolyte wet mass) loading on the crystal microbalance. Note that the initial exaggerated frequency drop is a result of a feed stream valve switching between the dry and humidified gas supply. If we initially assume that the Sauerbrey equation holds as an accurate measure of mass of water

added to the composite resonator's ionomer layer, Equation (24) can be used to determine the membrane's water uptake at a given humidity using the differences between its dry mass, wet mass and its IEC. The result for a 33 nm and a 60 nm thick membrane is shown in Figure 43.

Many sources confirm an increased Nafion water sorption and subsequent swelling with increasing RH; the more water in the operating environment, the greater the swelling (up until the point of maximum hydration) [79, 80, 85, 145].

As the contacting nitrogen's RH is increased, the resonant frequency decreases; this process is understood to be instantaneous with thin film ionomers; [86] however, as can be seen, frequency stabilisation takes some time in this case. The frequency stabilisation period is directly attributed to the equilibration of the membrane water content with the operating atmosphere – the extended equilibration time can be attributed to the dew point humidifier PID control.

The water uptake for a 33 and 60 nm electrolyte is reported in Figure 43, and both electrolytes show good agreement to one another and to published literature, following the third-order polynomial trend for Nafion water uptake at specific RHs [79, 80, 85, 145].

The Nafion water uptake values obtained at higher ($\geq$ 70%) RHs in this investigation are higher than some presented by other authors for studies also conducted in the vapour phase [80, 84, 86]; the anomaly between the uptake in the liquid and vapour phase is commonly attributed to Schroeder's Paradox [146]. Schroeder's Paradox is a phenomenon used to describe the difference in solvent uptake by a polymer when exposed to saturated vapour and pure liquid. However, work presented by many authors, including Zawodzinski *et al.* [84], has been unable to fully understand why Schroeder's Paradox affects the Nafion ionomer and have explained the issue as a result of experimental setup, procedure discrepancies, time frames and have also ruled out the effect of sorption kinetics. The water uptake results presented here in the vapour phase at the highest relative humidities are comparable to those often achieved in liquid phase investigations [79, 84] and, not for

the first time show little or no contribution from the Schroeder's Paradox effect [147, 148]. This effect can be further explored using CAS.

Nafion is expected to be fully hydrated in the vapour phase with a water uptake value of ~22 [79, 84]. Work by Krtil *et al.* [85] has shown that this value is obtained using a cast QCM in humidified nitrogen at a RH near 100%; however, in this case, these values are obtained around 92% RH, according to Figure 43. This variation can be attributed to instrumentation accuracy (the dew point humidifier is accurate to ± 1.5 ^{O}C) and limits the use of the Sauerbrey equation applied to this system. Crystal admittance spectroscopy provides a more robust analysis of crystal loading than the Sauerbrey equation affords.

Figure 44a shows the Nyquist plot admittance response for the cast Nafion composite resonator operating in a range of RHs. The Nyquist plot can help delineate the effects of contacting rigid mass and viscoelastic properties of the composite resonator. The resonator's magnitude of admittance response is shown in Figure 44b, and is the plot most often used to describe how a system's properties have been affected.

As the RH increases and the ionomer hydrates, the general trends observed in Figure 44 are that the diameter of the admittance locus decreases and the magnitude of the admittance plot shifts to a lower frequency, with a decrease in amplitude ($|Y|_{max}$). When fitting this response using the BVD modified circuit, it results in an increased R_2 resistance term and suggests an increasingly viscoelastic contacting media. For further reference and supplementary theory on how to interpret the admittance data, the reader is referred to Section 2.5 and [2, 16, 37].

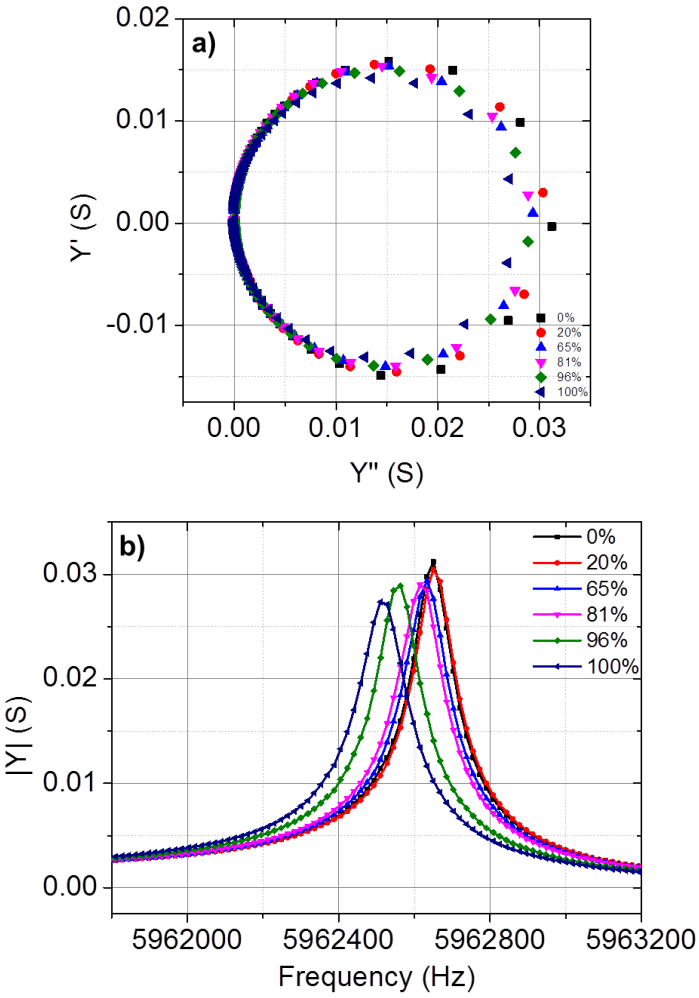

Figure 44: A snapshot of the CAS response for a 33 nm Nafion composite resonator operating through a range of RHs and hydration states: (a) admittance locus and (b) magnitude of admittance Bode plot.

The $|Y|_{max}$ peak describes the effect that humidity has on the composite resonator's viscoelastic properties and occurs at the series resonant frequency (f_s). Figure 45a and b further emphasise the effect that hydration has on the magnitude of admittance by plotting the change in the series resonant frequency (f_s) (frequency at which the $|Y|_{max}$ occurs) and the value of $|Y|_{max}$ through the range of operating RHs, compared to the value at 0 % RH respectively.

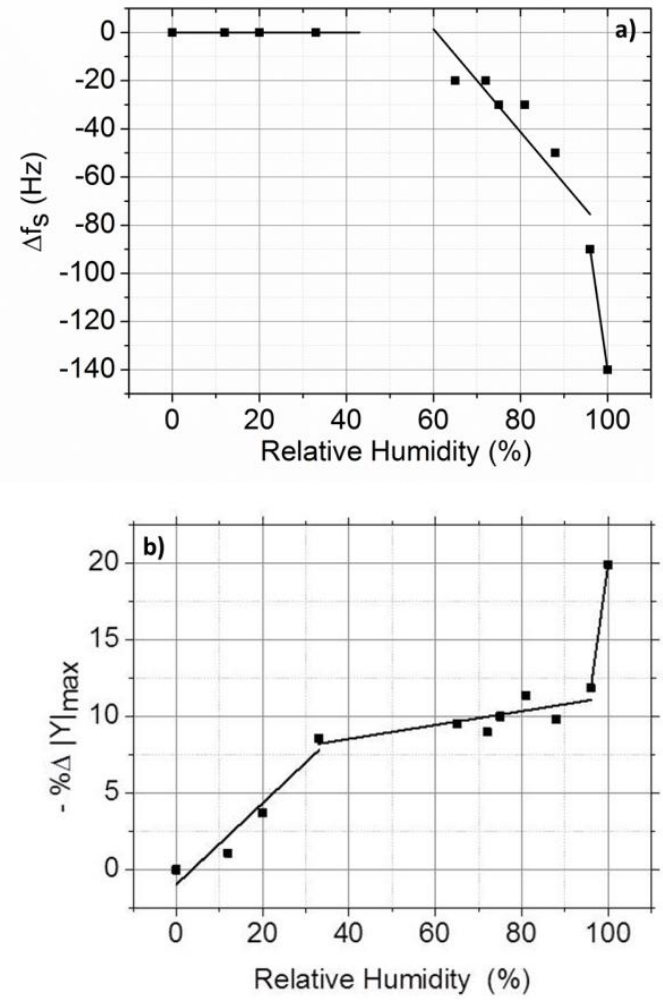

Figure 45: (a) Series resonant frequency and (b) percentage decrease in the amplitude of admittance as a function of RH for a 33 nm Nafion composite resonator (linear sections added as a guide to the eye).

Initially, at RHs ≤ 34%, Figure 45a shows no change in the series resonant frequency with increasing RH; however, Figure 45b shows that the amplitude of the $|Y|_{max}$ peak decreases steadily by 8%. Between 34 -96% RH, Figure 45a shows a decreasing f_s indicating that the composite resonator continues to load water, but when examining Figure 45b, this loading regime is thought to have a significantly less viscoelastic effect on the resonator with increasing RH compared to the regime between $0 - 33$ % RH. This is represented by a steep change in f_s by 90 Hz and the corresponding slowdown in the percentage change of only 8.5% across the period, as seen

in the $|Y|_{max}$ plot shown in Figure 45b. The reader is reminded that perfect rigid loading (i.e. no viscoelastic effect) will see a consistent $|Y|_{max}$ amplitude, with a decreasing resonant frequency corresponding to the mass of the contacting species – relatable using the Sauerbrey Equation. Above 96% RH, there is a sharp decrease in the resonator's f_s (50 Hz) and $|Y|_{max}$ (9%) amplitude, as represented in Figure 45a and b respectively. This change is commonly referred to as an additional viscous loading; such as a contacting liquid, e.g. water.

The magnitude of admittance plots indicate the presence of two loading regimes; one at low RHs in which there is limited water uptake (constant f_s) but significant viscoelastic changes in the Nafion membrane, followed by a larger water uptake with more 'rigid-type' loading characteristics at higher RHs. Following these loading regimes, the sharp decreases in f_s and the $|Y|_{max}$ amplitude suggests contacting water on the hydrated membrane's surface. The presence of two distinct loading regimes coupled with the water uptake plots shown in Figure 43, is consistent with the theory discussed by Zawodzinski *et al.* [84], which showed water loading to occur in two regions (ion solvation followed by micro-channel hydration and swelling [136]). It must be noted here that though it is suggested that the solvation and swelling regimes dominate with increasing RH respectively, there will be elements of both mechanisms at all RHs as shown by previous Environmental Ellipsometric Porosimetry studies [80]. Both Figure 45a and b show that above 96% RH the membrane's viscoelasticity increases significantly – even more so than the initial loading regime. This large change in the composite resonator's viscoelasticity is likely due to contacting liquid water on the surface of the composite resonator as the membrane becomes fully hydrated and cannot further load any water. This coincides with roughly the same RH at which the predicted maximum hydration occurs (water uptake $\lambda = 22$ [79, 84]), seen in Figure 43.

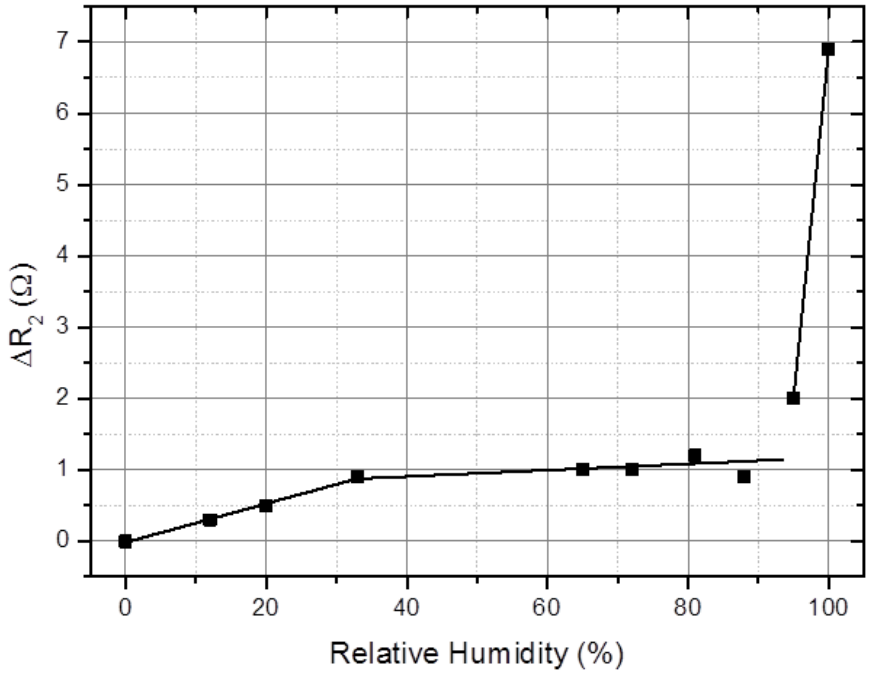

Figure 46: Change in composite resonator's resistance (R_2) in the modified BVD equivalent circuit as a function of RH (linear sections added as a guide to the eye).

As shown in Figure 46, the viscoelastic component can be represented by fitting the L_2 and R_2 terms; however, for simplicity of fitting and comparison, the L_1 and L_2 terms are frequently combined and the R_2 value (representing the power dissipation from the QCM surface into the contacting media) can be used to represent the relative shift in the composite resonator's viscoelastic properties [2, 37, 113, 136].

Figure 46 initially shows that as the RH is increased to 34%, R_2 increases steadily by 1 Ω as the ionomer becomes more viscoelastic. Beyond 34% RH it can be seen that the rate of resistance change decreases significantly, increasing by only 0.2 Ω up until the RH reaches 88%. Though R_2 doesn't vary significantly between 34% and 88% RH, it must be noted that there are still loading processes occurring on the membrane, as discussed and demonstrated in Figure 43 and Figure 45.

Finally, above 88% and specifically 96% RH, R_2 increases sharply – this indicates a significant increase in viscoelasticity of the composite resonator. The sharp change observed in the composite resonators R_2 and consequent viscoelasticity supports the data seen in Figure 45a and b, and is significantly sharper than the R_2 changes seen previously; this suggests the presence of a contacting liquid; whether that liquid water is contacting on the ionomer / nitrogen or gold / ionomer interface still remains unclear.

AS-4 Ionomer

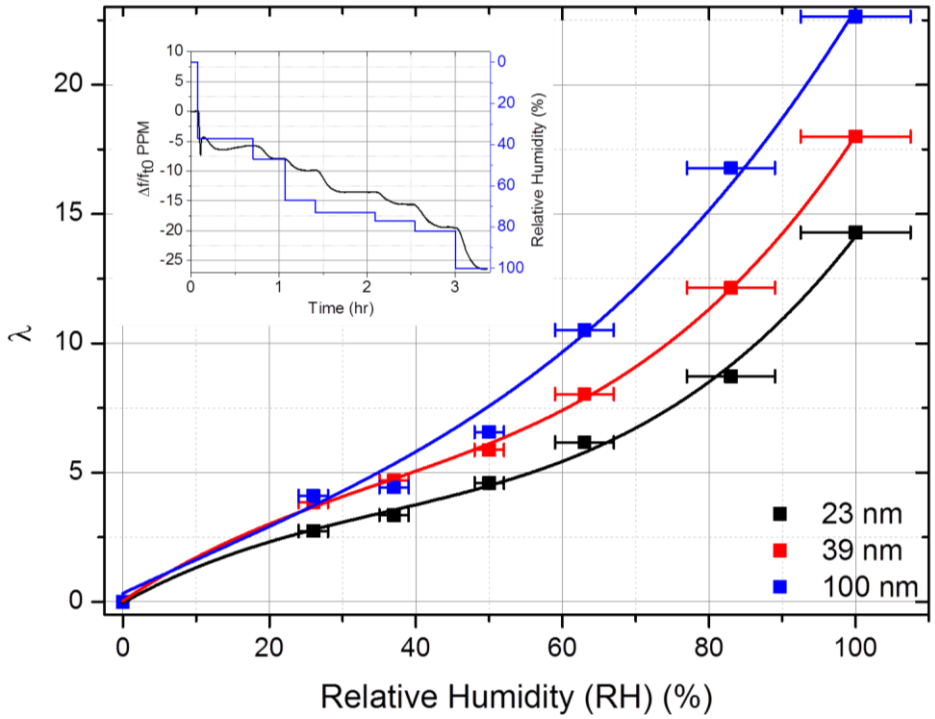

Figure 47: AS-4 ionomer water uptake for a 23 nm (black), 39 nm (red) and 100 nm (blue) thick ionomers operating through a range of RHs. The frequency response for a 39 nm composite resonator operating through the humidity range is shown in the inset

As with the Nafion water uptake calculations, both the dry and wet mass of the AS-4 ionomer must be known in order to determine its water uptake. Once again, in order to determine the mass of the wet ionomer, cast AS-4

composite resonators are operated under variable RH environments; the frequency response of the 39 nm AS-4 composite resonator is shown in Figure 47 inset for reference.

The general frequency trend observed in Figure 47 is similar to that of Nafion where increasing RH results in a reduction of the QCM's resonant frequency. Again, as the valve is switched from the dry nitrogen stream to the humidified stream, there is an initial sharp frequency drop artefact. Figure 47 shows the water uptake values determined experimentally for a 23 nm, 39 nm and 100 nm AS-4 ionomer thickness; as with Nafion, the results here also follow a third order polynomial trend.

Whilst not extensively tested, some literature pertaining to commercial sheet AAEMs exist [149, 150] and results indicate lower water uptake values compared to Nafion, as can be observed here. The third-order polynomial water uptake trends are comparable to those published by Li *et al.* for sheet AAEM [114]; however, there is no information on the effect the thickness of the cast AAEM has on its water uptake. Figure 47 shows that at lower RHs ($\leq 50\%$) there is only a small difference in water uptake for different ionomer thicknesses; however, at higher RHs ($\geq 50\%$) the thicker ionomers exhibit a larger water uptake. The reason for this discrepancy is still unclear, but could be a result of the interaction of the thinner ionomer with the electrode, constraining the film from swelling and absorbing water; or alternatively the formation of a water impermeable layer as a result of disordering of channels at the gas/ ionomer interface.

The results presented in Figure 47 suggest a lower water uptake for the AS-4 ionomer compared to a Nafion ionomer with comparable thickness – as suggested within the published literature [96, 150, 151], all of which report water uptakes between 18 and 20 when operated in water. It is important to note that the frequency response shown in Figure 47 (inset) indicates very similar levels of water loading to that of Nafion shown in Figure 43; however, the AAEM with a much higher IEC results in a lower water uptake per exchange site. The difference in uptake values is likely due to the variance in wettability of the main chains (the polytetrafluoroethylene polymer backbone in Nafion and the hydrocarbon polymer backbone in the AAEM)

and side chains (the sulfonic acid group and the quaternary ammonium group in acid and alkaline membranes), respectively [114].

AAEM swelling reports are scarce, and those available are for studies investigating in-house fabricated AAEMs. However, literature from Li *et al.* [114] has suggested from *ex-situ* testing that the commercial AAEM thickness remains almost unchanged during the water uptake process; whereas Nafion increases by almost 40% when fully hydrated [152].

The theory presented by Li *et al.* can be explored using the QCM and CAS. Following the work presented on Nafion and the Cluster-Network model, it is understood that as the membrane swells, its viscoelasticity will slowly increase in-line with the operating RH [136], after some period of ion solvation (rapid viscoelastic effects). However, theoretically, if there is very little change in the membrane thickness during the water uptake process (i.e. no swelling – as predicted by [114]), there should be negligible viscoelastic change, and hence no change in the system's R_2 or $|Y|_{max}$ amplitude, but instead only in f_s.

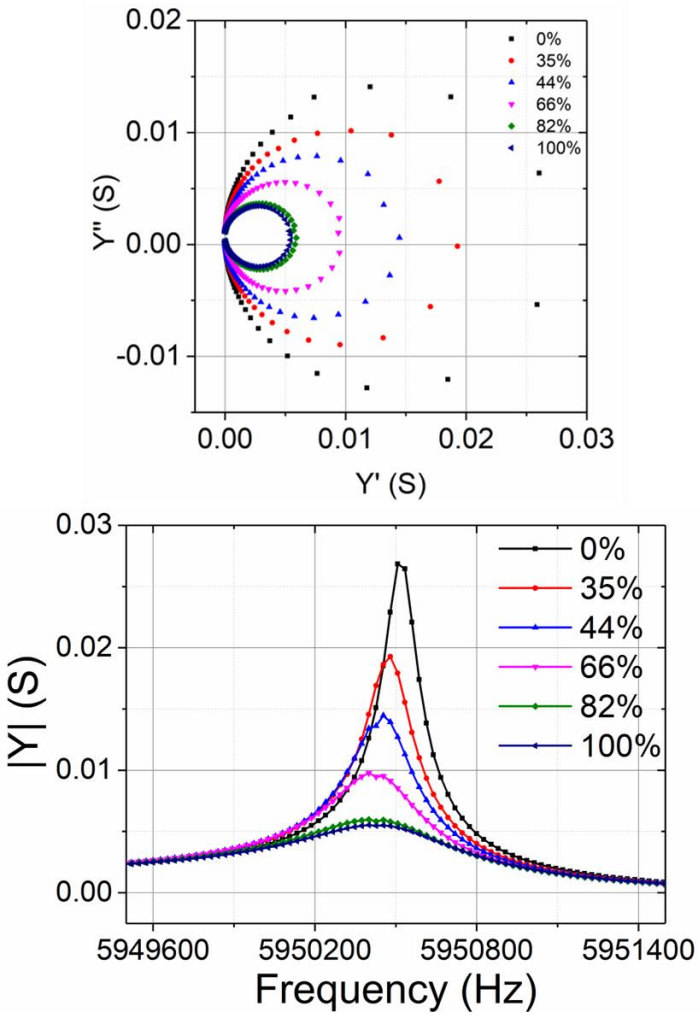

Figure 48: Segment of CAS results for a 39 nm AAEM composite resonator operating through a range of RHs and hydration states: (a) Admittance locus and (b) magnitude of admittance plot

Figure 48 shows the admittance responses for the cast AS-4 composite resonator operating through a range of RHs. The AS-4's Nyquist and Bode plots at different RHs are shown in Figure 48a and b, respectively; as with Nafion it shows that increasing RH results in a decreasing admittance locus diameter – albeit with significantly bigger shifts than with Nafion. The Bode plot shows that while the frequency decreases with increasing RH, the decrease in $|Y|_{max}$ amplitude is very significant, and again much greater than for Nafion, this is further explored in Figure 49.

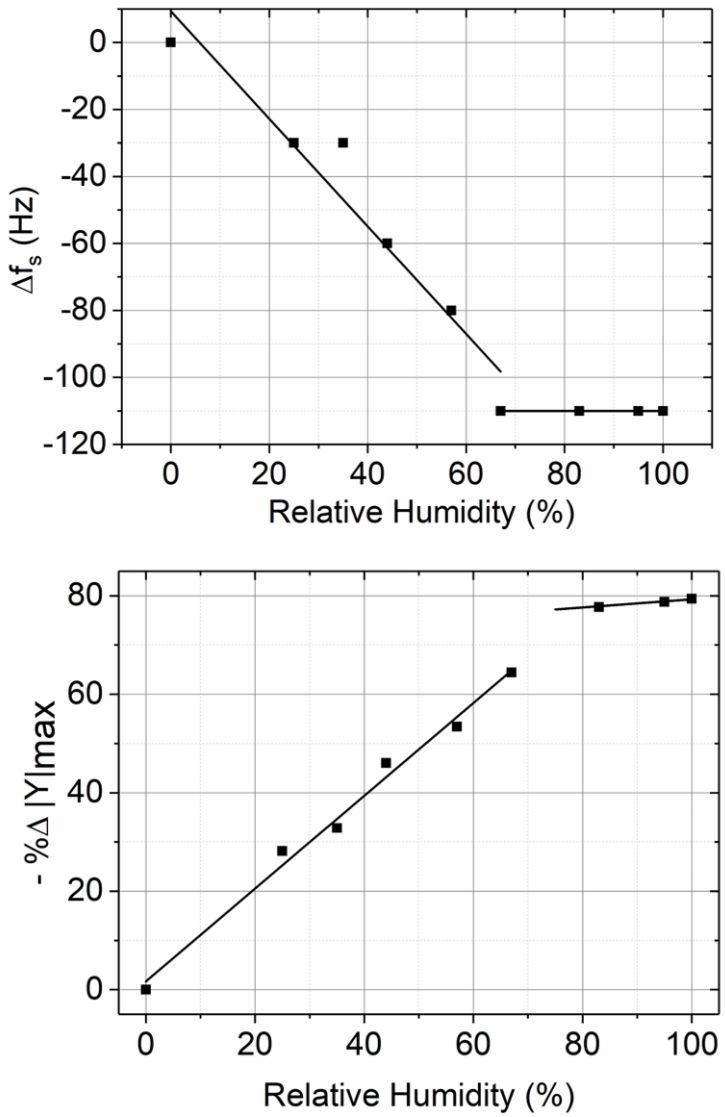

Figure 49: (a) Change in series resonant frequency and (b) percentage decrease in amplitude of admittance for a 39 nm AAEM composite resonator versus RH and hydration (linear sections added as a guide to the eye).

The understanding of how AAEMs respond to humidification is still ambiguous with scarce yet conflicting literature available. However, once more, the changes observed in the magnitude of admittance plot (Figure 48b) generally indicate viscoelastic loading effects with increased humidification. Figure 49a and b show the composite resonator's series resonant frequency (f_s) and the percentage change in the amplitude of the magnitude of the admit-

tance peak, respectively. As suggested above, the initial Nafion water loading relates to the ionomer ion solvation below 34% RH; this is represented by water sorption that increases the composite resonator's viscoelasticity.

The results in Figure 49a suggest that the AS-4 ionomer follows a similar trend to the Nafion ionomer; however, the initial 'viscoelastic dominant / ion solvation' regime loads significantly more water (110 Hz) that lasts through a larger humidity range (0 – 66% RH). Above 66% RH in Figure 49a however, water loading is seemingly unaffected by additional RH. Above 66% RH, the Δf_s remains constant (beyond the system's resolution). The magnitude of admittance peak amplitude plot shown in Figure 49b indicates that as the RH is increased between 0 – 66% the amplitude of the $|Y|_{max}$ decreases significantly to roughly 65% of the original value. However, between 82 - 100% RH, the change in amplitude of $|Y|_{max}$ slows significantly and drops by only 3%. When compared with the Nafion ionomer uptake mechanisms and the water uptake recorded in Figure 47 and Figure 48, the results suggest that above 66% RH the ionomer enters a more 'rigid-type' loading mechanism, i.e swelling [136] – similar to that seen in the Nafion ionomer above 35% RH. Unlike Nafion, the suggested membrane swelling region is a small RH window in which no change in f_s, and minute changes in $|Y|_{max}$ indicate minuscule ionomer swelling, supporting the theory of Li *et al.* [114].

The AS-4 admittance response suggests the presence of two loading regimes – similar to that of Nafion (excluding the proposed contacting water on the Nafion ionomer). As with Nafion, the AAEM's initial loading regime has significantly larger viscoelastic effects on the ionomer when compared to that of the second regime; this presents a significantly more rigid-type load to the composite resonator. Unlike the Nafion membrane, the AS-4 ionomer does not exhibit effects of contacting liquid water, even at the highest RHs, which indicates that the ionomer may still be undergoing hydration and swelling.

The results could be suggestive of a modified version of the two-stage Nafion water loading mechanisms presented by Zawodzinski *et al.* [84] The AAEM

ionomer is reported to have significantly more functional groups compared to Nafion to compensate for a shortfall in its ionic conductivity; thus the ion solvation process is likely to require significantly larger quantities of water molecules to overcome the ionomer's hydrophobic nature, and consequently leads to a large decrease in f_s during solvation when compared to the Nafion ionomer. At RHs > 66%, the change in the resonator's viscoelasticity decreases significantly and suggests, as with Nafion, a period of ionomer swelling – the corresponding Δf_s is 0 and indicates negligible water loading – this may suggest that the quantity of water loaded for ionomer swelling is greater for Nafion than the AAEM ionomer.

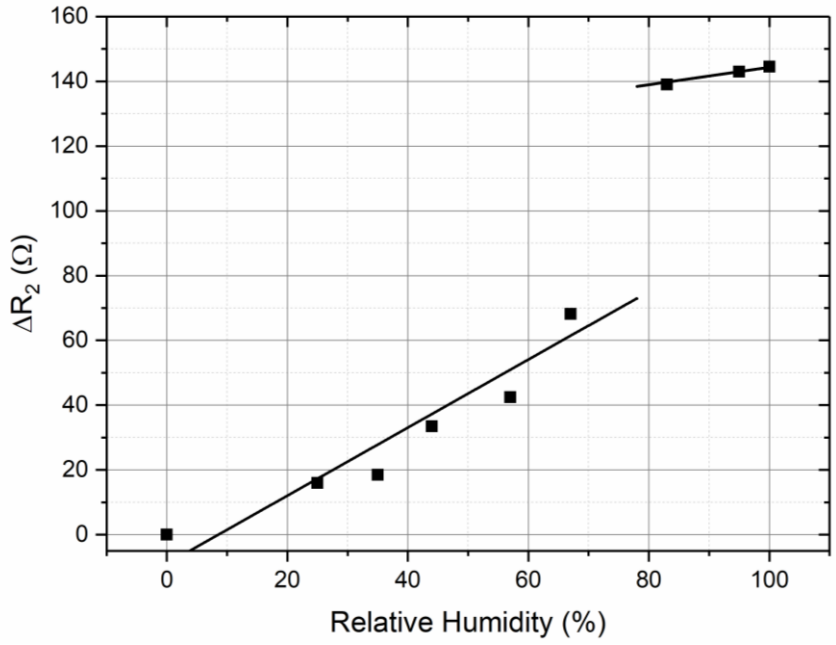

Figure 50: Change in the AS-4's composite resonator's resistance *(R_2)* in the modified BVD equivalent circuit as a function of RH (linear sections added as a guide to the eye).

The R_2 fit data is shown in Figure 50 for the ionomer water uptake through a range of RHs. Initially, the resistance increases very steadily up to 66% RH, showing a large viscoelastic change in the composite resonator, corresponding well with Figure 49. Between 66% and 82% RH, there is a sharp resistance change of 50 Ω and this represents a large increase in the

resonator's viscoelasticity. Above 82% RH, the R_2 rate of increase slows considerably through to 100% RH. As with Nafion, the slow-down in the rate of increase of R_2 is suggestive of a period of low viscoelastic change compared to the solvation region and can be attributed to ionomer swelling.

Water Uptake and Hydration Conclusions

The work presented during this investigation explores the water uptake, sorption mechanics and swelling characteristics of thin film Nafion and the commercially available AS-4 AAEM ionomer from the vapour phase using a QCM.

The QCM frequency response has shown, as reported by other authors, that the water uptake is lower for the AAEM ionomer compared to that of Nafion at a given relative humidity. The active oscillation has also shown that unlike Nafion, the AAEM water uptake is not independent of film thickness.

CAS has been applied to this system for the first time to help better understand the sorption characteristics and swelling of Nafion and AS-4 ionomers. The experimental results suggest some similarities in loading mechanisms between the two, albeit to varying magnitudes. Both the Nafion and AS-4 ionomer exhibit a process of high viscoelasticity increases as ions within the ionomer are solvated. The results presented show that the Nafion solvation occurs at a significantly lower relative humidity and water uptake value compared to the AAEM ionomer; beyond the solvation period, the ionomer channels begin to absorb water and swell. The Nafion ionomer exhibits significantly larger water uptake during the swelling regime, suggesting a superior swelling ratio than that of the AS-4.

3.4.2.2. Ionomer Degradation

As discussed in Section 3.2.4.2, AAEM ionomers have shown degradation through instability within the alkaline media when operated at temperatures $\geq 65\ ^{O}C$ in several systems.

The following investigation compares the AS-4 ionomer's instability (degradation) as a function of its hydration at steady state using the QCM, CAS and mass spectrometry.

CAS was implemented during this investigation as a means to determine the effect on the ionomer's viscoelasticity from the exposure to elevated temperatures. CAS was employed as frequency response alone would indicate a change in the composite resonator's operation that would be difficult to attribute directly to the effect of degradation.

However, to develop the parameters of the investigation such as the degradation onset temperature and investigative timeframe, it was first necessary to understand the limitations of the experimentation through the active response. These parameters are further described in Figure 51, Figure 52 and Figure 53.

To determine the ionomer's instability onset temperature the base rig was altered as shown in Figure 31. An *in-situ* AS-4 cast 100 nm composite resonator was then operated within the setup initially at 55 ^{O}C with a 100 ml min^{-1} flow of 50% RH nitrogen through the cell; as the resonator obtained stable frequency responses the operating temperature was ramped and held at 1 ^{O}C intervals as shown in Figure 51. The resonator provided stable frequency responses during operation at temperatures between 55 ^{O}C – 64 ^{O}C; however, when operating at 65 ^{O}C, the response is not as expected. At 65 ^{O}C the composite resonator initially begins to stabilise at a new resonant frequency; however, the initial stabilisation period is short-lived and followed by a sudden increase in the resonator's frequency by 1.6 ppm before re-stabilisation. Figure 51 inset further illustrates the effect occurring on the microbalance and indicates that the composite resonator is 'losing mass' until it stabilises at a new frequency.

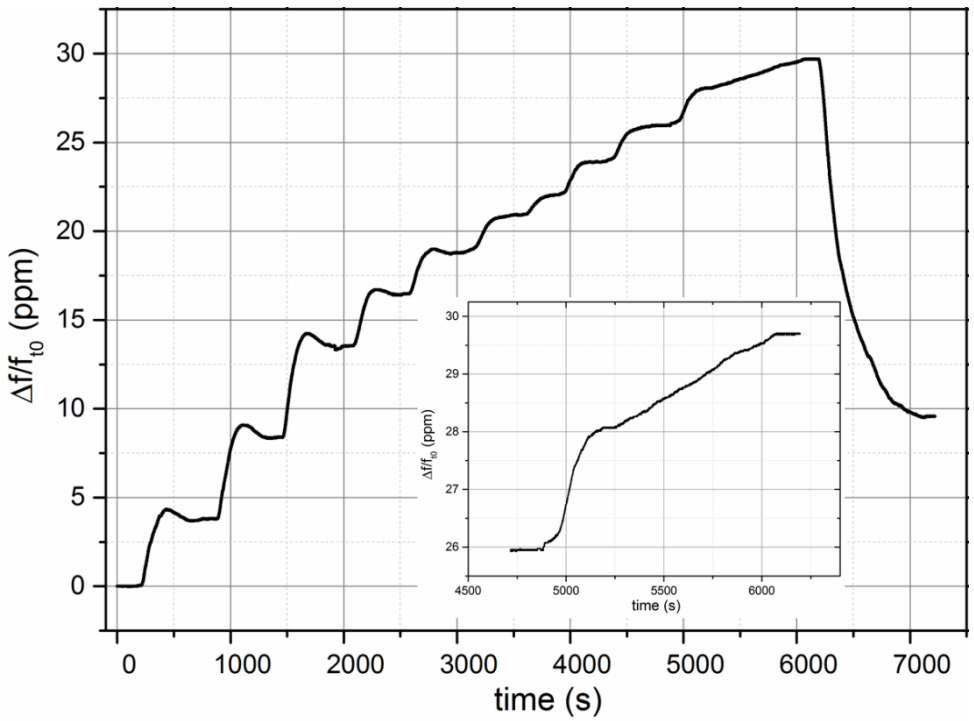

Figure 51: The measured frequency response for a 100 nm composite resonator when operating at temperatures between 55 ^{O}C and 65 ^{O}C. The inset image shows a zoomed in analysis of the frequency response for the composite resonator when operating at 65 ^{O}C.

This investigation explores the effect hydration has on the AS-4 ionomer's instability within the alkaline media when operated at elevated temperatures. Figure 51 suggests that the ionomer shows signs of degradation at 65 ^{O}C and whilst it is not possible to accurately quantify the degraded mass (due to differences in the operation temperature), further analysis of Figure 51 inset shows that the proposed ionomer degradation suggested by the indicated mass loss lasts 1300 seconds (~ 22 mins).

However, before determining the experimental timeframe required for this investigation, further analysis of the composite resonator operating at elevated temperatures in a variety of hydration states was required, examples of which are shown in Figure 52 and Figure 53.

Figure 52 shows the frequency response for a 100 nm cast AS-4 ionomer operating at 66% RH and 55 ^{O}C. Once a stable frequency is recorded, the operating temperature is then increased to 65 ^{O}C and held for 50 mins. At the elevated temperature, the composite resonator initially begins to settle at a new pseudo-resonant frequency (similar to as shown in Figure 51 inset); however, after a short period of time, the resonant frequency begins to increase (without external stimulation) indicating mass loss from the composite resonator. At the elevated temperature, the composite resonator stabilises at a new resonant frequency after ~ 35 mins of operation. When the system is cooled to 55 ^{O}C, the composite resonator indicates a steady state increase in frequency (mass loss) equivalent to 1.9 ppm.

The reader is reminded that the QCM can operate at a range of temperatures without any signs of hysteresis as shown in Section 3.4.1.1 and therefore the frequency shifts observed here can be attributed directly to changes in the contacting ionomer. However, through active oscillation alone it is not possible to determine whether the observed frequency change can be credited solely to mass loss.

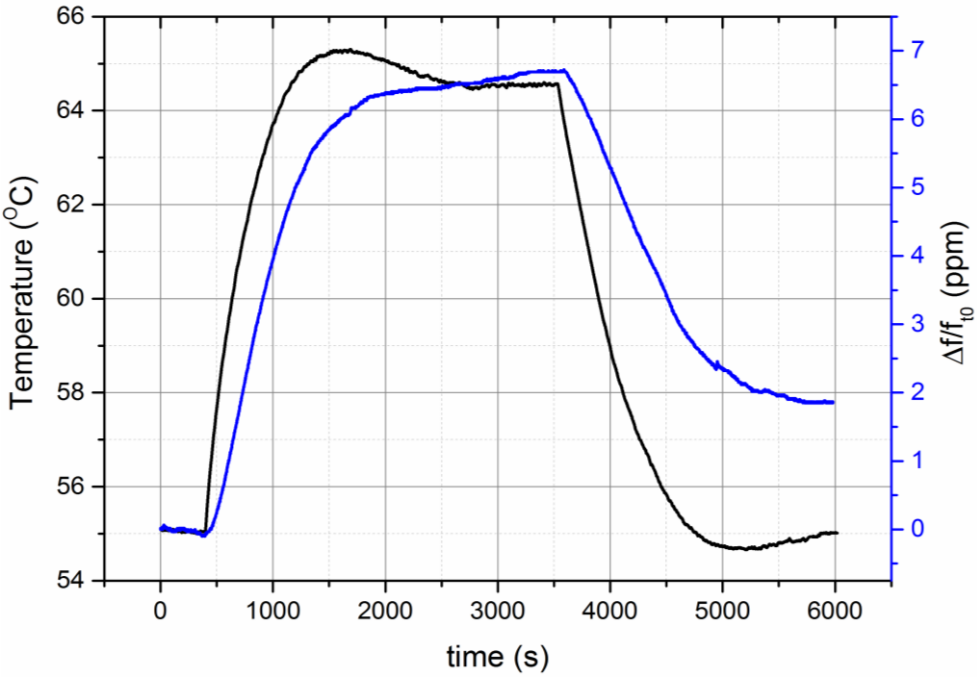

Figure 52: The measured frequency response profile for a 100 nm AS-4 composite resonator operating at 55 ^{O}C, 65 ^{O}C and again at 55 ^{O}C at 66% RH

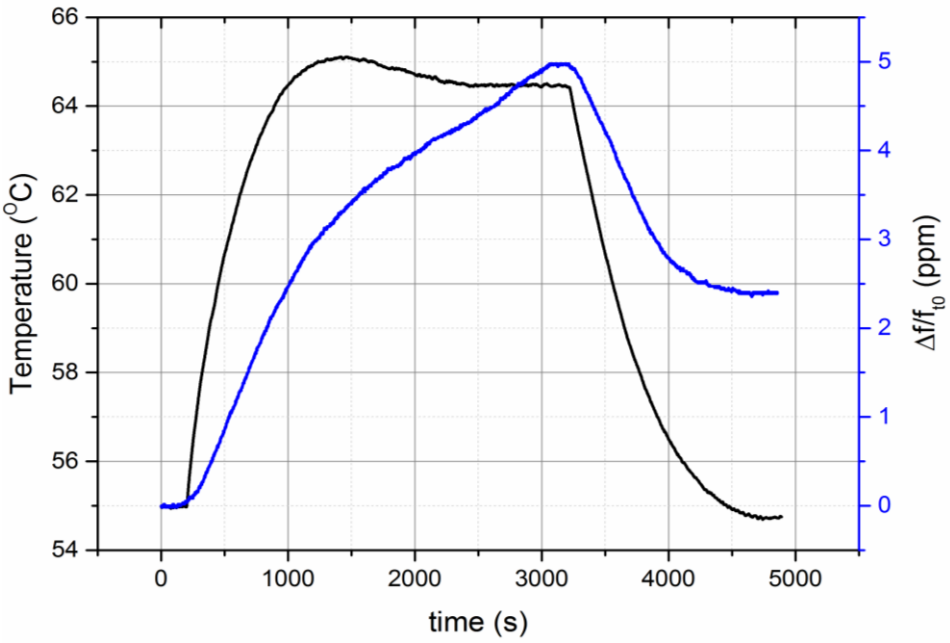

Figure 53: The measured frequency response profile for a 100 nm AS-4 composite resonator operating at 55 °C, 65 °C and again at 55 °C at 11% RH

The second example shown here in Figure 53 is for an identical investigation to that presented in Figure 52; however, for a system operating at 11% RH. Figure 53 shows a similar yet slightly altered trend to that seen at 66% RH. It can be seen that in the system operating at 11% RH, that the AS-4 composite resonator is affected by the ionomer's instability within the alkaline media more quickly and does not settle at an initial pseudo steady-state resonant frequency. The microbalance frequency continues to increase from the moment the elevated temperature increase is initiated by the system for ~ 40 mins until a new resonant frequency is reached. When the system cools to 55 °C, the composite resonator records a steady state increase in the frequency of 2.4 ppm.

In each of the above examples, the AS-4 composite resonator response has suggested signs of degradation when operated at elevated temperatures. In every case, the composite resonator achieved a new resonant frequency after 45 mins of operation at elevated temperatures. Whilst not the focus of this investigation, the active responses shown in Figure 52 and Figure 53 indicate two similar yet slightly different transient degradation responses and this is

further discussed in Section 3.5.1. The measured shift in frequency for these investigations is very similar and whilst useful at indicating composite resonator mass change, it does not provide enough information to understand the nuances of the degradation process. The implementation of the steady state investigation using CAS provides a more comprehensive insight into the processes occurring on the ionomer surface during the degradation process.

The admittance data for the composite resonator operating at 55°C before and after the rise in operating temperature (to 65°C for 50 mins) were recorded (an example of which is shown in Figure 54) and fitted using the modified equivalent circuit shown in Figure 12. The example shown here is for a system operating at 55 ^{O}C before and after operation at 65 ^{O}C at 11% RH. As can be seen in Figure 54b inset, the composite resonator shows signs of a damped $|Y|_{max}$ and thus a reduced viscoelasticity after operation at elevated temperatures. The change in the systems viscoelasticity indicates that the measured active frequency responses are a result of degradation of the ionomer's side chains and not a process of the ionomer 'burning off' at high temperatures, as discussed below.

The system's viscoelasticity can be represented by the R_2 term in the equivalent circuit [2, 113, 136], and is the main component of interest in this investigation. The relative difference in viscoelasticity can be represented by the shift in R_2. The percentage change in R_2 before and after composite resonator operation at elevated temperatures for a range of relative humidities is shown in Figure 55.

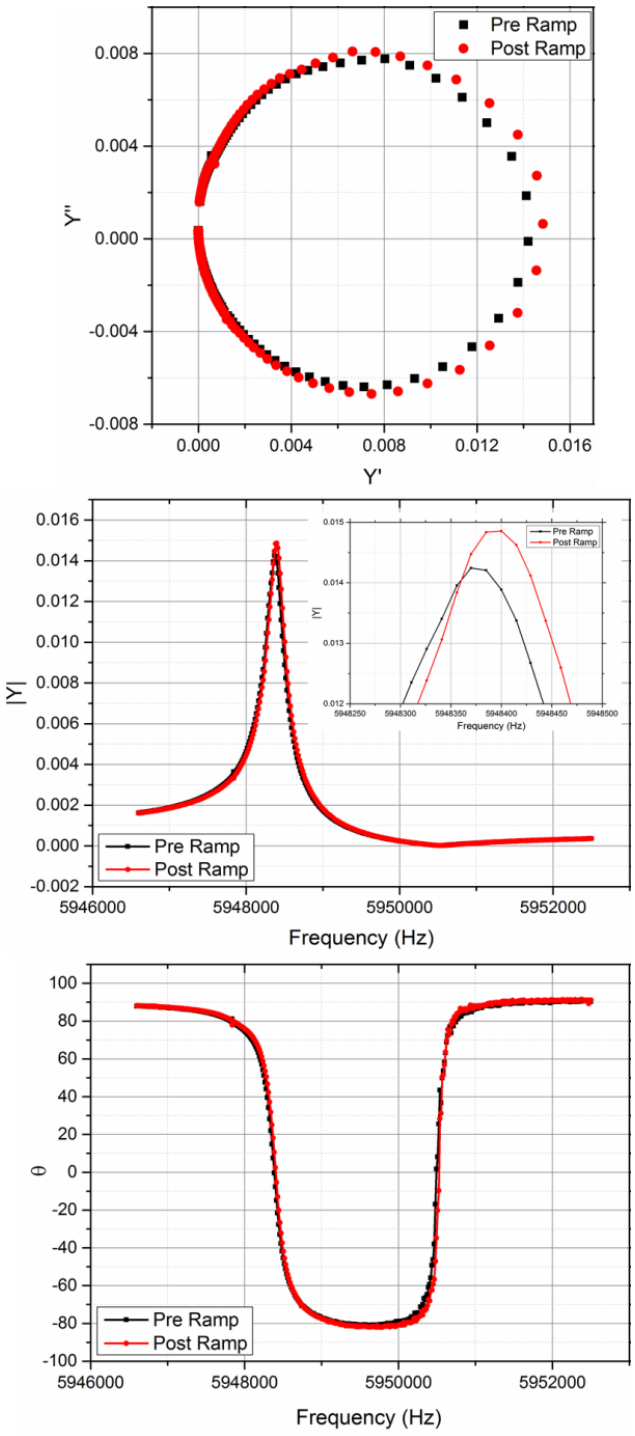

Figure 54: CAS response for a 100 nm AS-4 composite resonator operating at 55 ^{o}C before (black line) and after (red line) operation at 65 ^{o}C and 11% RH for 50 mins. Figure b inset shows an enlarged version of the $|Y|_{max}$ peaks for each response

Each data point shown in Figure 55 relates to an individual investigation (such as that shown in Figure 54) and is conducted with a freshly cast 100 nm composite resonator held at a specific RH; consequently, there is no additional hydration contribution to the composite resonator's viscoelasticity. This allows the percentage shifts in R_2 to be directly related to the composite resonator's viscoelasticity and subsequently to the processes occurring on the ionomer.

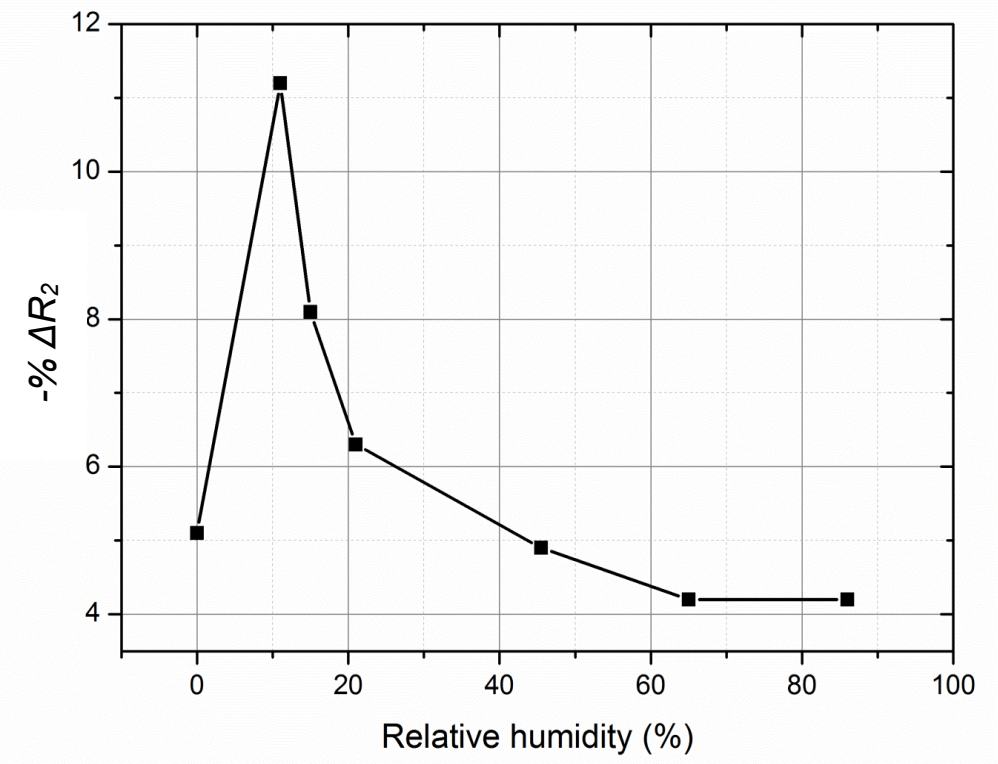

Figure 55: The composite resonator's percentage shift in R_2 (representing the viscoelastic change in the film) when operating before and after exposure to elevated temperatures as a function of relative humidity.

It can be seen that in general (initially excluding the -% ΔR_2 shift at 0% RH), as the relative humidity increases, the shift in the viscoelasticity of the ionomer layer, represented by the % change in R_2, decreases from -11.2% at 11% RH to -4.2% at 88% RH.

Recalling the observed AS-4 hydration mechanisms presented in Section 0 indicates the presence of two distinct water uptake regimes; the first occurring between $0 - 66\%$ relative humidity where the ionomer adsorbs water molecules that are used primarily for ionomer solvation, followed by a region above 66% RH in which the adsorbed water acts to swell the previously solvated ionomer channels [113].

Figure 55 shows that there is no change in $-\Delta R_2$ with increasing hydration above ~66% RH, suggesting that the ionomer may be insensitive to RH as a degrading factor above this point.

Comparing the observed trend in Figure 55, with the water uptake mechanism data presented in Section 0, it can be seen that the $-\%\ \Delta R_2$ shift is most significant during ionomer solvation, i.e. between 11% and 66% RH. Below 66% RH, the ionomer is only partially solvating, the OH^- ions and the cationic headgroups are more reactive and thus aggressive degradation can occur [108].

In the second water loading mechanism (above 66% RH in this system) where the ionomer is fully solvated and undergoing swelling, the corresponding ionomer's $-\%\ \Delta R_2$ is significantly lower. This suggests that as the ions within the ionomer solvate, the degradation reaction becomes less aggressive. At 66% and 88% RH, a constant shift in $-\%\ \Delta R_2$ is recorded and correlates with the fact that the ionomer is fully solvated and in the swelling regime [113].

The experimental observations shown here support the computational and experimental theories proposed by Chempath *et al.* [105] and Macomber *et al.* [108] respectively (albeit for different systems), showing that hydration does indeed improve the ionomer's resistance to degradation at elevated temperatures.

At 0% RH, $-\%\ \Delta R_2$ changes by only 5.1% (Figure 55). This is likely to be due to 'collapsed' ionomer channels (similar to that of Nafion); and only through hydration of the channels can they expand and allow the movement of OH^- ions to the cationic head groups [46]. Thus, at 0% RH the channels

impede access of OH^- ions, which results in minimal membrane degradation (and viscoelastic change associated with the shift in R_2).

Whilst the QCM is able to provide useful insight into what is happening at the interfacial level of the ionomer, it does not provide chemical information on the degradation process. By applying in-line mass spectrometry to the humidification chamber exhaust, it is possible to distinguish between regimes of membrane degradation and stability.

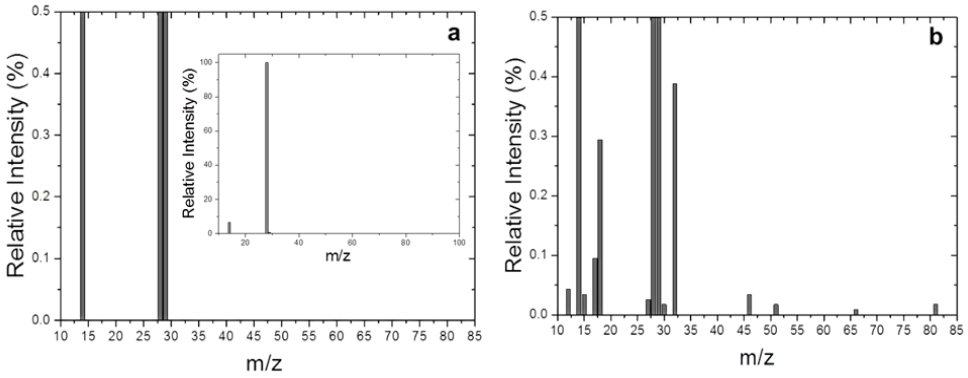

Figure 56: In-line mass spectrometry data for the composite resonator operating at: a) 55°C (inset shows the full relative intensity scale) and b) 65°C. (the results presented here are taken at 0% RH)

The mass spectrum is shown in Figure 56a and the inset represents the system when the composite resonator is operating at 55°C under a dry flow of nitrogen. This measurement is performed at 0% RH to simplify the analysis and remove water and constituent element peaks from the data. As expected, peaks appear at mass numbers 14, 28 and 29, indicating the presence of only nitrogen. This confirms that there is no discernible membrane degradation at 55°C, and that the system is completely closed to air (discounting the possibility of the formation of carbonates in the presence of CO_2).

Figure 56b, shows the mass spectrum when operated at 65°C at 0% RH (after 30 mins); the presence of additional mass number peaks are observed and summarised in Table 4.

Table 4: Mass number peaks registered in Figure 56b when the composite resonator is operating at 65°C and suggested corresponding elements and hydrocarbon fractures.

m/z number	Possible elements / fractures	m/z number	Possible elements / fractures
12	C^+	**32**	CH_3OH^+
15	CH_3^+	**46**	NO_2^+
17	$^{17}O^+$	**51**	$C_4H_3^+$
18	H_2O^+	**66**	$C_5H_6^+$
27	$C_2H_3^+$	**81**	$C_5H_5O^+$
30	$CH_2NH_2^+$		

Table 4 suggests possible element and hydrocarbon (side chain and / or backbone) fractures related to the mass numbers seen in Figure 56b; these correlate with the type of species expected for AAEM degradation products, as seen in Figure 20, Figure 21 and Figure 22 and [109-112]. Whilst it is not possible to confirm the exact products without specific knowledge of the proprietary AS-4 ionomer structure, the results clearly show the effect of operating at elevated temperature, and support the attribution of viscoelastic shifts seen on the QCM to ionomer degradation within the system.

Ionomer Degradation Conclusions

QCM analysis of AS-4 thin films under accelerated thermal degradation conditions has been performed as a function of the relative humidity of the gas stream and hence the ionomer's hydration state. Experimental results align with the theories proposed by Chempath *et al.* [105] and Macomber *et al.* [108], and suggest that humidity plays an important role in AAEM ionomer thermal degradation stability and that degradation can be minimised by ensuring a well-hydrated membrane that is operating in the 'swelling' mode; however, degradation through instability within the alkaline media cannot be entirely avoided. For this system, a RH above ~ 66% shows reduced membrane degradation, corresponding to the point at which the ionomer is fully solvated.

3.4.2.3. Carbonate Ion Interaction

The motivation for the carbonate ion interaction investigation is outlined in Section 3.2.4.3 and examines how ionomer hydration affects the AS-4's interaction with atmospheric levels of CO_2. In conducting this investigation a new *ex-situ* membrane test rig was developed as shown in Figure 33 and QCM base rig setup is employed with an additional air inlet stream as shown in Figure 32.

During this experiment, the AS-4 composite resonator is operated under a constant flow of 100 ml min^{-1} nitrogen at a specific relative humidity. With a stable resonant frequency, the humidified nitrogen flow is swapped to a humidified air flow also at 100 ml min^{-1} and at the same relative humidity. Maintaining the same relative humidity ensures that the effect of humidification is not contributing to the composite resonator's frequency response.

QCM gaseous environment stability

Firstly, the QCM's frequency response was investigated for operating in each gaseous environment. To do so, an unperturbed microbalance was operated in a nitrogen environment (100 ml min^{-1}) at 55 ^{o}C and 40% RH until stable in oscillation; the nitrogen flow was then replaced by a flow of air (100 ml min^{-1}). The measured frequency response is shown in Figure 57 where the blue section depicts operation in nitrogen and the white section, operation in air.

Figure 57 shows no significant change in the microbalance operation in either nitrogen or air. The ppm changes shown in Figure 57 are similar in both environments and are akin to the system's resolution determined in Section 3.4.1; suggesting that the QCM's operation is unaffected by operation in either environment.

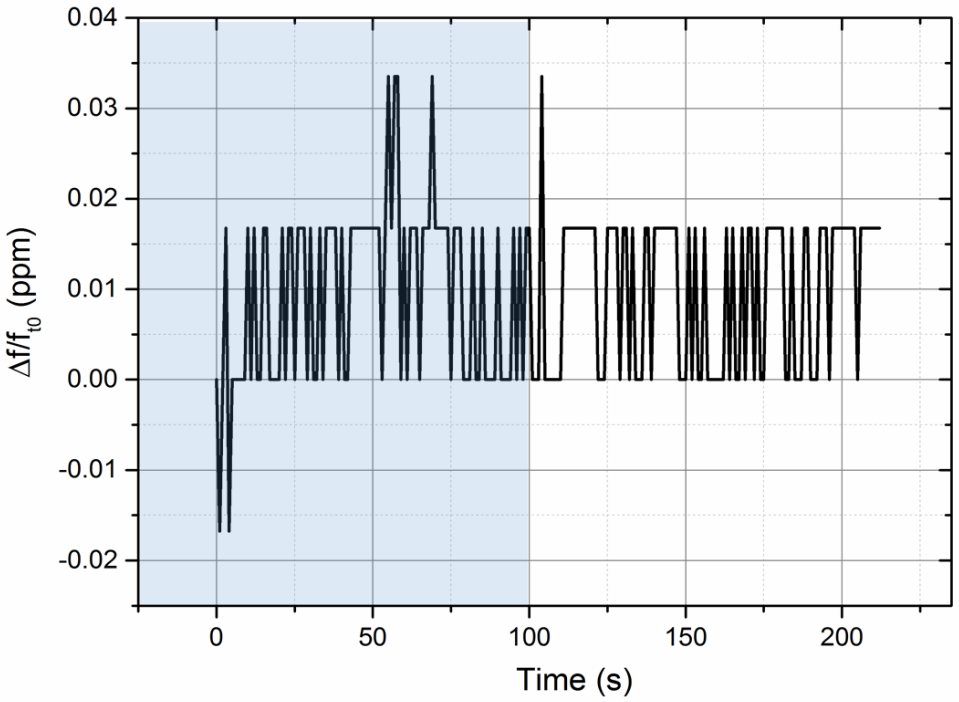

Figure 57: Unperturbed microbalance operation under a nitrogen and subsequently air environments at 55 ^{O}C and 40% relative humidity

Nafion Operation

The second stage of this investigation sees the same procedure described above conducted for a Nafion cast composite resonator. The purpose of this investigation is to act somewhat as a control; Nafion operation is expected to be unaffected by operation in nitrogen and air. For this investigation, a 33 nm Nafion layer is cast onto the microbalance electrode as described in Section 3.3.3 and operated at 55 ^{O}C and 40% RH. The frequency response for the Nafion composite resonator is shown in Figure 58 and shows a negligible change when the operating environment changes from nitrogen to air. In this case, the composite resonator's operation remains stable in both environments, indicating no evidence of deposition, depletion or fundamental changes to the composite resonator.

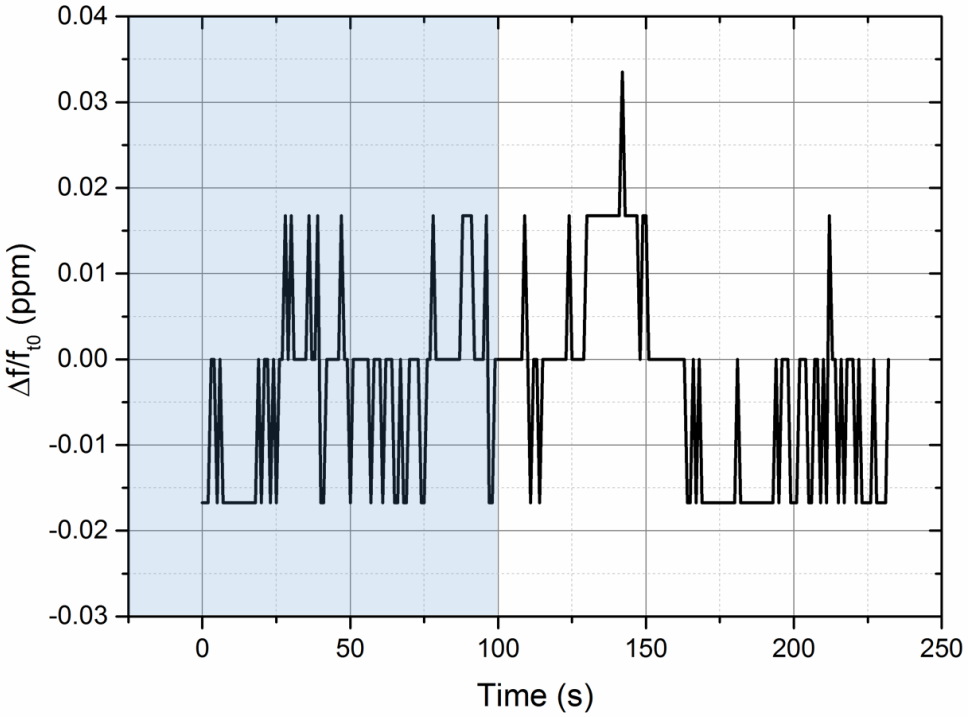

Figure 58: Resonant frequency and resistance response for a 33 nm cast Nafion microbalance operating under a nitrogen and subsequently air environment at 55 ^{o}C and 40% relative humidity.

AS-4 carbonate Ion Interaction

AAEM EIS Resistance Measurements

The first part of this investigation explores how humidity affects the high-frequency Ohmic resistance of a commercially available alkaline anion-exchange sheet membrane (A201, Tokuyama) operating in atmospheric levels of CO_2 (air).

Figure 59 shows the % change in the measured high-frequency resistance for A201 sheet AAEMs held at different RHs when operating in nitrogen (blue section) and subsequently in air of the same RH.

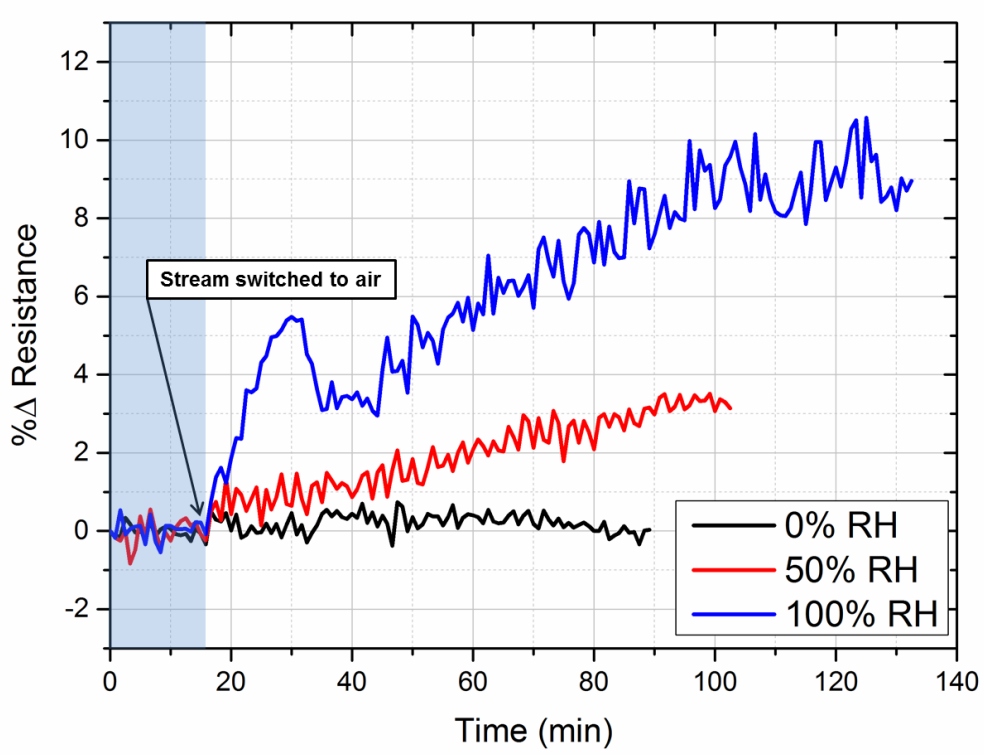

Figure 59: The % ohmic resistance change for the A201 membranes when operating in nitrogen (blue section) and subsequently in air containing atmospheric carbon dioxide at 0, 50 and 100% RH at 55 °C (represented as 50 s averaged intervals).

It can be seen that when the AAEM is operated at 0% RH, there is no significant or sustained change in resistance when the operating conditions are changed from N_2 to air. However, at 50% and 100% RH, there is a distinct increase in the membrane's steady-state resistance by 3.3% and 9%, respectively. It can also be seen that the transient response and associated stabilisation period of each membrane increase with RH; this is expected as at higher RHs there is more activity in the membrane with increased water available and a potential equilibrium between liquid water formation and removal.

The effect of humidity on performance for an OH^- conducting membrane when operating in air has yet to be considered in the literature; however, decreases in performance when operating in air have been demonstrated elsewhere in functioning fuel cell systems [118, 153]. In functional fuel cell

system studies, however, the measured shifts in performance cannot solely be considered as an interaction with CO_2 because of other factors, including the Nernstian effect of changing oxidant partial pressures of the fuel stream (O_2 → air) during the switchover (discussed elsewhere [50]) . The data presented in Figure 59 for the A201 membranes operating in atmospheric CO_2 suggest a distinct trend between its measured resistances with increasing operational humidity.

Active Microbalance Response

The QCM is used here alongside the findings from the AS-4 water uptake and hydration mechanism investigation results, presented in Section 0, to examine the effect of the AS-4 ionomer interaction with CO_2 at different relative humidities.

During this investigation, the ionomers' viscoelasticity changes are not a focus beyond the hydration mechanisms, as shown in Section 0. Therefore, traditional mass monitoring using the QCM is employed here as a means to understand the interaction of CO_2 (and carbonate ions) with the AS-4 ionomer whilst in various yet consistent hydration states.

Once cast and annealed at 0% RH, each drop-cast composite resonator was operated at a specific relative humidity, initially in nitrogen and subsequently in air (~400 ppm CO_2); this was repeated for eight freshly cast 65 ± 4 nm composite resonators, each operated at a specific relative humidity within the range of 0% - 88%, as shown in Figure 60a and b. Figure 60a shows the transient frequency response, and Figure 60b presents the processed steady-state differences for the same data. In both cases, the frequency shift for each microbalance response is reported in f/f_0 (ppm) to normalise the microbalance's inherent resonant frequency and thus allow direct comparison.

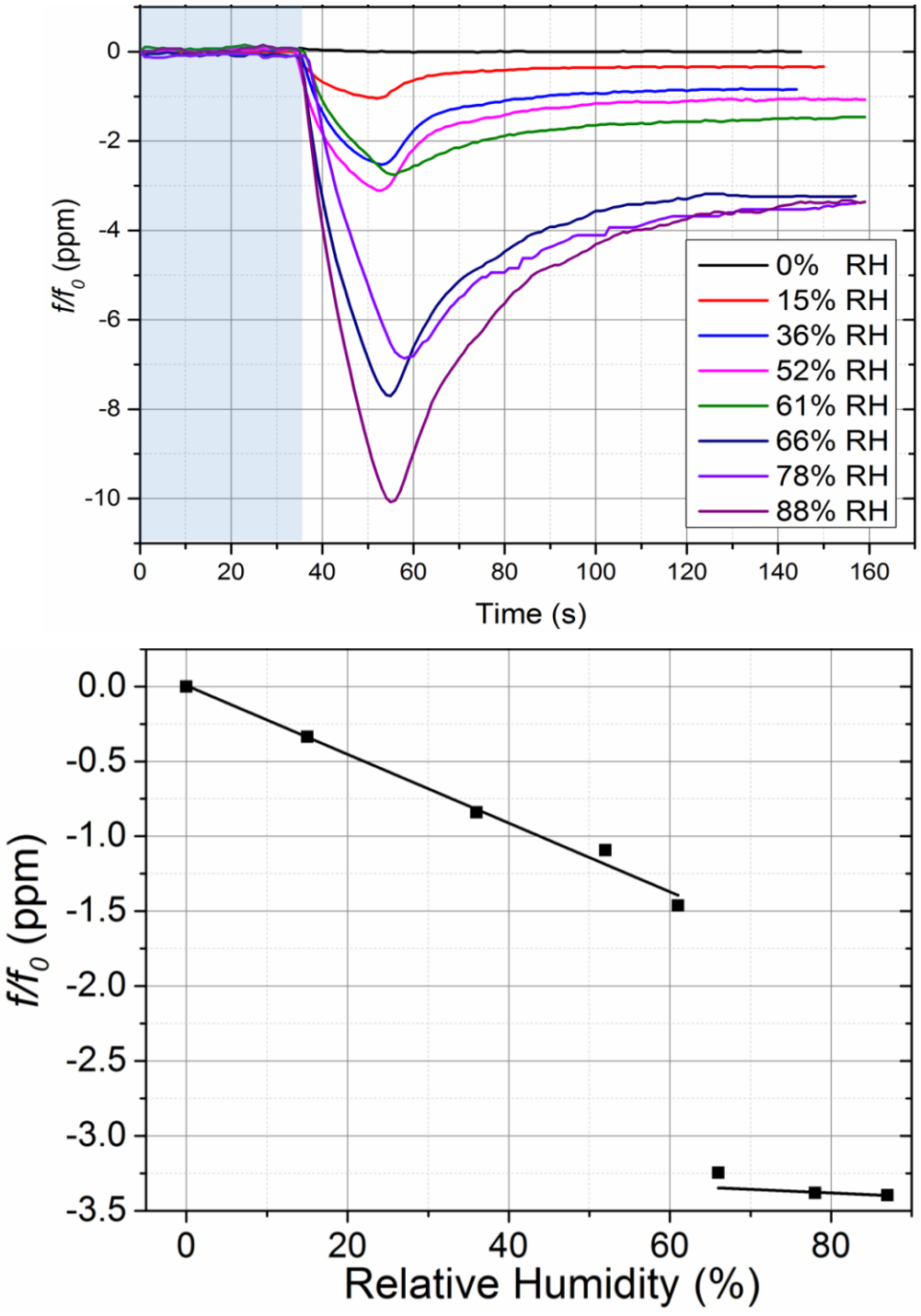

Figure 60: (a) Transient frequency responses for AS-4 composite resonators operating in nitrogen and subsequently in air at a range of RHs. (b) Change in the composite resonators' steady state frequency response when operating in nitrogen and subsequently in air at a range of RHs.

The transient frequency response shown in Figure 60a reveals an immediate drop in the composite resonator's frequency upon the introduction of air into the system. In general, the magnitude of the frequency drop increases with the system's relative humidity. After the initial frequency drop, the composite resonator's resonant frequency increases and settles at a new stable steady-state value. The difference between the steady-state operation in N_2 and in air is processed and presented in Figure 60b.

This initial frequency drop shown in Figure 60a is not experienced for the AS-4 ionomer operating at 0% RH, nor with either the unperturbed or Nafion composite resonators shown in Figure 57 and Figure 58. This suggests that the initial frequency drop is a result of the (partially) hydrated ionomer's interaction and equilibration with the dissolved CO_2 in the contacting operating environment. The sheet membrane resistance study presented in Figure 59 also shows a similar phenomenon occurring at 100% RH where after the operating environment is changed, the membrane's resistance initially increases sharply only to fall soon after.

Figure 60b shows that for a composite resonator held at 0% RH (when there is no water in the system); there is no change in the resonator's resonant frequency when switched from operation in nitrogen to air. This agrees with the membrane resistance result seen in Figure 59 for 0% RH. In the range between 0% and 62% RH, Figure 60b shows a linear increase with each composite resonator's relative steady state frequency shift with increasing RH when switched to operation in air. At 66% RH, the composite resonator shows a step change of 1.8 ppm from the investigation conducted at 62 % RH. Between 66% - 88% RH, increased operational RH has shown to have a significantly smaller effect on each of the composite resonators' frequency shifts.

The AS-4 hydration investigation presented in Section 0 suggests that the ionomer initially undergoes a solvation period ($\leq$ 66% RH) in which ion conducting channels begin to open as cationic headgroups become fully solvated, followed by swelling of these ionomer channels between 66% and 100% RH.

It is expected that access of CO_2 to the pore network structure will have an effect on the extent of interaction with the AS-4 ionomer. As the RH increases during this investigation, it is possible that more CO_2 is able to permeate into the humidified channels within the membrane. This would allow an increased production of carbonic acid within the system (Equation (18)), which can react with the hydroxyl anions (Equations (18) - (22)) [121]. With increasing RH, the system is expected to become more acidic as the CO_2 uptake increases (and hence carbonate ion formation); more of the cationic head groups interact with the increased concentration of available carbonate ions which results in an effective mass increase (decreasing f/f_0). The initial frequency drop seen in the transient response in Figure 60a suggests the presence of equilibrium between the carbonate ion interaction and the ionomer. The magnitude of the initial interaction increases with increasing RH as potentially more dissolved CO_2 is able to permeate into more hydrated channels and thus increased access to and interaction with the cationic head groups before equilibration begins. Figure 60b suggests that the extent of CO_2 uptake increases linearly with humidity between 0 - 62% RH; however, between 62% - 66% RH there is a significant step change which remains approximately constant between 66% and 88% RH.

Figure 60a and b suggests a correlation between the degree of membrane hydration and the extent of CO_2 uptake. During the linear solvation regime, the results suggest a corresponding linear opening of the membrane pores allows increasing access of CO_2, and hence more interaction between cationic head groups and carbonate ions. Once the channels are thought to be fully open ($\geq$ 66% RH as suggested by [113]), all cationic sites can become accessible as the ionomer is fully solvated and changes in RH have little effect on CO_2 uptake.

Carbonate Ion Interaction Conclusion

Interaction of CO_2 with AAEMs is a potentially potent cause of performance degradation. Results here suggest that loss of membrane ion conductivity on exposure to CO_2 is a function of membrane hydration; increasing membrane hydration leads to more substantial resistance increases. Thin-film ionomer studies using the QCM have allowed for very accurate measurement of CO_2 uptake (carbonate interaction) into the membrane. Exposing the cast

membrane to atmospheric levels of CO_2 in air and operating at the typical operating temperature of the membrane in a device (55 °C), suggests that there is a correlation between CO_2 uptake and the level of hydration of the membrane; the pore opening regime resulting in a linear increase in CO_2 uptake as water permeates the pore system and cation headgroups become increasingly accessible to CO_2. The transition to the pore swelling phase sees a step increase in CO_2 uptake as the network is fully open and continues to swell with water but does not lead to a significant increase in CO_2 uptake with increasing RH.

3.5 Conclusions

During this study, the development of AS-4 cast composite QCM's have been established through a novel in-situ casting procedure. The composite resonators developed throughout this study range in ionomer layer thicknesses of $20 - 100$ nm. These thicknesses have been determined using the Sauerbrey equation and were chosen to ensure fulfilment of the standing wave condition, even when loaded.

Throughout this study, the composite resonator has been implemented within bespoke rig designs and repeatedly tested and calibrated for use in each investigation. In each case the frequency response contribution has been confirmed only to be a factor of the conditions under investigation.

The study presented within this chapter has encompassed a detailed analysis of the thin film AS-4 ionomer using the QCM through three individual investigations. These investigations have been discussed and concluded in the necessary sections; however, a brief overview is given here alongside suggested future work.

The initial work investigated the water uptake, swelling characteristics and sorption mechanics of thin film Nafion and AS-4 ionomers from the vapour phase. The Nafion investigation provided *in-situ* results that agreed with proposed theories in the literature by authors such as Zawodzinski *et al.* and provided a useful means by which to validate the experimental setup for the relatively unknown AS-4 ionomer investigations. The first AS-4 investigation presented within this study has suggested the ionomers hydration mechanisms occur in part similar to that of Nafion with two distinct regimes; the first being a solvation period at RHs $\leq 66\%$ in which adsorbed water is used to solvate ions within the ionomer followed by a swelling regime at higher RHs.

The second part of the study explores the AS-4 ionomer instability and degradation when operated at elevated temperatures as a function of its hydration state. The theories presented in this section indicate that the degradation pathways are more dominant when the ionomer is partially hydrated and specifically during the solvation period as defined by the initial

investigation. When the ionomer is operating during the swelling regime, the results indicate that the ionomer performs more stably within the alkaline media and shows fewer signs of degradation. The experimental results obtained align with the theories proposed by Chempath *et al.* [105] and Macomber *et al.* [108], and implies that humidity plays an important role in AAEM ionomer stability within the alkaline media and that degradation can be minimised by ensuring a well-hydrated membrane that is operating in the 'swelling' mode.

The final investigation presented within this chapter uses sheet AAEM EIS in conjunction with thin film AS-4 composite resonators to assess the carbonate ion interaction as a function of ionomer hydration. The findings suggest that during the solvation regime there is a linear increase in CO_2 uptake as channels hydrate and water permeates the pore system and cation headgroups become increasingly accessible to CO_2. The transition to the pore swelling regime sees a step increase in CO_2 uptake as the pore network becomes fully open and additional water is used for swelling. Increasing RH does not however result in increased CO_2 uptake.

3.5.1 Future work

A further specific investigation into the transient water uptake at varying ionomer thicknesses and thus an analysis of the sorption kinetics will provide an interesting further insight into the AS-4's hydration mechanisms. Equally an examination of the ionomer hydration and dehydration cycling will provide useful insight into how the water uptake and hydration mechanisms change (or creep) with cycling and consequently how factors such as degradation and carbonate ion interaction are affected by changing ionomer characteristics. This investigation will provide useful insight for operators regarding operation at different stages of the membrane lifespan.

A supplementary transient degradation study will help elucidate the kinetics of the instability process and may provide guidance on how individual degradation pathways dominate the kinetic responses. This future analysis may provide operators with the information required to halt specific degradation mechanisms as a means to accessing the kinetic advantage of operating at elevated temperatures.

Finally, to further understand the carbonate ion interaction phenomenon, an additional transient study is proposed to fully elucidate the effect that hydration has on the ionomer's ability to form immobilised salts. The transient study should focus on the initial frequency response shown in Figure 60a to determine the effect additional RH has on the initial interaction with the ionomer and the subsequent kinetics of the carbonate ion interaction.

4 Fouling detection in high temperature media

The work presented in this chapter advances the BAW resonator's operation further; operating with a heavy crude oil sample, under variable pressure and temperature and with surface developed iron layers. This study outlines the development and initial application of a high-temperature gallium orthophosphate ($GaPO_4$) BAW resonator for in-situ fouling detection during transportation and refining of heavy crude oil.

4.1 Introduction

Future renewable technologies such as fuel cells still have technical hurdles to overcome before wide-spread application. Therefore, during the transition to the low carbon economy the world will continue to rely on traditional electricity generation methods. It is therefore critical that elements of the future focus remain on increasing the efficiencies and attaining cost reduction (and stabilisation) of processes such as crude oil refinement to meet the ever increasing demands in the short term.

With dwindling supplies of traditional crude oil; there has been significant interest by the industry to draw on alternative resources such as heavy crude oil. Heavy crude oil is a plentiful resource [154] which can act as a viable substitute for conventional crude oils [155, 156]. However, variation in heavy crude composition makes transportation and refinement of these heavily viscous products difficult. The high viscosity and constituents of heavy crude oil require alteration of conventional transmission transport pipelines and refinery equipment. These alterations include dilution, heating, partial upgrading, oil-in-water systems and core annular flow. The effect of each of these improved transport methods is not currently well understood, and in many cases may promote fouling and / or corrosion within the transportation pipelines and refinery equipment.

This chapter outlines the development of an *in-situ* electrochemical feedback sensor for heavy crude oil pipeline fouling detection throughout the production chain. The work presented here tests the gallium orthophosphate resonator's ability to operate not only at elevated pressure and temperatures seen in heavy crude transmission lines and refinery equipment but also with an electrodeposited iron layer and in contact with a viscous contacting media. The gallium orthophosphate crystal microbalance (GCM) provides a unique assessment of how the conditions and also the composition / grade of oil samples affect the rate of fouling at the pseudo iron interface. Subsequently, the development and production of an on-site device to assess the rate and extent of fouling of particular grades of heavy crude oil is proposed in collaboration with the QNRF.

4.2 Literature Review

4.2.1 Crude Oil

Crude oil is classified as all liquid organic compounds under reservoir conditions. It is a non-uniform material which has a complex mixture of gaseous, liquid and solid hydrocarbon compounds that occur in sedimentary rock deposits the world over.

The history of crude oil begins over 5000 years ago in shallow wells; its seepage was used as a means for waterproofing, lighting and painting. Today, crude oil is one of the most consumed materials in modern society, providing more than half the world's energy supply in its refined forms. It is also used to generate raw materials for plastics and other products, as well as fuel for energy, heating and transport. Crude oil is made up of a complex mixture of hydrocarbon compounds, containing varying quantities of nitrogen, oxygen and sulphur compounds [157].

Crude oil composition varies considerably based on its reservoir location, such that even two adjacent wells could potentially produce different grade crudes. Similarly, the oil drilled at the top of the well could be (and often is) considerably different in composition to that drilled from further depths. Table 5 shows the broad elemental composition range for traditional crude oils [158].

Table 5: Traditional crude oil composition [158].

Element	Composition Range (wt %)
C	83.0 - 87.0
H	10.0 - 14.0
N	0.1 - 2.0
O	0.05 - 1.5
S	0.05 - 6.0
Metals	0.01

4.2.1.1. Heavy Crude Oil

Crude oil is often classified as conventional, heavy or extra heavy; these are usually defined by a combination of specific gravity [157], and the American Petroleum Institute (API) gravity as shown in Figure 61.

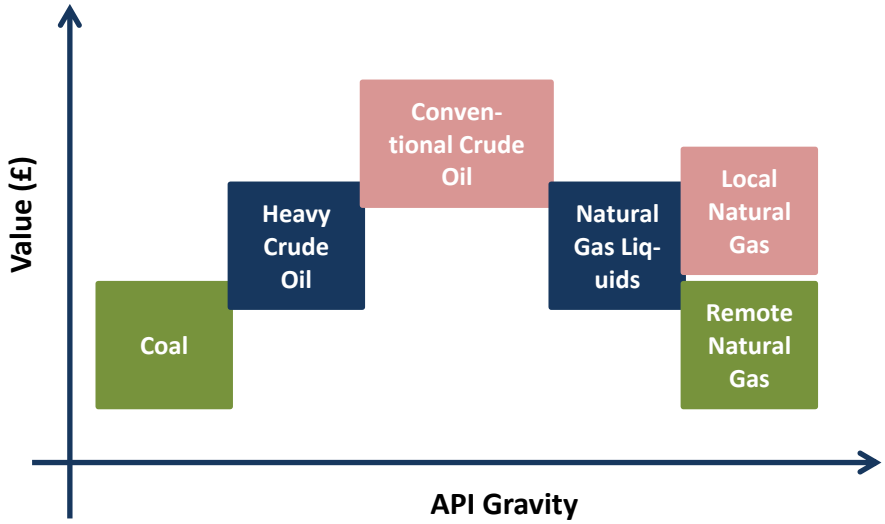

Figure 61: API gravity classification

Heavy crude is the main focus of this investigation and is defined by a $\leq 20^{o}$ API and typically a sulphur content above 2% wt.

All forms of crude oil contain a mixture of alkanes, cycloalkanes, aromatics, polycyclic aromatics, sulphur, nitrogen and oxygen containing compounds plus many more. The main proportion of crude oil contains alkanes, cycloalkanes and aromatics, with a larger proportion of polycyclic aromatics present in heavy crude. The complex composition of crude oil makes characterisation by molecular type or elemental analysis difficult and consequently, it is commonplace to characterise by hydrocarbon group type [159, 160].

The SARA separation analysis shown in Figure 62 is most populous in literature and separates the crude oil components into four chemical classes based on differences in solubility and polarity. The SARA fractions are Saturates (including waxes), Aromatics, Resins and Asphaltenes [161, 162].

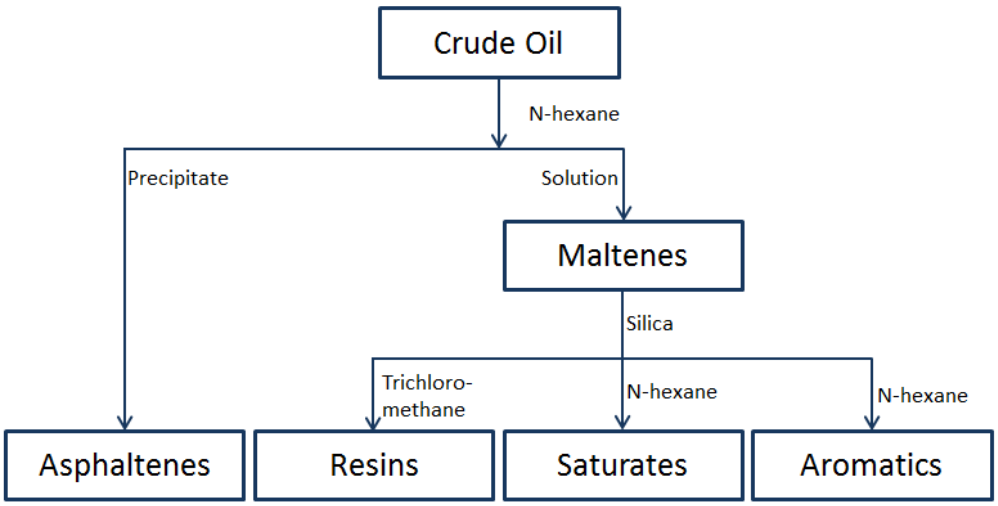

Figure 62: SARA separation analysis schematic

Saturates include straight chained, branched alkanes and cycloalkanes. They are single bonded and non-polar hydrocarbons. Cycloalkanes can comprise of one or several rings, often with alkyl side chains. Saturates are the lightest fraction in crude oil and the proportion of saturates decreases with increasing molecular weight fractions. Saturates contain many subcategories, the most important of which are waxes ranging C20 to C30; consisting mainly of straight chain alkanes [161]. At low temperatures, wax precipitates as a solid and affects the emulsion stability properties of crude oil.

Aromatics include benzene and its structural derivatives and are present in all crudes and contain aromatic rings, alkyl chains and cycloalkane rings. Aromatics are classified by the number of aromatic rings in the molecule and are prefixed as mono-, di-, and tri-aromatics. Polar, higher molecular weight aromatics can also be classified as a resin or asphaltene fraction [162].

Resin contains polar molecules made up of nitrogen, oxygen or sulphur and is defined as the fraction soluble in light alkanes such as pentane and heptane, but insoluble in liquid propane. Resins are structurally similar to asphaltenes, but have a lower molecular weight (typically $\leq$ 1000 g/mole); they also have a higher H/C ratio (1.2-1.7) than asphaltenes (0.9-1.2) [163]. As shown in Figure 62, asphaltenes are the polar, non-volatile fraction of crude that is insoluble in n-alkanes (i.e. pentane or heptane). The polarity,

molecular weight and aromaticity of precipitated asphaltenes generally increase with increasing carbon number of n-alkane precipitant.

Asphaltenes are crude oil's heaviest components; their precipitate appears black / brown in colour and has an undefined melting point and decomposes at temperatures in excess of 300-400 ^{o}C (at atmospheric pressure). Asphaltene precipitation is shown to be affected by changes in temperature [164, 165], pressure [166-168] and oil composition [169].

The motivation for this work stems from the need to develop an *in-situ* sensor that can elucidate the fouling properties of specific compositions of heavy crude oils and the effect of operating conditions at various points within the production chain. A specific emphasis is placed on asphaltene precipitation throughout this study given its unpredictable solubility within the bulk accelerated by changes in operating conditions as explored in Section 4.2.3.

4.2.2 Transportation and Refining

To convert crude oil into its useful products, it must first be transported to a refinery. Methods of transport have varied over the decades from disused whisky barrels to trucks with the most popular being pipeline transportation. Before transportation through the pipeline, the crude oil mixture that comes out of the ground is pre-treated and impurities such as water, sand and gas are stripped away from the mixture [154, 170]. The oil is transported to the refinery in transmission pipelines, which can be up to 56" diameter and are typically made of carbon steel.

With the necessary move to heavy crude oils to meet consumer demands, pipelines and refinery equipment that previously processed conventional crude oils are now subject to the more variable composition SARA components in the heavy crude mixture. However, without a better understanding of how these components specifically affect the system's flow assurance and the subsequent implementation of the necessary amendments, pipelines and other refinery equipment are subject to fouling and arterial blockages.

4.2.3 Fouling

Fouling in a system is the formation of an undesirable phase that interferes with normal operation / processing. Foulant often appears as a solid, but can also exist as a liquid in the gas phase operation or an emulsion in the liquid phase [171]. The main source of pipeline fouling from heavy crude oil comes from the saturate and asphaltene fractions, with smaller contributions from water emulsions and organic solids.

Fouling (or deposition) in pipelines, risers and processing equipment can have severe effects on flow assurance and oil production efficiency. The fouling build-up in pipelines and other refinery equipment can cause increased pressure drops, resulting in reduced throughput, higher utility costs and reduced revenue. In some cases, pipelines and processing facilities can plug and rupture, halting production altogether and lead to potentially huge economic and environmental losses.

4.2.3.1. Waxes

The wax present in crudes consists primarily of paraffin and naphthenic hydrocarbons; (C18 - C36) and (C30 - C60) respectively. The hydrocarbons state of matter (gas, liquid or solid) is defined by the temperature and the pressure of the crude. As the crude flows through a cold pipe (with a wall temperature below the cloud point of the crude mixture – e.g. on the seabed) macrocrystalline and microcrystalline crystals of wax may form on the wall. Wax crystals continue to grow until the whole inner wall is covered, with increasing wax wall thickness, there is a corresponding increase in pressure drop across the pipe. To maintain a constant flow rate, the pumping power must increase and thus the overall power requirement for the crude transport increases.

The arterial blockage problems caused by waxes can be controlled by heating the pipe to above its cloud point and insulation. However, with these systems not commonly installed, frequent and expensive chemical antifoulants and pigging operations (Figure 63) have become necessary [170, 172].

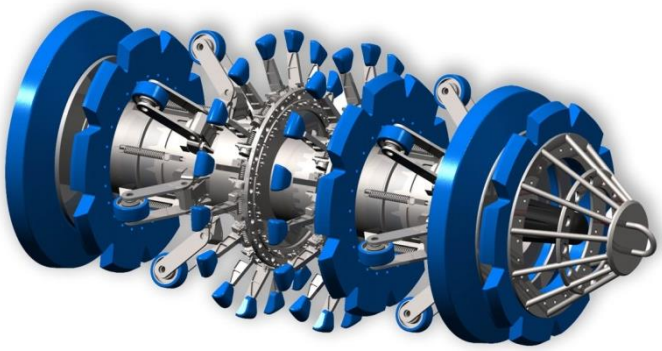

Figure 63: In-line pig schematic

4.2.3.2. Asphaltenes

Heavy crude oils contain large amounts of asphaltenes which can destabilize and precipitate due to changes in temperature and pressure, shear (turbulent flow), the presence of CO_2 as well as any change in the oil composition [173-175]. Asphaltene precipitation and deposition presents major issues for operators as these processes can occur in various parts of the production chain. Depositions can begin at the well, where they reduce the reservoir's wettability [176] and thus oil recovery, plug rock pores and deposit directly onto the well walls [177-180]. Destabilized asphaltenes are the largest cause of arterial blockages in pipelines and wellbores [181], they continue to plague the production all the way through and even deposit onto and destroy refinery equipment and catalyst material [182-185].

To mitigate the economic and environmental costs that could arise as a result of asphaltene precipitation from an oil feedstock, researchers have worked extensively on two primary solutions; asphaltene conversion and rejection.

Asphaltene conversion is the process of reducing the asphaltene aggregate concentration (see Section 4.2.3.3) in an oil through the addition of diluents, solubilizing agents and chemical inhibitors [186-188] or blending with stabilizing oils [189]. This is an expensive process which when carried out incorrectly can potentially have worse ramifications than the original feedstock; therefore, intimate knowledge of the oil sample and additives is required.

Operators often over-specify the quantities of diluents added to the oil to meet the pipelines density and viscosity specifications during transport to refineries [175]. The diluent is sometimes recovered and recycled at the refinery for later use at great expense.

Asphaltene rejection is carried out using one or more of: solvent deasphalting, emulsion extraction [190, 191], ultrafiltration [192], selective oxidation of heteroatoms, carbon rejection and most commonly selective adsorption [193]. Asphaltene rejection methods are less specific and often aim to convert asphaltenes into coke and other fuel sources [175].

4.2.3.3. Asphaltene Deposition

Asphaltenes comprise a range of individual molecules (with molar masses ~500 g/mol) of varying and unknown compositions often defined by a solubility group and characterised using its bulk properties. Asphaltenes often appear black / brown [194] and are generally comprised of a pericondensed polyaromatic backbone with alkyl linkages, paraffinic rings and aliphatic side chains with nitrogen, oxygen and sulphur heteroatoms. The heteroatoms form a range of functional groups, of which the most common are given in Table 6 [195, 196]. Recent ion cyclotron resonance mass spectrometry studies have confirmed asphaltenes follow the island model / configuration in which a polyaromatic core is surrounded with pendant-like alkyl groups [197, 198].

Table 6: Asphaltene heteroatom's common functional groups

Heteroatom	N	O	S
Functional Groups	Pyridine Quinoline Pyrrolic	Hydroxyl Carboxyl Carbonyl	Sulfoxide Thiophene Sulfidic

Asphaltenes exist as a distribution of self-assembled nanoaggregates. Aggregation varies based on the asphaltene concentration [199, 200], solvent power of the oil matrix / suspending solution [201], temperature and pressure [202, 203] and the presence of resins [204]. The Yen-Mullins model indicates that nanoaggregates further combine to form aggregates (clusters or

floccules) that are suspended within the matrix that can precipitate [200]. A small angle neutron scattering (SANS) study by Simon *et al.* has shown these clusters to range in size between $3 - 10$ nm [205], whilst other work by Mullins *et al.* has shown nanoaggregate clusters to be closer to 5 nm in size [200, 206]. Gray *et al.* have described the nanoaggregates formed by the asphaltene molecules to follow supramolecular assemblies rather than the typical micelle assemblies; a direct consequence of the variety of functional groups that the heteroatoms can form [207]. Gray *et al.* continue to discuss that the asphaltene intramolecular forces are a combination of hydrogen bonding, acid-base interactions, coordination complexes, Van de Waals and π-π stacking. Whilst these forces are individually weak, supramolecular chemistry suggests that together they combine to provide strong interactions. It is these forces that cause asphaltene molecule agglomeration that are thought to feature in asphaltene-surface interactions, and hence deposition.

Whilst asphaltene deposition is an undesirable phenomenon throughout the processing chain, understanding asphaltene-surface interactions will help to both partially upgrade the oil product by selective removal of asphaltenes that may precipitate and cause depositions (rejection) as well as manage additives and conditions under which depositions may occur (conversion).

Asphaltene deposition is a complex process that is affected by many variables; this has resulted in large inconsistencies within the literature [175, 208] and makes understanding the fundamental processes difficult. Some of the key variables that affect asphaltene deposition are discussed in this section; however, for an exhaustive review, the reader is directed to [175].

Suspending Solvent

Most asphaltene deposition work in the literature is carried out using model oil (C5-C7), precipitated asphaltenes (from a range of sources) and employs various sorbing surfaces including glass, rock, metals, metal oxides, polymers and many more. The source and concentration of the asphaltenes used in each investigation affect its aggregation and hence deposition properties; making a direct comparison between studies difficult. Equally the model oil / solvent used in many investigations to suspend the asphaltenes also has a

significant effect on the deposition characteristics, for example strong solvents such as nitrobenzene cause ionization allowing ion exchange mechanisms to dominate [209], whilst weak solvents allow increased asphaltene molecule aggregation and hence more successful deposition [208, 210, 211].

Asphaltene Molecules

The physical properties and characteristics of the asphaltene molecules vary considerably depending on their source. Many current studies isolate asphaltene from a range of sources including crude (conventional and heavy), shale oil, residua, processed and cracked oil. The size and physical characteristics of the asphaltene molecules govern how they form nanoaggregates and subsequently aggregates [184], which has a direct impact on how strongly they are able to interact with the surface as well as its diffusion rates in solution [199].

SARA Composition

As discussed in Section 4.2.1, crude oil is made up of several fractions including saturates, aromatics, asphaltenes and resins; each fraction has different chemical and physical properties and affects asphaltene deposition in a variety of ways. Aromatics and saturates have been shown not to affect the asphaltene deposition as they do not adsorb and therefore compete for active sites, resins have however shown to have varying effects on asphaltene deposition [212]. Studies within the literature indicate that the smaller sized resins molecules are able to diffuse through the bulk of the suspending solution to the sorbent sites more quickly than the asphaltenes; however, the asphaltene-asphaltene interactions prove more significant and displace the resins on the sorbent surface [208, 213, 214]. A QCM study by Ekholm *et al.* [213], has shown the addition of resins to a model oil increased the thickness of the deposited layer compared to asphaltenes alone, this was thought to be the result of either intercalation of resins within the asphaltene aggregates or the termination of aromatic asphaltenes reorganisation into compact layers by the resins [215]. Another study by Castillo *et al.* which showed indefinite asphaltene growth proved that the addition of resins disrupted and limited the growth of the deposition [216]. Adams [175] has suggested

that the limitation on asphaltene deposition growth as a result of resin interaction supports the supramolecular aggregate model put forward by Gray *et al.* [207].

Water

The hydrogen bonding between asphaltene molecules and subsequently their aggregates has also been shown to be affected in the presence of water [217]. As before, with the molecule aggregation affected, the asphaltene-surface interactions are also been shown to be affected by the presence of water [218]. A study by Jeon *et al.* has postulated that the presence of water does not only reduce deposition through its effect on asphaltene aggregation but also because the water molecules actively compete for surface adsorption sites [219]. The presence of water has also shown to corrode pipelines and other processing equipment, leaving behind metal oxide surfaces [181, 219]. A study by Nalwaya *et al.* has shown that the presence of metal compounds to has a dramatic effect on the solution's polarity, and resulted in elevated asphaltene precipitation and deposition [220].

Temperature

Pierre *et al.* have shown asphaltene aggregates to decrease in size with increasing model oil suspension's temperature; relating to weaker asphaltene-surface interactions and hence reduced depositions [203, 221]. However, a study by Xing *et al.* has shown that this reduced deposition only occurs when investigating short reaction times [222]. However, industrial patent applications that focus on oil feedstocks (rather than asphaltene-model oil suspensions) have reported increased deposition (on a range of different media) at higher temperatures ($\geq$ 200 ^{o}C) [223-225]. This phenomenon is thought to occur as model oil solutions with dissolved asphaltenes in solvents are designed to study asphaltene behaviour in controlled environments; however, these studies do not explore the harsh realities under which the industry must operate. Industrial applications study asphaltene deposition in viscous crudes and heavy oil vacuum residue and must apply heat to reduce the viscosity of the heavy oils.

Enhanced deposition may be seen at elevated temperatures in feedstock oil as the viscosity decreases, increasing diffusion rates of the asphaltenes within the oil, as well as releasing aggregates from the association and thus exposing more active sites. This phenomenon results in the formation of small aggregates which are able to move through the oil and interact with the surface [175].

The variation in the literature indicates that there is no current conclusive method by which to understand fouling characteristics of an incoming heavy crude oil feedstock. Whether the user is interested in using selective adsorption (or other rejection techniques) or a method of conversion such as the implementation of anti-foulant chemicals, an industry standard technique to understand the conditions that govern asphaltene deposition under conditions akin to those used in industry does not exist.

Nalco Co. is a world leader in asphaltene conversion and anti-fouling chemical manufacture [226-228]. As part of their investigations, they have developed a range of large volume experiments to study the asphaltene deposition of a particular heavy crude oil feedstock. The patent literature and input from their R&D scientists indicate that their *ex-situ* analysis takes roughly 30 days before feeding back to the field on how to proceed with handling and processing of the new feedstock [229].

High volume, time-intensive studies for each new oil well is an impractical solution to understanding the asphaltene precipitation characteristics of a given heavy crude feedstock. The following sections discuss the development of an *in-situ* BAW resonator process for the elucidation of the asphaltene deposition characteristics of an incoming feedstock in a low volume, non-time intensive study. The proposed device will provide the user with a process by which to change and understand conditions (temperature and pressure) either to replicate those along the production chain (conversion) or to promote precipitation for partial upgrading (rejection) for specific feedstock oil using low volume and non-time intensive studies.

4.2.4 Microbalance Application

The application of a BAW microbalance as an *in-situ* oil fouling sensor is of much interest to both industry and academia. It should be noted here that the previously used quartz crystal microbalance in Chapter 3 is not useful for this application as will be discussed in Section 4.4.1 as the oil temperatures for this application can be higher than the critical twinning temperature of quartz and thus a high temperature alternative microbalance had to be identified.

Microbalances are very versatile in their operation, and consequently piezoelectric materials that can operate stably and consistently at high temperature are extremely desirable. For this reason, much research has and continues to be done in developing next generation piezoelectric materials that can successfully satisfy the high-temperature application need. Some of these are discussed below [230, 231].

4.2.4.1. High-Temperature BAW Resonators

Lithium Tetraborate ($Li_2B_4O_7$)

$Li_2B_4O_7$ is a pyroelectric material, i.e. it produces an electrical potential when exposed to changing temperatures. Specific cut angles are useful as piezoelectric devices; however, pyroelectric properties combined with low ionic conductivity limit the frequency range at high temperatures. However, some studies have shown at particular cut angles, the resonator can achieve zero temperature coefficients making $Li_2B_4O_7$ useful for mass monitoring in variable temperature conditions. Further studies have shown that lithium tetraborate undergoes a phase transition around 500 ^{O}C, affecting its ferroelectric properties and limiting its use as a high-temperature sensor [230].

Aluminium Nitride (AlN)

Although AlN is able to operate at temperatures up to 1150 ^{O}C, it has poor oxidation resistance and impurities drastically reduces the resonator's reliability at high temperature [232].

Langasite ($La_3Ga_5SiO_{14}$) (LGS)

LGS has proven stable oscillation up to 1400 °C, with reliable results recorded up to 1000 °C. LGS is very similar in structure to quartz; however, it does not seem to undergo a phase transition at elevated temperatures and has previously been used in a range of high-temperature resonator investigations [230, 233, 234].

Gallium Orthophosphate (GaPO4)

Gallium orthophosphate has a Curie temperature of 970 °C and has been successfully implemented as an *in-situ* mass monitoring device for solid oxide fuel cell coking studies at ≥ 700 °C [137, 138].

Both the gallium orthophosphate and LGS share similar upper operating temperatures, 970 °C and 1000 °C, respectively. However, Fritze *et al.* [233] demonstrated through crystal impedance spectroscopy that the $GaPO_4$ microbalance dissipates significantly less energy than the LGS, hence improving its Q-factor (Section 2.3.2). Consequently, when developing the LGS crystals, operators must employ doping techniques to reduce energy losses at high temperatures. The choice of microbalance for this investigation is further discussed in Section 4.3.2.

4.2.4.2. Electrode Iron Deposition

To develop a microbalance for use as an *in-situ* fouling sensor, the GCM electrode in contact with the heavy crude oil requires a representative surface. This will allow the resonator to detect similar (if not more) levels of asphaltene deposition, as would be expected within the pipeline or refinery equipment, allowing the GCM to act as a pseudo fouling analyser / early warning sensor. Therefore a rigid iron layer was to be deposited onto the electrode surface; this can be done through a variety of methods including, but not limited to, electrodeposition or sputtering.

Whilst much of the equipment and pipelines involved in the oil refining industry are typically made from carbon steel, iron deposition is somewhat more convenient; yet still provides an accurate *in-situ* representation of the fouling processes occurring at the surface. Iron provides a large amount of

flexibility; it can be deposited as a hard and brittle metal which can become soft and malleable by heat treating. Similarly, iron can be deposited as a soft and ductile metal which can be hardened through the use of carburizing, cyaniding and nitriding. Kepple *et al.* have shown the fatigue strength of surfaces prepared by case hardening electrodeposited iron is equal to the best commercial rolling element bearing materials [235]. Like typical 'refinery iron', electrodeposited iron can be welded or plated by other materials and due to its high purity shows reasonable corrosion resistance (as would be expected from carbon steel).

4.2.4.3. Iron Electrodeposition

Iron plating by electrodeposition represents a mature process with applications dating as far back as the First World War; including electrotype production in Russia and weapon rebuilding in Germany for example [236, 237].

The process of iron electrodeposition can be carried out using a range of electrode configurations, plating baths (such as ferrous sulphate and ferrous chloride baths), as well as operating conditions. There is significant yet conflicting information available in the literature regarding the electrodeposition technique and theory, but a typical methodology and setup is described here.

In a typical 3-electrode setup, the object of interest (to be plated) is connected to a potentiostat and held as the working electrode within an electrolyte such as iron(II) sulphate at a constant pH and temperature along with a reference and counter electrode, as shown in Figure 64. The counter electrode allows the bath to be held at a specific potential whilst the reference electrode provides control over the electrodes potential. If a BAW resonator such as the QCM is applied as the working electrode within this system, the *in-situ* mass monitoring of the electrodeposition is made possible as the QCM operates as an electrochemical QCM (eQCM) as discussed in Section 2.7. The operation of the eQCM allows a secondary measure to determine the efficiency of the electrochemical deposition process as discussed in Section 4.3.3.

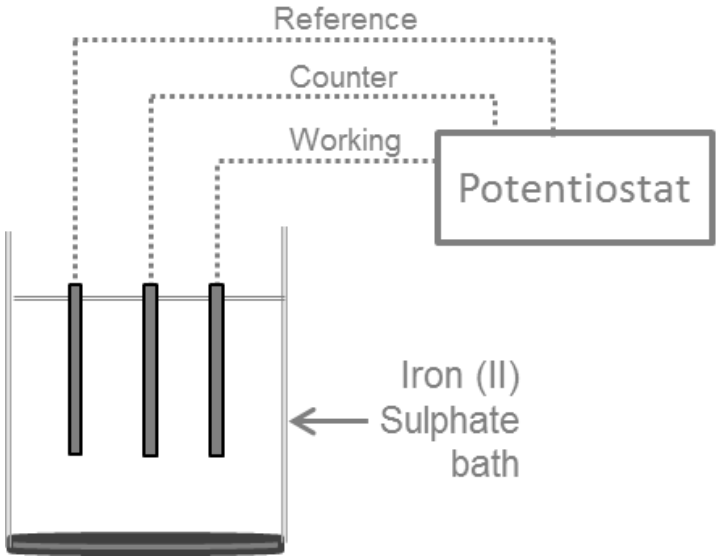

Figure 64: Typical 3-electrode electrodeposition experimental set-up

When the system is first developed, typically a cyclic voltammogram (CV) is generated which is used to identify the characteristics of the system including the operating conditions under which electrodeposition is likely to occur. With the 'plating region' identified (either through the CV or literature values), the system can then be run in either chronoamperometry or chronopotentiometry mode in which either the system's potential or current is held constant respectively. This is further discussed in Section 4.3.3.

4.2.4.4. Sputtering

Iron can also be deposited using a sputtering technique in which high-speed particles bombard an iron target with enough energy to force surface atoms within the target to escape. The escaped atoms or molecules are then free to travel to the substrate surface to be deposited as a film.

In its very basic form, sputtering involves holding both the target and the substrate in a vacuum chamber, with a potential applied across the two allowing the target to take the role of the cathode and the substrate the anode. A plasma is then created through the ionization of a sputtering gas

such as argon, which is used to bombard the target allowing iron atoms to be released and form a film on the substrate surface.

The technique of sputtering iron is well documented within the literature, with methods to improve layering as well as ideal operating conditions discussed by several authors [238-240].

4.3 Methodology

This project was initially conducted in collaboration with Nalco Co. as part of an initiative to reduce the lag time with their *ex-situ* high volume, time-intensive fouling analysis. Nalco's current *ex-situ* analysis is applied to any incoming heavy crude sample and allows them to determine the conditions / amount of anti-fouling chemical required for efficient heavy crude transportation and refinement.

The rig described in this section has been designed to replicate the studies conducted by Nalco Co. but for a low volume, low time analysis. The rig is designed to replicate the conditions and fouling probability anywhere within a typical production chain or partial upgrading facility with operable temperatures between $25 - 750$ ^{O}C and pressures of $0 - 120$ psi.

4.3.1 Rig Design

In order to conduct a replicable *in-situ* low volume study to compare to the higher volume work at Nalco Co., this project required the microbalance to operate at both high temperature and pressure, whilst in contact with a heavy crude sample. To truly act as an *in-situ* sensor that can imitate the necessary adsorbing surface (e.g. pipeline walls or sacrificial adsorbate), the microbalance was also required to be surface modified, and in this case, a replicable pipeline iron layer was deposited as discussed in Section 4.2.4.2. A pressure chamber with means for heating had to be developed; the resulting rig is shown in Figure 65 and the pressure chamber is further discussed in Section 4.3.1.1.

The rig set-up shown in Figure 65 comprises a pressure chamber, the heat source is a bespoke ceramic knuckle heater developed in conjunction with Elmatic Heaters (Cardiff, UK), a zero grade argon bottle (BOC, UK) connected via nylon piping (FTI, Sussex) was used for pressurisation. The pressure chamber is also connected to a pressure gauge (PG), pressure relief valve (PRV) and electrical outputs. The electrical outputs include a thermocouple as well as connections from the microbalance to both the Solartron

1260 FRA (USA) and the QCM frequency analyser (Stanford Research Systems, USA). The microbalance analysis equipment is as described in Section 3.3.2.

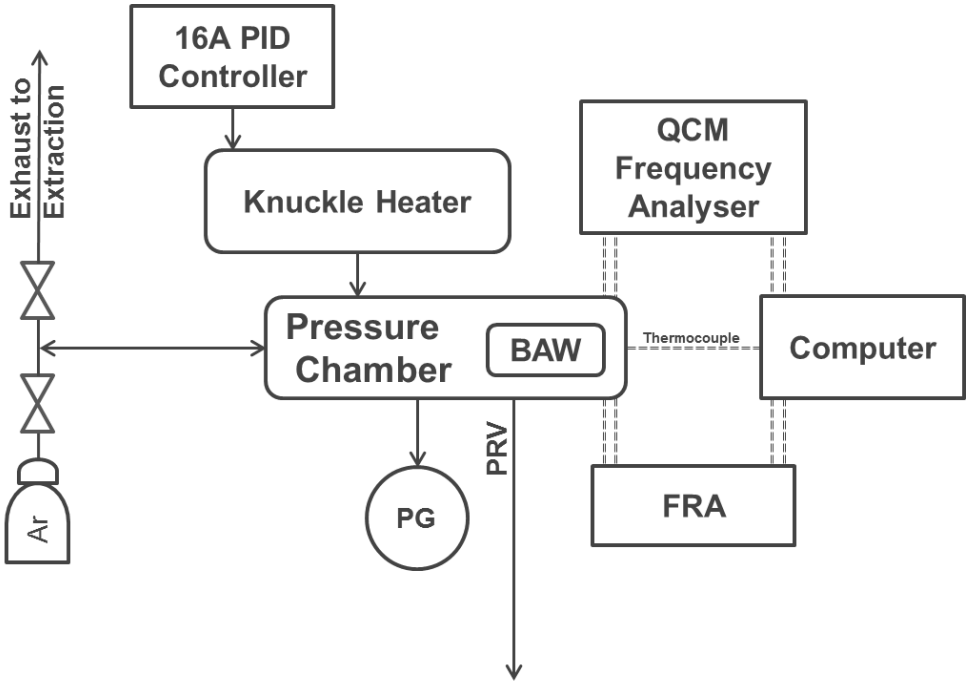

Figure 65: Accelerated fouling detection rig Set-up

4.3.1.1. Pressure Chamber

The chamber design was of critical importance to this study as it not only had to replicate the conditions typically found in transmission pipelines and refinery equipment, but also had to provide stable control of temperature and pressure. Stable control over conditions ensured that pressure and temperature variation would not affect the composite resonator's frequency response and allowed the fouling characteristics of the crude to accurately mimic that seen within the production chain. Simultaneously, the chamber was also designed to allow for *in-situ* measurements from the operating GCM under the same conditions, to the analytical equipment at atmospheric conditions.

To facilitate conditions seen at various points within the production chain, the rig was designed to allow chamber pressurisation of up to 120 psi with

a highly sensitive pressure gauge, whilst allowing heating of up to 750 ^{O}C. The chamber was designed and constructed to house an operating microbalance with the necessary electrical connections to and from the frequency analyser or Solartron as well as a thermocouple operating at the crystal surface. Figure 66 shows the 3D pressure vessel schematic, inside the microbalance holder and stage can also be seen – these are further discussed in Section 4.3.2.2.

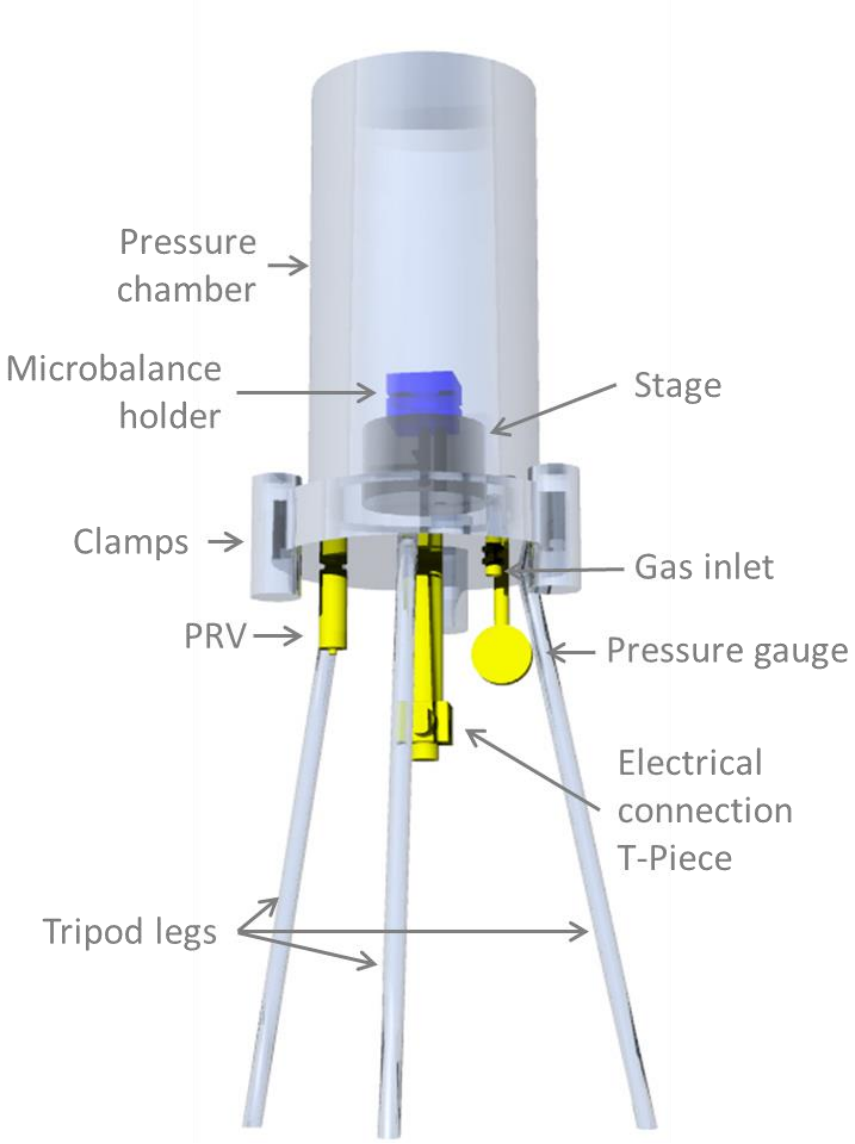

Figure 66: Pressurised chamber housing the microbalance holder and elevation stage

The chamber base plate shown in Figure 66 was designed to have the provisions for three 1/4 inch BSP threaded holes into the chamber and one 1/2 inch BSP threaded hole in the middle. These taps were used to connect four male-male unions and used for a pressure gauge, a pressure relief valve, an inlet / outlet valve for pressurization, a thermocouple and electrical connections to and from the crystal respectively. Whilst maintaining a seal on each connection is relatively straightforward using parallel threads and doughty seals, the connection that allowed the microbalance electrodes to attach to the Solartron and frequency analysers proved somewhat more difficult. The platinum wire connections used to attach the microbalance electrodes to the analysis equipment was required to be held under pressure at one end and removed to atmosphere for measurement without releasing pressure from the vessel on the other. As well as removing the Pt wire without releasing pressure, the connection had to ensure that the Pt wires didn't touch the vessel or each other to prevent shorting the connection. This connection therefore required further design work and engineering and is further described in Figure 67.

Figure 67 shows a schematic of the electrical connection T-piece used to connect the BAW resonator in the pressurised chamber to the measuring equipment at atmospheric pressure. The design uses a length of 1/2 inch stainless steel pipe with three 3 mm ceramic fishbone bead tubes encased, providing insulation to carry the electrical connections and thermocouple from the crystal to the T-piece junction located at the base of the pipe.

The T-piece is used as it allows the electrical connections to be separated and passed through in-house fabricated plastic sheathed rods sealed with high-temperature cement and out of the chamber without any de-pressurization of the system. Plastic ferrules were used to insulate and attach the rods to the T-piece to ensure electrical conductivity between the crystal and the analysers was uninterrupted.

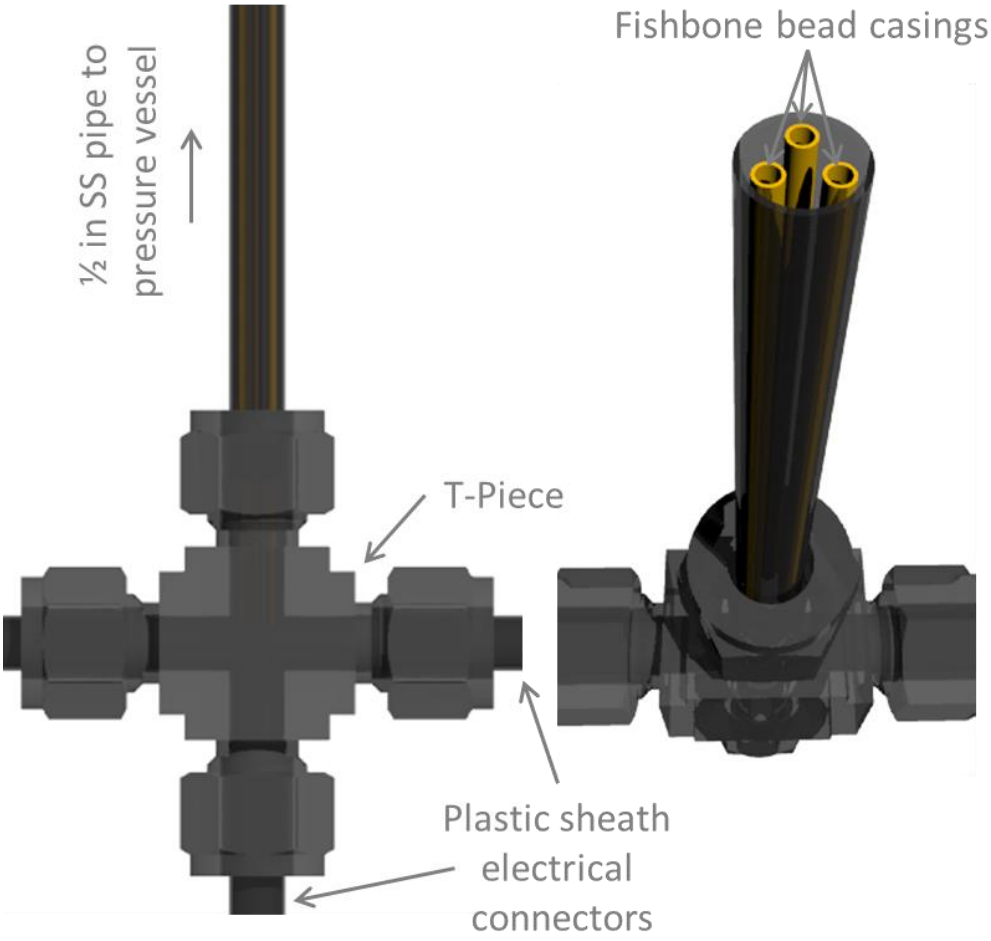

Figure 67: Electrical T-piece connection schematic detailing internal wiring channels developed from fish bone beads

4.3.2 Microbalance

Section 4.2.4 highlights the available BAW resonators for application at high temperatures. The $GaPO_4$ and LGS resonators have shown operation within the investigative range of this project and up to 970 ^{O}C and 1000 ^{O}C respectively. However, as discussed by Fritze *et al.* [233], the $GaPO_4$ resonator has significantly less energy dissipation than the LGS and thus an improved Q-factor. In this investigation, the BAW's Q-factor will be significantly reduced with viscous heavy crude oil contacting media. Whilst doping techniques to reduce both the LGS's frequency fluctuations and energy

dissipation at high temperatures exist, there is still no industry standard, making a comparison between different temperatures and investigations difficult.

The $GaPO_4$ microbalance (GCM) is a commercially available resonator which like quartz can be cut at different angles to provide varying characteristics. Recent work and publications from the Electrochemical Innovation Lab [137, 138] has provided a level of confidence in the technology and has shown reproducibility of results (albeit in the gas phase). Piezocryst (Austria) offers a range of bespoke angle of cut GCMs, each with specific zero temperature coefficients. Bespoke R-30 GCMs were developed in collaboration with Piezocryst for this investigation and are further discussed below.

4.3.2.1. Background

Like quartz, the GCM operation is dependent on the crystal's angle of cut; where increasing the angle results in an increased temperature range in which frequency is most stable. Changing the cut angle also changes the coupling, temperature dependence and dampening of the resonator.

Figure 68 is reproduced from Krispel *et al.* [241] and depicts the relationship between the cut angle and the theoretical temperature coefficient of frequency (TCF) and the predicted coupling coefficient. The coupling coefficient is defined as the efficiency at which electrical energy is converted to acoustic energy [242].

Figure 68 shows that there are only two cut angles at which the TCF registers a zero coefficient; the Hi-Q and Hi-K. Hi-K occurs at -16.5° and has a coupling coefficient twice that found in AT-cut quartz [243] and provides a significantly higher coupling coefficient than that of Hi-Q. Therefore, most GCMs are cut and operate within this region.

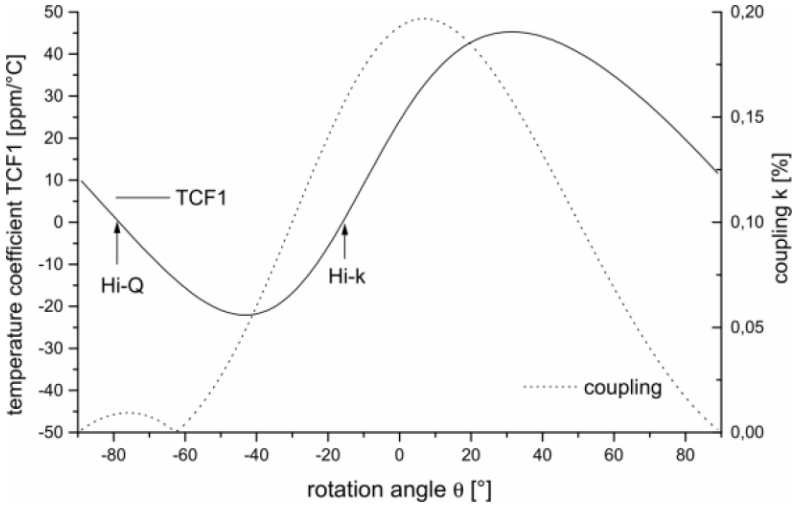

Figure 68: The corresponding temperature and coupling coefficients for a $GaPO_4$ crystal's angle of cut, reproduced from [241].

This project employs Y-11.1° cut angle GCM R-30 resonators; chosen for its location near the Hi-K point and higher in angle to maximise the coupling coefficient and reduce the resistance and drive level dependence (DLD) [241]. At a cut angle of Y-11.1°, the GCMs frequency shows excellent stability at temperatures up to 800 °C as shown in Figure 69. This temperature range is considered to cover the operating temperatures of current and future crude oil production chains, whilst providing high temperature-frequency coefficient stability, improved coupling, resistance and DLDs for the investigative range of experiments.

Y-11.1° cut GCMs also provides piezoelectric characteristics 100 times less sensitive to temperature variances than AT-cut quartz above 400 °C. Figure 69 shows the variation in the GCMs and QCMs temperature coefficient; the GCM reduces linearly between temperatures of 0 °C and 600 °C, unlike that of quartz which increases by the cube of the operating temperature. The GCM has also shown operation up to as high as 970 °C before transitioning into its β-phase and thus irreversibly losing its piezoelectric qualities as a result of twinning [244-247].

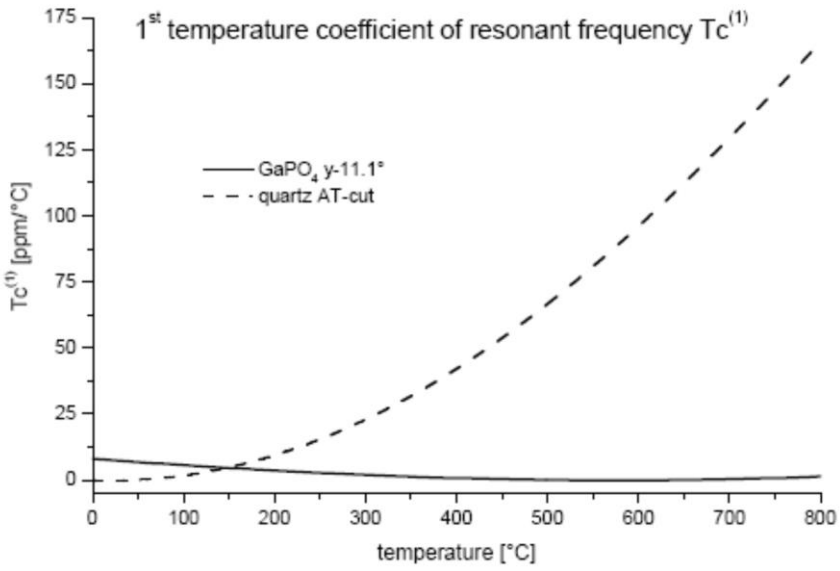

Figure 69: Temperature coefficients of $GaPO_4$ at Y-11.1° cut compared to AT-cut quartz, reproduced from [248].

As with the QCM, the R-30 GCM is developed with an understanding of energy trapping (Section 2.3.2) and has a convex geometry to produce stable frequency responses and high Q-factors.

The GCM possesses an electrochemical coupling coefficient k^2 four times that of quartz [249], and combines better damping resistances and low conductivity (10^{-7} Ω cm^{-1} at 700 °C) to provide higher operating efficiencies compared to quartz.

The GCM devices used throughout this investigation are similar to those employed in Chapter 3 and have a double anchor electrode with a resonant frequency of 6 MHz and offer 0.4 ng mass monitoring resolution. The electrodes are 200 nm platinum plates attached to the gallium using a 20 nm titanium adhesive layer. The R-30 microbalances are commercially available from Piezocryst (Graz, Austria), and are compatible with the industrial standard holders and analysis equipment.

4.3.2.2. Microbalance Holder

In designing the rig, it was critical to ensure that the GCM was held in such a way to have excellent electrical connections from each electrode to either a frequency or impedance analyser, whilst operating under a range of temperatures and pressures and in contact with the heavy crude sample.

The convex GCM operates similarly to the QCM and therefore the holder is able to make use of the energy trapping phenomenon and clamps the microbalance at its edge with minimal effect to its oscillation [133].

The holder schematic is shown in Figure 70 and maintains many of the features from the fuel cell holder described in Section 3.3.2.2; albeit with a few adjustments.

The major difference is the introduction of two spring-loaded pogo-pin connectors to provide one point of connection to either electrode on the crystal surface. The GCMs are significantly thinner and more fragile than the QCMs used in the fuel cell study. These pins allow for a more stable connection with equal pressure loading from above and below and do not affect the O–rings in contact with the crystal. An additional hole and 2 in-house fabricated high-temperature O-rings (Grafoil) were added to the holder base in order to expose the crystal centre to pressure from both sides.

The second addition to the holder is the raised platform which can be seen in Figure 66; this platform provides added stability to the holder, helps isolate the electrical connections and allows the holder to be centralised within the heated pressure chamber.

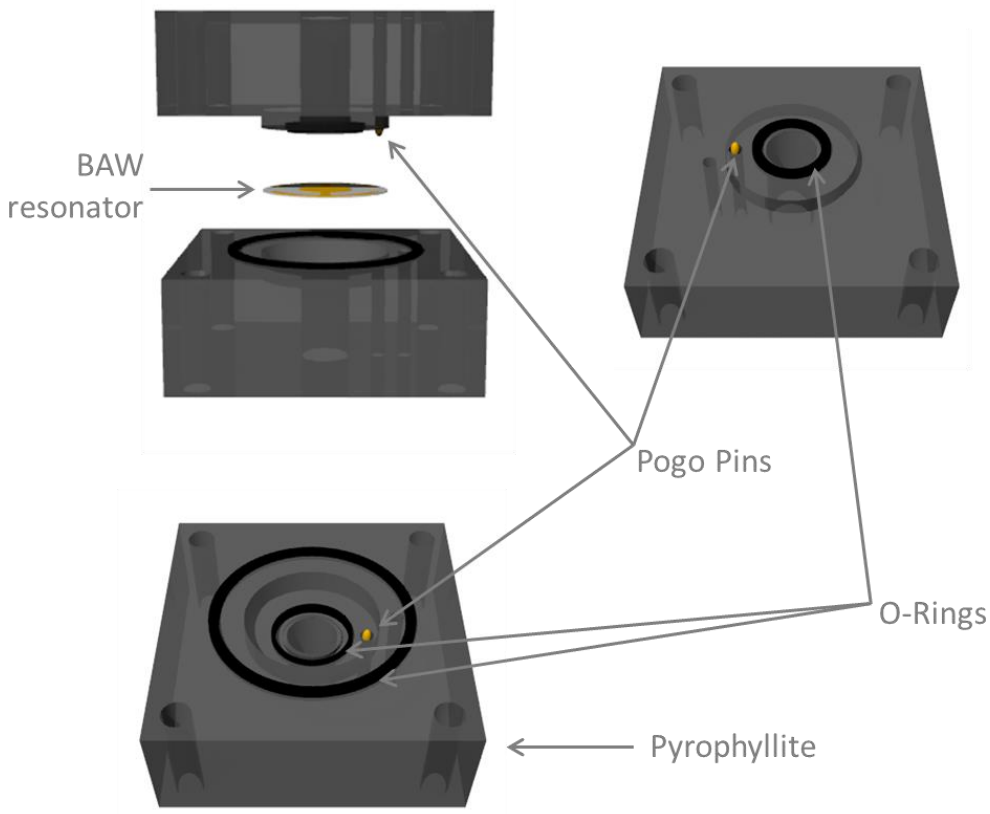

Figure 70: Microbalance holder schematic. Manufactured in-house using one piece of unfired pyrophyllite and rapid prototyping equipment

4.3.3 Iron Electrodeposition

To demonstrate the application of the GCM as a suitable *in-situ* resonator for this application, a surface developed iron layer was deposited on its top electrode. As discussed in Section 4.2.4.2, the iron could be sputtered or electrodeposited; the latter was chosen for the variety of finishes that the technique could provide (through fast, slow and layer deposition) as well as the control afforded to the process through the *in-situ* mass monitoring using the electrochemical GCM (eGCM) and subsequent efficiency analysis as discussed below and in Section 2.7.

Iron electrodeposition in this investigation was carried out using an iron(II) sulphate heptahydrite ($FeSO_4.7H_2O$) aqueous electrolyte with a concentration of 0.9 M. This electrolyte was chosen as it can be operated at room temperature, produces smooth deposits with a low tendency to pit and allows layering for thicker deposits [250].

In order to electrodeposit the iron onto only one side of the GCM as well as allow the GCM to operate as an eGCM, a holder that would ensure the top electrode maintained contact with the electrolyte, whilst both front and back electrodes remained electrically connected to the analyser was required. The holder initially designed in-house proved difficult to seal the electrical connections on both sides from the contacting bath and therefore a commercially available Gamry instruments holder was purchased and modified for the application, as shown in Figure 71.

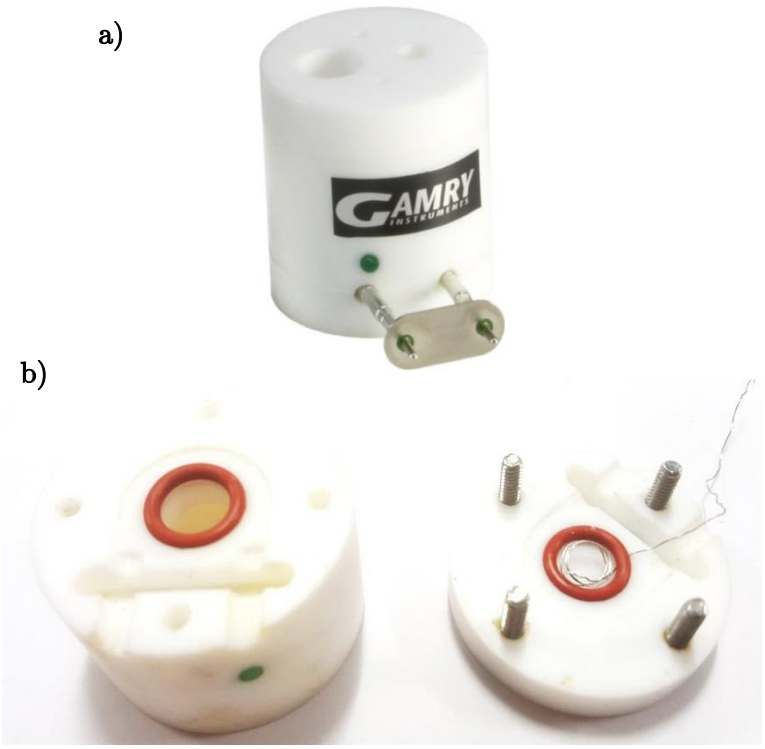

Figure 71: Gamry instruments BAW holder modified for use as an eGCM holder with an electrodeposition bath shown here a) closed and b) open, indicating its operation.

With the holder modified to allow the GCM to be run as an eGCM during the electrodeposition process, it was connected to a potentiostat (Gamry, USA) through a face bias as shown in Figure 72. In this setup, the microbalance is operated with one electrode in the iron sulphate bath, and one electrode exposed to air.

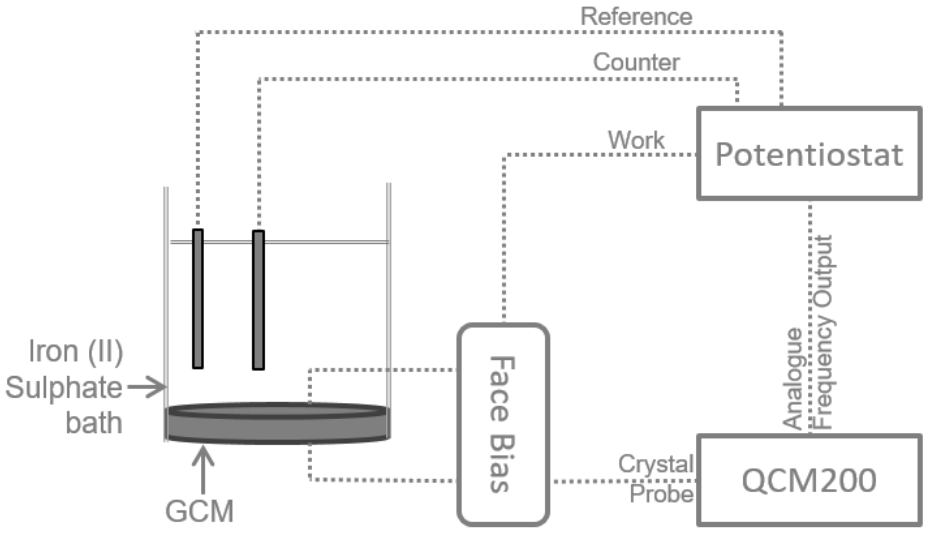

Figure 72: eGCM electrodeposition bath set up for iron electrodeposition

The system has been set up to allow operation similar to that indicated in the literature for other plating experiments from iron(II) sulphate baths albeit with the eGCM replacing the working electrode. The initial setup employed was constructed as described in the literature [250, 251] with a 0.9M iron(II) sulphate bath at pH 5, 25 ^{O}C operating at -50 mA cm^{-2}. However, the system was also arranged to allow cyclic voltammetry sweeps for further elucidation of the current window in which iron would be electrodeposited and removed from the microbalance surface. Several GCMs were subsequently operated within the bath under slightly varying conditions to understand the variance of the electrodeposited layer quality; this was subsequently assessed using SEM and EDX as shown in Section 4.4.3. Finally, the electrodeposited iron GCM (iGCM) was passively operated using CAS to ensure the mass loading was within the GCM's operable limits and provided a composite resonator with a suitable Q-factor range.

Equations (27) – (30) were used to determine the optimal time in which to apply a current for plating a specific mass of iron onto the working electrode.

Firstly, the charge (Q) can be calculated from the applied current (i) and time (τ) as shown in Equation (27):

$$Q = i.\tau \tag{27}$$

The number of moles of iron transferred for a given charge is calculated using the relationship with the Faraday constant (F) as indicated in Equation (28).

$$moles\ (Fe) = {}^{Q}\!/_{2F} \tag{28}$$

The mass deposited onto the working electrode (m) and the subsequent layer thickness (t_{Fe}) can be determined using the density (ρ) and Equations (29) and (30).

$$m\ (Fe) = mol\ (Fe) \times Molar\ mass \tag{29}$$

$$t_{Fe} = {}^{m}\!/_{\rho A} \tag{30}$$

The application of the eGCM allowed an *in-situ* mass deposition to be calculated to determine the deposition efficiency, and true layer thickness as discussed in Section 4.4.2.

4.3.4 Crude Sample

The heavy crude sample used during this investigation was kindly provided by the R&D analysis centre at Nalco Co. and is a bituminous vacuum residue from the North Sea.

4.4 Results and Discussion

With the literature having identified the GCM as a potentially suitable *in-situ* resonator for this high-temperature application, the first part of this section analyses and confirms the GCM's suitability for this investigation. This includes the application of the microbalance at elevated temperatures, operation under pressure and with a contacting viscous medium.

The suitability studies performed in this section are coupled with and presented alongside GCM calibration studies. This provides a better understanding of the GCM's operation at elevated temperatures and pressures as well as in contact with highly viscous media.

4.4.1 Suitability and Calibration Studies

The QCM represents a mature instrument in nano-gram resolution mass monitoring systems; as such where possible the QCM response is also shown for comparison and used as a benchmark for stable BAW resonator operation.

4.4.1.1. Temperature

The first part of this temperature calibration investigation explores the QCM's usable temperature range; the literature suggests that ≥ 450 ^{O}C the QCM becomes unusable due to lattice twinning effects [252-254]. The results of this investigation are presented in Figure 73.

Figure 73 shows the QCM's frequency shifts when operating through a range of temperatures up to 600 ^{O}C in air (100 ml min^{-1}). Whilst the QCM operates effectively at low temperatures ($\leq$ 400 ^{O}C), the frequency response is well within the operable range. However, as the temperature increases, there is initially a sharp frequency spike (8,000 ppm) when the resonator is held at 400 ^{O}C; the recorded spike ppm is much higher than an operable shift in frequency. After the spike, the QCM's frequency response returns to within the operable region; however, as the temperature is further ramped, the frequency spikes sharply to 650,000 ppm at 435 ^{O}C; far beyond the QCM's

operable range. The frequency response continues to remain above the operable range as the temperature is increased to 600 ^{O}C.

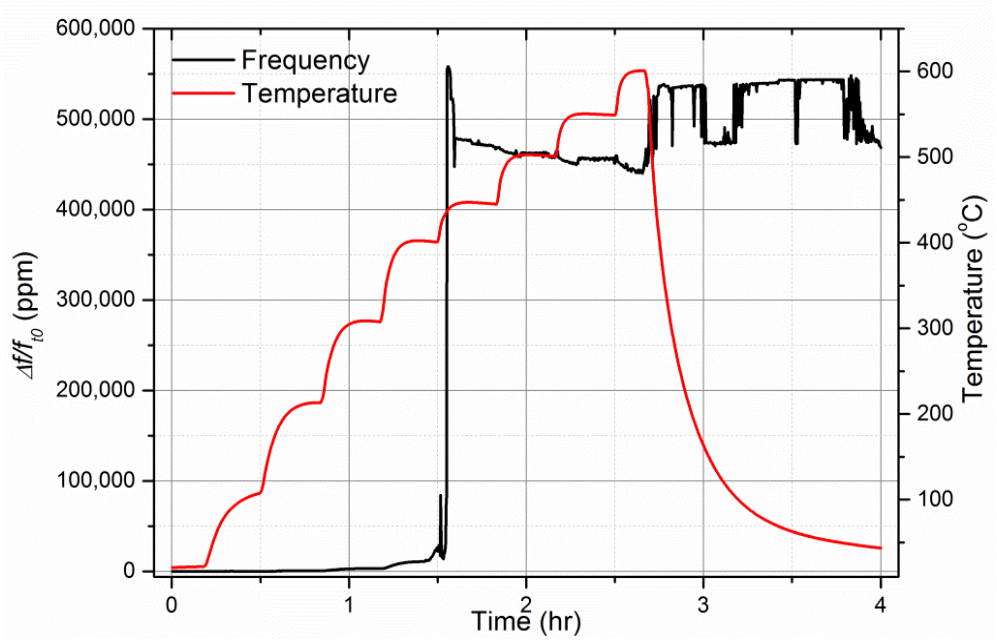

Figure 73: QCM frequency response for operation between 25 ^{O}C and 600 ^{O}C, showing failure at 435 ^{O}C [255].

When the heat is removed, and the QCM cools to room temperature, the resonator shows hysteresis as the frequency response does not return to anywhere near its original value – the microbalance has failed. The failure of the QCM is likely a result of twinning in which the lattice structures become so excited that they shift irreparably, and the resonant frequency can no longer be reached.

As discussed in Section 4.3.2.1, the GCM has proven operation at temperatures up to 972 ^{O}C in our labs in a gaseous environment [137, 140, 255]. Figure 74 replicates the above study using a $GaPO_4$ microbalance and shows operation at temperatures up to 900 ^{O}C in air at 100 ml min^{-1}.

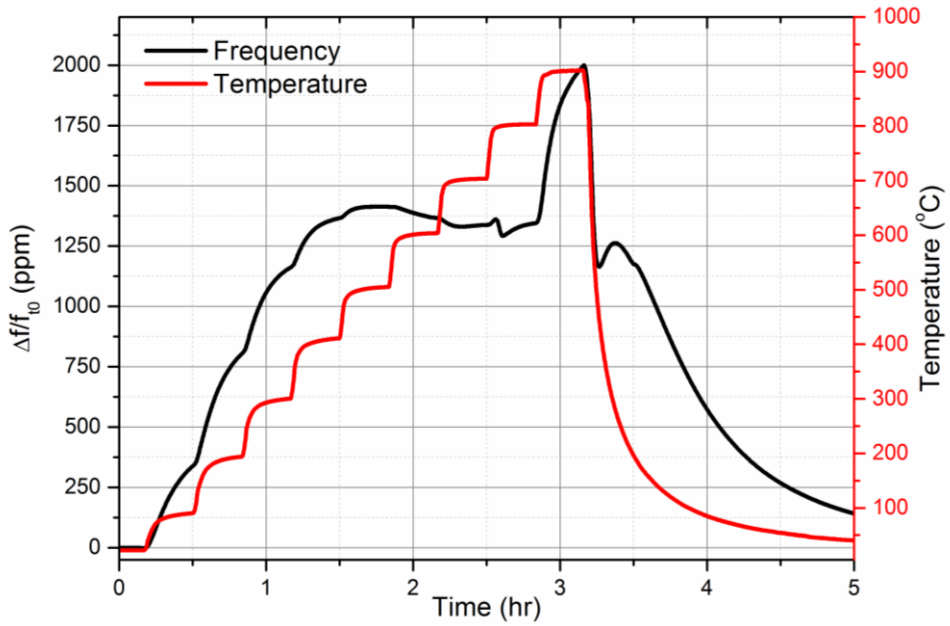

Figure 74: GCM frequency response for operation up to 900 °C, showing a reduced temperature coefficient between 400 – 600 °C [255]

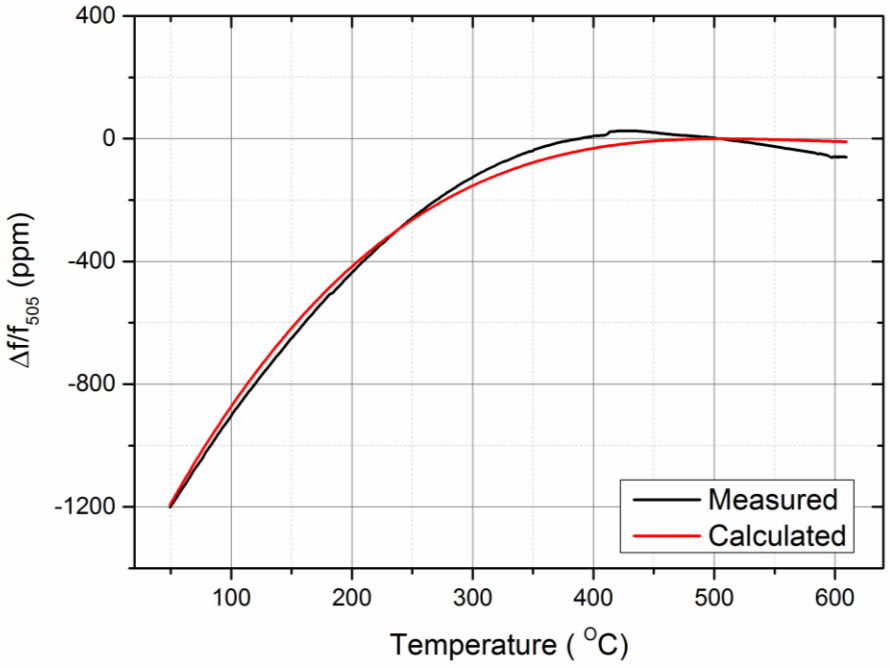

Figure 75: Measured and calculated GCM temperature profiles for operation between 50 °C and 600 °C.

Initially, Figure 74 shows indicates that as the temperature increases between 25 – 400 ^{O}C the frequency response increases linearly by 1375 ppm. However, between 400 – 800 ^{O}C there is a significantly more plateaued frequency response which is further depicted and discussed in Figure 75. Finally, as the system begins to cool, it can be seen that the ppm also drops and begins to return to its original value as the microbalance approaches room temperature.

Figure 75 shows the measured and calculated frequency responses for a GCM operating at temperatures between 50 and 610 ^{O}C. The calculated trend is determined using Equation (31) from Piezocryst [248].

$$f(T) = f_0(T)[1 + a(T - T_0) + b(T - T_0)^2 + c(T - T_0)^3] \quad (31)$$

Table 7: Piezocryst's GCM frequency and temperature relationship nomenclature.

f(T)	Frequency (*Hz*) dependent on temperature (*T*)
f₀(T)	Initial frequency (*Hz*) dependent on initial temperature (when $T=T_0$)
T	Temperature (^{o}C)
T₀	505 ^{o}C (stabilized reference temperature)
a	0.00831 ppm/^{o}C
b	-0.00186 ppm/^{o}C^{2}
c	8.5x10^{-6} ppm/^{o}C^{3}

Both the calculated and measured frequency responses compare well; showing minimal effect of temperature on the microbalance's frequency response between 400 – 600 ^{O}C.

However, as this investigation requires precise microbalance frequency responses at all operable temperatures it was important to ensure that the GCM exhibited no frequency drift when operating at specific temperatures. The operable temperature range for this investigation is expected to be between 300 - 600 ^{O}C and so the microbalance's frequency stability within this range is reported in Figure 76.

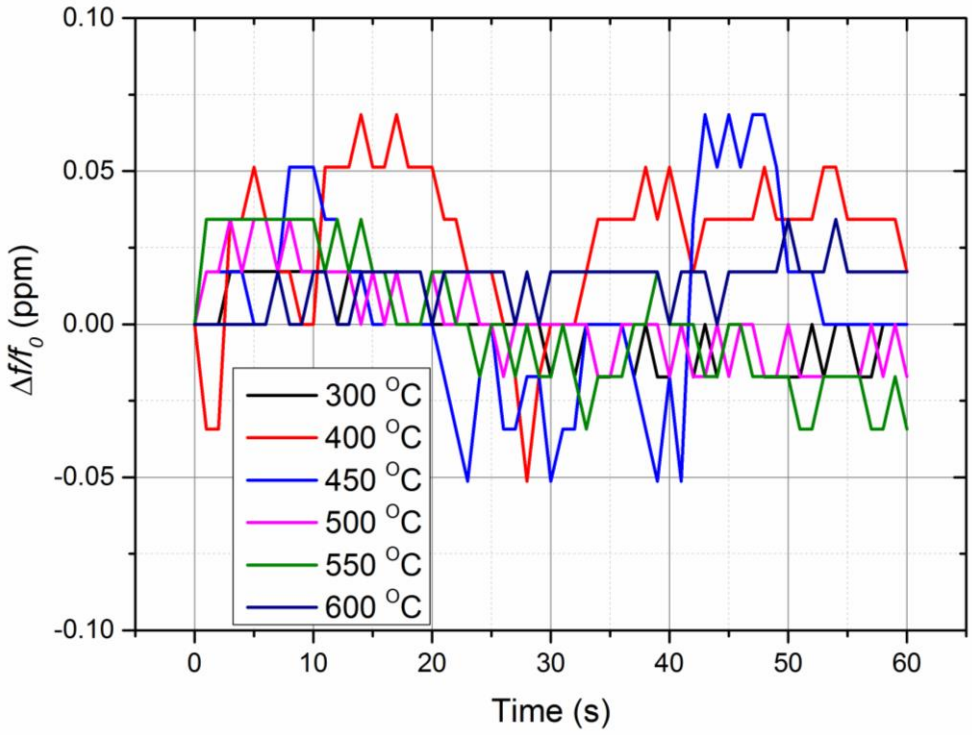

Figure 76: GCM temperature stability shown at temperatures between 300 °C and 600 °C.

In Figure 76 the GCM has shown excellent stability at all temperatures investigated, comparable to that of the QCM shown in Figure 34 with a resolution of ± 0.05 ppm. As discussed in Section 4.3.2.1, the GCM used for this investigation has been specifically cut at Y11.1° so the temperature coefficient is lowest between 400 – 600 °C, and 0 at 505 °C. Whilst this investigation is carried out at distinct temperatures, low TCFs near the operable range ensure that any slight variation in operation temperature will have a minimal effect on the microbalance's frequency response, as confirmed in Figure 75.

4.4.1.2. Contacting Viscous Medium

With the GCM having proven both operation and excellent stability when operated within the investigative temperature range, a study into how the microbalance responds with a contacting crude oil sample was conducted. The QCM has been shown to operate with heavy organic contacting media above certain temperatures [14]; the temperature at which a resonant frequency is first registered is referred to as the critical temperature (T_C).

The application of a heavy organic to a BAW resonator under temperature is not well understood, and whilst there have been similar studies carried out by Yao and Zhou and Nomura and Okuhara [14, 20] for example (Section 2.4), the application of admittance to uncover the composite resonator's 'true' critical temperature and the subsequent fulfillment of the standing wave condition is novel.

For this study ~ 0.02 mg of vacuum residue was added to the microbalance surface; the microbalance was subsequently heated and its operation monitored. The crude sample was too viscous to be poured and so a small quantity was heated to 50 ^{O}C on a hot plate and pipetted onto the double anchor electrode similar to as shown in Figure 77. Even with ~ 0.02 mg (measured using a scale) of contacting crude, the resonator could not operate effectively and reported frequencies well above the operable range. Therefore, a similar study to that carried out by Nomura and Okuhara [14] was carried out to investigate if the composite resonator could attain a T_c.

Figure 77: The crude-GCM composite resonator shown here before heating to disperse the heavy crude.

A 6 MHz R-30 GCM was prepared as shown in Figure 77 and inserted into the ceramic holder shown in Figure 70. It was initially heated and held at 50 ^{O}C to allow the crude sample to spread evenly across the central electrode, preventing issues that result from radial mass loading (Section 2.4.3). The sample was then slowly heated (1 ^{O}C min^{-1}) from 150 to 530 ^{O}C under 100 ml min^{-1} nitrogen.

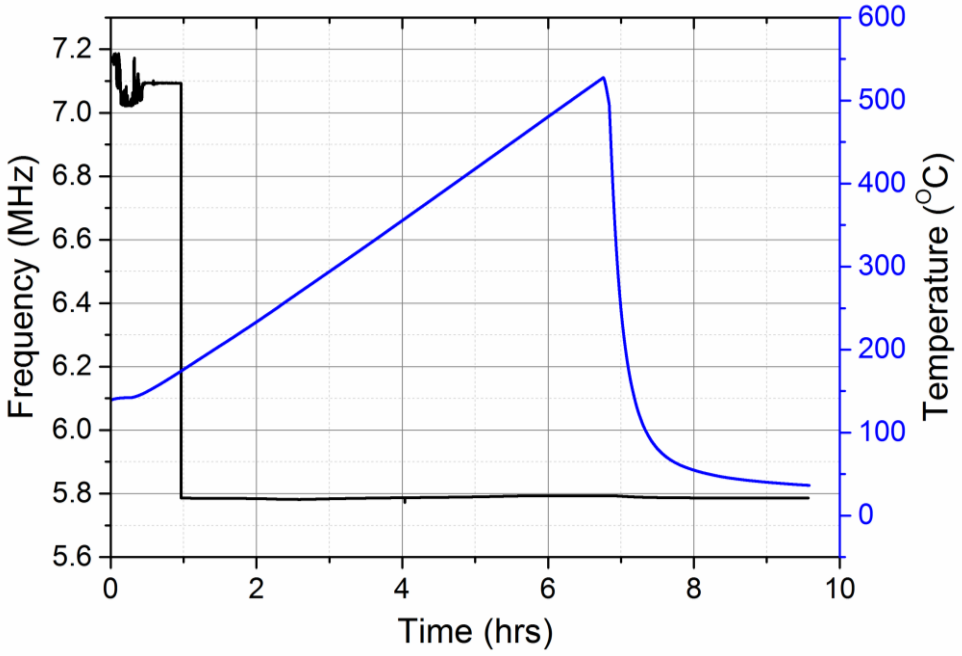

Figure 78: The frequency response for a GCM-crude sample heated between 150 – 530 ^{O}C in order to determine the composite resonator's critical temperature.

Figure 78 shows the frequency response for the GCM-crude resonator operating between 150 and 530 ^{O}C. At temperatures ≤ 176 ^{O}C, the GCM is operating well away from its resonant frequency (7.1 MHz); the recorded frequency is a response often seen when the crystal is overloaded resulting from incomplete wave interference and subsequent harmonics as a result of the contacting crude's high viscosity. However, as the temperature increases above 176 ^{O}C, the resonator begins to operate nearer to its real resonant frequency (5.8 MHz); this is likely as the crude sample becomes less viscous

with applied temperature, allowing the TAW to propagate through the contacting media; this temperature is often referred to as the composite resonator's critical temperature (T_C) [14].

More information can be obtained by using crystal admittance spectroscopy (CAS) and is unique to this study. Figure 79a-c shows the CAS responses for the GCM-crude resonator operating at all temperatures at which an admittance response could be generated, the results suggests that even though the loaded GCM provides a frequency response near what would be expected when operating at 176 ^{o}C; the GCM does not fulfil the standing wave condition (Section 2.2). Without registering 2 $\theta = 0$ points, the loaded resonator (under the given conditions) cannot fulfil the standing wave condition; the harmonics are prone to spurious constructive and destructive interference of the standing wave propagating the microbalance. As the GCM operates using the standing wave phenomenon, without perfectly timed interference of the two waves propagating the resonator, the resonant frequency registered is likely to be unpredictable as the wave reflects at the electrode surfaces producing incomplete harmonics.

Figure 79a-c and Table 8 shows that it is only when the GCM-crude resonator is operated at 215 ^{o}C that it first fulfil the standing wave condition. Beyond this temperature, it can also be seen that the resonator operates as expected and registers 2 $\theta = 0$ points for each investigation. The results in Figure 78 and Figure 79 have for the first time shown using CAS that the T_C does not occur at the first temperature at which the microbalance first reads a resonant frequency near what is expected. The results also confirm that the GCM is able to successfully operate with a highly viscous contacting medium at temperatures above its T_C.

Table 8: Temperature vs. θ_{min}

T (^{o}C)	Θ_{min}
204	3.42
209	0.58
215	-0.18
218	-0.94
220	-1.05

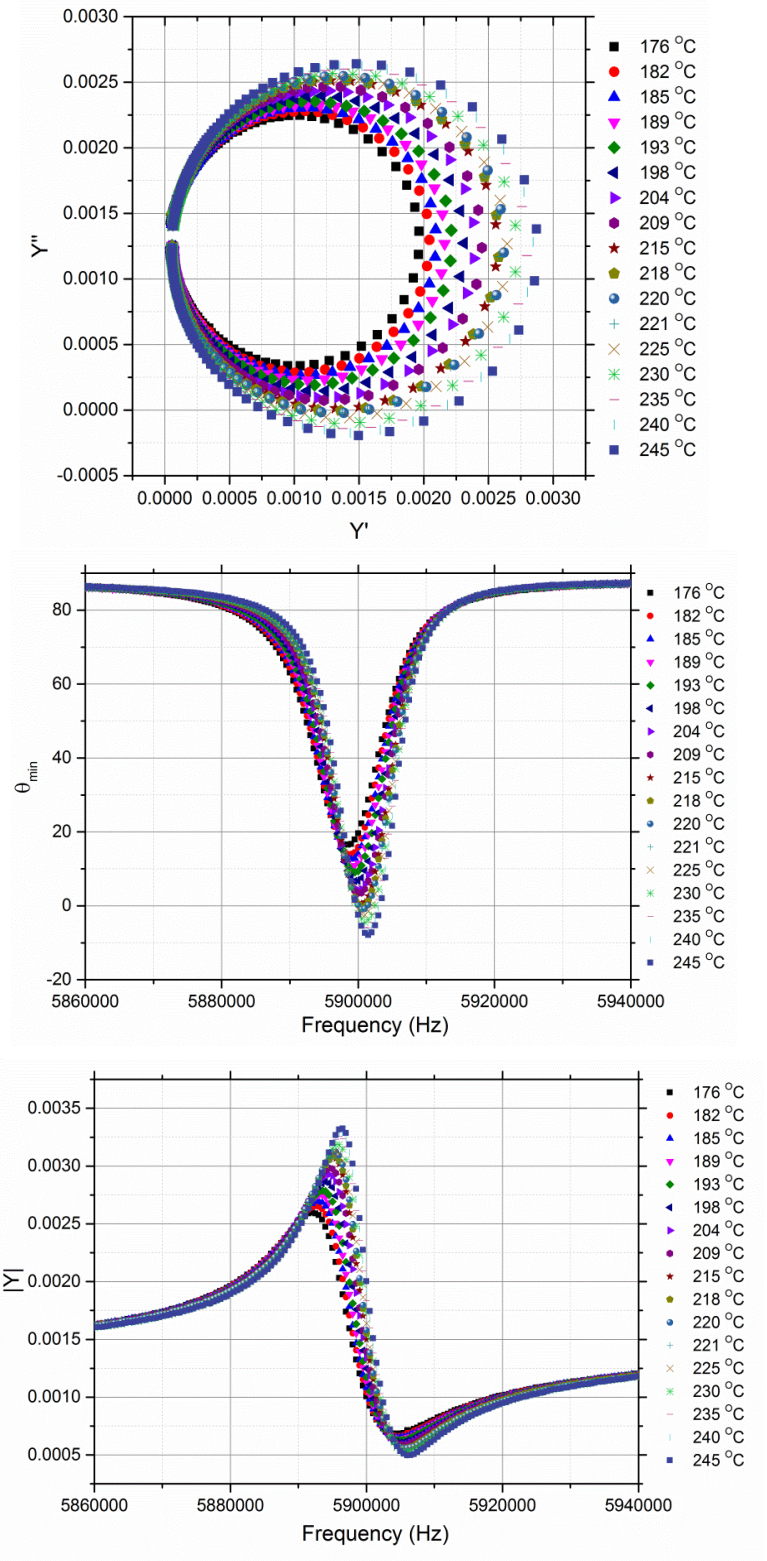

Figure 79: CAS responses for the GCM-crude resonator operating at temperature between 176 – 245 °C in order to determine the 'true' critical temperature.

The frequency response in Figure 78 between the T_C (215 ^{O}C) and 530 ^{O}C is further examined in Figure 80. The data has been presented using $T_C = 215$ ^{O}C as a base from which to measure frequency change on the GCM-crude resonator with temperature. Figure 80 initially shows that increasing the temperature between 215 ^{O}C and 260 ^{O}C results in a decrease in the resonator's resonant frequency. This is in line with the data gathered from Figure 79 but in opposition to the data seen in Figure 74 and suggests that this frequency shift can be accredited to a combination of TCF $\neq 0$ (Section 4.4.1.1), but more likely due to changes in the contacting medium viscoelasticity.

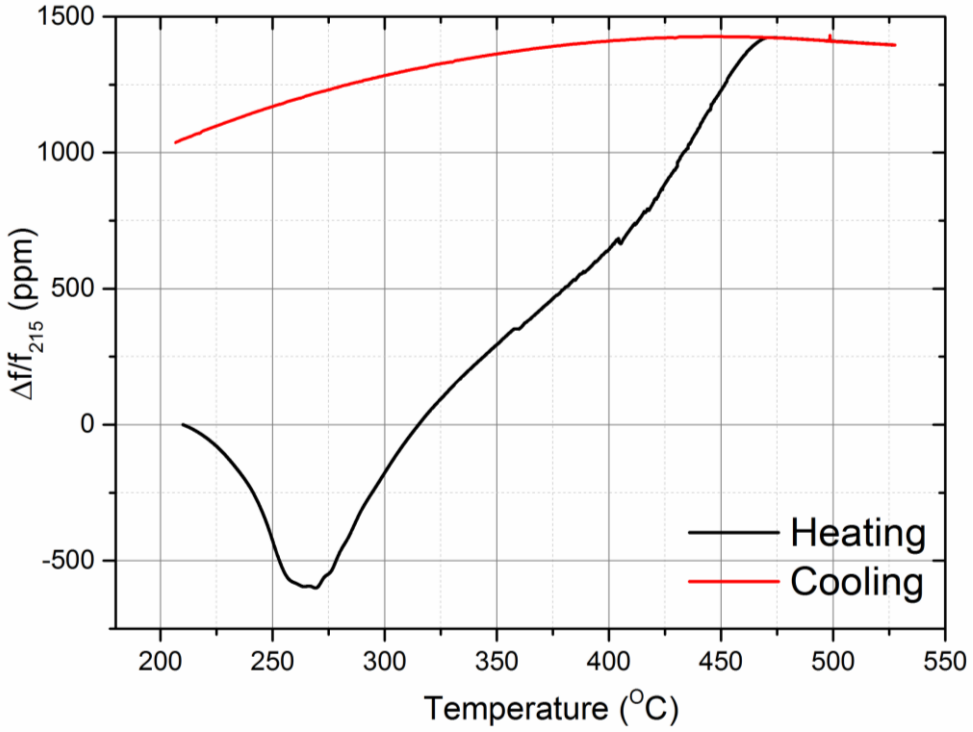

Figure 80: The heating and cooling frequency responses for a GCM-crude resonator operating between 215 – 530 ^{O}C

However, between 255 ^{O}C and 270 ^{O}C (TCF $\neq 0$), there is minimal change in resonant frequency; this is likely due to factors other than the change in resonator operation with temperature and is likely a phase transition of the contacting media. As the figure is further analysed, it can be seen that above 270 ^{O}C, as the temperature increases, the GCMs frequency also begins to

increase. With TCF $\neq 0$, the increase in frequency is expected with increasing operating temperature; however, the increasing frequency may also be used to indicate a loss of mass on the microbalance's surface. As the temperature continues to increase, the increase in frequency suggests a continual decrease in the contacting mass on the composite resonator's surface until 470 ^{O}C. The resonator then registers the same frequency shift when operating between 470 ^{O}C and 530 ^{O}C during the heating and cooling phase. As the resonator cools, the frequency response is measured as shown in Figure 80, and indicates an increase in frequency of 1037 ppm at 215 ^{O}C when cooling compared to heating. This change in frequency relates to a reduction in the microbalance's contacting mass by 0.022 mg. This is very similar to the mass originally added to the system (albeit measured more accurately using the GCM than a conventional mass balance), and suggests that the contacting crude has evaporated from the resonator electrode. This is confirmed visually after post-mortem examination of the GCM.

Figure 80 suggests that the evaporation of the crude sample begins at temperatures above 275 ^{O}C and has highlighted the need for the application of pressure to the system. The application of pressure to both heavy crude refining and transportation is commonplace and is used to allow the application of heat whilst maintaining the crude below its cloud point. Therefore, to provide an accurate representation of the fouling that may occur within the production chain, the microbalance must itself show stability when operated under pressure.

4.4.1.3. Pressure Stability

Transmission pipelines and refinery equipment throughout the production chain can typically operate at pressures up to 100 psi (6.8 bar). It was, therefore, essential to ensure the microbalance's operation at similar (and higher) pressures was stable in order to isolate the response from the final analysis and attribute observations solely to the interfacial processes.

As discussed in Chapter 2, the QCM has in the past been employed as an interfacial sensor in systems held under constant pressure. The GCM literature has yet to report operation under similar conditions and so is further

explored here. As before, the QCM's operation and responses are used in this investigation as a baseline for successful resonator operation.

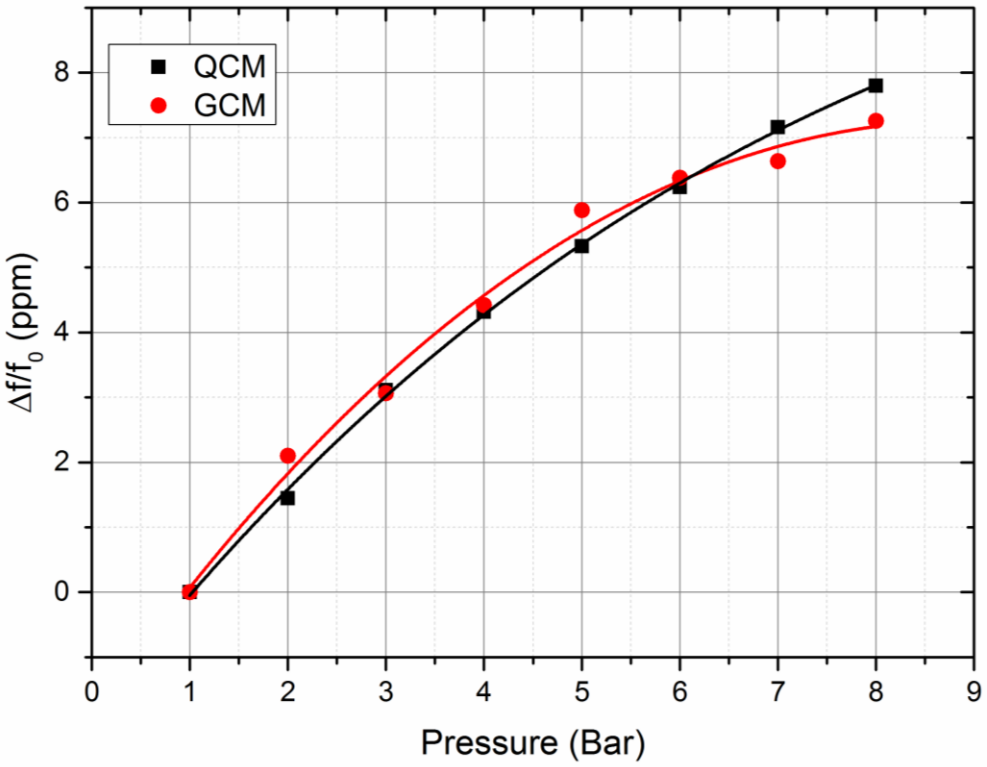

Figure 81: The frequency shift for a QCM (black plot) and a GCM (red plot) for operation under pressure between 1 and 8 bar (gauge).

For this investigation, a 6 MHz QCM (Inficon) and a 6 MHz R-30 GCM (Piezocryst) were operated in the ceramic holder within the pressure vessel as shown in Figure 70 and Figure 66 respectively. Both microbalances were subjected to operation at 30 ^{o}C and pressures between 1 and 8 bar (gauge) in an argon environment; the ppm frequency responses are shown in Figure 81.

Both microbalances show the ability to operate through this pressure range with small ($\leq$ 8 ppm) but comparable decreases in frequency response with increasing pressure; following similar second order polynomial responses.

The GCM does, however, show a lower pressure coefficient when operating between 5 – 8 bar compared to the QCM response.

Figure 82 shows a sample of the QCM stability data obtained when the microbalance was operated through the aforementioned pressure range.

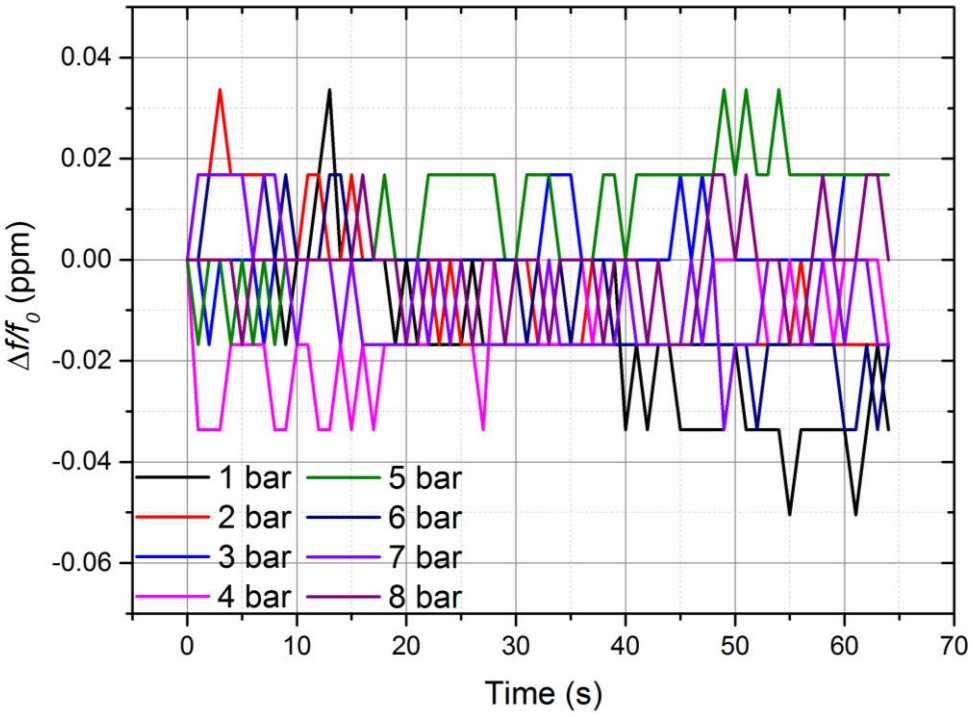

Figure 82: QCM frequency stability when operating at pressures between 1-8 bar

The QCM shows excellent stability with a ± 0.04 ppm system resolution throughout the investigative pressure range.

Figure 83 shows that the GCM also exhibits minimal frequency fluctuations (± 0.025 ppm) when operating at varying pressure; indicating that the GCM is also able to operate as a useful interfacial mass monitoring tool under pressure.

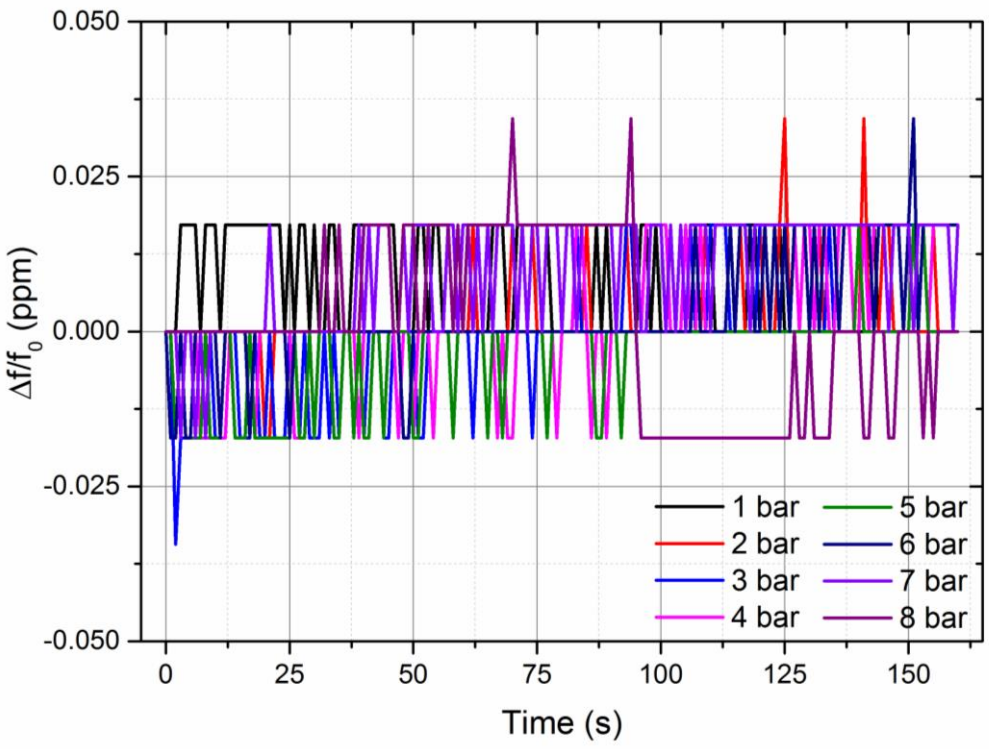

Figure 83: GCM frequency stability when operating at pressures between 1-8 bar

The QCM and GCM admittance responses when operating under pressure $1-8$ bar are shown in Figure 84 and Figure 85 respectively. These responses were measured to ensure that the resonant profiles would still fulfil the standing wave condition and that there were no other factors were affected by operation under pressure.

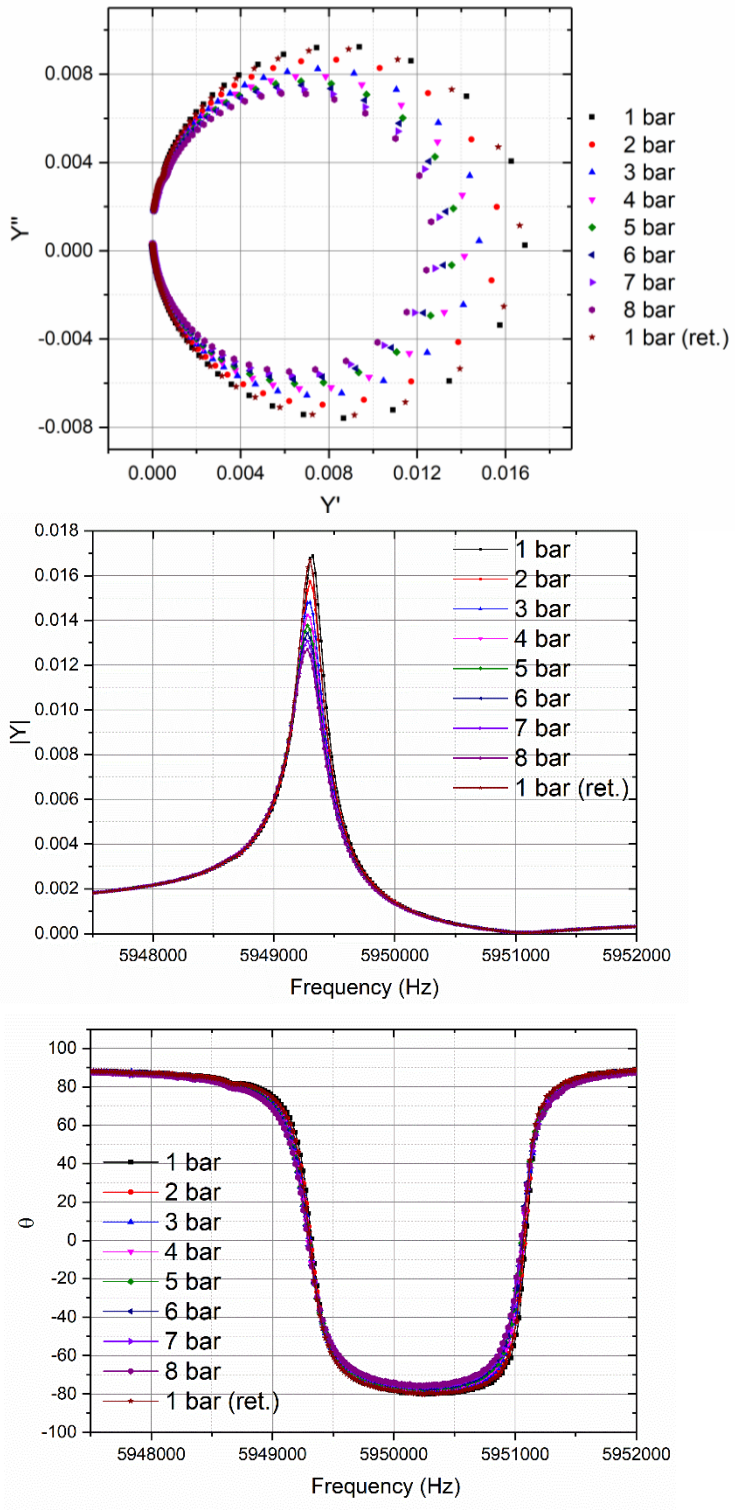

Figure 84: The admittance response for a QCM operating in pressurised environments of 1 – 8 bar.

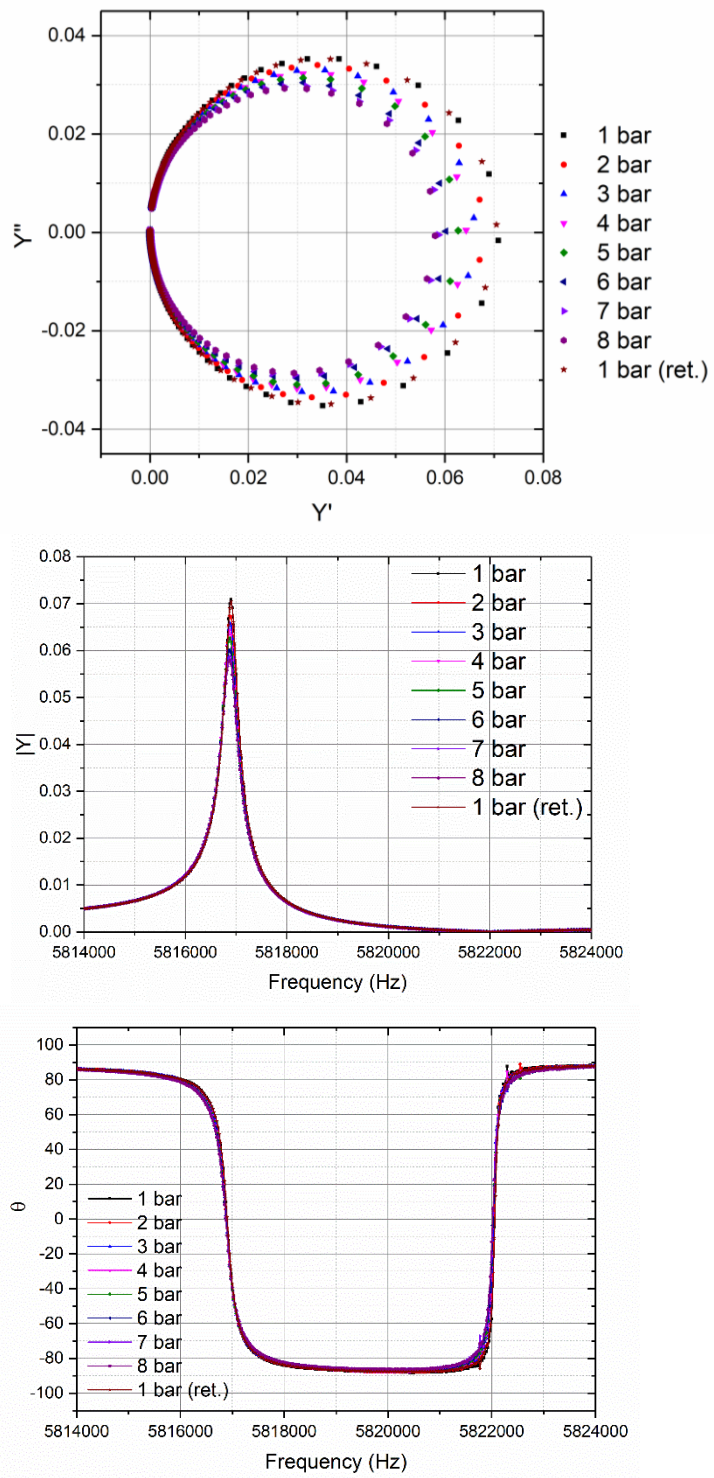

Figure 85: The admittance response for a GCM operating in pressurised environments of 1 – 8 bar.

Figure 84 and Figure 85 show the QCM and GCM admittance responses for the resonators operating under pressures 1 – 8 bar respectively. In both instances, the resonator responds similarly to the application of pressure – the oscillation is increasingly damped with increased pressure, similar to a small contacting viscous medium. Figure 84 and Figure 85 indicate that both resonators are able to successfully oscillate and fulfil the standing wave condition when operating under these pressures. Furthermore, the Bode plots in both investigations show only minute increases in the viscoelastic fitting components and thus have very little effect on the system's Q-factor indicating the usability of both resonators in pressurised environments. However, the admittance responses do confirm the trend in Figure 81 and suggest that the QCM response (with relatively larger changes in loci diameter, $|Y|_{max}$ and θ_{min}) is more damped when operated at elevated pressures compared to that of the GCM.

This section suggests that the GCM is able to operate as a useful interfacial resonator at pressures up to 8 bar.

Section 4.4.1 has shown the calibration studies for a GCM operating at replicable production chain temperatures, pressures and with a heavy contacting crude sample. Where possible, this has been compared to the QCM, the industry-leading BAW resonator. The GCM has shown through these studies that it can be operated stably and can, therefore, be used as an accurate *in-situ* BAW resonator for the proposed high temperature and pressure fouling investigation.

However, to truly elucidate the fouling activity at the oil / iron interface, the GCM required an iron layer deposited on its exposed electrode as discussed in Section 4.3.3. The process of iron electrodeposition for this system is explored below.

4.4.2 Iron Electrodeposition

This investigation deposits iron onto the GCM surface through the process of electrodeposition as discussed in Section 4.3.3. The benefit of being able to employ the GCM as an eGCM provided a means by which to determine the electrochemical efficiency of the plating technique.

The iron electrodeposition explored within this section is by no means extensive and this is further discussed in Section 4.5.1.

The electrodeposition study was conducted as suggested in the literature and employed the setup as described in Figure 72 with the GCM connected as an eGCM that acted as the working electrode, a platinum counter and a hydrogen reference suspended within the 0.9 M pH 5 iron(II) sulphate electrolyte operated at 25 ^{O}C.

Given the high viscosity of the contacting oil media to be employed within this study, thin iron layers were desirable in order to maintain the composite resonators high Q-factor. Therefore a representative thin iron layer (80 - 100 nm) was intended to be deposited on the GCM's double-anchor electrode surface.

4.4.2.1. Literature Value Plating Procedure

The first electrodeposition procedure was carried out as described in Section 4.3.3 and by [250, 251] and is hereunder referred to as the literature coat; the system was held at -15 mA (-50 mA cm^{-2}) for 4 seconds. The electrochemistry dictated by Equations (27) – (30) suggested that these conditions should yield an iron layer of 17.9 ng with a resulting thickness of 80.9 nm on the eGCM surface.

The eGCM's *in-situ* frequency response for this investigation is shown in Figure 86; initially, the frequency change registers 0 ppm whilst the system is not held at any current. Once the system's current is applied, the eGCM's frequency drops sharply and remains at this lower value until the systems applied current is removed. The resonator's frequency then returns to a

similar value as before the deposition; albeit slightly lower due to the additional contacting mass.

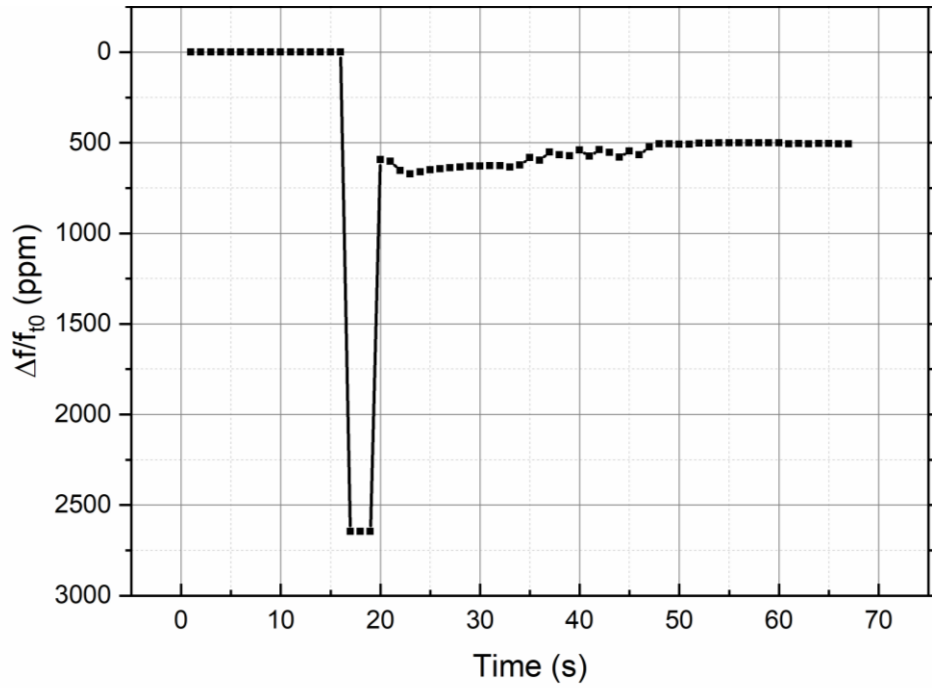

Figure 86: eGCM response for iron electrodeposition when the system is held at -15 mA for 4 s (literature plating values).

The shift in eGCM frequency during the electroplating process measures 507.66 ppm as shown in Figure 86 and indicates a deposition of 10.6 ng and thus a layer thickness of 47.5 nm. The predicted and *in-situ* measured masses were then used to calculate an electroplating efficiency of 58.7 %. This is lower than expected but compounded by a large amount of gas evolution at the working electrode when the potential was applied.

The iron layer electrodeposited during this investigation was dark grey in colour indicating an undesirable, excessively stressed deposition likely a result of Fe(III) salt deposits and hydrogen gas evolution. This was further examined through SEM and EDX studies as presented in Figure 87.

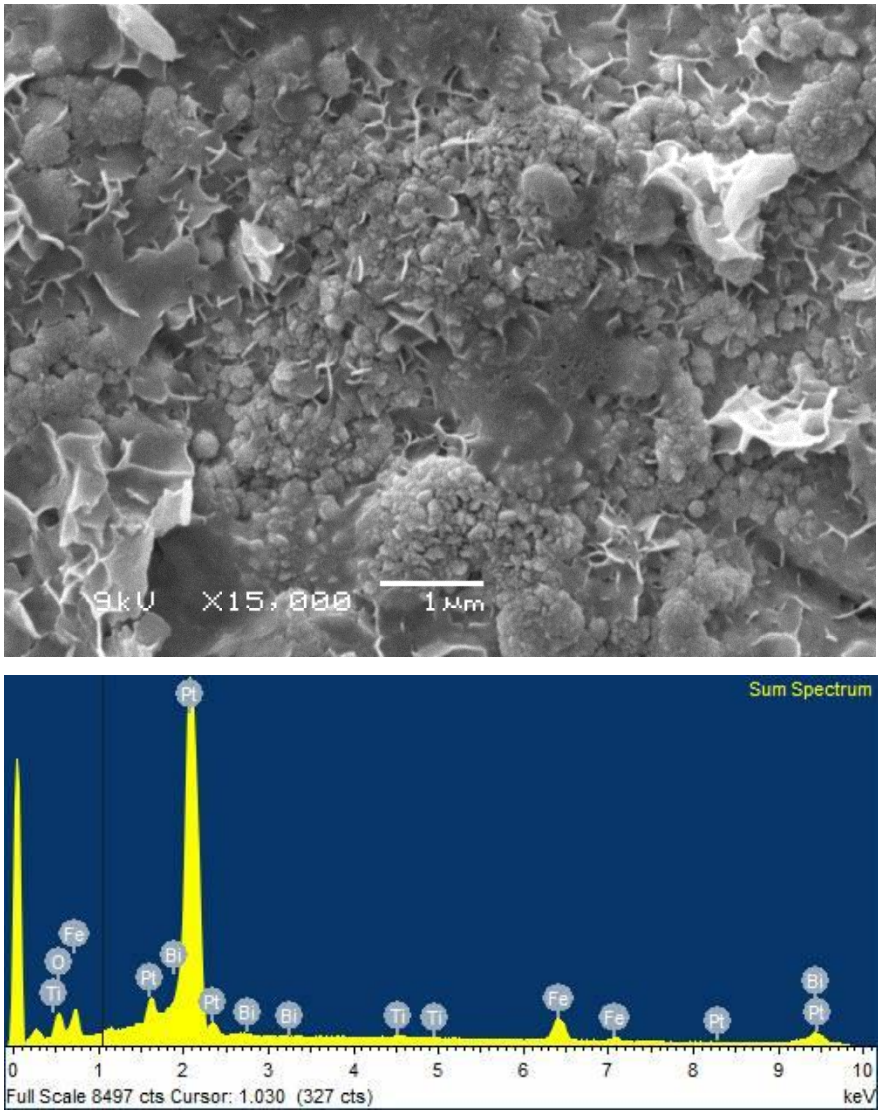

Figure 87: Literature coated iron electrodeposited iGCM SEM and EDX analysis

The SEM image and corresponding EDX data shown in Figure 87 indicate that iron is electroplating to the GCM's Pt electrode. However, the deposition using the literature values creates a rough, uneven layer with large defects and growths. The defects and growths in the layer will result in a larger surface area which would be expected to foul more easily than a smoother surface expected within the refinery equipment. This deposition provides a useful option for accelerated fouling and testing and the CAS results shown in Section 4.4.3 indicates its usability as a good quality composite BAW resonator.

However, in order to develop smoother more consistent electrodeposited layers, alternative deposition conditions were required. To understand the nuances of the electrodeposition system, a cyclic voltammogram was conducted using the system described in Figure 72. The resulting negative potential window (relevant to the plating process) of the CV is shown and annotated in Figure 88.

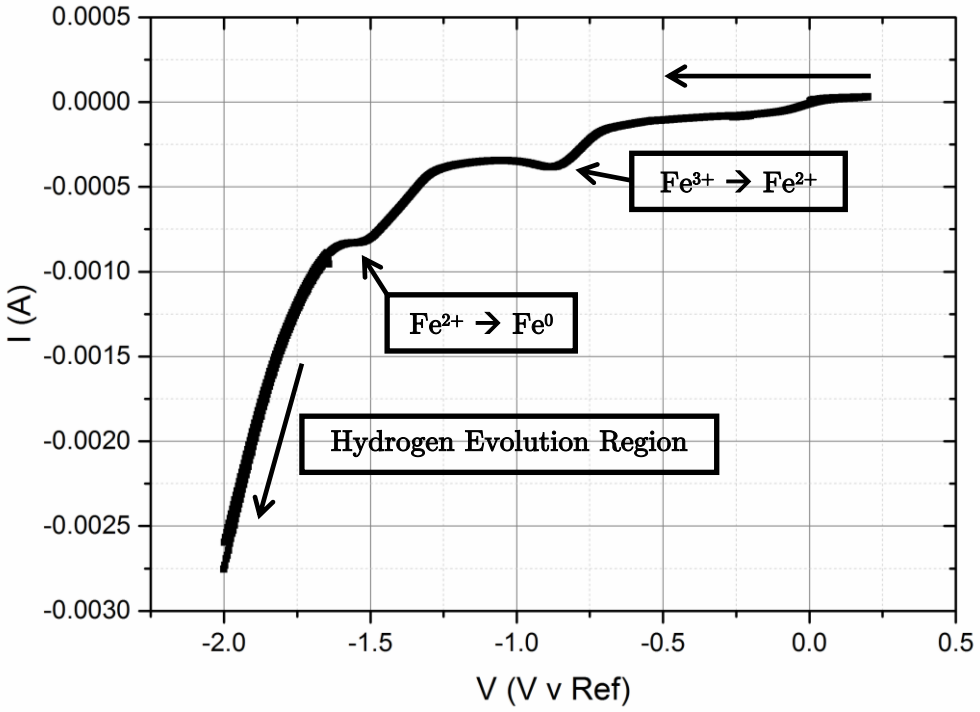

Figure 88: Relevant plating negative potential section of a cyclic voltammogram employing the electrodeposition setup described in Figure 72, with a GCM working electrode

The partial CV in Figure 88 confirms the findings from Section 4.4.2.1, indicating that when the system is operated at -15 mA (50 mA cm^{-2}) as suggested in the literature, there is a poor layer likely formed due to large amounts of hydrogen evolution also occurring at the electrode. The GCM in this case is operating deep in the hydrogen evolution region which begins at voltages below -1.65 V and is characterised by the sharp downward tail. The CV indicates the Fe^{3+} ions are converted to Fe^{2+} at the feature seen at - 0.8 V and that the Fe^{2+} is further reduced at -1.5 V to produce Fe^{0}. The production of Fe^{0} at -1.5 V indicates the beginning of the plating region; it

is thought that holding the system near to this region will provide the smoothest possible deposition layer.

4.4.2.2. Calculated Value Plating Procedure

With the aid of the partial CV in Figure 88, the plating potential was determined to be around -1.5 V and -0.9 mA (-3mA cm^{-2}). Using the same apparatus as outlined in Figure 72, and Equations (27) – (30) the system was held at the aforementioned plating potential for 80 s. As before, this relates to a theoretical iron deposition of 20.89 μg and a corresponding iron layer thickness of 94.7 nm; this process is hereunder referred to as the calculated value plating procedure.

Figure 89 shows the eGCM profile for this deposition and similarly to Figure 86 shows a sharp drop in the system's resonant frequency when the current is applied to the system. Once more, when the current is removed from the system, the eGCM returns to operation with a new resonant frequency 831 ppm lower than its initial start frequency.

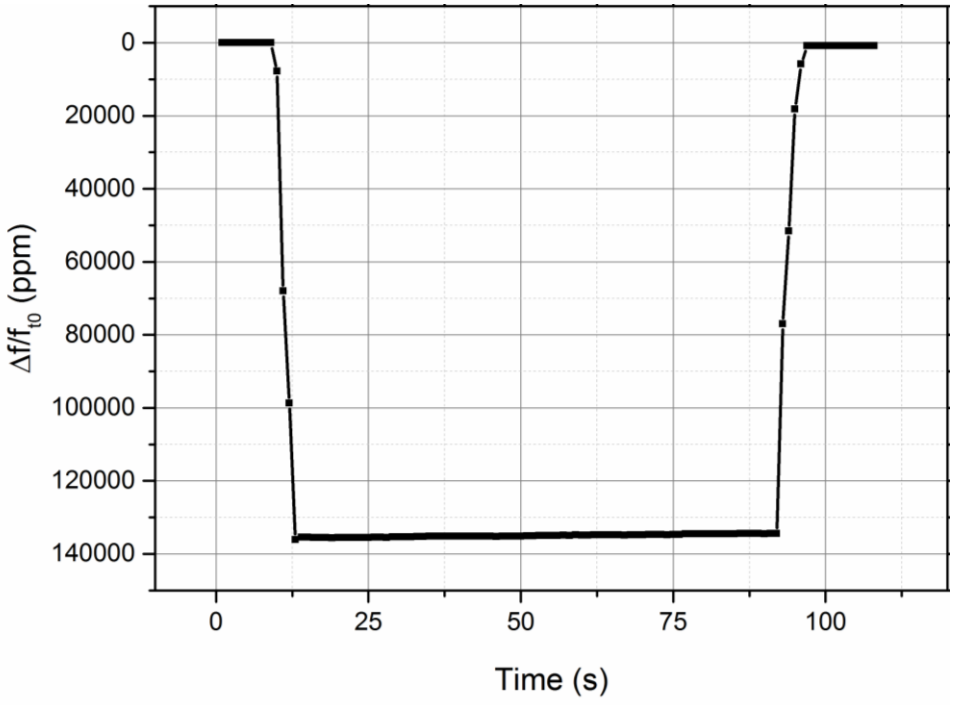

Figure 89: eGCM frequency response for the iron electrodeposition process when the system is held at -0.9 mA for 80s.

A 831 ppm shift relates to an additional contacting mass on the resonator surface of 17.4 μg and thus a layer thickness of 77.1 nm. The resulting layer deposition efficiency is significantly improved to 81 %.

On visual inspection of the iGCM, shown in Figure 90, the calculated coat layer appears grey in colour with a sheen finish which is in line with the observations in the literature [250].

Figure 90: Calculated value plating procedure iGCM, where the dark grey central area shows the addition of the iron layer to the platinum double anchor electrode.

The resulting iGCM from the calculated value plating procedure was further examined using SEM and EDX studies and the results are shown in Figure 91. The analyses once more indicate the presence of an iron electrodeposited layer on the electrode surface that appears to have a smoother and more homogenous finish with fewer defects and growths. Section 4.4.3 also indicates that the calculated coated iGCM is able to operate as a high-quality composite resonator.

The consistency of the layer is likely to have led to the slight sheen seen on the electrodeposited layer shown in Figure 90 and is more representative of the iron that will be seen within refinery equipment and transmission pipelines.

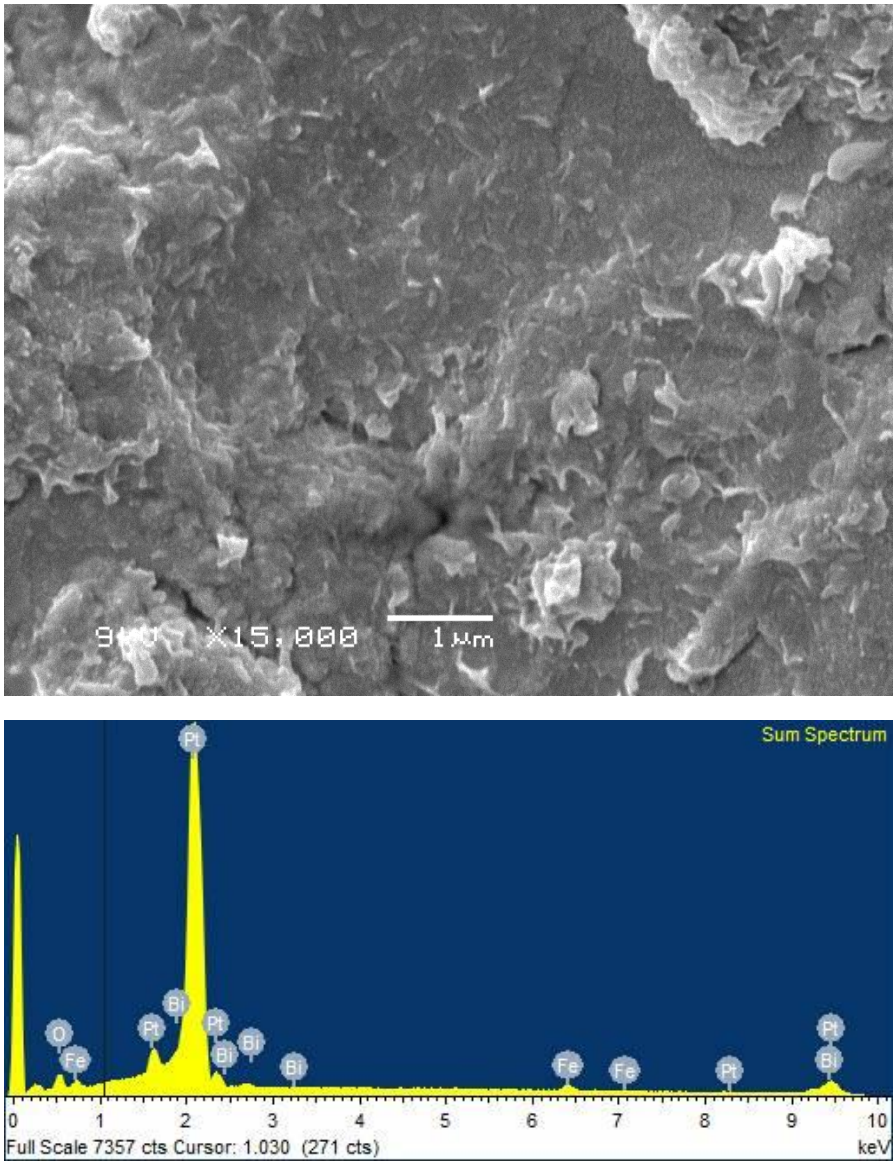

Figure 91: Calculated coat iron electrodeposited iGCM SEM and EDX analysis

4.4.3 iGCM Operation

The GCM has shown in the above sections to operate stably under the proposed conditions of this investigation; this section examines how the iGCM composite resonator operates under the same temperature and pressure conditions.

The studies presented in this section are designed to determine whether the iGCM composite resonator is able to withstand operating under these conditions for the proposed investigation.

4.4.3.1. Standing Wave Condition

In this section, the literature and calculated plated iGCMs' fulfilment of the standing wave condition is examined. The deposited layer in both cases was intended to be a thin film in order to maintain the composite resonators Q-factor during operation. Figure 92 shows the admittance response for both iGCMs. Both iGCM responses indicate the presence of a series and parallel resonant frequency and show little deviation from a typical GCM admittance response confirming their usability as suitable *in-situ* resonators for this application. It must also be noted that the differences seen in Figure 92 a and b are likely to be as a result of inherent differences in the resonator's properties, rather than the layer deposition; however, this is further discussed in Section 4.5.1.

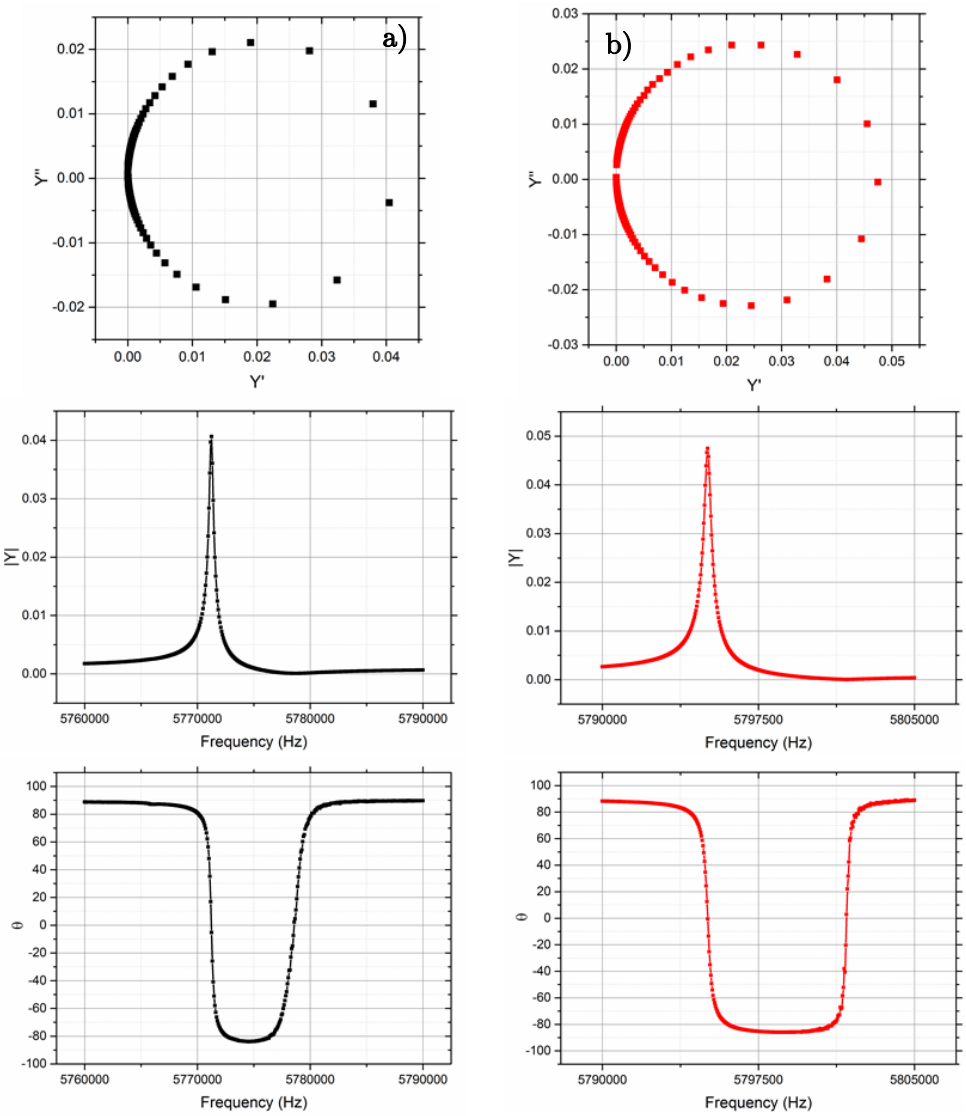

Figure 92: iGCM CAS responses for the a) literature and b) calculated platings, indicating minimal change to the system's Q-factor as a result of iron electrodeposition of 10.9 and 17.4 ng respectively

The final part of the calibration investigation presented here will look at the stability of the iGCM under the required investigative conditions. As this investigation is most likely to employ the calculated coat iGCM, it is used exclusively in each of the following stability tests.

4.4.3.2. Temperature Stability

Figure 93 shows the iGCM's frequency stability when operating in an environment of flowing argon (100 ml min^{-1}) at temperatures between 250 – 600 ^{O}C. The frequency stability shown here is comparable to the original GCM and shows minimal drift during operation (± 0.03 ppm) throughout this temperature range. The stability of the iGCM resonator during the investigative range of temperatures suggests that the composite resonator is a suitable choice for high temperature *in-situ* application.

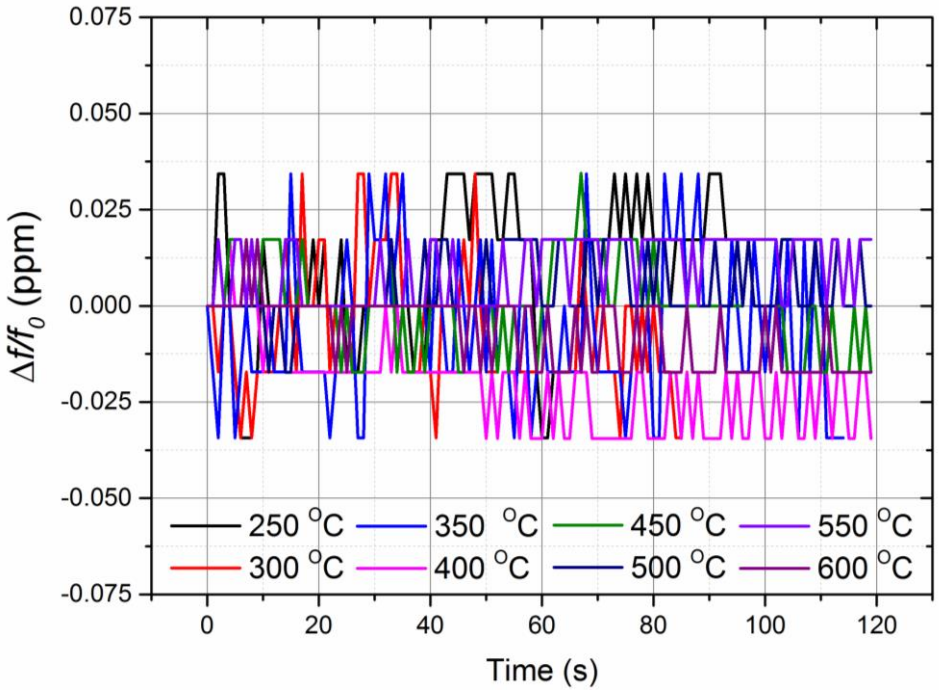

Figure 93: iGCM frequency stability when operating in an environment of flowing argon (100 ml min^{-1}) at a range of temperatures between 250 – 600 ^{O}C

4.4.3.3. Pressure Stability

The iGCM's frequency stability when operated in a pressurised argon environment between 1 – 8 bar is shown in Figure 94.

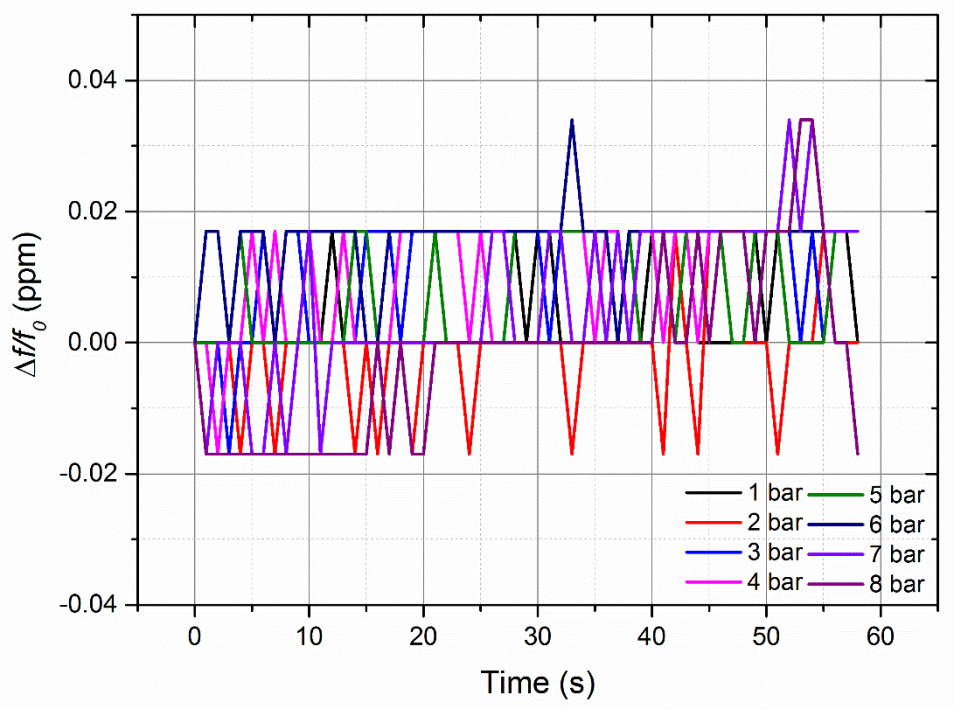

Figure 94: iGCM frequency stability when operated in argon at pressures between 1 – 8 bar.

Once more, the iGCM has shown excellent frequency stability, comparable to that of the original GCM at all pressures. This indicates that the iGCM can be used as a reliable *in-situ* mass monitoring device when held under the investigative pressure range.

4.4.3.4. Pressure and Temperature Stability

The final stability subsection investigates the iGCM's operation under combined temperature and pressure. Two representative studies for this investigation are presented in Figure 95 and monitor the iGCM's frequency response when held at 250 ^{o}C and 5 bar and at 350 ^{o}C at 3 bar.

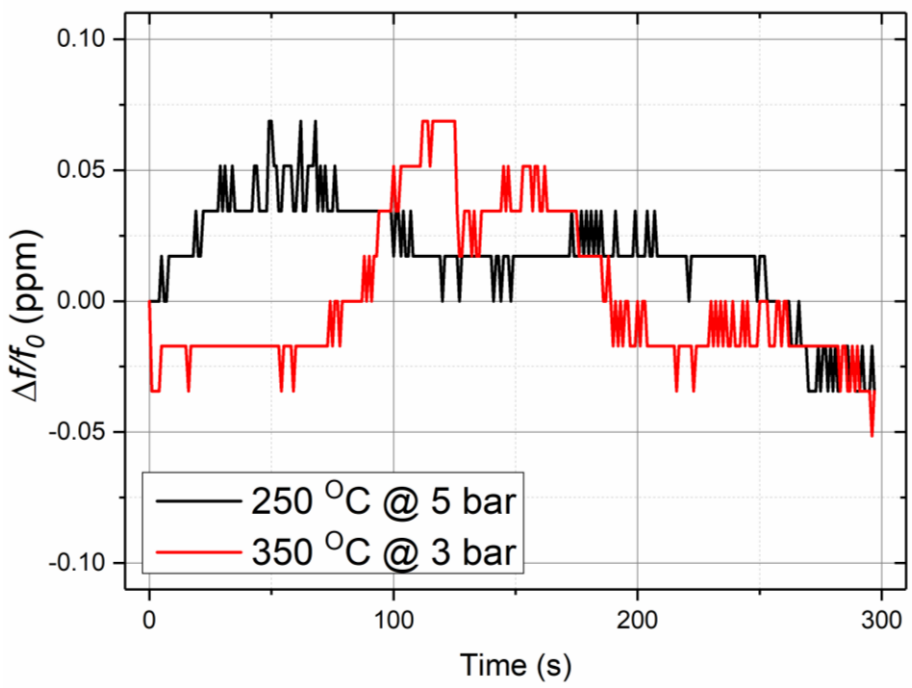

Figure 95: iGCM frequency response when held under two test conditions of 250 °C at 5 bar (black line) and 350 °C at 3 bar (red line).

Extracts of 5 minutes for each study are shown in Figure 95 and indicate that the microbalance operates stably under the given conditions. In each case, it must be noted that there is a slight sinusoidal frequency response for each investigation (albeit negligible ± 0.05 ppm) which is as a result of the PID control on the knuckle heater whilst operating within a pressurised system – once more this can be taken as the system's resolution. However, the microbalance shows excellent frequency stability in both cases akin to the drift seen in the GCM temperature and pressure studies shown in Figure 76 and Figure 83 respectively.

The above investigations suggest that the iGCM and rig set up are able to successfully operate with the proposed investigative parameters required to replicate the conditions within transmission oil pipelines and refinery equipment.

4.4.4 *In-situ* Application

This project has the versatility to take many future forms as discussed in Section 4.5.1; however, in its harshest connotation, the iGCM will operate with a raw contacting heavy crude sample under a range of investigative conditions. In order to assess the system's ability to cope with the harshest possible conditions, a representative investigation is presented here for an iGCM operating at 300 ^{O}C and 3.5 bar with a ~ 0.01 mg contacting heavy crude sample.

4.4.4.1. Active Response

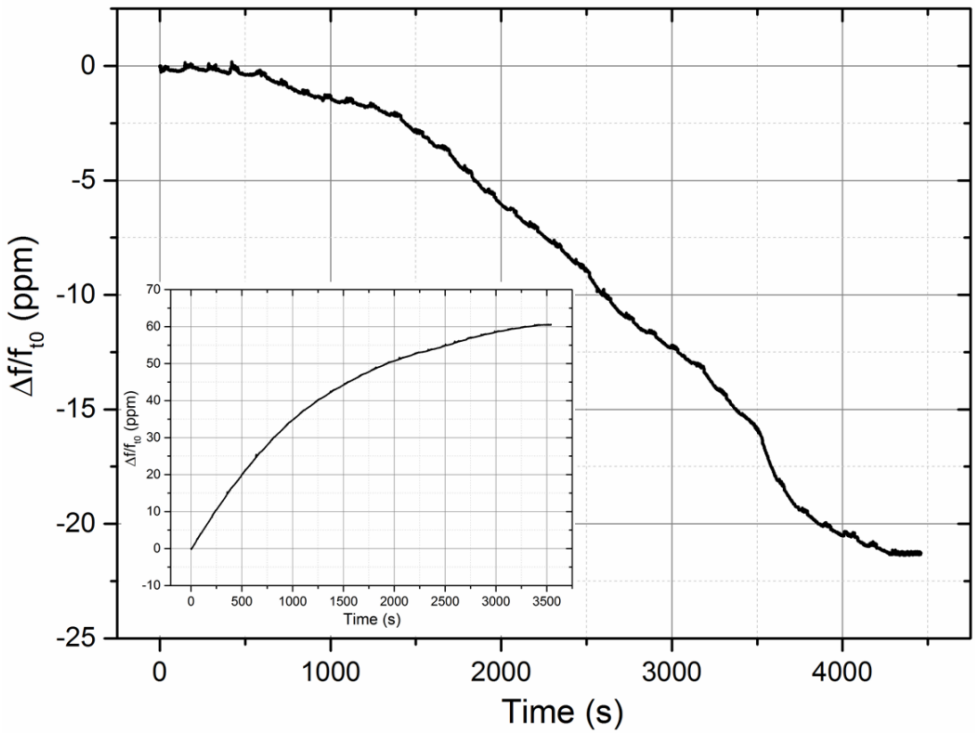

Figure 96: The active iGCM response when in contact with ~ 0.01 mg of heavy vacuum residue. The response is initially taken after composite resonator stabilisation and the inset image shows the active response between achieving T_C and reporting a stable frequency response.

The frequency response for this investigation after the composite resonator initially achieves its T_C is shown in Figure 96 inset. After the T_C has been achieved, the resonator's frequency continues to increase as the pressurised vessel and contacting media reach an equilibrium temperature and the resonator's frequency stabilises. The main Figure shows the frequency response of the vessel and composite resonator when operating at 300 ^{O}C and 3.5 bar. Initially, the frequency remains relatively stable with small fluctuations (similar in magnitude to that seen in Figure 95); a direct result of the PID control pulse heating mechanism. However, after roughly 10 mins, the measured frequency response begins to decrease and continues to decrease over the next 60 mins. At 4300 s, the resonator's resonant frequency stabilises at a new value 21.2 ppm lower than the initial frequency. A decrease in frequency of this nature suggests an additional contacting mass on the microbalance surface. However, with the active response alone, it is not possible to determine whether this mass change is at the oil – iron interface, the oil – argon interface or due to a change in the contacting crude's physical characteristics.

4.4.4.2. Passive Response

The passive responses for this study are taken at the start ($time = 0$) and end of the active response investigation ($time = 4500$ s) and are presented in Figure 97. The CAS response shows a decreasing admittance locus, a slight 'leftward' shift in both the magnitude of admittance and theta plots with a decreased $|Y|_{max}$ and increased θ_{min} value. When compared to the analysis presented in Section 2.6.3, these responses indicate an increase in the viscoelastic component of the modified BVD shown in Figure 12. With constant temperature and pressure applied within the system, the effect of these can be assumed to be negligible.

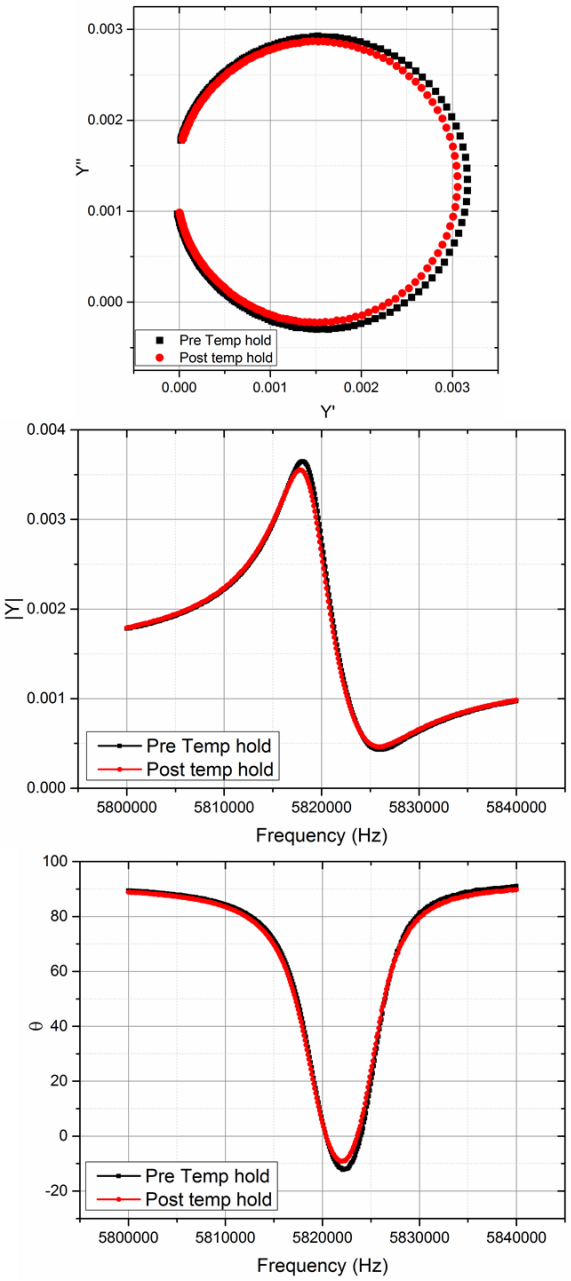

Parameter	Pre-Temp hold	Post-Temp hold
Loci Diameter	3.17×10^{-3}	3.06×10^{-3}
$\lvert Y_{max} \rvert$ frequency (Hz)	5.8181×10^{6}	5.8177×10^{6}
$\lvert Y_{max} \rvert$	3.65×10^{-3}	3.55×10^{-3}

Figure 97: The admittance response for the iGCM in contact with 0.01 mg of heavy vacuum residue before and after being held at 300 °C and 3.5 bar. Key metrics are also presented

When the passive and active responses are compared, the results suggest that the oil sample undergoes a transition to a more viscous phase increasing the composite resonator's resistance to operation and thus resulting in a reduced resonant frequency.

The increased viscoelastic component of the composite resonator may be as a result of asphaltene agglomeration and precipitation from the oil sample propagating towards and depositing onto the iron layer on the iGCM. Asphaltene agglomeration and precipitation are expected to form dendritic-type deposits on the iron surface that begin to build up as described in Section 4.2.3.3. Deposits of any kind from the crude sample are likely to cause changes in the system's viscoelastic component as the sample itself changes, but more likely as a result of the effect of the deposition itself. However, it is only through the implementation of a surface analysis technique that the proposed theories can be confirmed, as discussed below.

4.4.4.3. Monitoring Deposits

After the investigations outlined above, the system was cooled, depressurised and the crude – iGCM was removed. The composite resonator maintained an evenly spread layer of oil on the top electrode confined by the Grafoil O-ring in the microbalance holder. The presence of the oil on the microbalance surface suggests that evaporation of the oil, as seen in Section 4.4.1.2, was not a contributing factor in this analysis. The oil however prevented further analysis at the interfacial level using SEM and EDX and so X-ray computed tomography and reconstruction were employed to further study the system.

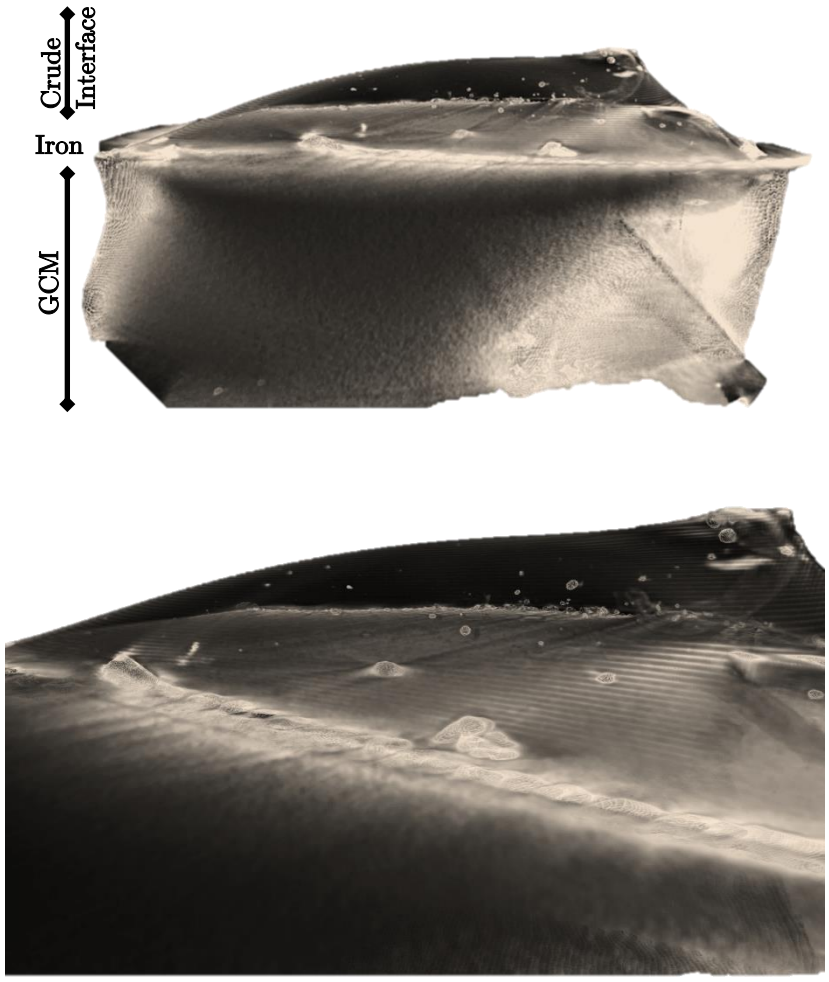

Figure 98: X-ray tomography reconstructions of a) the iron – crude interface on the GCM and b) a zoomed in image of the same.

Figure 98 shows the X-ray reconstructions of the iron – crude interface after the testing described above. Within the crude sample, particles of varying sizes can be observed both at the interface as well as suspended within the media. Whilst it is not possible to conclusively determine what these unidentified floating objects (UFOs) are without further elemental analysis, their presence at the interface may suggest the occurrence of asphaltene precipitation, migration and deposition towards the iron layer. However, further analysis to confirm this phenomenon is required as discussed in Section 4.5.1

4.5 Conclusion

Whilst very much in its infancy, the work presented in this Chapter outlines the development of an *in-situ* low-volume, rapid analysis BAW resonator study to elucidate the fouling properties of specific heavy crude oil blends. The literature review presented in Section 4.2 describes the conditions and factors that are understood to affect the fouling characteristics of heavy crude oil and specifically asphaltene precipitation along with traditional methods of combating these issues. The iGCM device proposed here could provide application for academia and industry alike in the area of both asphaltene rejection and conversion to understand both the effect of operating conditions and the presence of chemical additives.

Within this chapter, the GCM has been identified as a suitable BAW resonator for application at both the required elevated temperatures and pressures necessary for the development of pseudo-refinery and transportation equipment necessary in the heavy crude oil production chain. The GCM has been operated as an electrochemical GCM (eGCM) as an *in-situ* mass monitoring device to determine plating efficiency in the development of the electrodeposited iron layer on the GCM (iGCM). The iGCM has been developed using literature plating values as well as a system specific calculated coat method. Both iGCMs' iron layers were analysed using SEM and EDX and the calculated coat iGCM was found to produce a more homogeneous finish with fewer defects. The calculated coat iGCM was further investigated and has also proven to maintain a high Q-factor and fulfil the standing wave condition as well as provide stable operation under the proposed investigative conditions.

The critical temperature of the crude-GCM composite resonator has also been explored and for the first time, the use of CAS has suggested that the traditional critical temperature may not occur as originally expected. A discussion of the propagation of the standing wave through the less viscous contacting media with the application of temperature is provided as a means to explain the composite resonators ability to fulfil the standing wave condition.

An example analysis of the crude-iGCM is provided in Section 4.4.4 and whilst not extensive shows the usability of the system in its harshest possible operating parameters with contacting raw heavy crude oil. The suite of techniques including active and passive microbalance operation alongside X-ray tomography reconstructions has been shown to provide an excellent analytical tool in the quest for the elucidation of fouling properties of a specific setup.

4.5.1 Future work

This work will be further developed in collaboration with the QNRF. There are several key areas of focus for the successful development of this system which are outlined as follows:

The electrodeposited iron layer used during this study has proven to be suitably stable for operation under the investigative conditions. However, further development and characterisation of the deposited iron layers to provide a means by which to assimilate the surfaces within different refinery equipment will prove useful in providing more accurate fouling characteristics. The iron layer development will play a significant role in how the system responds to fouling and is expected to be a major part of the development of this device for widespread use

The oil sample delivery to the iGCM will also be a key factor in producing repeatable end-user results. Whilst the microbalance has shown operation above the critical temperature when in contact with the heavy crude sample, the current method of pipetting the raw heavy crude sample onto the microbalance will need further development. Many researchers use model oils and re-dissolved precipitated asphaltenes during their investigations, as discussed in Section 4.2.3.3; the implementation of these samples and / or other pre-treatment techniques to determine the repeatability of results is of critical importance moving towards the standalone device.

As this system is very much in its infancy, it requires extensive testing and calibrating along-side known systems and quantities in order to verify its accuracy and usability. Operating this system with samples known to produce specific fouling levels and characteristics is an important step in verifying the small volume, rapid sample analysis.

The X-ray computed tomography reconstruction for the microbalance surface operating under a crude sample is shown in Figure 98. Whilst it shows the presence of 'UFOs' at the oil microbalance interface, it is difficult to characterise exactly what is present. Further work to develop a process of understanding a fouling deposition and / or asphaltene agglomeration and precipitation is required (possibly at a beam-line with EDX) to confirm exactly what is being measured and subsequently imaged.

The future of this project lays in the development of a standalone product; an on-site device capable of providing a low volume, rapid and accurate determination of the fouling properties of a particular heavy crude oil source. The end user should be able to use the device to regulate how a particular heavy crude may affect the refinery or transportation equipment and take the necessary steps to prevent or promote certain outcomes. The development of this device can be in many forms, including a vessel that provides a heated and pressurised flow of sample oil over the resonator's surface. The development of such a device may prove difficult and costly to develop, but will provide the industry with a much-needed feedback sensor.

5 Overall Conclusions

5.1 Technique

Throughout this thesis, surface developed BAW resonators have been established using a range of methods including *in-situ* polymer casting onto a QCM for AAEM characterisation and iron electrodeposition using the eGCM for heavy crude oil fouling detection. In each case, the techniques provided thin-film, smooth, reproducible layers with thicknesses ranging between $20 - 100$ nm. Each surface developed BAW resonator has been tested to ensure fulfilment of the standing wave condition; even when loaded. Crystal admittance spectroscopy and equivalent circuits have been used alongside active frequency responses throughout these studies and has provided additional insight into the phenomena occurring at the interfacial layer.

Each study presented within this thesis has an associated bespoke rig design set up to simulate environments that would typically be found in both an operating fuel cell (Chapter 3) and within the heavy crude oil production chain (Chapter 4). Together with the experimental rig setups, the surface developed BAW resonators have been tested and extensively calibrated to ensure the frequency response contributions were as a result of the variable under test only. Where possible, the investigations have been developed along-side existing technologies and similar literature investigations as a means for technique verification.

Overall, the results presented within the two studies conducted in this thesis have shown the versatility of the BAW resonator technology and provided useful insight into the interfacial phenomena occurring within each energy system.

5.2 Application

The study specific conclusions and proposed future work is presented within the corresponding chapters within this thesis, thus only an overview is presented here.

The first study focuses primarily on the commercially available AS-4 ionomer as a representative industry standard AAEM. The first investigation presented within this study has suggested the ionomer's hydration mechanisms occur in part similar to that of Nafion with a solvation period at RHs $\leq 66\%$ followed by a swelling regime at higher RHs. The second part of the study explores the AS-4 ionomer instability and degradation when operated at elevated temperatures as a function of its hydration state. The theories presented in this section indicate that the degradation pathways are more dominant when the ionomer is partially hydrated and specifically during the solvation regime. When the ionomer is operating during the swelling regime, the results indicate that the ionomer is more stable within the alkaline media and shows fewer signs of degradation. The final investigation presented within Chapter 3 assesses the carbonate ion interaction of the AS-4 ionomer as a function of ionomer hydration. The findings suggest that the ionomer shows increased interaction with the carbonate ions as it becomes more solvated. This phenomenon is thought to be a direct result of channel hydration and access of the carbonate ions to the cationic functional headgroups.

In each case, the information gathered using the QCM in combination with other *ex-situ* techniques will provide the industry with useful insight into the ionomer's operation in order to guide future ionomer integration and development.

Chapter 4 outlines the initial development of an *in-situ* feedback sensor for heavy crude oil fouling detection and characterisation. This Chapter presents a thorough examination of a high-temperature BAW resonator (GCM) for operation in harsh conditions (pressure and temperature akin to those seen within the oil refinery and transportation industries) with an electrodeposited iron layer and in contact with a viscous contacting media. The *ex-situ* X-ray computed tomography investigation presented shows the presence of 'UFOs' both within the contacting oil media and on the iGCM surface, potentially indicating the occurrence of asphaltene precipitation and deposition onto the iGCM surface. The future of this project in collaboration with the QNRF is the development and production of an on-site device to assess the fouling characteristics of particular samples of heavy crude oil.

This thesis has shown that the applications of BAW resonators for in-situ interfacial investigations can provide a powerful tool to offer useful insights to the processes occurring at the interfacial level to guide future technological advancements.

6 References

[1] R. L. Filler, "The Acceleration Sensitivity of Quartz Crystal-Oscillators - a Review," (in English), *Ieee Transactions on Ultrasonics Ferroelectrics and Frequency Control,* vol. 35, no. 3, pp. 297-305, May 1988.

[2] D. A. Buttry and M. D. Ward, "Measurement of Interfacial Processes at Electrode Surfaces with the Electrochemical Quartz Crystal Microbalance," (in English), *Chemical Reviews,* vol. 92, no. 6, pp. 1355-1379, Sep-Oct 1992.

[3] J. F. Alder and J. J. Mccallum, "Piezoelectric-Crystals for Mass and Chemical Measurements - a Review," (in English), *Analyst,* vol. 108, no. 1291, pp. 1169-1189, 1983.

[4] A. W. Czanderna. C. Lu, *Applications of Piezoelectric Quartz Crystal Microbalances*. Elsevier, 1984.

[5] G. Sauerbrey, "Verwendung Von Schwingquarzen Zur Wagung Dunner Schichten Und Zur Mikrowagung," (in English), *Zeitschrift Fur Physik,* vol. 155, no. 2, pp. 206-222, 1959.

[6] M. Rodahl, F. Hook, A. Krozer, P. Brzezinski, and B. Kasemo, "Quartz-Crystal Microbalance Setup for Frequency and Q-Factor Measurements in Gaseous and Liquid Environments," (in English), *Review of Scientific Instruments,* vol. 66, no. 7, pp. 3924-3930, Jul 1995.

[7] D. M. Ullevig, J. F. Evans, and M. G. Albrecht, "Effects of Stressed Materials on the Radial Sensitivity Function of a Quartz Crystal Microbalance," (in English), *Analytical Chemistry,* vol. 54, no. 13, pp. 2341-2343, 1982.

[8] H. Fukuyo, N. Oura, A. Yokoyama, and S. Nonaka, "Thickness-Shear Vibration of Circular Biconvex at-Cut Plates," (in English), *Electrical Engineering in Japan,* vol. 94, no. 3, pp. 36-42, 1974.

[9] I. Koga, "Radio-Frequency Vibrations of Rectangular at-Cut Quartz Plates," (in English), *Journal of Applied Physics,* vol. 34, no. 8, pp. 2357-&, 1963.

[10] H. Sekimoto, "Analysis of Trapped Energy Resonators with Circular Electrodes," (in English), *Ieee Transactions on Sonics and Ultrasonics,* vol. 31, no. 6, pp. 664-669, 1984.

[11] L. V. Rajakovic, B. A. Cavic-Vlasak, V. Ghaemmaghami, K. M. R. Kallury, A. L. Kipling, and M. Thompson, "Mediation of Acoustic Energy Transmission from Acoustic-Wave Sensors to the Liquid-Phase by Interfacial Viscosity," (in English), *Analytical Chemistry,* vol. 63, no. 6, pp. 615-621, Mar 15 1991.

[12] T. Nomura and O. Hattori, "Determination of Micromolar Concentrations of Cyanide in Solution with a Piezoelectric Detector," (in English), *Analytica Chimica Acta,* vol. 115, no. Mar, pp. 323-326, 1980.

[13] P. L. Konash and G. J. Bastiaans, "Piezoelectric-Crystals as Detectors in Liquid-Chromatography," (in English), *Analytical Chemistry,* vol. 52, no. 12, pp. 1929-1931, 1980.

[14] T. Nomura and M. Okuhara, "Frequency-Shifts of Piezoelectric Quartz Crystals Immersed in Organic Liquids," (in English), *Analytica Chimica Acta,* vol. 142, no. Oct, pp. 281-284, 1982.

[15] S. Bruckenstein and M. Shay, "Insitu Weighing of Atom Layer Thick-Films at Electrodes," (in English), *Abstracts of Papers of the American Chemical Society,* vol. 186, no. Aug, pp. 45-Anyl, 1983.

[16] M. Thompson, A. L. Kipling, W. C. Duncan-Hewitt, L. V. Rajakovic, and B. A. Cavic-Vlasak, "Thickness-Shear-Mode Acoustic-Wave Sensors in the Liquid-Phase - a Review," (in English), *Analyst,* vol. 116, no. 9, pp. 881-890, Sep 1991.

[17] K. K. Kanazawa and J. G. Gordon, "The Oscillation Frequency of a Quartz Resonator in Contact with a Liquid," (in English), *Analytica Chimica Acta,* vol. 175, no. Sep, pp. 99-105, 1985.

[18] K. K. Kanazawa and J. G. Gordon, "Frequency of a Quartz Microbalance in Contact with Liquid," (in English), *Analytical Chemistry,* vol. 57, no. 8, pp. 1770-1771, 1985.

[19] S. Bruckenstein and M. Shay, "Experimental Aspects of Use of the Quartz Crystal Microbalance in Solution," (in English), *Electrochimica Acta,* vol. 30, no. 10, pp. 1295-1300, 1985.

[20] S. Z. Yao and T. A. Zhou, "Dependence of the Oscillation Frequency of a Piezoelectric Crystal on the Physical Parameters of Liquids," (in English), *Analytica Chimica Acta,* vol. 212, no. 1-2, pp. 61-72, Sep 15 1988.

[21] S. J. Martin, G. C. Frye, and S. D. Senturia, "Dynamics and Response of Polymer-Coated Surface-Acoustic-Wave Devices - Effect of Viscoelastic Properties and Film Resonance," (in English), *Analytical Chemistry,* vol. 66, no. 14, pp. 2201-2219, Jul 15 1994.

[22] P. A. Topart and M. A. M. Noel, "High-Frequency Impedance Analysis of Quartz-Crystal Microbalances .2. Electrochemical Deposition and Redox Switching of Conducting Polymers," (in English), *Analytical Chemistry,* vol. 66, no. 18, pp. 2926-2934, Sep 15 1994.

[23] R. Schumacher, G. Borges, and K. K. Kanazawa, "The Quartz Microbalance - a Sensitive Tool to Probe Surface Reconstructions on Gold Electrodes in Liquid," (in English), *Surface Science,* vol. 163, no. 1, pp. L621-L626, 1985.

[24] R. Schumacher, "The Quartz Microbalance - a Novel-Approach to the Insitu Investigation of Interfacial Phenomena at the Solid Liquid Junction," (in English), *Angewandte Chemie-International Edition in English,* vol. 29, no. 4, pp. 329-343, Apr 1990.

[25] W. H. Zhu, W. Z. Wei, Z. H. Mo, L. H. Nie, and S. Z. Yao, "Piezoelectric Detection of Water with a Separated Electrode," (in English), *Analytical Chemistry,* vol. 65, no. 19, pp. 2568-2571, Oct 1 1993.

[26] H. E. Hager, "Fluid Property Evaluation by Piezoelectric-Crystals Operating in the Thickness Shear Mode," (in English), *Chemical Engineering Communications,* vol. 43, no. 1-3, pp. 25-38, 1986.

[27] T. A. Zhou, L. H. Nie, and S. Z. Yao, "On Equivalent-Circuits of Piezoelectric Quartz Crystals in a Liquid and Liquid Properties .1. Theoretical Derivation of the Equivalent-Circuit and Effects of Density and Viscosity of Liquids," (in English), *Journal of Electroanalytical Chemistry,* vol. 293, no. 1-2, pp. 1-18, Oct 25 1990.

[28] H. L. Bandey, S. J. Martin, R. W. Cernosek, and A. R. Hillman, "Modeling the responses of thickness-shear mode resonators under various loading conditions," (in English), *Analytical Chemistry,* vol. 71, no. 11, pp. 2205-2214, Jun 1 1999.

[29] M. E. Orazem and B. Tribollet, *Electrochemical impedance spectroscopy* (The Electrochemical Society series). Hoboken, N.J.: Wiley, 2008, pp. xxxi, 523 p.

[30] J. R. Scully, D. C. Silverman, and M. W. Kendig, *Electrochemical impedance : analysis and interpretation* (Stp, no. 1188). Philadelphia: ASTM, 1993, p. 480 p.

[31] W. G. Cady, *Piezoelectricity; an introduction to the theory and applications of electromechanical phenomena in crystals*, New rev. ed. New York,: Dover Publications, 1964.

[32] G. P. Martin, B. E. Loveday, and C. Marriott, "The Effect of Bromhexine Hydrochloride on the Viscoelastic Properties of Mucus from the Mini-Pig," (in English), *European Respiratory Journal,* vol. 3, no. 4, pp. 392-396, Apr 1990.

[33] H. L. Bandey, S. J. Martin, R. W. Cernosek, and A. R. Hillman, "Equivalent-circuit model for the TSM resonator with a viscoelastic film near film resonance," (in English), *Chemical Sensors Iv, Proceedings of the Symposium,* vol. 99, no. 23, pp. 320-325, 1999.

[34] H. Muramatsu, E. Tamiya, and I. Karube, "Computation of Equivalent-Circuit Parameters of Quartz Crystals in Contact with Liquids and Study of Liquid Properties," (in English), *Analytical Chemistry,* vol. 60, no. 19, pp. 2142-2146, Oct 1 1988.

[35] R. Beck, U. Pittermann, and K. G. Weil, "Impedance Analysis of Quartz Oscillators, Contacted on One Side with a Liquid," (in English), *Berichte Der Bunsen-Gesellschaft-Physical Chemistry Chemical Physics,* vol. 92, no. 11, pp. 1363-1368, Nov 1988.

[36] A. L. Kipling and M. Thompson, "Network Analysis Method Applied to Liquid-Phase Acoustic-Wave Sensors," (in English), *Analytical Chemistry,* vol. 62, no. 14, pp. 1514-1519, Jul 15 1990.

[37] S. J. Martin, V. E. Granstaff, and G. C. Frye, "Characterization of a Quartz Crystal Microbalance with Simultaneous Mass and Liquid Loading," (in English), *Analytical Chemistry,* vol. 63, no. 20, pp. 2272-2281, Oct 15 1991.

[38] S. J. Martin, H. L. Bandey, R. W. Cernosek, A. R. Hillman, and M. J. Brown, "Equivalent-circuit model for the thickness-shear mode resonator with a viscoelastic film near film resonance," (in English), *Analytical Chemistry,* vol. 72, no. 1, pp. 141-149, Jan 1 2000.

[39] J. F. Rosenbaum, *Bulk acoustic wave theory and devices* (The Artech House acoustics library). Boston: Artech House, 1988, pp. xiv, 462 p.

[40] M. S. Yang and M. Thompson, "Multiple Chemical Information from the Thickness Shear Mode Acoustic-Wave Sensor in the Liquid-Phase," (in English), *Analytical Chemistry,* vol. 65, no. 9, pp. 1158-1168, May 1 1993.

[41] T. Nomura and T. Nagamune, "Internal Electrolytic Determination of Silver in Solution with a Piezoelectric Quartz Crystal," (in English), *Analytica Chimica Acta,* vol. 155, no. Dec, pp. 231-234, 1983.

[42] T. Nomura, M. Watanabe, and T. S. West, "Behavior of Piezoelectric Quartz Crystals in Solutions with Application to the Determination of Iodide," (in English), *Analytica Chimica Acta,* vol. 175, no. Sep, pp. 107-116, 1985.

[43] T. Nomura and M. Maruyama, "Effect of Metal-Ions on a Piezoelectric Quartz Crystal in Aqueous-Solution and the Adsorptive Determination of Iron(Iii) as Phosphate," (in English), *Analytica Chimica Acta,* vol. 147, no. Mar, pp. 365-369, 1983.

[44] K. K. Kanazawa and O. R. Melroy, "The Quartz Resonator - Electrochemical Applications," (in English), *Ibm Journal of Research and Development,* vol. 37, no. 2, pp. 157-171, Mar 1993.

[45] N. Oyama and T. Ohsaka, "Coupling between Electron and Mass-Transfer Kinetics in Electroactive Polymer-Films - an Application of the in-Situ Quartz-Crystal Electrode," (in English), *Progress in Polymer Science,* vol. 20, no. 5, pp. 761-818, 1995.

[46] T. D. Gierke, G. E. Munn, and F. C. Wilson, "The Morphology in Nafion Perfluorinated Membrane Products, as Determined by Wide-Angle and Small-Angle X-Ray Studies," (in English), *Journal of Polymer Science Part B-Polymer Physics,* vol. 19, no. 11, pp. 1687-1704, 1981.

[47] E. J. Roche, M. Pineri, R. Duplessix, and A. M. Levelut, "Small-Angle Scattering Studies of Nafion Membranes," (in English), *Journal of Polymer Science Part B-Polymer Physics,* vol. 19, no. 1, pp. 1-11, 1981.

[48] M. Fujimura, T. Hashimoto, and H. Kawai, "Small-Angle X-Ray-Scattering Study of Perfluorinated Ionomer Membranes .1. Origin of 2 Scattering Maxima," (in English), *Macromolecules,* vol. 14, no. 5, pp. 1309-1315, 1981.

[49] R. P. O'Hayre, *Fuel cell fundamentals*, 2nd ed. Hoboken, N.J.: John Wiley & Sons, 2009, pp. xxv, 546 p., 4 p. of plates.

[50] J. Larminie and A. Dicks, *Fuel cell systems explained*, 2nd ed. Chichester, West Sussex: J. Wiley, 2003, pp. xxii, 406 p.

[51] J. R. Varcoe and R. C. T. Slade, "Prospects for alkaline anion-exchange membranes in low temperature fuel cells," (in English), *Fuel Cells,* vol. 5, no. 2, pp. 187-200, Apr 2005.

[52] M. A. Hickner, A. M. Herring, and E. B. Coughlin, "Anion Exchange Membranes: Current Status and Moving Forward (vol 51, pg 1727, 2013)," (in English), *Journal of Polymer Science Part B-Polymer Physics,* vol. 52, no. 4, pp. 347-347, Feb 15 2014.

[53] G. Merle, M. Wessling, and K. Nijmeijer, "Anion exchange membranes for alkaline fuel cells: A review," (in English), *Journal of Membrane Science,* vol. 377, no. 1-2, pp. 1-35, Jul 15 2011.

[54] J. Cheng, G. H. He, and F. X. Zhang, "A mini-review on anion exchange membranes for fuel cell applications: Stability issue and addressing strategies," (in English), *International Journal of Hydrogen Energy,* vol. 40, no. 23, pp. 7348-7360, Jun 22 2015.

[55] Y. J. Wang, J. L. Qiao, R. Baker, and J. J. Zhang, "Alkaline polymer electrolyte membranes for fuel cell applications," (in English), *Chemical Society Reviews,* vol. 42, no. 13, pp. 5768-5787, 2013.

[56] G. W. Li, J. Pan, J. J. Han, C. Chen, J. T. Lu, and L. Zhuang, "Ultrathin composite membrane of alkaline polymer electrolyte for fuel cell applications," (in English), *Journal of Materials Chemistry A,* vol. 1, no. 40, pp. 12497-12502, 2013.

[57] R. Jervis *et al.*, "Hydrogen Oxidation on PdIr/C Catalysts in Alkaline Media," (in English), *Journal of the Electrochemical Society,* vol. 161, no. 4, pp. F458-F463, 2014.

[58] R. Jervis, N. Mansor, C. Gibbs, C. A. Murray, C. C. Tang, and D. J. L. Brett, "Novel PdIr/C Catalysts for the Hydrogen Oxidation Reaction in Alkaline Media," (in English), *Polymer Electrolyte Fuel Cells 13 (Pefc 13),* vol. 58, no. 1, pp. 637-650, 2013.

[59] S. Srinivasan, D. J. Manko, H. Koch, M. A. Enayetullah, and A. J. Appleby, "Recent Advances in Solid Polymer Electrolyte Fuel-Cell Technology with Low Platinum Loading Electrodes," (in English), *Journal of Power Sources,* vol. 29, no. 3-4, pp. 367-387, Feb 1990.

[60] G. F. McLean, T. Niet, S. Prince-Richard, and N. Djilali, "An assessment of alkaline fuel cell technology," (in English), *International Journal of Hydrogen Energy,* vol. 27, no. 5, pp. 507-526, May 2002.

[61] J. R. Varcoe, R. C. T. Slade, G. L. Wright, and Y. L. Chen, "Steady-state dc and impedance investigations of H-2/O-2 alkaline membrane fuel cells with commercial Pt/C, Ag/C, and Au/C cathodes," (in English), *Journal of Physical Chemistry B,* vol. 110, no. 42, pp. 21041-21049, Oct 26 2006.

[62] S. Gu *et al.*, "A Soluble and Highly Conductive Ionomer for High-Performance Hydroxide Exchange Membrane Fuel Cells," (in English), *Angewandte Chemie-International Edition,* vol. 48, no. 35, pp. 6499-6502, 2009.

[63] S. F. Lu, J. Pan, A. B. Huang, L. Zhuang, and J. T. Lu, "Alkaline polymer electrolyte fuel cells completely free from noble metal catalysts," (in English), *Proceedings of the National Academy of Sciences of the United States of America,* vol. 105, no. 52, pp. 20611-20614, Dec 30 2008.

[64] N. J. Robertson, H. A. Kostalik, T. J. Clark, P. F. Mutolo, H. D. Abruna, and G. W. Coates, "Tunable High Performance Cross-Linked Alkaline Anion Exchange Membranes for Fuel Cell Applications," (in English), *Journal of the American Chemical Society,* vol. 132, no. 10, pp. 3400-3404, Mar 17 2010.

[65] V. Mehta and J. S. Cooper, "Review and analysis of PEM fuel cell design and manufacturing," (in English), *Journal of Power Sources,* vol. 114, no. 1, pp. 32-53, Feb 25 2003.

[66] Y. Wang, K. S. Chen, J. Mishler, S. C. Cho, and X. C. Adroher, "A review of polymer electrolyte membrane fuel cells: Technology, applications, and needs on fundamental research," (in English), *Applied Energy,* vol. 88, no. 4, pp. 981-1007, Apr 2011.

[67] N. Mansor *et al.*, "Development of Graphitic-Carbon Nitride Materials as Catalyst Supports for Polymer Electrolyte Fuel Cells," (in English), *Polymer Electrolyte Fuel Cells 13 (Pefc 13),* vol. 58, no. 1, pp. 1767-1778, 2013.

[68] W. Vielstich, A. Lamm, and H. A. Gasteiger, *Handbook of fuel cells : fundamentals, technology, and applications*. Chichester, England ; Hoboken, N.J.: Wiley, 2003, p. 4 v.

[69] S. Srinivasan, D. J. Manko, H. Koch, M. A. Enayetullah, and A. J. Appleby, "Recent Advances in Solid Polymer Electrolyte Fuel-Cell Technology with Low Platinum Loading Electrodes," (in English), *Space Electrochemical Research and Technology (Sert) 1989,* vol. 3056, pp. 95-113, 1989.

[70] E. Agel, J. Bouet, and J. F. Fauvarque, "Characterization and use of anionic membranes for alkaline fuel cells," (in English), *Journal of Power Sources,* vol. 101, no. 2, pp. 267-274, Oct 15 2001.

[71] K. Fukuta, H. Inoue, Y. Chikashige, and H. Yanagi, "Improved Maximum Power Density of Alkaline Membrane Fuel Cells (AMFCs) by the Optimization of MEA Construction," (in English), *Batteries and Energy Technology (General) - 217th Ecs Meeting,* vol. 28, no. 30, pp. 221-225, 2010.

[72] F. T. Bacon, "The High Pressure Hydrogen-Oxygen Fuel Cell," (in English), *Industrial and Engineering Chemistry,* vol. 52, no. 4, pp. 301-303, 1960.

[73] R. P. O'Hayre, *Fuel cell fundamentals*. Hoboken, NJ: John Wiley & Sons, 2006, pp. xxii, 409 p.

[74] M. Cifrain and K. V. Kordesch, "Advances, aging mechanism and lifetime in AFCs with circulating electrolytes," (in English), *Journal of Power Sources,* vol. 127, no. 1-2, pp. 234-242, Mar 10 2004.

[75] E. Gulzow and M. Schulze, "Long-term operation of AFC electrodes with CO2 containing gases," (in English), *Journal of Power Sources,* vol. 127, no. 1-2, pp. 243-251, Mar 10 2004.

[76] L. A. Adams, S. D. Poynton, C. Tamain, R. C. T. Slade, and J. R. Varcoe, "A carbon dioxide tolerant aqueous-electrolyte-free anion-exchange membrane alkaline fuel cell," (in English), *Chemsuschem,* vol. 1, no. 1-2, pp. 79-81, 2008.

[77] M. Unlu, J. Zhou, and P. A. Kohl, "Self Humidifying Hybrid Anion-Cation Membrane Fuel Cell Operated Under Dry Conditions," (in English), *Fuel Cells,* vol. 10, no. 1, pp. 54-63, Feb 2010.

[78] S. Chempath, J. M. Boncella, L. R. Pratt, N. Henson, and B. S. Pivovar, "Density Functional Theory Study of Degradation of Tetraalkylammonium Hydroxides," (in English), *Journal of Physical Chemistry C,* vol. 114, no. 27, pp. 11977-11983, Jul 15 2010.

[79] T. J. Mason, J. Millichamp, T. P. Neville, P. R. Shearing, S. Simons, and D. J. L. Brett, "A study of the effect of water management and electrode flooding on the dimensional change of polymer electrolyte fuel cells," (in English), *Journal of Power Sources,* vol. 242, pp. 70-77, Nov 15 2013.

[80] G. C. Abuin, M. C. Fuertes, and H. R. Corti, "Substrate effect on the swelling and water sorption of Nafion nanomembranes," (in English), *Journal of Membrane Science,* vol. 428, pp. 507-515, Feb 1 2013.

[81] H. L. Yeager and A. Eisenberg, "Perfluorinated Ionomer Membranes - Introduction," (in English), *Acs Symposium Series,* vol. 180, pp. 1-6, 1982.

[82] K. Schmidt-Rohr and Q. Chen, "Parallel cylindrical water nanochannels in Nafion fuel-cell membranes," (in English), *Nature Materials,* vol. 7, no. 1, pp. 75-83, Jan 2008.

[83] T. A. Zawodzinski, T. E. Springer, F. Uribe, and S. Gottesfeld, "Characterization of Polymer Electrolytes for Fuel-Cell Applications," (in English), *Solid State Ionics,* vol. 60, no. 1-3, pp. 199-211, Mar 1993.

[84] T. A. Zawodzinski *et al.*, "Water-Uptake by and Transport through Nafion(R) 117 Membranes," (in English), *Journal of the Electrochemical Society,* vol. 140, no. 4, pp. 1041-1047, Apr 1993.

[85] P. Krtil, A. Trojanek, and Z. Samec, "Kinetics of water sorption in Nafionthin films - Quartz crystal microbalance study," (in English), *Journal of Physical Chemistry B,* vol. 105, no. 33, pp. 7979-7983, Aug 23 2001.

[86] A. Kongkanand, "Interfacial Water Transport Measurements in Nafion Thin Films Using a Quartz-Crystal Microbalance," (in English), *Journal of Physical Chemistry C,* vol. 115, no. 22, pp. 11318-11325, Jun 9 2011.

[87] D. L. Wood, J. Chlistunoff, J. Majewski, and R. L. Borup, "Nafion Structural Phenomena at Platinum and Carbon Interfaces," (in English), *Journal of the American Chemical Society,* vol. 131, no. 50, pp. 18096-18104, Dec 23 2009.

[88] M. A. Modestino *et al.*, "Self-Assembly and Transport Limitations in Confined Nafion Films," (in English), *Macromolecules,* vol. 46, no. 3, pp. 867-873, Feb 12 2013.

[89] D. K. Paul, K. Karan, A. Docoslis, J. B. Giorgi, and J. Pearce, "Characteristics of Self-Assembled Ultrathin Nafion Films," (in English), *Macromolecules,* vol. 46, no. 9, pp. 3461-3475, May 14 2013.

[90] S. K. Dishari and M. A. Hickner, "Antiplasticization and Water Uptake of Nafion Thin Films," (in English), *Acs Macro Letters,* vol. 1, no. 2, pp. 291-295, Feb 2012.

[91] M. B. Satterfield and J. B. Benziger, "Viscoelastic Properties of Nafion at Elevated Temperature and Humidity," (in English), *Journal of Polymer Science Part B-Polymer Physics,* vol. 47, no. 1, pp. 11-24, Jan 1 2009.

[92] C. W. Monroe, T. Romero, W. Merida, and M. Eikerling, "A vaporization-exchange model for water sorption and flux in Nafion," (in English), *Journal of Membrane Science,* vol. 324, no. 1-2, pp. 1-6, Oct 31 2008.

[93] Y. Tabuchi, R. Ito, S. Tsushima, and S. Hirai, "Analysis of in situ water transport in Nafion (R) by confocal micro-Raman spectroscopy," (in English), *Journal of Power Sources,* vol. 196, no. 2, pp. 652-658, Jan 15 2011.

[94] L. An, T. S. Zhao, Y. S. Li, and Q. X. Wu, "Charge carriers in alkaline direct oxidation fuel cells," (in English), *Energy & Environmental Science,* vol. 5, no. 6, pp. 7536-7538, Jun 2012.

[95] J. R. Varcoe, M. Beillard, D. M. Halepoto, J. P. Kizewski, S. D. Poynton, and R. C. T. Slade, "Membrane and Electrode Materials for Alkaline Membrane Fuel Cells," (in English), *Proton Exchange Membrane Fuel Cells 8, Pts 1 and 2,* vol. 16, no. 2, pp. 1819-1834, 2008.

[96] J. R. Varcoe *et al.*, "Anion-exchange membranes in electrochemical energy systems," (in English), *Energy & Environmental Science,* vol. 7, no. 10, pp. 3135-3191, Oct 2014.

[97] L. An, T. S. Zhao, Q. X. Wu, and L. Zeng, "Comparison of different types of membrane in alkaline direct ethanol fuel cells," (in English), *International Journal of Hydrogen Energy,* vol. 37, no. 19, pp. 14536-14542, Oct 2012.

[98] K. N. Grew and W. K. S. Chiu, "A Dusty Fluid Model for Predicting Hydroxyl Anion Conductivity in Alkaline Anion Exchange Membranes," *Journal of The Electrochemical Society,* vol. 157, no. 3, pp. B327-B337, 2010.

[99] Y. S. Li and T. S. Zhao, "Understanding the performance degradation of anion-exchange membrane direct ethanol fuel cells," (in English), *International Journal of Hydrogen Energy,* vol. 37, no. 5, pp. 4413-4421, Mar 2012.

[100] F. Karas, J. Hnat, M. Paidar, J. Schauer, and K. Bouzek, "Determination of the ion-exchange capacity of anion-selective membranes," (in English), *International Journal of Hydrogen Energy,* vol. 39, no. 10, pp. 5054-5062, Mar 26 2014.

[101] B. Bauer, H. Strathmann, and F. Effenberger, "Anion-Exchange Membranes with Improved Alkaline Stability," (in English), *Desalination,* vol. 79, no. 2-3, pp. 125-144, Dec 1990.

[102] S. Chempath, J. M. Boncella, L. R. Pratt, N. Henson, and B. S. Pivovar, "Density Functional Theory Study of Degradation of Tetraalkylammonium Hydroxides," *The Journal of Physical Chemistry C,* vol. 114, no. 27, pp. 11977-11983, 2010/07/15 2010.

[103] A. A. Zagorodni, D. L. Kotova, and V. F. Selemenev, "Infrared spectroscopy of ion exchange resins: chemical deterioration of the resins," (in English), *Reactive & Functional Polymers,* vol. 53, no. 2-3, pp. 157-171, 2002.

[104] V. Neagu, I. Bunia, and I. Plesca, "Ionic polymers - VI. Chemical stability of strong base anion exchangers in aggressive media," (in English), *Polymer Degradation and Stability,* vol. 70, no. 3, pp. 463-468, 2000.

[105] S. Chempath *et al.*, "Mechanism of tetraalkylammonium headgroup degradation in alkaline fuel cell membranes," (in English), *Journal of Physical Chemistry C,* vol. 112, no. 9, pp. 3179-3182, Mar 6 2008.

[106] E. N. Komkova, D. F. Stamatialis, H. Strathmann, and M. Wessling, "Anion-exchange membranes containing diamines: preparation and

stability in alkaline solution," (in English), *Journal of Membrane Science,* vol. 244, no. 1-2, pp. 25-34, Nov 15 2004.
[107] W. K. Musker, "Nitrogen Ylides from Tetramethylammonium Salts," (in English), *Journal of Chemical Education,* vol. 45, no. 3, pp. 200-&, 1968.
[108] C. S. Macomber, J. M. Boncella, B. S. Pivovar, and J. A. Rau, "Decomposition pathways of an alkaline fuel cell membrane material component via evolved gas analysis," (in English), *Journal of Thermal Analysis and Calorimetry,* vol. 93, no. 1, pp. 225-229, Jul 2008.
[109] C. G. Arges and V. Ramani, "Two-dimensional NMR spectroscopy reveals cation-triggered backbone degradation in polysulfone-based anion exchange membranes," (in English), *Proceedings of the National Academy of Sciences of the United States of America,* vol. 110, no. 7, pp. 2490-2495, Feb 12 2013.
[110] C. G. Arges, L. H. Wang, J. Parrondo, and V. Ramani, "Best Practices for Investigating Anion Exchange Membrane Suitability for Alkaline Electrochemical Devices: Case Study Using Quaternary Ammonium Poly(2,6-dimethyl 1,4-phenylene)oxide Anion Exchange Membranes," (in English), *Journal of the Electrochemical Society,* vol. 160, no. 11, pp. F1258-F1274, 2013.
[111] D. Y. Chen and M. A. Hickner, "Degradation of Imidazolium- and Quaternary Ammonium-Functionalized Poly(fluorenyl ether ketone sulfone) Anion Exchange Membranes," (in English), *Acs Applied Materials & Interfaces,* vol. 4, no. 11, pp. 5775-5781, Nov 2012.
[112] A. D. Mohanty, S. E. Tignor, J. A. Krause, Y. K. Choe, and C. Bae, "Systematic Alkaline Stability Study of Polymer Backbones for Anion Exchange Membrane Applications," (in English), *Macromolecules,* vol. 49, no. 9, pp. 3361-3372, May 10 2016.
[113] V. J. Bharath *et al.*, "Measurement of water uptake in thin-film Nafion and anion alkaline exchange membranes using the quartz crystal microbalance," (in English), *Journal of Membrane Science,* vol. 497, pp. 229-238, Jan 1 2016.
[114] Y. S. Li, T. S. Zhao, and W. W. Yang, "Measurements of water uptake and transport properties in anion-exchange membranes," (in English), *International Journal of Hydrogen Energy,* vol. 35, no. 11, pp. 5656-5665, Jun 2010.
[115] S. C. B.R. Einsla, L.R. Pratt, J.M. Boncella, J. Rau, C. Macomber and B.S. Pivovar "Stability of Cations for Anion Exchange Membrane Fuel Cells " *ECS Transactions,* vol. 11, no. 1, pp. 1173-1180, 2007.
[116] J. A. Vega, C. Chartier, S. Smith, and W. E. Mustain, "Effect of Carbonate on Oxygen Reduction, Hydrogen Oxidation and Anion Exchange Membrane Chemical Stability," (in English), *Polymer Electrolyte Fuel Cells 10, Pts 1 and 2,* vol. 33, no. 1, pp. 1735-1749, 2010.
[117] J. F. Zhou, M. Unlu, J. A. Vega, and P. A. Kohl, "Anionic polysulfone ionomers and membranes containing fluorenyl groups for anionic fuel cells," (in English), *Journal of Power Sources,* vol. 190, no. 2, pp. 285-292, May 15 2009.
[118] Fakuta K., Inoue H., Watanabe S., Yanagi H., "In-Situ Observation of CO2 through the Self-purging in Alkaline Membrane Fuel Cell (AMFC) " *ECS Transactions,* vol. 23-27, no. 19, 2009.
[119] Y. Matsui, M. Saito, A. Tasaka, and M. Inaba, "Influence of Carbon Dioxide on the Performance of Anion-Exchange Membrane Fuel Cells," (in English), *Ecs Transactions,* vol. 25, no. 13, pp. 105-110, 2010.
[120] J. L. Yan and M. A. Hickner, "Anion Exchange Membranes by Bromination of Benzylmethyl-Containing Poly(sulfone)s," (in English), *Macromolecules,* vol. 43, no. 5, pp. 2349-2356, Mar 9 2010.
[121] H. Yanagi and K. Fukuta, "Anion Exchange Membrane and Ionomer for Alkaline Membrane Fuel Cells (AMFCs)," (in English), *Proton Exchange Membrane Fuel Cells 8, Pts 1 and 2,* vol. 16, no. 2, pp. 257-262, 2008.
[122] A. Tewari, V. Sambhy, M. U. Macdonald, and A. Sen, "Quantification of carbon dioxide poisoning in air breathing alkaline fuel cells," (in English), *Journal of Power Sources,* vol. 153, no. 1, pp. 1-10, Jan 23 2006.

[123] T. P. Pandey *et al.*, "Interplay between water uptake, ion interactions, and conductivity in an e-beam grafted poly(ethylene-co-tetrafluoroethylene) anion exchange membrane," (in English), *Physical Chemistry Chemical Physics,* vol. 17, no. 6, pp. 4367-4378, 2015.

[124] A. H. England, A. M. Duffin, C. P. Schwartz, J. S. Uejio, D. Prendergast, and R. J. Saykally, "On the hydration and hydrolysis of carbon dioxide," (in English), *Chemical Physics Letters,* vol. 514, no. 4-6, pp. 187-195, Oct 6 2011.

[125] V.J. Bharath et al., "Effect of humidity on the interaction of CO_2 with alkaline anion exchange membranes probed using the quartz crystal microbalance," *International Journal of Hydrogen Energy,* vol. 42, no. 38, pp. 24301-24307, 2017.

[126] Q. J. Duan, S. H. Ge, and C. Y. Wang, "Water uptake, ionic conductivity and swelling properties of anion-exchange membrane," (in English), *Journal of Power Sources,* vol. 243, pp. 773-778, Dec 1 2013.

[127] V. J. Bharath *et al.*, "Alkaline anion exchange membrane degradation as a function of humidity measured using the quartz crystal microbalance," (in English), *International Journal of Hydrogen Energy,* vol. 42, no. 9, pp. 6243-6249, Mar 2 2017.

[128] K. M. Lakin, "A review of thin-film resonator technology," (in English), *Ieee Microwave Magazine,* vol. 4, no. 4, pp. 61-67, Dec 2003.

[129] J. M. Slater and E. J. Watt, "Examination of Ammonia Poly(Pyrrole) Interactions by Piezoelectric and Conductivity Measurements," (in English), *Analyst,* vol. 116, no. 11, pp. 1125-1130, Nov 1991.

[130] S. R. Systems, "QCM100- Quartz Crystal Microbalance Theory and Calibration," Available: http://www.thinksrs.com/downloads/PDFs/ApplicationNotes/QCMTheoryapp.pdf

[131] C. K. O'Sullivan and G. G. Guilbault, "Commercial quartz crystal microbalances – theory and applications," *Biosensors and Bioelectronics,* vol. 14, no. 8–9, pp. 663-670, 1999.

[132] J. P. Kizewski, N. H. Mudri, R. Zeng, S. D. Poynton, R. C. T. Slade, and J. R. Varcoe, "Alkaline Electrolytes and Reference Electrodes for Alkaline Polymer Electrolyte Membrane Fuel Cells," (in English), *Polymer Electrolyte Fuel Cells 10, Pts 1 and 2,* vol. 33, no. 1, pp. 27-35, 2010.

[133] E. R. Benes, R. Groschl, F. Seifert, and A. Pohl, "Comparison between BAW and SAW sensor principles," (in English), *Ieee Transactions on Ultrasonics Ferroelectrics and Frequency Control,* vol. 45, no. 5, pp. 1314-1330, Sep 1998.

[134] J. A. Vega and W. E. Mustain, "Effect of CO2, HCO3- and CO3-2 on oxygen reduction in anion exchange membrane fuel cells," (in English), *Electrochimica Acta,* vol. 55, no. 5, pp. 1638-1644, Feb 1 2010.

[135] L. A. Diaz, G. C. Abuin, and H. R. Corti, "Methanol sorption and permeability in Nafion and acid-doped PBI and ABPBI membranes," (in English), *Journal of Membrane Science,* vol. 411, pp. 35-44, Sep 1 2012.

[136] J. John *et al.*, "An Electrochemical Quartz Crystal Microbalance Study of a Prospective Alkaline Anion Exchange Membrane Material for Fuel Cells: Anion Exchange Dynamics and Membrane Swelling," (in English), *Journal of the American Chemical Society,* vol. 136, no. 14, pp. 5309-5322, Apr 9 2014.

[137] J. Millichamp *et al.*, "Application of a GaPO4 Crystal Microbalance for the Detection of Coke Formation in High-Temperature Reactors and Solid Oxide Fuel Cells," (in English), *Industrial & Engineering Chemistry Research,* vol. 50, no. 13, pp. 8371-8375, Jul 6 2011.

[138] J. Millichamp *et al.*, "A study of carbon deposition on solid oxide fuel cell anodes using electrochemical impedance spectroscopy in combination with a high temperature crystal microbalance," (in English), *Journal of Power Sources,* vol. 235, pp. 14-19, Aug 1 2013.

[139] J. Larminie and A. Dicks, *Fuel cell systems explained*, 2nd ed. Chichester, West Sussex: J. Wiley, 2003, pp. xxii, 406 p.

[140] J. W. Elam and M. J. Pellin, "GaPO(4) sensors for gravimetric monitoring during atomic layer deposition at high temperatures," (in English), *Analytical Chemistry,* vol. 77, no. 11, pp. 3531-3535, Jun 1 2005.

[141] F. Pascal-Delannoy, B. Sorli, and A. Boyer, "Quartz Crystal Microbalance (QCM) used as humidity sensor," (in English), *Sensors and Actuators a-Physical,* vol. 84, no. 3, pp. 285-291, Sep 1 2000.

[142] S. Y. Kwon, Y. I. Choi, J. C. Kim, and H. S. Nham, "A highly stable quartz crystal microbalance sensor and its application to water vapor measurements," (in English), *Journal of the Korean Physical Society,* vol. 48, no. 1, pp. 161-165, Jan 2006.

[143] K. Jaruwongrungsee, A. Tuantranont, Y. Wanna, A. Wisitsoraat, and T. Lomas, "Quartz Crystal Microbalance Humidity Sensor using Electrospun PANI Micro/nano Dots," (in English), *2007 7th Ieee Conference on Nanotechnology, Vol 1-3,* pp. 316-319, 2007.

[144] H. K. John J, Rivera-Meléndez J, Kostalik HA 4th, Rus ED, Wang H, Coates GW, Abruña HD., "An electrochemical quartz crystal microbalance study of a prospective alkaline anion exchange membrane material for fuel cells: anion exchange dynamics and membrane swelling.," *J Am Chem Soc,* pp. 5309–5322, 2014.

[145] T. A. Zawodzinski *et al.*, "A Comparative-Study of Water-Uptake by and Transport through Ionomeric Fuel-Cell Membranes," (in English), *Journal of the Electrochemical Society,* vol. 140, no. 7, pp. 1981-1985, Jul 1993.

[146] C. Vallieres, D. Winkelmann, D. Roizard, E. Favre, P. Scharfer, and M. Kind, "On Schroeder's paradox," (in English), *Journal of Membrane Science,* vol. 278, no. 1-2, pp. 357-364, Jul 5 2006.

[147] L. M. Onishi, J. M. Prausnitz, and J. Newman, "Water-nafion equilibria. Absence of Schroeder's paradox," (in English), *Journal of Physical Chemistry B,* vol. 111, no. 34, pp. 10166-10173, Aug 30 2007.

[148] J. R. Varcoe, R. C. T. Slade, E. L. H. Yee, S. D. Poynton, and D. J. Driscoll, "Investigations into the ex situ methanol, ethanol and ethylene glycol permeabilities of alkaline polymer electrolyte membranes," (in English), *Journal of Power Sources,* vol. 173, no. 1, pp. 194-199, Nov 8 2007.

[149] J. R. Varcoe, "Investigations of the ex situ ionic conductivities at 30 degrees C of metal-cation-free quaternary ammonium alkaline anion-exchange membranes in static atmospheres of different relative humidities," (in English), *Physical Chemistry Chemical Physics,* vol. 9, no. 12, pp. 1479-1486, 2007.

[150] D. Stoica, L. Ogier, L. Akrour, F. Alloin, and J. F. Fauvarque, "Anionic membrane based on polyepichlorhydrin matrix for alkaline fuel cell: Synthesis, physical and electrochemical properties," (in English), *Electrochimica Acta,* vol. 53, no. 4, pp. 1596-1603, Dec 31 2007.

[151] G. C. Abuin, P. Nonjola, E. A. Franceschini, F. H. Izraelevitch, M. K. Mathe, and H. R. Corti, "Characterization of an anionic-exchange membranes for direct methanol alkaline fuel cells," (in English), *International Journal of Hydrogen Energy,* vol. 35, no. 11, pp. 5849-5854, Jun 2010.

[152] J. T. Hinatsu, M. Mizuhata, and H. Takenaka, "Water-Uptake of Perfluorosulfonic Acid Membranes from Liquid Water and Water-Vapor," (in English), *Journal of the Electrochemical Society,* vol. 141, no. 6, pp. 1493-1498, Jun 1994.

[153] G. W. Li *et al.*, "Carbonation effects on the performance of alkaline polymer electrolyte fuel cells," (in English), *International Journal of Hydrogen Energy,* vol. 40, no. 20, pp. 6655-6660, Jun 1 2015.

[154] A. Saniere, I. Henaut, and J. F. Argillier, "Pipeline transportation of heavy oils, a strategic, economic and technological challenge," (in English), *Oil & Gas Science and Technology-Revue D Ifp Energies Nouvelles,* vol. 59, no. 5, pp. 455-466, Sep-Oct 2004.

[155] M. S. Rana, V. Samano, J. Ancheyta, and J. A. I. Diaz, "A review of recent advances on process technologies for upgrading of heavy oils and residua," (in English), *Fuel,* vol. 86, no. 9, pp. 1216-1231, Jun 2007.

[156] S. Chopra, L. Lines, D. Schmitt, and M. Batzle, "Heavy Oils: Reservoir Characterization and Production Monitoring Preface," (in English), *Heavy Oils: Reservoir Characterization and Production Monitoring,* vol. 13, pp. Xvii-Xix, 2010.

[157] J. G. Speight, *The chemistry and technology of petroleum*, 4th ed. (Chemical industries, no. 114). Boca Raton: CRC Press/Taylor & Francis, 2007, p. 945 p.

[158] J. A. Moulijn, M. Makkee, and A. v. Diepen, *Chemical process technology*. New York: John Wiley & Sons, 2001, pp. xii, 453 p.

[159] K. J. Leontaritis, "The asphaltene and wax deposition envelopes," (in English), *Fuel Science & Technology International,* vol. 14, no. 1-2, pp. 13-39, 1996.

[160] C. Bollet, J. C. Escalier, C. Souteyrand, M. Caude, and R. Rosset, "Rapid Separation of Heavy Petroleum-Products by High-Performance Liquid-Chromatography," (in English), *Journal of Chromatography,* vol. 206, no. 2, pp. 289-300, 1981.

[161] J. R. Becker, *Crude oil waxes, emulsions, and asphaltenes*. Tulsa, Okla.: Pennwell Books, 1997, pp. ix, 276 p.

[162] N. Aske, H. Kallevik, and J. Sjoblom, "Determination of saturate, aromatic, resin, and asphaltenic (SARA) components in crude oils by means of infrared and near-infrared spectroscopy," (in English), *Energy & Fuels,* vol. 15, no. 5, pp. 1304-1312, Sep-Oct 2001.

[163] J. Sjoblom *et al.*, "Our current understanding of water-in-crude oil emulsions. Recent characterization techniques and high pressure performance," (in English), *Advances in Colloid and Interface Science,* vol. 100, pp. 399-473, Feb 28 2003.

[164] B. J. Fuhr, C. Cathrea, L. Coates, H. Kalra, and A. I. Majeed, "Properties of Asphaltenes from a Waxy Crude," (in English), *Fuel,* vol. 70, no. 11, pp. 1293-1297, Nov 1991.

[165] L. H. Ali and K. A. Alghannam, "Investigations into Asphaltenes in Heavy Crude Oils .1. Effect of Temperature on Precipitation by Alkane Solvents," (in English), *Fuel,* vol. 60, no. 11, pp. 1043-1046, 1981.

[166] A. Hirschberg, L. N. J. Dejong, B. A. Schipper, and J. G. Meijer, "Influence of Temperature and Pressure on Asphaltene Flocculation," (in English), *Society of Petroleum Engineers Journal,* vol. 24, no. 3, pp. 283-293, 1984.

[167] P. Fotland, "Precipitation of asphaltenes at high pressures; Experimental technique and results," (in English), *Fuel Science & Technology International,* vol. 14, no. 1-2, pp. 313-325, 1996.

[168] H. Laux, I. Rahimian, and D. Browarzik, "Flocculation of asphaltenes at high pressure. I. Experimental determination of the onset of flocculation," (in English), *Petroleum Science and Technology,* vol. 19, no. 9-10, pp. 1155-1166, 2001.

[169] E. Y. Sheu, "Physics of asphaltene micelles and microemulsions - Theory and experiment," (in English), *Journal of Physics-Condensed Matter,* vol. 8, no. 25A, pp. A125-A141, Jun 17 1996.

[170] L. Z. Pillon, "Interfacial Properties of Petroleum Products," (in English), *Interfacial Properties of Petroleum Products,* vol. 120, pp. 1-348, 2007.

[171] T. R. Bott, *Fouling of heat exchangers* (Chemical engineering monographs, no. 26). Amsterdam ; New York: Elsevier, 1995, pp. xxii, 524 p.

[172] J. N. H. Tiratsoo, *Pipeline pigging technology*, 2nd ed. Houston: Gulf Pub. Co., 1992, pp. xx, 460 p.

[173] J. S. Buckley and J. X. Wang, "Crude oil and asphaltene characterization for prediction of wetting alteration," (in English), *Journal of Petroleum Science and Engineering,* vol. 33, no. 1-3, pp. 195-202, Apr 2002.

[174] S. Asomaning, "Petroleum chemistry and the fouling behavior of crude oils.," (in English), *Abstracts of Papers of the American Chemical Society,* vol. 226, pp. U259-U259, Sep 2003.

[175] J. J. Adams, "Asphaltene Adsorption, a Literature Review," (in English), *Energy & Fuels,* vol. 28, no. 5, pp. 2831-2856, May 2014.

[176] C. Drummond and J. Israelachvili, "Fundamental studies of crude oil-surface water interactions and its relationship to reservoir wettability," (in

English), *Journal of Petroleum Science and Engineering,* vol. 45, no. 1-2, pp. 61-81, Nov 30 2004.

[177] R. Z. Syunyaev, R. M. Balabin, I. S. Akhatov, and J. O. Safieva, "Adsorption of Petroleum Asphaltenes onto Reservoir Rock Sands Studied by Near-Infrared (NIR) Spectroscopy," (in English), *Energy & Fuels,* vol. 23, pp. 1230-1236, Mar-Apr 2009.

[178] J. S. Buckley and Y. Liu, "Some mechanisms of crude oil/brine/solid interactions," (in English), *Journal of Petroleum Science and Engineering,* vol. 20, no. 3-4, pp. 155-160, Jun 1998.

[179] J. L. M. de la Cruz, F. J. Arguelles-Vivas, V. Matias-Perez, C. D. Duran-Valencia, and S. Lopez-Ramirez, "Asphaltene-Induced Precipitation and Deposition During Pressure Depletion on a Porous Medium: An Experimental Investigation and Modeling Approach," (in English), *Energy & Fuels,* vol. 23, pp. 5611-5625, Nov 2009.

[180] M. Vafaie-Sefti and S. A. Mousavi-Dehghani, "Application of association theory to the prediction of asphaltene deposition: Deposition due to natural depletion and miscible gas injection processes in petroleum reservoirs," (in English), *Fluid Phase Equilibria,* vol. 247, no. 1-2, pp. 182-189, Sep 15 2006.

[181] A. Cosultchi, P. Rossbach, and I. Hernandez-Calderon, "XPS analysis of petroleum well tubing adherence," (in English), *Surface and Interface Analysis,* vol. 35, no. 3, pp. 239-245, Mar 2003.

[182] T. Masuda and K. Hashimoto, "Deactivation of zeolite catalysts by coke," (in English), *Deactivation and Testing of Hydrocarbon-Processing Catalysts,* vol. 634, pp. 62-76, 1996.

[183] C. H. Bartholomew, "Mechanisms of catalyst deactivation," (in English), *Applied Catalysis a-General,* vol. 212, no. 1-2, pp. 17-60, Apr 30 2001.

[184] C. Marchal, E. Abdessalem, M. Tayakout-Fayolle, and D. Uzio, "Asphaltene Diffusion and Adsorption in Modified NiMo Alumina Catalysts Followed by Ultraviolet (UV) Spectroscopy," (in English), *Energy & Fuels,* vol. 24, pp. 4290-4300, Aug 2010.

[185] I. Gawel, D. Bociarska, and P. Biskupski, "Effect of asphaltenes on hydroprocessing of heavy oils and residua," (in English), *Applied Catalysis a-General,* vol. 295, no. 1, pp. 89-94, Oct 13 2005.

[186] M. Barcenas, P. Orea, E. Buenrostro-Gonzalez, L. S. Zamudio-Rivera, and Y. Duda, "Study of medium effect on asphaltene agglomeration inhibitor efficiency," (in English), *Energy & Fuels,* vol. 22, no. 3, pp. 1917-1922, May-Jun 2008.

[187] C. L. Chang and H. S. Fogler, "Peptization and coagulation of asphaltenes in apolar media using oil-soluble polymers," (in English), *Fuel Science & Technology International,* vol. 14, no. 1-2, pp. 75-100, 1996.

[188] J. A. Ostlund, M. Nyden, H. S. Fogler, and K. Holmberg, "Functional groups in fractionated asphaltenes and the adsorption of amphiphilic molecules," (in English), *Colloids and Surfaces a-Physicochemical and Engineering Aspects,* vol. 234, no. 1-3, pp. 95-102, Feb 26 2004.

[189] S. W. Hasan, M. T. Ghannam, and N. Esmail, "Heavy crude oil viscosity reduction and rheology for pipeline transportation," (in English), *Fuel,* vol. 89, no. 5, pp. 1095-1100, May 2010.

[190] U. G. Romanova, H. W. Yarranton, L. L. Schramm, and W. E. Shelfantook, "Investigation of oil sands froth treatment," (in English), *Canadian Journal of Chemical Engineering,* vol. 82, no. 4, pp. 710-721, Aug 2004.

[191] Y. X. Zhao and F. Wei, "Simultaneous removal of asphaltenes and water from water-in-bitumen emulsion: I. Fundamental development," (in English), *Fuel Processing Technology,* vol. 89, no. 10, pp. 933-940, Oct 2008.

[192] A. Duong and K. J. Smith, "A model of ceramic membrane fouling during heavy oil ultrafiltration," (in English), *Canadian Journal of Chemical Engineering,* vol. 75, no. 6, pp. 1122-1129, Dec 1997.

[193] H. L. Wang, G. Wang, B. J. Shen, C. M. Xu, and J. S. Gao, "Upgrading Residue by Carbon Rejection in a Fluidized-Bed Reactor and Its Multiple Lump Kinetic Model," (in English), *Industrial & Engineering Chemistry Research,* vol. 50, no. 22, pp. 12501-12511, Nov 16 2011.

[194] O. C. Mullins *et al.*, "The colloidal structure of crude oil and the structure of oil reservoirs," (in English), *Energy & Fuels,* vol. 21, no. 5, pp. 2785-2794, Sep-Oct 2007.

[195] O. C. Mullins, E. Y. Sheu, Fine Particle Society. Meeting, American Chemical Society. Division of Fuel Chemistry., and American Chemical Society. Division of Petroleum Chemistry., *Structures and dynamics of asphaltenes / edited by Oliver C. Mullins and Eric Y. Sheu*. New York: Plenum Press, 1998, pp. x, 438 p.

[196] J. F. Schabron *et al.*, "Waxphaltene Determinator Method for Automated Precipitation and Redissolution of Wax and Asphaltene Components," (in English), *Energy & Fuels,* vol. 26, no. 4, pp. 2256-2268, Apr 2012.

[197] O. C. Mullins, *Asphaltenes, heavy oils, and petroleomics*. New York: Springer, 2007, pp. xxi, 669 p.

[198] H. Sabbah, A. L. Morrow, A. E. Pomerantz, and R. N. Zare, "Evidence for Island Structures as the Dominant Architecture of Asphaltenes," (in English), *Energy & Fuels,* vol. 25, no. 4, pp. 1597-1604, Apr 2011.

[199] S. Acevedo *et al.*, "Importance of asphaltene aggregation in solution in determining the adsorption of this sample on mineral surfaces," (in English), *Colloids and Surfaces a-Physicochemical and Engineering Aspects,* vol. 166, no. 1-3, pp. 145-152, Jun 15 2000.

[200] O. C. Mullins *et al.*, "Advances in Asphaltene Science and the Yen-Mullins Model," (in English), *Energy & Fuels,* vol. 26, no. 7, pp. 3986-4003, Jul 2012.

[201] S. Q. Wang, J. J. Liu, L. Y. Zhang, J. Masliyah, and Z. H. Xu, "Interaction Forces between Asphaltene Surfaces in Organic Solvents," (in English), *Langmuir,* vol. 26, no. 1, pp. 183-190, Jan 5 2010.

[202] R. Tanaka, E. Sato, J. E. Hunt, R. E. Winans, S. Sato, and T. Takanohashi, "Characterization of asphaltene aggregates using X-ray diffraction and small-angle X-ray scattering," (in English), *Energy & Fuels,* vol. 18, no. 4, pp. 1118-1125, Jul-Aug 2004.

[203] F. M. Faus, P. Grange, and B. Delmon, "Influence of Asphaltene Deposition on Catalytic Activity of Cobalt Molybdenum on Alumina Catalysts," (in English), *Applied Catalysis,* vol. 11, no. 2-3, pp. 281-293, 1984.

[204] P. M. Spiecker, K. L. Gawrys, C. B. Trail, and P. K. Kilpatrick, "Effects of petroleum resins on asphaltene aggregation and water-in-oil emulsion formation," (in English), *Colloids and Surfaces a-Physicochemical and Engineering Aspects,* vol. 220, no. 1-3, pp. 9-27, Jun 30 2003.

[205] S. Simon, J. Jestin, T. Palermo, and L. Barre, "Relation between Solution and Interfacial Properties of Asphaltene Aggregates," (in English), *Energy & Fuels,* vol. 23, no. 1, pp. 306-313, Jan-Feb 2009.

[206] O. C. Mullins, D. J. Seifert, J. Y. Zuo, and M. Zeybek, "Clusters of Asphaltene Nanoaggregates Observed in Oilfield Reservoirs," (in English), *Energy & Fuels,* vol. 27, no. 4, pp. 1752-1761, Apr 2013.

[207] M. R. Gray, R. R. Tykwinski, J. M. Stryker, and X. L. Tan, "Supramolecular Assembly Model for Aggregation of Petroleum Asphaltenes," (in English), *Energy & Fuels,* vol. 25, no. 7, pp. 3125-3134, Jul 2011.

[208] A. Zahabi and M. R. Gray, "Kinetics and Properties of Asphaltene Adsorption on Surfaces," (in English), *Energy & Fuels,* vol. 26, no. 2, pp. 1009-1018, Feb 2012.

[209] E. Czarnecka and J. E. Gillott, "Formation and Characterization of Clay Complexes with Bitumen from Athabasca Oil Sand," (in English), *Clays and Clay Minerals,* vol. 28, no. 3, pp. 197-203, 1980.

[210] A. Abudu and L. Goual, "Adsorption of Crude Oil on Surfaces Using Quartz Crystal Microbalance with Dissipation (QCM-D) under Flow Conditions," (in English), *Energy & Fuels,* vol. 23, pp. 1237-1248, Mar-Apr 2009.

[211] S. E. Moschopedis, J. F. Fryer, and J. G. Speight, "Investigation of Asphaltene Molecular-Weights," (in English), *Fuel,* vol. 55, no. 3, pp. 227-232, 1976.

[212] K. Kumar, E. Dao, and K. K. Mohanty, "AFM study of mineral wettability with reservoir oils," (in English), *Journal of Colloid and Interface Science,* vol. 289, no. 1, pp. 206-217, Sep 1 2005.
[213] P. Ekholm, E. Blomberg, P. Claesson, I. H. Auflem, J. Sjoblom, and A. Kornfeldt, "A quartz crystal microbalance study of the adsorption of asphaltenes and resins onto a hydrophilic surface," (in English), *Journal of Colloid and Interface Science,* vol. 247, no. 2, pp. 342-350, Mar 15 2002.
[214] S. Acevedo, M. A. Ranaudo, G. Escobar, L. Gutierrez, and P. Ortega, "Adsorption of Asphaltenes and Resins on Organic and Inorganic Substrates and Their Correlation with Precipitation Problems in Production Well Tubing," (in English), *Fuel,* vol. 74, no. 4, pp. 595-598, Apr 1995.
[215] O. Leon *et al.*, "Adsorption of native resins on asphaltene particles: A correlation between adsorption and activity," (in English), *Langmuir,* vol. 18, no. 13, pp. 5106-5112, Jun 25 2002.
[216] J. Castillo, S. Goncalves, A. Fernandez, and V. Mujica, "Applications of photothermal displacement spectroscopy to the study of asphaltenes adsorption," (in English), *Optics Communications,* vol. 145, no. 1-6, pp. 69-75, Jan 1 1998.
[217] S. I. Adersen, J. M. del Rio, D. Khvostitchenko, S. Shakir, and C. Lira-Galeana, "Interaction and solubilization of water by petroleum asphaltenes in organic solution," (in English), *Langmuir,* vol. 17, no. 2, pp. 307-313, Jan 23 2001.
[218] J. C. Petersen and H. Plancher, "Model studies and interpretive review of the competitive adsorption and water displacement of petroleum asphalt chemical functionalities on mineral aggregate surfaces," (in English), *Petroleum Science and Technology,* vol. 16, no. 1-2, pp. 89-131, 1998.
[219] Y. W. Jeon, S. H. Yi, and S. J. Choi, "Adsorption of Asphaltene Functionalities and Asphaltene on Goethite," (in English), *Fuel Science & Technology International,* vol. 13, no. 2, pp. 195-214, 1995.
[220] V. Nalwaya, V. Tantayakom, P. Piumsomboon, and S. Fogler, "Studies on asphaltenes through analysis of polar fractions (vol 43, pg 7682, 2004)," (in English), *Industrial & Engineering Chemistry Research,* vol. 43, no. 23, pp. 7682-7682, Nov 10 2004.
[221] H. Alboudwarej, D. Pole, W. Y. Svrcek, and H. W. Yarranton, "Adsorption of asphaltenes on metals," (in English), *Industrial & Engineering Chemistry Research,* vol. 44, no. 15, pp. 5585-5592, Jul 20 2005.
[222] C. Xing, R. W. Hilts, and J. M. Shaw, "Sorption of Athabasca Vacuum Residue Constituents on Synthetic Mineral and Process Equipment Surfaces from Mixtures with Pentane," (in English), *Energy & Fuels,* vol. 24, pp. 2500-2513, Apr 2010.
[223] K. C. S. Yao, "Removal of basic nitrogen compounds from extracted oils by use of acidic polar adsorbents and the regeneration of said adsorbents," United States, 1989. Available: http://www.freepatentsonline.com/4846962.html.
[224] D. Y. H. Ngan, "Process for removal of polynuclear aromatics from a hydrocarbon in an endothermic reformer reaction system," United States, 1989. Available: http://www.freepatentsonline.com/4804457.html.
[225] M. Gorbaty, "SELECTIVE ADSORPTION PROCESS FOR RESID UPGRADING," 1999. Available: http://www.freepatentsonline.com/WO1999031199.html.
[226] C. Russell and R. Sharpe, "Characteristics of heavy residue pyrolysis: A systematic approach to the design of fouling mitigation strategies using chemical additives," (in English), *Abstracts of Papers of the American Chemical Society,* vol. 244, Aug 19 2012.
[227] K. U. Ogbuneke, C. E. Snape, J. M. Andresen, S. Crozier, C. Russell, and R. Sharpe, "Identification of a Polycyclic Aromatic Hydrocarbon Indicator for the Onset of Coke Formation during Visbreaking of a Vacuum Residue," (in English), *Energy & Fuels,* vol. 23, pp. 2157-2163, Mar-Apr 2009.
[228] C. A. Russell, S. Crozier, and R. Sharpe, "Observations from Heavy Residue Pyrolysis: A Novel Method To Characterize Fouling Potential and

Assess Antifoulant Additive Performance," (in English), *Energy & Fuels,* vol. 24, pp. 5483-5492, Oct 2010.
[229] G. T. S. Savage, Russell, Christopher A. "SURFACE PASSIVATION METHOD FOR FOULING REDUCTION," United States, 2016. Available: http://www.freepatentsonline.com/y2016/0237357.html.
[230] D. Damjanovic, "Materials for high temperature piezoelectric transducers," (in English), *Current Opinion in Solid State & Materials Science,* vol. 3, no. 5, pp. 469-473, Oct 1998.
[231] T. Stevenson *et al.*, "Piezoelectric materials for high temperature transducers and actuators," (in English), *Journal of Materials Science-Materials in Electronics,* vol. 26, no. 12, pp. 9256-9267, Dec 2015.
[232] A. D. Katnani and K. I. Papathomas, "Kinetics and Initial-Stages of Oxidation of Aluminum Nitride - Thermogravimetric Analysis and X-Ray Photoelectron-Spectroscopy Study," (in English), *Journal of Vacuum Science & Technology a-Vacuum Surfaces and Films,* vol. 5, no. 4, pp. 1335-1340, Jul-Aug 1987.
[233] H. Fritze, M. Schulz, H. Seh, and H. L. Tuller, "Sensor application-related defect chemistry and electromechanical properties of langasite," (in English), *Solid State Ionics,* vol. 177, no. 26-32, pp. 2313-2316, Oct 31 2006.
[234] M. Schulz, J. Sauerwald, D. Richter, and H. Fritze, "Electromechanical properties and defect chemistry of high-temperature piezoelectric materials," (in English), *Ionics,* vol. 15, no. 2, pp. 157-161, Apr 2009.
[235] R. K. Kepple, E. R. Mantel, Klingenm.Oj, and R. L. Mattson, "Electrodeposited and Hardened Iron for Rolling Contact Fatigue Applications," (in English), *Mechanical Engineering,* vol. 92, no. 9, pp. 70-&, 1970.
[236] W. A. Macfadyen, "An aspect of electrolytic iron deposition," (in English), *Transactions of the Faraday Society,* vol. 15, no. 3, pp. 0098-0133, Jun 1920.
[237] V. Kellog, "Russian scientific aid," (in English), *Science,* vol. 56, pp. 717-717, Jul-Dec 1922.
[238] T. S. Baer and J. N. Anno, "Sputtering of Iron by Fast-Neutrons," (in English), *Journal of Applied Physics,* vol. 43, no. 5, pp. 2453-&, 1972.
[239] N. Imanishi, H. Ohta, S. Ninomiya, and A. Itoh, "Emission energy distribution of secondary ions produced through the electronic sputtering process under heavy ion bombardment," (in English), *Nuclear Instruments & Methods in Physics Research Section B-Beam Interactions with Materials and Atoms,* vol. 164, pp. 803-808, Apr 2000.
[240] B. Schweer and H. L. Bay, "On the Velocity Distribution of Excited Fe-Atoms by Sputtering of Iron," (in English), *Applied Physics a-Materials Science & Processing,* vol. 29, no. 2, pp. 53-55, 1982.
[241] F. Krispel *et al.*, "Properties and applications of singly rotated GaPO¡sub¿4¡/sub¿ resonators," in *Frequency Control Symposium and PDA Exhibition Jointly with the 17th European Frequency and Time Forum, 2003. Proceedings of the 2003 IEEE International*, 2003, pp. 668-673.
[242] P. W. Krempl, C. Reiter, W. Wallnofer, and J. Neubig, "Temperature sensors based on GaPO¡sub¿4¡/sub¿," in *Ultrasonics Symposium, 2002. Proceedings. 2002 IEEE*, 2002, vol. 1, pp. 949-952 vol.1.
[243] J. Nosek and M. Pustka, "About the coupling factor of the gallium orthophosphate (GaPO¡sub¿4¡/sub¿) and its influence to the resonance-frequency temperature dependence," in *Frequency Control Symposium and PDA Exhibition Jointly with the 17th European Frequency and Time Forum, 2003. Proceedings of the 2003 IEEE International*, 2003, pp. 674-678.
[244] D. Damjanovic, "Materials for high temperature piezoelectric transducers," *Current Opinion in Solid State and Materials Science,* vol. 3, no. 5, pp. 469-473, 1998.
[245] K. Jacobs, P. Hofmann, D. Klimm, J. Reichow, and M. Schneider, "Structural Phase Transformations in Crystalline Gallium Orthophosphate," *Journal of Solid State Chemistry,* vol. 149, no. 1, pp. 180-188, 2000.

[246] H. Seh and H. Tuller, "Defects and Transport in Langasite II: Donor-doped ($La_3Ga_{4.75}Nb_{0.25}SiO_{14}$)," *Journal of Electroceramics,* vol. 15, no. 3, pp. 193-202, 2005.

[247] H. Seh and H. Tuller, "Defects and transport in langasite I: Acceptor-doped ($La_3Ga_5SiO_{14}$)," *Journal of Electroceramics,* vol. 16, no. 2, pp. 115-125, 2006.

[248] P. A. S. GmbH, "High Temperature Microbalance Sensor Crystals," P. A. S. GmbH, Ed., ed. Graz: Piezocryst Advanced Sensorics GmbH, 2006.

[249] J. Detaint, B. Capelle, O. Cambon, and E. Philippot, "Properties of AT cut gallium phosphate resonators," in *Frequency Control Symposium and Exhibition, 2000. Proceedings of the 2000 IEEE/EIA International*, 2000, pp. 145-157.

[250] M. Schlesinger and M. Paunovic, *Modern electroplating*, 5th ed. (The electrochemical society series, no. 52). Hoboken, NJ: Wiley, 2010, pp. xv, 729 p.

[251] S. L. Diaz, J. A. Calderon, O. E. Barcia, and O. R. Mattos, "Electrodeposition of iron in sulphate solutions," (in English), *Electrochimica Acta,* vol. 53, no. 25, pp. 7426-7435, Oct 30 2008.

[252] T. L. Anderson, J. W. Laughner, and R. E. Newnham, "Laser-Induced Twins in Piezoelectric Quartz," (in English), *American Ceramic Society Bulletin,* vol. 55, no. 4, pp. 418-418, 1976.

[253] T. L. Anderson, R. E. Newnham, L. E. Cross, and J. W. Laughner, "Laser-Induced Twinning in Quartz," (in English), *Physica Status Solidi a-Applied Research,* vol. 37, no. 1, pp. 235-245, 1976.

[254] O. Cambon *et al.*, "Crystal growth of GaPO4, a very promising material for manufacturing BAW devices," (in English), *Annales De Chimie-Science Des Materiaux,* vol. 26, no. 1, pp. 79-84, Jan-Feb 2001.

[255] J.S.Millichamp, "Development of a novel high temperature crystal microbalance in-situ sensor for the study of electrode processes in solid oxide fuel cells," PhD, Chemical Engineering, UCL, 2013.